Quantifying Chromosomal Instability in Cancer

from first principles toward clinical value

by
Andrew R. Lynch

A dissertation submitted in partial fulfillment of the requirements for the degree of

Doctor of Philosophy
(Cellular and Molecular Pathology)

at the
University of Wisconsin – Madison
2023

Date of final oral examination: May 11th, 2023

The dissertation is approved by the following members of the Final Oral Committee:

Mark E. Burkard M.D., Ph.D., Professor, Medicine
Richard B. Halberg Ph.D., Professor, Medicine
Gopal Iyer Ph.D., Assistant Professor, Human Oncology
Donna M. Peters Ph.D., Professor, Pathology & Laboratory Medicine

TABLE OF CONTENTS

FIGURES AND TABLES

MANUSCRIPTS INCLUDED

Manuscript 1 (Chapters 1 & 5) — The Reckoning of Chromosomal Instability: past, present, and future. *Under review.*

Manuscript 2 (Appendix 1) — Toward a Unified Model of CIN: relating mechanism, mis-segregation rate, and nullisomy over single divisions *(working title). In progress.*

Manuscript 4 (Chapter 3) — A survey of CIN measures across inducible mechanistic models *(working title). In preparation.*

Manuscript 3 (Chapter 2) — Quantifying chromosomal instability from intratumoral karyotype diversity using agent-based modeling and Bayesian inference. *Andrew R Lynch, Nicholas L Arp, Amber S Zhou, Beth A Weaver, Mark E Burkard (2022). eLife 11:e69799*

Manuscript 5 (Chapter 4) — CINFER: an interactive web-based platform for inferring ongoing chromosome mis-segregation rates from single cell DNA sequencing data *(working title). In preparation.*

FINANCIAL SUPPORT

This work was supported by the following grants...

Project Grants

NCI Research Project Grant **R01CA234904**

NIGMS Research Project Grant **R01GM141068**

Training Grants

NCI Individual National Research Service Award **F31CA254247**

UW Cellular and Molecular Pathology NIGMS Institutional Training Grant **5T32GM081061**

UW Genomic Sciences NHGRI Training Grant **5T32HG002760**

UW Medical Scientist Training Program NIGMS Training Grant **T32GM008692**

- *Funded co-author Nick Arp (DOI: 10.7554/eLife.69799)*

UW Molecular and Cellular Pharmacology NIGMS Training Grant **T32GM008688**

- *Funded co-author Amber Zhou (DOI: 10.7554/eLife.69799)*

Resource Grants

University of Wisconsin Carbone Cancer Center Support Grant **P30CA014520**

NIH Shared Instrument Grant **1S10RR025483-01**

ABBREVIATIONS

ABC — approximate Bayesian computation

AO — anaphase-onset

bDNAseq — bulk DNA sequencing

bRNAseq — bulk RNA sequencing

CFS — contextual chromosome fitness score

CIN — chromosomal instability

NEB — nuclear envelope breakdown

scDNAseq — single cell DNA sequencing

scRNAseq — single cell RNA sequencing

TOE scores — Tumor-Oncogene-Essential gene scores

WGD — whole genome doubling

To the giants on whose shoulders I've stood…

… and those on whose I've leant.

ACKNOWLEDGMENTS

It's hard to overstate the challenge of pursuing a PhD. Spending years of your life on projects with indeterminate endpoints, working all hours of the day, solving some of the world's most challenging problems, with little in the way of income, all in an environment, necessarily, rife with intense skepticism. The prospect alone is a hurdle in itself. So why do it at all? Hopefully it's because you're a curious person who is passionate about a field of study. Though, maybe you feel it's part of your family legacy. Maybe you weren't ready to stop going to school to go get a 'big kid job.' Maybe you just want to prove to yourself that you can do it. Maybe you have a chip on your shoulder, and you want to prove it to someone else. Whatever the case, having the choice to pursue a PhD is a privilege, particularly if your way is paid, and not without its perks: flexibility, autonomy, and (hopefully) meaningful work. All of this is to say that the pursuit of a PhD is different for everyone, and it cannot be done alone. It will almost certainly always be a grind, but what differentiates a successful and positive experience from one mired, guideless, and miserable, is 'your people'. The people you meet along the way and who help in the endeavor, whether they know it or not.

To my thesis committee members, Drs. Donna Peters, Gopal Iyer, and Rich Halberg, who have been nothing but supportive and straightforward over the last five years — thank you for the productive discussions, sage advice, positive outlook, and prompt responses to so many recommendation letter requests.

To Dr. Zsuszanna Fabry, Joanne Thornton, and the rest of the Cellular and Molecular Pathology Training Program — thank you for giving me a chance and a fantastic jumping-off point for my scientific training.

To Drs. Dave Schwartz and Louise Pape, and the rest of the Genomic Sciences Training Program — thank you for revealing to me the boundless potential of genomics and encouraging us to ask the big questions.

To Becky Bound — thank you for guiding me through my first NIH grant submission, which opened so many doors.

To the thousands of faceless, anonymous programmers who take the time to write open-source software, helpful blog posts, and answer community questions — thank you for teaching me so much and helping me troubleshoot my code-woes. You're absolute heroes.

To those working in UW-Madison's several core facilities and other organizations which provide campus-wide services, namely Dr. Kathryn Fox with the UWCCC Flow Cytometry Core and Drs. Les Henderson and Kim Oxendine with the Wisconsin State Laboratory of Hygiene — thank you for answering so many questions and spending so much of your own time helping me work toward my goals.

To my fellow lab-members and others in the 'Mitosis Super Group', past and present — namely, Alka Choudhary, Rob Lera, James Johnson, Ryan Denu, Yang Hu, Roshan Norman, Saveda Majety, Rachel Sundstrom, Emily Kaufman, Zhouyuan Shen, Sherry Bradford, Anuoluwapo Mattix, Sierra Auleta, Madi Sass, Rebeca Garcia Varela, Ramya Varadarajan, Amber Zhou, John Tucker, Sarah Allen, Pippa Cosper — thank you. You

have all been instrumental to my work and development as a scientist. You've taught me to learn and to teach, done favors, worked toward my goals, provided helpful conversations, welcome distractions, baked goods, and support. I couldn't have done it without you.

To the leaders of the Mitosis Super Group, Drs. Beth Weaver and Mark Burkard, who have been my closest mentors — thank you both for your guidance and attention. To Mark, in particular, thank you for your enthusiastic outlook and for nurturing a positive, rigorous training environment. Most of all, thank you for trusting me to pursue this project with the resources and independence it required. Since we met when I interviewed for graduate school in early 2017, you have helped me to achieve my goals and build my confidence as a scientist. For that I'm grateful.

To my family and friends, who have instilled in me the necessary values for success, who supported my goals at every step, who listened with interest and tried their best to 'get it,' who ceaselessly expressed their pride and love, and who would do so 'even if I weren't getting a PhD.' Thank you, Mom, for instilling in me your work ethic and attention to detail and for always asking if I'm doing okay. Thank you, Dad, for instilling in me your good-humor to get through the hard-times and for always checking in and expressing your enthusiasm for things I'm doing. Thank you, Jeff, for impressing upon me your curiosity. I've always thought you were the 'smart one.' Christian, Jake, and Gus — my oldest friends. Thanks for keeping me grounded. Your unwavering presence and support continue to mean the world to me. Jake in particular, your astounding creativity running our D&D campaign got us all through the pandemic. I can't express how appreciative I am of

that alone. On that note, thank you Kirsten and Jody for your support as well. I love you all.

To Sassy and Django, if you're reading this — thank you for being the goodest pups.

Lastly and mostly, Erin, words cannot express how important your support was to this endeavor. Graduate school can be isolating, lonely, and disheartening. The best times I've had were the times I've been with you. You lift me up and wash away the self-doubt that so often arises. You make me pause to appreciate the exciting and rewarding moments too. Your ceaseless encouragement and reassurance have kept me going throughout the last few years. I love you dearly.

ABSTRACT

In normal tissue, mitosis is strictly regulated to ensure equal segregation of chromosomes into each daughter cell. However, this process can become dysregulated and fail in several ways causing chromosome mis-segregation, which is persistent in cancer. This persistent chromosome mis-segregation, otherwise called chromosomal instability (CIN), results in continuous gains and losses of chromosomes over time and is a nearly universal feature of cancer biology. The level of CIN (i.e., the rate at which these gains and losses occur in tumors) contributes to cancer progression in several ways. By rapidly increasing intratumoral genomic heterogeneity and promoting metastasis, drug resistance, and a litany of downstream mutational processes, elevated CIN associates with poor prognosis. On the other hand, elevated CIN is also associated with enhanced response to some chemotherapies. However, despite the clinical significance of the innate level of CIN in patients' tumors, there is no clinically accessible method of measuring CIN. Such a measure would improve patient prognostication and help determine who should receive certain chemotherapies. To overcome this obstacle, I have improved our overall approach to measuring CIN. Combining single cell genomics, which is becoming increasingly available, with bioinformatics, and computational experiments in tumor evolution, I have developed a method which can reliably infer quantitative mis-segregation rates from single cell DNA. Importantly, this method accounts for the confounding effect of ongoing karyotype selection. In validating this method, I elucidated the baseline mis-segregation rates that mediate the mechanism of action of paclitaxel as well as the range of mis-segregation rates that occur in breast and colorectal cancer. In development of this approach,

I also uncovered the primary mode of ongoing karyotype selection and threshold conditions for populations' tolerance of nullisomy, complete loss of a homologous set of chromosomes. When performed in tandem in cell-line models with inducible CIN, I find that this method outperforms most other CIN measures and that another widely used method of CIN measurement, the CIN70 score, does not actually reflect ongoing CIN. I then demonstrate a user-friendly tool that delivers this method for any who wish to measure CIN in their experimental or clinically derived samples. The work described here improves our understanding of the relevant rates (and their limits) of chromosome mis-segregation in cancer and brings us closer to the clinical measure of CIN.

1

THE RECKONING OF CHROMOSOMAL INSTABILITY: PAST AND PRESENT

Adapted from Lynch, Bradford, and Burkard. (Manuscript 1). Under review.

INTRODUCTION

During a series of lectures on applications of electricity in 1883, Sir William Thompson stated, “In physical science, a first essential step in the direction of learning any subject is to find principles of numerical reckoning and methods for practicably measuring some quality connected with it” (1). The timing of Thompson’s talk coincided with a wave of seminal work in the nascent fields of chromosome biology and cell division. Two of Thompson’s contemporaries, Theodor Boveri and David Paul von Hansemann, with remarkable prescience, proposed a role for abnormal cell divisions in tumorigenesis (2–4). These observations served as seeds for what would later be understood as a basic mechanism of oncogenesis: chromosomal instability (CIN). Though Boveri’s and Hansemann’s hypotheses are now supported by numerous additional findings, and CIN is an established feature of tumor biology, we still lack “principles of numerical reckoning” that would allow for the rapid measure of CIN in human cancers.

Understanding CIN and its consequences has progressed hand-in-hand with fundamental knowledge of cell and chromosome biology. From the inception of microscopy as

a scientific method and the first observations of cells' nuclei, new methods of observation and measurement have uncovered ever deeper insights into cell division, its errors, and their frequency and consequences in disease. Yet there are still many questions about CIN's contribution to cancer progression. These questions will be advanced by improved quantitative measures of CIN.

In this review, we discuss the origins of CIN as a field (Figure 1.1) and how methodological development has impacted the field and our understanding of the CIN's causes, consequences, and frequency (particularly in the context of cancer). We then propose a standardization of CIN measures, Mis-segregations per Diploid Division (MDD) (Table A2.1), and look forward to the future of the field, asking, "what can new CIN measures give us?"

THE GIANTS OF CIN: A SHORT HISTORY

Microscopy, Cytology, and the Birth of Modern Biology (1665-1888)

Though Theodor Boveri and David Paul von Hansemann are commonly cited as the earliest investigators of CIN, there is a rich history of work that enabled Boveri's observations in Ascaris megalocephala (nematode) and Paracentrotus lividus (sea urchin) and Hansemann's in cancers and which informed their eventual hypotheses. Of course, none of these studies would have been possible without the compound microscope. Though invented in the late 16th century (5), leading to Robert Hooke's first observation of and coining of the term cell (6), it wasn't until Antonie van Leeuwenhoek that animal cells were regularly studied under the compound microscope. Of particular relevance here is Leeuwenhoek's observation of the nucleus — which he referred to as a globule — in the blood

cells of salmon and cod (7, 8). Leeuwenhoek did not understand these globules' significance at the time as it was just one of the many discoveries characteristic of the cellular cataloging he and Hooke undertook, the phenomenology which would become a characteristic of cell science until the mid-20th century. His observation of the nucleus was of course a critical discovery for many fields including those of genetics, cell division and chromosome biology. The name nucleus was eventually coined in 1831 by Robert Brown while studying the cellular morphology and reproduction of orchids (9). Brown's detailing of nuclei, made possible by the development of the achromatic microscope, came at the fore of a wave of consequential studies throughout the rest of the 19th century that would transform biology.

A few years later, a Botanist named Hugo von Mohl who studied algae made a crucial observation which we now take for granted. His alga were dividing. Hugo von Mohl became the first to suggest that new cells are generated by division (10). This was later confirmed by Robert Remak in 1852 (11) and popularized by Rudolf Virchow in 1855 (12). The work of Mohl and Remak refuted the hypothesis of spontaneous cellular generation and was summarized by Virchow as, "*omnis cellula e cellula*" — "all cells from cells." This itself was an extension of Francesco Redi's, "*omne vivum ex vivo*" — "all life from life" (13), which turned out to be a timely homage.

Over the next decade, Charles Darwin and Alfred Wallace would describe their new theory of natural selection (14) and Gregor Mendel would publish his studies of heredity in pea plants (15). Though the latter's work would go unnoticed for some time, the concept of heredity was not new and the identity of the physical carriers of heredity were frequently

speculated upon. In 1869 Friedrich Miescher would isolate chromatin, which he named *nuclein*, from nuclear extracts of surgical bandages and in 1877 Oscar Hertwig discovered the mechanism of sexual fertilization and the involvement of the nucleus, later noting that Miescher's *nuclein* is the key component of fertilization and heredity (16–19). Yet the structures that actually packaged *nuclein* in the nucleus had yet to be visualized. So, in 1879, Julius Arnold became the first to publish drawings of individual chromosomes (yet unnamed) in the dividing cells of tumors (20). Moreover, many of these drawings depicted the characteristic 'Y' and 'X' shaped metaphase plates of multipolar mitotic cells, a common phenotypic expression of chromosomal instability. However, the chromosomes in Arnold's renderings are simplistic. It wasn't until Walther Flemming pioneered the use of aniline dyes as histological stains and published his seminal 1882 book, *Zellsubstanz, Kern und Zelltheilung*, that a modern view of cell division took shape (though, it is worth noting that Flemming's initial findings, without the stunning drawings, were first published in 1878, before Julius Arnold's) (21). In the stained tissue sections of salamanders, Flemming saw dividing cells bearing 'thread-like' structures after which he would coin the name *mitosis* (after the Greek for *thread*). The unprecedented resolution allowed Flemming to carefully characterize discrete phases of mitosis and how his nuclear threads moved throughout. Finally, in a manuscript relating karyokinesis and fertilization published in 1888, Heinrich Wilhelm Gottfried von Waldeyer-Hartz would rename Flemming's 'nuclear threads' as 'stainable bodies', or *chromosomes* (22, 23).

Chromosome Biology at the Nexus (1889-1914)

Though Oscar Hertwig had concluded that the nucleus was the carrier of heredity, his work had been observational; he had no experimental evidence. Enter Theodor Boveri. Boveri had joined the laboratory of Richard Hertwig (Oscar's brother) at the Zoological Institute in Munich around 1886 (24). Building on the Hertwig's previous work on the merogonic fertilization of enucleated sea urchin eggs (25), Boveri showed that fertilization of enucleated *Sphaerechinus* eggs with the sperm of *Echinus* produced a merogone hybrid (i.e., produced asexually from a haploid and enucleated germ cells) resembling the *Echinus* species. Thus, in 1889, he definitively concluded that the nucleus, rather than the cytoplasm, is the carrier of heredity (26).

In parallel, Boveri performed experiments in the double-fertilization of sea urchin eggs, characterizing the morphology of the resulting cell divisions. Work which resulted in the most comprehensive collection of examples of abnormal mitoses up to that point (27). This was quickly followed by David Paul von Hansemann's celebrated illustrations of abnormal mitoses in carcinoma cells, depicting every phenotypic expression of CIN we see today (3, 4). Hansemann was the first to acknowledge that "asymmetric" karyokinesis is an abnormal event that would lead to daughter cells with unequal chromosome numbers and that they are commonly observed in cancer, thus seeding what would become the field of chromosomal instability. Gino Galeotti supported Hansemann in his assessment, further noting that more proliferative tumors exhibit more frequent asymmetric divisions, perhaps the first published acknowledgment of the relative levels of CIN between tumors (28). Though, Hansemann later clarified his thoughts on their importance in cancer as

being a consequence, not a cause, of anaplasia (29, 30). Nevertheless, Hansemann's views certainly influenced Boveri's and in 1902, in a study on multipolar mitoses in sea urchin eggs, he first speculated that asymmetric divisions, including multipolars, may be a cause of tumor formation (31).

Boveri was influenced by another scientist whose work had only recently been brought to his attention. In 1900, three botanists independently rediscovered and confirmed Gregor Mendel's laws of inheritance (32–35). The Mendelian laws provided a framework that complemented Boveri's (and Beneden's) previous observations of meiosis. The eggs of the roundworm *Ascaris*, upon maturation, undergo a division (meiosis) that results in daughter nuclei about half the size of the mother (haploidy) and that egg and sperm nuclei of *Ascaris* contribute equally to fertilization (27, 36–38). Further analysis of dispermic-fertilized sea urchin development after multipolar divisions allowed Boveri to conclude that each individual chromosome is important to development and are the mediators of Mendel's laws of heredity (39). In combination with the contemporaneous work of Walter Sutton in mapping Mendelian patterns back to the homologous chromosomes of grasshoppers (*Brachystola*), wherein he states, *"Thus the phenomena of germ-cell division and of heredity are seen to have the same essential features,"* this collective work of Boveri and Sutton at this time became known as the Boveri-Sutton chromosome theory of inheritance (40, 41). However, the theory had its detractors. Of note is the work of Paolo Della Valle who opposed the concept of chromosome individuality and posited that chromosome numbers are not constant but vary around a typical chromosome number for the

species. He described this as *teoria dei cromosomi labile* — or *chromosome instability* (42, 43).

A year before Boveri's death, spurred by Otto Aichel's supposition of tumorigenesis via cell-fusion-induced aneuploidy, Boveri laid forth his perspective in detail, recalling his earlier view that asymmetric division and resulting aneuploidy was the cause of tumorigenesis (2). His much-lauded treatise would draw on ideas from decades of cytology to natural selection to genetics. The synthesis of these concepts, now fundamental, but controversial at the time, is a remarkable demonstration of scholarship, logic, and creativity. While defending his primacy on the topic, he also provides ample credit to the ideas of David Paul von Hansemann whose findings certainly guided his thinking. Though not acknowledged or cited, the additional intellectual contributions of his wife Marcella O'Grady Boveri (24, 44, 45) as well as Drs. Nettie Stevens, Mary Hogue, and Alice Boring, all of whom worked in his laboratory, should not be ignored. These factors come together here to develop a hypothesis with profound foresight and lasting relevance:

> *Abnormal mitoses can generate a host of different chromosome combinations so that, if our hypothesis is correct in principle, those combinations that make a cell a tumour cell must turn up occasionally, whether this is due merely to the absence of certain chromosomes or, in addition, to an excess of one sort of chromosome relative to the others.*
>
> *However this might arise, a particular tumour will be the result.*

The New Science of Instability (1914-1941)

The identification of chromosomes as units of heredity was a watershed moment for genetics. With it came the recognition that abnormal chromosome segregation may affect form and function, not just in tumors, but in all tissues of all organisms. Calvin Bridges, working under Thomas Hunt Morgan, would publish his proofs of chromosome theory (46–48). He coins the term *non-disjunction* and demonstrates that this failure of chromosome separation causes sex differences and gynandromorphism, the presentation of both sex organs, in *Drosophila*. He also calls on contemporaneous work in other plant and animal model systems which display somatic variegation or mosaicism which were of rising interest.

The study of germinal and somatic variegation largely began in the wake of the rediscovery of Mendel's work as it was noted that the phenotypes of many plants do not conform to the principles he laid out. References to *germinal instability* arose in relation to variegation within and between species of *Oenothera* (49). Later, *genetic instability* was commonly used more generally to refer to germinal and somatic variegation in a host of organisms including *Oenothera* (50)*, Drosophila, and* maize. However, these mentions were rarely attributed explicitly to chromosome mis-segregation and often focused on genes responsible for variegation. With few exceptions (51, 52), the quantitative nature of these studies on somatic variegation primarily focused on the frequency and degree of phenotypic outcomes rather than the frequency of segregation errors (50, 53–55). The explicit association of abnormal chromosome structure and segregation with somatic mosaicism, particularly in *Drosophila* and maize, was catalyzed by the increasing availability

of X-ray technology in research labs throughout the 1920s-30s. Irradiation caused variation in eye color, morphology of leg bristles and wings as well as gynandromorphism; all noted in relation to increases in chromosome abnormalities (56–63).

The study of cytogenetic variation and its effect on organismal form and fitness became a full-fledged discipline of its own. However, most studies, despite experimentation with crossing and irradiation, produced largely phenomenological conclusions with speculation on molecular mechanisms. Dr. Barbara McClintock changed this. Interested in the variegated striations of pigment on the stalks of *Zea mays*, Dr. McClintock sought the mechanism of this variegation. By 1938, she had already identified and mapped the locus responsible for the appearance of this recessive pigmentation (*Bm1*) and demonstrated (along with Dr. George Beadle) that stalk and endosperm variegation corresponded to the presence of ring-shaped or ‘sticky‘ mitotic chromosomes (64–68). Putting these pieces together, she showed 1) irradiation of pollen spores causes chromosome breaks, rearrangements, and fusions which produce chromatin bridges during mitosis; 2) these bridges break during mitosis and subsequently form dicentric chromosomes; 3) these dicentric chromosomes also produce mitotic chromatin bridges, generating continuous chromosome rearrangement; 4) the *Bm1* locus can be maintained or lost through these cycles, and 5) that this continuous genetic alteration determines the variegated patterns on the stalks of *Zea mays* (69–71). Dr. Barbara McClintock detailed the first complete mechanism of chromosomal instability — breakage-fusion-bridge cycles — from cause, to mitotic defect, to genetic alteration, to phenotypic expression. Her work ushered the

field of chromosomal instability from the phenomenological to the mechanistic and molecular.

CIN as a Quantitative Science (1941-1960)

That X-ray's and other mutagens elicit mitotic errors in model organisms, cultures, and tumors themselves, which coincide with carcinogenic (and therapeutic) properties was not lost on researchers of the 40's and 50's (72). PC Koller, seeking to characterize mitotic abnormalities in the absence of these mutagens, coupled rapid fixation and staining with enhanced contrast, allowing a broad survey of mitosis in a variety of tumors (73). His new method allowed quicker microscopic characterization of mitosis in a large number of tumors from different sources. Additionally, he observed that chromosome bridges were the most common mitotic error and that, within a single tumor, cell-to-cell chromosome counts and region-specific error rates are variable, evidence of the intratumor heterogeneity (ITH) so evident today (74). His improvement of mitotic chromosome preparation and analysis was one of three concurrent methodological developments critical for the quantitative study of chromosomal instability, along with phase-contrast microscopy and tissue culture.

Phase-contrast microscopy (75), was rapidly adopted by cell biologists. Leveraging interference between background light with light scattered as it passes through the cell, phase-contrast illuminates cellular structures without the use of toxic dyes, critical for the longitudinal study of cell division. Phase-contrast microscopy allowed for detailed descriptions of the dynamics of chromatin coiling (76), mitotic duration (77), and confirmation of the presence of mitotic spindle fibers (78, 79).

Tissue culture developed rapidly during the 1940s-50s as a result of the race to develop a polio vaccine (80), and enhanced our ability to isolate tumor cells and interrogate the longitudinal nature of genetic instability and its effect on cell fitness. By 1955, the first immortalized cell line (HeLa) had been established and Harry Eagle would publish his 'minimum essential medium' for tissue culture (81, 82).

Dr. Albert Levan's laboratory used phase-contrast microscopy and improved methods of tissue culture and chromosome analysis (73, 83, 84), to interrogate CIN's role in cancer and to establish a fundamental principle of human karyotypes. Using a new hypotonic preparation of mitotic chromosomes for counting, they identified near-diploid and near-tetraploid mouse tumors from ascites samples. The near-tetraploid cells seeded tumors in different mouse strains, while growth of near-diploid tumor cells was strain-specific, early evidence that karyotypes may affect tumor aggressiveness and immune evasion (85). While visiting Levan's laboratory, Dr. Joe Hin Tjio further improved this hypotonic chromosome preparation to precisely enumerate human chromosomes. In 1956 the two would publish *The chromosome number of man*, and go on to lead a convention to settle the nomenclature of the human karyotype (86, 87). Notably, the discovery came four years after Rosalind Franklin's famous *Image 51* of DNA's structure was taken (88).

Finally, recalling the term *chromosomal instability,* Levan and Biesele performed serial culture and mitotic and chromosomal analysis of normal mouse skin cells in an experiment similar to what might be performed today (89). Using mitotic chromosome counts and analysis of abnormal anaphases over generations of cultured normal cells, they that normal cells generally maintain the normal complement of chromosomes, yet occasionally

acquire chromosomal instability. The karyotypes of their chromosomally unstable populations changed and diversified over time as the fittest cells outcompeted the others, eventually exhibiting malignant properties such as continuous growth and the ability to form tumors when re-seeded in mice. They confirmed that evolutionary action on chromosomal instability can drive malignancy and did so using the modernized methods of analysis employed today.

THE OBSERVABLE

Modern Cytogenetics

Mitotic chromosomes and micronuclei. Levan and colleagues' methodological improvements catalyzed the field of cytogenetics. The ability to accurately identify the correct number of chromosomes lead to identification of conditions caused by aneuploid karyotypes and chromosomal instability. The aneuploid causes of Down Syndrome (47, +21), Klinefelter Syndrome (47, XXY), and Turner's Syndrome (45, XO) were all identified in 1959 (90–92). The Philadelphia chromosome, which Nowell and Hungerford described as a 'minute' chromosome, was also identified in 1959 in chronic granulocytic leukemia (93). Then, DNA rings (or double minutes) were identified among the scatter of mitotic chromosome spreads of many cancer cell samples and, as McClintock had concluded, are the result of DNA damage (94). Later, chromosome breakage syndromes like Bloom Syndrome and Fanconi Anemia would be identified by their increased frequency of abnormal chromosomes (95, 96). Total and abnormal chromosome counts were the mainstay of cytogenetics for many years and remain in use. While time consuming and insufficient for determining mis-segregation rates, the distribution of chromosome counts

provides a window to chromosomal diversity and polyploidy (97, 98). The variation in the population can be estimated as the the standard deviation of the count distribution or the percent of non-modal chromosome counts, both measures of CIN. Further, chromosome counts are more direct than phenotype-inferred quantification of non-disjunction rates such as those previously used in *Oenothera* and *Zea mays* (49, 66).

With the rise of mitotic chromosome analysis in the 1950's-60's, the presence of micronuclei in human samples was quickly recognized (99). Micronuclei, small nuclei which may contain chromosome fragments to multiple chromosomes, often result from chromosome mis-segregation, and thereby chromosome pulverization, or chromothripsis (100–105). Analogous to the frequency of abnormal mitotic chromosomes, the frequency of micronuclei in interphase cells has been used to quantify CIN (106). This is advantageous as micronuclei are often observable in cancer tissue sections, though the number and identity of chromosomes, particularly acentric chromosomes, in a micronucleus is challenging to determine.

The development of chromosome banding protocols addressed the problem of chromosome identity in routine mitotic chromosome analysis (107, 108). This likewise improved the detection of structural variation in karyotypes and resulted in a new nomenclature for karyotype alterations. For example, the Philadelphia chromosome was found to be a reciprocal translocation — t(9;22) (109). Since the development of banding protocols, a host of new fluorometric karyotyping techniques, such as multicolor-FISH and spectral karyotyping have been developed (110, 111). These can be multiplexed with banding protocols and are faster to prepare and analyze, but offer less resolution than a

simple banding analysis. Much like distributions of chromosome counts, the diversity of karyotypes has been used as a measure of CIN (112). Nevertheless, the numerical and structural complexity and heterogeneity of these karyotype data provide a more granular view of the diversity within the population and complexity of rearrangements in a given cell. Over time, karyotypes from thousands of samples reported in the literature have been compiled into catalogs and databases (113, 114), which themselves have been used to assess the relative levels of CIN between cancer types (115, 116).

Fluorescence in situ hybridization (FISH). The concomitant development and proliferation of stable fluorescent dyes (117) and *in situ* DNA hybridization methods (118–120) enabled the fluorescent detection of specific DNA sequences and improved measures of cell-cell variation of chromosome copy numbers. Because FISH probes can be targeted to centromeric and telomeric DNA repeat sequences and multiplexed using different fluorochromes, FISH allows measurement of the variance for a limited set of chromosomes across a population. By subcloning and expanding cells for a fixed number of divisions, the resulting variance of FISH probes can be used to calculate a range of mis-segregation rates. While not feasible in a clinical setting, this method has been used in cancer cell line experiments to estimate the first empirically derived chromosomal mis-segregation rates (*per chromosome per division*) or mis-segregations per diploid division (MDD) (121–123). Though it is worth noting that these measures don't account for natural selection on karyotypes or non-random chromosome mis-segregation.

Limitations of cytogenetics. Although cytogenetic studies have been critical to the field, they are a proxy measure of a dynamic process — a snapshot in time. Chromosome

counts, banding patterns, and FISH-based measures all may be subject to natural selection on karyotypes, thus masking the true variability generated by CIN. Both chromosome counts and FISH are prone to noise and artifacts of sample preparation due to poor chromosome spreading and tissue sectioning. Individually, chromosome counts require mitotic cells to obtain a sample, which may not always be possible and biases samples toward cells viable enough to enter the cell cycle. Because FISH probes target specific sequences, they likely will not detect structural changes to the target chromosome, thus underestimating structural and potentially numerical CIN. Micronuclei frequencies are indicative of abnormal mitoses, but cannot, on their own, reveal if a mis-segregation has occurred. Accordingly, inferences of CIN from any of these methods should be interpreted in light of these limitations.

Modern Mitotic Imaging

In addition to the advancements that led to the development of FISH, the foundation for the use of fluorescence microscopy in cell biology was laid by advancements throughout the 1950's (invention of the laser), '60's (isolation of GFP), and '70's (inception of recombinant molecular cloning) (124–127). The subsequent development of myriad fluorophores that can be expressed in cells and observed in real time ensured that direct observation of mitosis remained the gold-standard measure of CIN (128, 129). Today, most microscopy experiments designed to study CIN use fluorescence to visualize one or more of the following: centrosomes or centrioles, kinetochores, centromeres, microtubules and, of course, chromosomes. Even the real-time visualization of specific homologous chromosomes is increasingly common using Cas-based systems to target

chromosome-specific repetitive sequences (130–132). Tagging the major structures involved in cell division has allowed more comprehensive analysis of the causes and consequences of mitotic defects in experimental and clinical *ex vivo* settings. However, traditional histological staining remains the most common method of assessing mitotic defects in patient tissue.

Mitotic phenotypes of CIN. There has been long-standing recognition that different types of mitotic errors likely signal different mechanisms by which CIN is acquired. For clarity, we will differentiate between a mitotic *phenotype* of CIN and the molecular *mechanism* that produces the phenotype. The canonical phenotypes of CIN have changed very little since the days of Flemming, Hansemann, and Boveri. While there is still much to be revealed about how defects in cellular processes produce CIN, the relative frequency of these defects can tell us a great deal about the cellular processes involved. Thus the identification of the primary phenotypes of CIN in certain cancers is important and remains of interest.

Lagging chromosomes are thought to be the most common mitotic defect across all cancers. These chromosomes, which lag behind the segregating chromosome masses during anaphase, commonly arise when microtubules from opposing poles attach to the same kinetochore and are not corrected (i.e., merotelic attachment). Lagging chromosomes have been the most commonly observed defect in cancer and non-cancer cell lines (133–137). This would suggest defective attachment error correction and/or spindle assembly checkpoint mechanisms as the primary source of CIN. However, in stained histological tissue sections from patients' tumors, lagging chromosomes can be challenging

to differentiate from bridging chromosomes, which, as McClintock discovered, are caused by DNA damage and breakage-fusion-bridge cycles. Chromosome bridges are the most common mitotic error in colorectal and ovarian cancer patient-derived organoids (138, 139), indicating unchecked DNA damage as a primary source of CIN in cancer. Alternatively, it could be that different cancer types have distinct landscapes of mitotic errors. Further highlighting this, a recent study found neither lagging nor bridging chromosomes, but misaligned chromosomes, as the most common CIN phenotype in primary and metastatic breast cancer tissue samples (140). Misaligned chromosomes arise from defective chromosome transit to the metaphase plate, attachment error correction, or spindle assembly checkpoint and vary in severity from slight misalignment at a metaphase plate to complete failure to congress (i.e., a polar chromosome). In primary breast cancers, misaligned chromosomes are found in 20% of mitoses compared to lagging in 15% and bridges in 10%. In metastatic breast cancer, the incidence of lagging and bridging chromosomes remained similar, but the incidence of misaligned chromosomes increased to 30%. Further, the incidence of misaligned chromosomes correlated best to CIN as measured by non-modal FISH probe counts on the same microarray. Importantly, lagging and bridging chromosomes can resolve to segregate to the correct daughter cell (141, 142). However, misaligned chromosomes, and polar chromosomes in particular, are more likely to result in mis-segregation. Slight misalignments often display attachment errors and portend subsequent lagging (143) while polar chromosomes guarantee mis-segregation as sister chromatids of the polar chromosome will fail to separate and remain in the same daughter cell. However, a caveat of fixed analysis of misaligned metaphase chromosomes

is that the misaligned phenotype is, by definition, prometaphase. Thus, the cell with a misaligned chromosome may just be in an early mitotic phase and could have segregated normally if additional time was allotted before fixation. By the same token, while anaphase is typically the most informative for the measure of CIN, misaligned chromosomes often go unobserved in anaphase.

Multipolar spindles diverge from previously discussed phenotypes in their frequency and consequences. Multipolar spindles are often produced by the presence of supernumerary centrosomes, which themselves arise from centrosome amplification through dysregulation of the centriole replication cycle (e.g., Plk4 overexpression), centriole fragmentation, or by failure to complete a previous mitosis (e.g., mitotic slippage and cytokinesis failure) (144). However, *de novo* spindle poles can arise without centrosomes through an uncharacterized mechanism. This is most clearly demonstrated in the presence of the chemotherapeutic drugs paclitaxel and vinorelbine, which stabilize and destabilize microtubules respectively. Multipolar spindles occur at a lower frequency in cancer than other CIN phenotypes. This may be due to the high, presumably lethal, rates of mis-segregation they are capable of producing. While lagging chromosomes in a bipolar setting often occur one or two at a time, multipolar spindles can produce many merotelic attachments that, if left uncorrected, can result in a significant number of lagging chromosomes, even after focusing down to a pseudo-bipolar phenotype (145, 146). Further, if multipolar spindles are not focused, multipolar division would produce a high rate of mis-segregation and nullisomy by nature of segregating a diploid genome into three or more daughter cells, even without accompanying attachment errors. Because cells undergoing

multipolar division rarely present discrete chromosome mis-segregations, measuring the rate of mis-segregation by microscopy is extremely difficult. This rate was measured using using scDNAseq at 18 missegregations per diploid division (MDD) (147).

To summarize, different phenotypes of CIN occur at different frequencies and at varying severities of chromosome mis-segregatation. For example, multipolar spinddles may occur at 5% in a given tumor, but mis-segregate 18 chromosomes; is this low or high CIN? What if 50% of cells mis-segregate 1 chromosome? The degree to which these mechanisms contribute to CIN should be taken into account when interpreting microscopic measures of CIN. Current approaches to quantifying CIN phenotypes by microscopy vary in resolution and effort. Measuring CIN as *'% abnormal mitoses'* is the least informative of a mis-segregation rate, but is easily quantified and summarized. A measurement such as *'% anaphases with polar chromosomes'* takes more time to record, but provides a sense of how much CIN is occurring. Meanwhile, a measurement like *'number of lagging chromosomes per anaphase'* gives an exact number of mis-segregations expected, assuming a given the rate of laggards that resolve into the correct daughter cell. However, this approach may not always be achievable as the number of individual chromosomes in an area can be challenging to discern, even with centromere labeling. Nevertheless, interpreting microscopic CIN measures in terms of the number of chromosomes that could potentially be mis-segregated is a more informative approach than using subjective terms like 'low' and 'high' CIN.

Advances in Imaging Quantification. New methods have been developed that may enhance our ability to quantify CIN by microscopy. One such method seeks to address

the specific problem of quantifying CIN caused by multipolar spindles, as previously mentioned. A recent study has used fluorescence intensity of labeled H2B to measure the net loss and gain of chromatin content in daughter cells resulting from multipolar divisions (148). Another has applied deep learning to histopathology images to identify abnormal mitoses and quantify CIN in the sample (149). While the accuracy of this approach was limited, advancements may enable rapid microscopic analysis of CIN in tissue. Cell biology-oriented machine learning classification platforms such as CellProfiler (150) and ilastik (151) could increase the speed of microscopic CIN measures in clinical and experimental samples. Flow Cytometry

Flow Cytometry

Flow cytometry was quickly adapted to measure DNA content and cell cycle kinetics after its invention in the late 1960's (152, 153). This allowed for the identification of conditions and compounds that altered the state of the canonical cell cycle profile. Flow cytometric assays have been used to identify polyploidy or cell cycle arrest, which may or may not be caused by CIN, in a variety of scenarios, including in the CIN syndrome Fanconi Anemia (154). However, unless the rate of mis-segregation is high enough to appreciably change the width of the G0/G1 peak, as experimentally-induced by drugs like paclitaxel, for example (147), flow cytometric cell cycle analysis is likely not sensitive enough to measure relative levels of CIN directly. Conversely, relatively recent advancement — imaging cytometry — has been shown to identify cells with micronuclei using specialized image analysis software and centromeric copy number alterations using FISH

probes. Therefore, imaging cytometry shows promise in estimating relative levels of CIN (155–157).

Phenotypic Reporters

As discussed previously, phenotypic readouts, such as the dark variegated patterns McClintock observed in *Zea mays*, were among the earliest measures of genetic instability. If the known gene that imparts a phenotypic trait is encoded on a mis-segregated chromosome, the phenotype of either daughter cell may be changed. Since then reporter assays have been developed to experimentally quantify mis-segregation rates.

In yeast, introduction of multiple selective and colorimetric reporters into a single chromosome has allowed the estimation of mis-segregation rates secondary to both polyploidization, mutation of cell cycle and spindle assembly genes, and environmental challenge (158–161). Similar to experiments using FISH probe diversity as a readout for mis-segregation, yeast with these selective markers can be subcloned and grown for a predetermined number of generations. These studies were among the first to show that polyploid cells tend to have higher rates of chromosome mis-segregation and, through cell cycle challenge, provide clues into the molecular origins of CIN.

More recently, a new class of experimental CIN reporter has been developed for human cells using human artificial chromosomes (HAC) constitutively expressing GFP. In similar fashion, over a predetermined number of generations, the rate of GFP loss in the population (as a result of mis-segregation of the HAC) is used to quantify mis-segregation rates using fluorescence microscopy or flow cytometry (162–164). While these reporter assays are some of the few methods capable of producing quantitative measures of

chromosomal mis-segregation rates, they do not account for karyotype selection. They may also be affected by mutations that cause the loss of the reporter phenotype, which would either underestimate or overestimate mis-segregation rates respectively. Further the possibility that HACs are mis-segregated more frequently than endogenous chromosomes would need to be considered when drawing conclusions using this method.

THE MOLECULAR

A section by Shermineh Bradford in Lynch, Bradford, and Burkard. (Manuscript 1) Under review.

Comparative Genomic Hybridization

Comparative Genomic Hybridization (CGH), an adjustment to FISH, was later developed to detect chromosome copy number variations (CNV) (165, 166). CGH utilizes different fluorescent dyes to hybridize to and label DNA and distinguish CNVs by comparing their relative intensity. However, despite this technique offering a higher resolution than FISH, sensing CNVS as minor as several hundred base pairs rapidly, it cannot detect structural CIN such as deletions and chromosomal rearrangements and relies on the use of chromosomes at the metaphase state.

Furthermore, to reduce the effect of false changes in signal intensity due to sample quality, the CGH method requires an adequate amount of high-quality genomic input. Later on, in 1997-1998 (165, 167), to overcome some of the disadvantages discussed above, array CGH (a-CGH) was implemented, benefiting through the knowledge gained from the Human Genome Project to use the data of identified locations throughout the genome for DNA microarray probes development. As a result, this optimized approach eliminated the need for metaphase chromosomes by hybridization to an array of mapped

sequences. Additionally, to adjust for low genome input in the CGH process, whole genome amplification approaches were adopted and added preceding genomic labeling (168).

Eventually, as the technology developed, CGH reached single cell resolution and ushered comprehensive characterization of cell-cell karyotype heterogeneity into the age of the molecular sequence. It was used to further characterize intratumoral heterogeneity and karyotypic differences between minimal residual and metastatic disease (169, 170). Though much of the same information could be obtained by traditional microscopic karyotype analysis, the advancement of single cell CGH allowed for analysis of non-mitotic cells and was an important step toward development of higher throughput sequencing technologies used today.

PCR-based assays

A relatively simple and cost-effective multiplex PCR-based assay was introduced in 2018 to sense CIN in formalin-fixed paraffin-embedded (FFPE) tumor biopsy specimens (171). In this approach, upon successful detection of microsatellite instability, allelic imbalances or loss of heterozygosity were assessed in only microsatellite-stable samples. This was accomplished by comparing the frequencies of the paternal and maternal alleles between normal and tumor tissues and setting an experimentally defined cut-off rate for each microsatellite indicator. The allelic imbalances were then used as a proxy for CIN measurement by associating it with a genome-wide analysis of chromosomal alterations in a subset of the TCGA tumor data. However, this method is only reliable in FFPE samples with higher than 24% tumor purity and requires a genomic sample from paired normal

tissue. Furthermore, the final analysis does not distinguish the gain or loss of a chromosomal region nor the rate of mis-segregations. Another limitation of this method is population averaging in pooled samples, which masks the cell-to-cell tumor heterogeneity leading to the imprecise measurement of ongoing CIN (171, 172). Masking cell-to-cell heterogeneity results in an ensemble profile of the most common aneuploid states, which is often conflated with CIN.

Bulk Genome Sequencing

The continuous developments in high throughput sequencing technologies allowed the detection of chromosome number alterations with greater accuracy than array CGH (168, 173, 174). Massively parallel whole genome sequencing (WGS) methods requiring high-depth coverage and later more cost-efficient shallow whole genome sequencing (sWGS) were adopted to measure chromosome copy number alterations. Due to its low-demanding computational platforms and storage-friendly data, sWGS rapidly became available in clinic and research settings to access the state of aneuploidy and intra-tumor heterogeneity (ITH) (175–178).

In bulk analysis, the accuracy of identified tumor's copy number alteration depends on the sample purity and, in most cases, will require sequencing reads from the matched normal sample. Furthermore, to analyze sWGS data, the common strategy is to normalize the read counts of each region of sample DNA to median read counts normalized through the whole sample's genome, making it challenging to infer since the relatively generated data will not directly represent the sample's karyotype.

Utilizing multiple regional bulk genome sequencing methods for tumors and paired primary tumor and their metastases further perpetuated the cancer evolution through karyotype heterogeneity, detecting the aneuploidy and confirming karyotype divergence and the possibility of chromosome instability in the tumor (179–182). The somatic copy number changes due to chromosomal instability can be used to assess the type and degree of cancer evolution by quantifying their allele-specific heterogeneity in paired primary and metastatic tumor studies. The systematic and prevalent formation of clonal and subclonal somatic copy number changes across tumor types imitate constant adjustment within the fitness landscape and enduring CIN throughout cancer evolution and metastasis. Furthermore, multi-sample phasing and higher sequencing depth to incorporate the mirrored allelic imbalance events in which two subclones simultaneously lose/gain a maternal or paternal allele of the matching chromosome provides a greater resolution of CIN's driving impact of ITH (182–184). Specific mutational events involved in the driving genome instability can be extracted from sWGS data employing non-negative matrix factorization parallel to copy number analysis shedding light on underlying mechanisms of CIN and providing a foundation for target therapy (185, 186).

Gene Expression Scores

Using computational methods and to identify the concurrent altered expression of the top 70 and 25 distinct genes in tumors with chromosomal aberrations, Carter et al. described the possibility of CIN as a tool to predict a patient's clinical response (187, 188). These studies identified correlations between the upregulation of these genes in CIN25 and CIN70 tumors and poor clinical outcomes across many cancer types. However, the

reliance on tumors' clonal aneuploidy masks the impact of intermittent aneuploidies caused by chromosomal instability.

In addition, a tumor with an aneuploidy state may not be undergoing CIN in its current state. In fact, some studies showed a negative correlation between chromosomally unstable tumors with CIN70, indicating that the increased gene score could also result from an altered proliferation rate (189). In addition, another set of genes, named HET70, that were completely independent of proliferation was later identified in tumors with ITH, which was also linked with poor clinical outcomes. These genes' direct correlation with CIN rates is yet to be determined (189, 190). Nevertheless, in mice harboring mutations in Kras and Mps1 previously shown to induce CIN and tumors, gene set enrichment analyses of CIN70 and HET70 genes show no indication of the expected increase in CIN over Kras mutated mice with wild type Mps1. To determine the directness of these measures, we would propose an analysis of the validity of these scores in models of induced CIN.

Single Cell Genomics and Transcriptomics

Single-cell methodologies were established to better understand ITH and cancer development (138, 191–196). A fully distinguished ITH allows the identification of chromosome copy number alterations in all clones including the minor subclones which might have been missed in bulk analysis, hence a more accurate way of measuring CIN rates. Some studies have found a correlation between direct measurement of CIN rates taken by time-lapse imaging of tumors in 2D or 3D cultures and single-cell genome sequencing analysis of CIN rate, though this correlation is not as strong as expected, indicating ongoing karyotype selection (138, 196). In addition, the single cell approaches offer solutions

to bulk sequencing shortcomings, such as the need for data deconvolution during phylogenetic tree reconstruction and misinterpretation of low single with noise during tumor evolution analysis.

One of the main constraints of analyzing each cell's genomic profile independently is the low input DNA which requires a whole genome amplification (WGA) step in order to gain adequate DNA input for library preparation. The WGA process is indeed a fault-prone step due to generating false-positive alternative alleles or incomplete amplification leading to variant alleles dropout. Nevertheless, pairing bulk genome sequencing and single-cell whole genome sequencing can resolve some of these problems, allowing for greater resolution in mapping cancer evolution and capturing CNA.

Before the discovery of single-cell RNA sequencing, multiple studies showed the effect of CNA on transcriptomic response using measurable whole-genome proteomics methods such as chromatography, mass spectrometry, phenotypic profiling (growth, metabolism), and whole genome expression array both in yeast and human cells (197–201). For instance, in 2007, Torres and colleagues demonstrated that the presence extra chromosomes in engineered aneuploid yeast stains increases the expression of the majority of the encoded gene on that chromosome. However, subsequent studies found that those yeast strains have dosage compensation at the protein level (202).

More recent studies utilizing single-cell RNA sequencing demonstrated that CIN could lead to transcriptional tumor heterogeneity in addition to genomic heterogeneity, and this transcriptional heterogeneity can be buffered at the proteomic stage (203). In addition, some common transcriptional alterations observed in aneuploid clones are independent

of copy number alterations; therefore, measuring CIN rates from RNA data alone is challenging due to regulation of gene expression and uneven genome coverage from RNA sequencing (204, 205).

Several computational approaches, such as HoneyBADGER, InferCNV, CopyKAT, CaSpER, and more recently, SCEVAN, detect CNA in individual cells from scRNA-sequencing data with the capacity of classifying malignant and non-malignant cells (206–210). Each method has advantages and disadvantages. One can find the best method that suits their particular input data type depending on the type of RNA sequencing data and its sequencing depth.

Combinatorial Methods

A 2012 study first discussed a possible connection between chromothripsis and formation of micronuclei (211) using an innovative strategy, "Look-Seq", to characterize individual cells via live imaging and analyze them, or their daughter cells, using single-cell whole-genome sequencing. Look-Seq provided the required evidence to demonstrate that chromothripsis can originate from fragmentation and reassembly of the micronuclei genome and that micronuclei formation may directly contribute to genomic instability and cancer (105). More recently, Look-Seq showed micronucleus formation and re-incorporation into a grand-daughter cell downstream of the CRISPR cut site, providing evidence of chromothripsis as an on-target consequence of CRISPR-Cas9 gene editing (212).

THE THEORETICAL

Instability and Clonal Evolution

In 1976, Dr. Peter Nowell synthesized the prior two decades' cancer biology research and formulated a hypothesis: "Acquired genetic lability permits stepwise selection of variant sublines and underlies tumor progression" (213). Prior to the discovery of any specific human oncogenes or tumor suppressors, Nowell describes his hypothesis using the example of chromosomal instability (though he states other mutations are likely important). He posited that cell populations, having undergone neoplastic transformation, can leverage continuous genetic instability to produce rare, advantageous variant clones (and many disadvantageous) that are selected over neighboring cells given the pressures of its local environment. Recognizing that most tumors are aneuploid, that most aneuploid tumors display some level of karyotypic diversity, but that most cells within a tumor share a predominant karyotypic pattern, Nowell believed that CIN played a critical role in increasing malignancy and that some specific karyotypes provide advantages over others, in part, by altering the dosage of genes on that chromosome. This theoretical framework, drawing on previous studies' evidence, closely predicted much of what we know of tumor and karyotype evolution today. This practice of modeling the dynamics of tumors' karyotypes to understand the interplay between selection and CIN, and how this affects extant karyotype diversity, continues to this day.

Computational Models of CIN

First attempts. The first computational models of CIN focused on understanding how observed distributions of chromosome numbers are achieved and how CIN interacts with

generic oncogenes to promote growth. Shackney and colleagues simulated numerical and structural CIN in the context of tetraploidization and activation of oncogenes and concluded that a rate of chromosome loss (secondary to tetraploidization) of 0.004 per chromosome (i.e., 1 loss per ~5 divisions in a diploid background) offered the best qualitative fit for observed chromosome count distributions. Given equal probability of gain and loss, their results would also imply a total mis-segregation rate of 0.008 (i.e., 1 mis-segregation per ~3 divisions in a diploid background) (214). Gusev and colleagues identified sought to establish the numerical bounds that delineate sustainable vs unsustainable CIN levels. Assuming all chromosomes are essential and lethal nullisomy as the only selective constraint, they concluded mis-segregation rates could reach as high as 0.13 (6 MDD) before limiting population growth through nullisomy. Using this upper bound, they subsequently modeled long term (50+ generations) dynamics of CIN with defined levels of CIN (low = 0.001, moderate = 0.01, high = 0.1, critical = 0.25 per chromosome) and concluded that a range of rates between 0.005 to 0.01 (0.23-0.46 MDD) recapitulated FISH results from a cell line experiment over a known number of generations. (215, 216). These results were somewhat higher than a concurrent analysis by Roschke and colleagues. Under the assumption that new aneuploid states are temporarily negatively selected, they placed average numerical CIN rates in colorectal and ovarian cancer cells at ~0.001 per chromosome (0.046 MDD) and the rate of structural CIN at ~0.001 per chromosome (0.046 MDD) for colorectal cancer and ~0.0001 per chromosome (0.0046 MDD) for ovarian cancers as measured by spectral karyotyping (217). These studies dealt with fundamental aspects of karyotype selection, such as the lethality of nullisomy, to achieve their CIN measures

and define its 'boundary conditions'. Yet, because there was insufficient information at the time, they did not consider the relative fitness levels of specific aneuploid karyotypes.

Reckoning with karyotype selection. Through a litany of large cancer datasets published since, we have gained a more granular view of karyotype variation among and within cancers. We've confirmed that aneuploidy is a feature of ~90% of tumors and identified common patterns of specific aneuploid states. Some chromosome gains and losses are common features of cancer as a whole. Some are common features of specific cancer subtypes or tissues of origin. However, individual tumors may deviate from these commonalities and karyotype variation is commonly observed within individual tumors as a result of CIN. Collectively, this implies a role for ongoing karyotype selection, the process by which different aneuploid karyotypes confer different fitness levels and outcompete or are overtaken by their neighbors, as Nowell predicted. Recurring pan-cancer and cancer-specific CNAs imply both convergent (or directional) selection and subsequent stabilizing (or negative) selection as metastases and relapse tumors tend to retain a similar karyotype to the primary despite potentially vast differences in environment (218, 219). Conversely, the presence of intratumoral karyotype heterogeneity implies some room for karyotypic drift and perhaps variable levels of selective pressure within a tumor. Positive selection of new relatively advantageous copy number alterations (CNAs) and negative selection of new relatively inhibitory CNAs, together, produce stabilizing selection in the tumor cell population. This stabilizing selection limits karyotypic drift to varying degrees, restraining the potential of new clones with karyotypes highly dissimilar to the clonal 'mode'. When the environment is altered or a new advantageous clone arises, the modal

karyotype shifts over time. In each case, the true rate of diversification as inferred by karyotype diversity may be masked by karyotype selection if unfit cells with new karyotypes are more or less fit. While many studies have assumed neutral karyotype selection in simulations or experiments relating CIN and karyotype diversity (121, 122, 196, 214–217, 220), others have sought to define the relationship between CIN and karyotype selection (or aneuploid fitness).

The density of oncogenes, tumor suppressor genes, and essential genes on chromosomes and chromosome arms has been shown to correlate with the frequency at which they are gained and lost in pan-cancer studies (221). In other words, chromosomes with many oncogenes/essential genes and few tumor suppressor genes tend to be gained whereas those with few oncogenes/essential genes and many tumor suppressors tend to be lost. This analysis assigned individual chromosomes and chromosome arms discrete scores to broadly describe whether its presence in a cancer karyotype enhances or suppresses cancer fitness. Subsequent studies used these scores to define the peaks and valleys of the aneuploid fitness landscape and how this is reflected in simulated populations' karyotypic makeup. As expected, these studies recapitulate the broad trends of cancer evolution: convergent karyotype evolution as defined by the pan-cancer chromosome scores they use and convergence on a near-triploid state (147, 184, 222, 222–224). Two of these studies conclude that the rate of mis-segregation that maximizes survival and adaptive potential over long timescales is 0.001 - 0.0014 per chromosome per division (i.e. 0.05 MDD or ~1 mis-segregation every 20 divisions) (223, 224). While this estimated mis-segregation rate is lower than observed in cancer cell lines, models of

karyotype evolution based on recurrent aneuploidies tend to produce a higher level of cell-cell karyotype heterogeneity than is typically observed in single cell cancer datasets (147, 224). This implies that, while directional selection may guide the broad patterns of aneuploidy, stabilizing selection likely controls the ongoing extent of karyotypic drift, and thus karyotype diversity, in tumor cell populations at a given time.

An alternative evidence-based model for selection of aneuploid cells comes from the recurrent observation that new aneuploid cells are less fit than their euploid or aneuploidy-adapted progenitor in equivalent environments. In this context, the number of genes encoded on an aneuploid chromosome positively correlates with its detriment to cellular fitness (198, 225–227). Fewer studies have investigated the effect of this stabilizing selection on karyotype diversity in tumors with CIN. We developed one such computational model by assigning chromosome scores based on their gene content normalized to the total estimated number of genes in the human genome. The sum of these scores represented a cell's fitness (euploid fitness = 1) Then, to model stabilizing selection, these scores were further modified depending on how far a cell's copy of a given chromosome is from the average ploidy of the population. We found that this model, compared to neutral selection or directional selection (via aforementioned pan-cancer chromosome scores) best recapitulates the amount of cell-cell karyotype variation observed in scDNAseq data from clinically-derived cancer samples (147). This evidence of stabilizing selection of karyotypes is in agreement with unreviewed work using similar methods (228).

Selection-aware computational inference of ongoing CIN. Because karyotype selection can mask true mis-segregation rates inferred by karyotype diversity alone, there is a need for methods that account for this. We previously developed a framework that uses the model described above as a uniform prior dataset against which real scDNAseq data can be compared (147). Further, this framework uses summary statistics for both karyotype heterogeneity and phylogenetic topology, which has previously been used to detect selection in populations (229–232), to infer mis-segregation rates. Using this method, we recovered the experimentally observed mis-segregation rate induced by the chemotherapeutic drug paclitaxel (0.42 per chromosome per division or MDD ~ 18 chromosomes). We also inferred a spectrum of mis-segregation rates occurring in normal colon and colorectal cancer organoids as well as a breast cancer biopsy using previously published datasets (138, 191). These ranged from 0.001 to 0.006 per chromosome per division, or an MDD of about 1 mis-segregation per 21 to 3 divisions respectively, values which fell within the range of mis-segregation rates in cell lines as observed by microscopy. This framework for inference of CIN, CINFER, is available online as a web-tool (https://andrewrlynch.shinyapps.io/CINFER/).

This selection-aware inference of ongoing CIN is of increasing interest. One yet unreviewed study has achieved similar results as above using similar methods (233). Another, which uses expression of interferon gamma-related genes as a proxy measure of chromosome mis-segregation, has also attempted to infer tumors' mis-segregations rates from scRNAseq (234). The link between mis-segregation and upregulation of interferon gamma is heterogeneous as the activity of the cGAS-Sting pathway is not uniform across cancers

(235). This may confound the utility of scRNAseq measures of CIN, and could explain the finding of a broad range of inferred mis-segregation rates with bounds well outside the expected, directly observed range.

While these methods are an advancement in measuring CIN in patients' tumors, further advancement is required before they could be considered a comprehensive measure and total replacement of previous methods. Namely, careful empirical study of karyotype selection dynamics, such as possible epistasis of higher order copy number interactions and environmental interactions, as well as inclusion of structural CIN at sub-chromosome arm resolution, which current models do not achieve.

THE FUNCTIONAL CONSEQUENCES OF MIS-SEGREGATION RATES

CIN is a scalar property of tumors, not a binary. This means the consequences of CIN in tumors are defined by the rate at which chromosomes mis-segregate (Figure 1.2), not just whether this occurs at all. Further, the functional consequences of chromosome mis-segregation are not linearly associated and, in many ways, seem paradoxical. For example, CIN can be both tumor promoting and tumor inhibiting. The context dependent nature of CIN's consequences has proved a challenging hurdle for its study of the years, though a clearer picture has emerged over the last fifteen years.

Aneuploidy, the immediate consequence of chromosome mis-segregation, is generally poorly tolerated in healthy human tissues. The absence of 'normal' aneuploid cells and the embryonic lethality of aneuploidy for most chromosomes suggests chromosome mis-segregation is almost always a lethal event in the normal course of cellular life.

Therefore, the consequences of mis-segregation rates in normal cells are straightforward and not relative, all mis-segregation seems to be bad mis-segregation.

Aneuploidy becomes more prevalent in diseased and stressed tissues. The nearly universal aneuploidy in cancer is an obvious example, but aneuploidy is also prevalent in pre-malignant anaplastic tissue as well as stromal cells within the primary tumor itself. The presence of widespread aneuploidy has also been reported in brain and liver tissue. This all suggests 1) the occurrence of ongoing chromosome mis-segregation in non-cancer tissues and 2) that aneuploidy caused by chromosomes mis-segregation is not sufficient for transformation of otherwise healthy tissue.

While transformation is not an immediate consequence of chromosome mis-segregation, it does seem to spur tumorigenesis. Several mouse models have shown that elevation of chromosome mis-segregation increases tumor formation over a mouse's lifetime. There are several explanations for this. Elevated chromosome mis-segregation could induce a chronic inflammatory response, which promotes tumorigenesis, and which is, itself, a consequence of aneuploidy. Perhaps it confers a higher baseline rate of DNA damage, increasing the likelihood of mutating cancer driver genes. Perhaps it just increases genomic diversity in pre-malignant tissue, providing a 'head start' of genomic diversity when transformation does occur. Identifying CIN's contribution to tumorigenesis is a challenge because ongoing cellular events in anaplastic tissue and incipient tumors is currently not possible *in vivo*. Though recent advances in whole-mouse lineage tracing present an interesting opportunity to study CIN before, during, and after tumorigenesis (236).

Chromosome mis-segregation rates contribute to a host of clinically aggressive features in human tumors, tumor models, and cell lines. Overall, elevated mis-segregation rates and large-scale chromosome CNA burden are associated with worse patient survival. For example, in a retrospective clinical analysis of tissue samples from diffuse large b-cell lymphoma patients, a two-fold higher frequency of mitotic aberrations was associated with 24% worse overall survival over a 12 year period (237). In a cohort of patients with non-small cell lung cancer whose tumors underwent multi-region sequencing, those with the highest levels of sub-clonal copy number heterogeneity exhibited a nearly 50% decrease in disease free survival over 2.5 years. Additionally, elevated chromosome mis-segregation rates been implicated in metastasis and chemotherapeutic resistance. Mouse xenograft tumors with higher CIN were more likely to spread metastases than those with lower CIN (238). This was due to induction of a pro-metastatic inflammatory response through innate sensing of cytosolic DNA caused by chromosome mis-segregations. Metastasized breast tumors, when examined at histology, also exhibit greater CIN that their primary counterpart (140), though this could be, in part, due to decreased stromal attachment (239). While the mechanism of CIN's promotion chemotherapeutic resistance is unclear in most cases, higher CIN does appear to confer this effect (240–243).

The apparent monotonically increasing effect of chromosome mis-segregation on tumor progression, as compared to its non-monotonic effect on tumorigenesis somewhat counter-intuitive. However, this could be a simple case of selecting out cells who evolve a CIN phenotype that is too aggressive. Though, cell lines with CIN are capable of dynamically decreasing their CIN level through additional mutation of spindle assembly

components (244). This raises the interesting prospect that tumors can devolve their high CIN phenotype if and when it becomes disadvantageous.

Despite its tumorigenicity and hastening of cancer progression, chromosome mis-segregation is not always sustainable. Some of the same studies using mouse models to demonstrate increased tumorigenesis from elevated CIN also showed that mice with the highest levels of CIN actually inhibited CIN (245–247). The point at which chromosome mis-segregation flips from tumor promoting to tumor inhibiting is unknown. There are real, numerical limits to the rate of mis-segregation a population of cells can tolerate. One example of a very clear threshold is the induction of nullisomy, or loss of all copies of a homologous set of chromosomes. With the exception of chromosome Y, nullisomy is not recurrently observed in any human tissue, including tumors. Cells rely on genes encoded on all chromosomes to survive and proliferate. Thus, nullisomy presents a well-defined and insurmountable challenge to cell survival. Indeed, cell death and reduced tumorigenicity occur at the highest rates of mis-segregation observed. This is true in both chemically and genetically induced models of CIN as well as innate rates of mis-segregation (138, 245, 247, 248). The extent to which nullisomy is the primary cause of mis-segregation-mediated cell death is unknown. However, estimates of mis-segregation rates required to induce nullisomy are far above what is commonly observed, even in most inducible models (Appendix 1, Figure A1.1). This suggests that elevated levels of genomic imbalance or DNA damage through mis-segregation, rather than nullisomy alone, may be sufficient to cause cell death.

Importantly, one of the most successful and widely used classes of chemotherapeutic agents, taxanes, work by inducing chromosome mis-segregation in cancer cells. By stabilizing microtubules and inducing *de novo* spindle poles during mitosis, it causes cells to undergo multipolar divisions, causing extensive chromosome mis-segregation, upwards of about 18 chromosomes per division (147, 249). On its own, 18 chromosome mis-segregations is about what is required for about 50% of an otherwise diploid population to experience nullisomy (Appendix 1, Figure A1.1). However, multipolar divisions also bias mis-segregations toward chromosome loss (Appendix 1, Figure A1.2-4). If these types of divisions go uncorrected, which can occur through spindle pole clustering, it all but guarantees nullisomy in diploid cells.

Unfortunately, about 50% of patients who receive paclitaxel receive no therapeutic benefit (250). Worse, there is no biomarker to indicate who will respond. One hypothesis for why this occurs is that spindle pole clustering effectively rescues daughter cells from nullisomy by preventing multipolar divisions, instead, allowing cells to divide on pseudo-bipolar spindles with relatively little consequence. A recent study has shown that the pre-existence of other CIN phenotypes, aside from multipolar mitotic spindles, can interact with the induction of multipolar divisions to sensitize cells to chromosome mis-segregation (251). This suggests that pre-existing CIN could be used as a biomarker for paclitaxel response. However, a biomarker is only as useful as one's ability to measure it.

Tumors' relative levels of CIN hold prognostic and predictive clinical value. However, these CIN levels are poorly defined because current CIN measures are insufficient for measuring CIN as a rate in human tumors. The clinical utility of CIN, as well as a

sounder understanding of its relative levels' complex roles in malignancy, can only be achieved through development better measures. Measures which are quick and accurate, which account for confounders like karyotype selection, and which are clinically accessible.

SCOPE

In the following work, I work to improve the measure of CIN to achieve the ideal qualities described above. I address the role of karyotype selection in masking karyotype heterogeneity, confounding the direct inference of mis-segregation rates, and develop a multidisciplinary approach to address this. This is validated experimentally and applied to tumor-derived samples. I also explore different models of karyotype selection and identify the predominant ongoing mode of natural selection acting on aneuploid karyotypes in tumors (Chapter 2). I further explore the algorithmic principles of CIN on which this approach is based to better define the extent to which chromosome mis-segregation rates are capable of remodeling karyotypes over a single division (Appendix 1). I then compare this new approach to measuring CIN against other measures in a comprehensive survey of CIN measures across several specific CIN phenotypes in inducible cell line models (Chapter 3). I also outline CINFER, a user-friendly tool which I developed to advance the rapid, selection-aware, measure of CIN (Chapter 4). Lastly, I discuss how this work will contribute to the study of CIN and its measurement in the clinic and look ahead to what the next generation of CIN measurement will bring (Chapter 5).

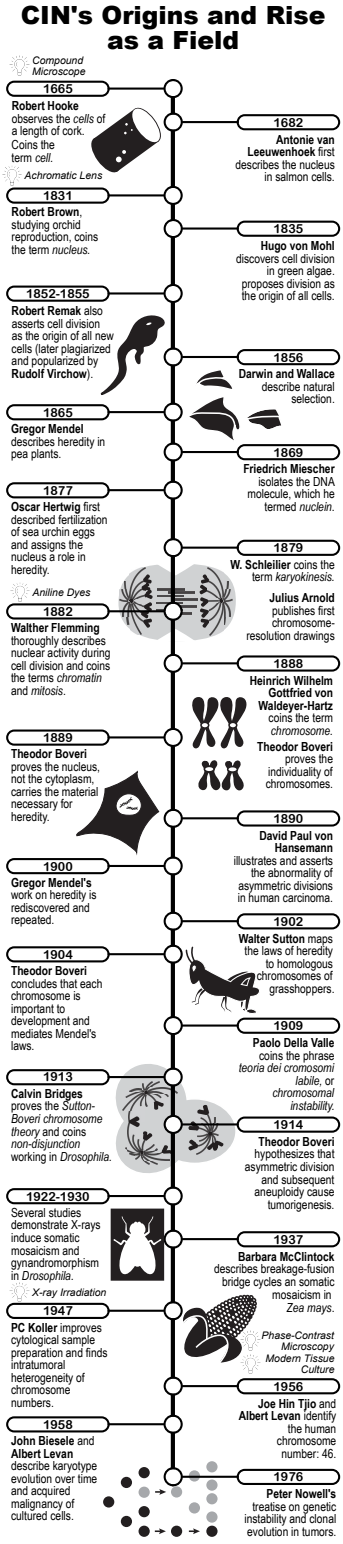

Figure 1.1 — CIN's origins and rise as a field

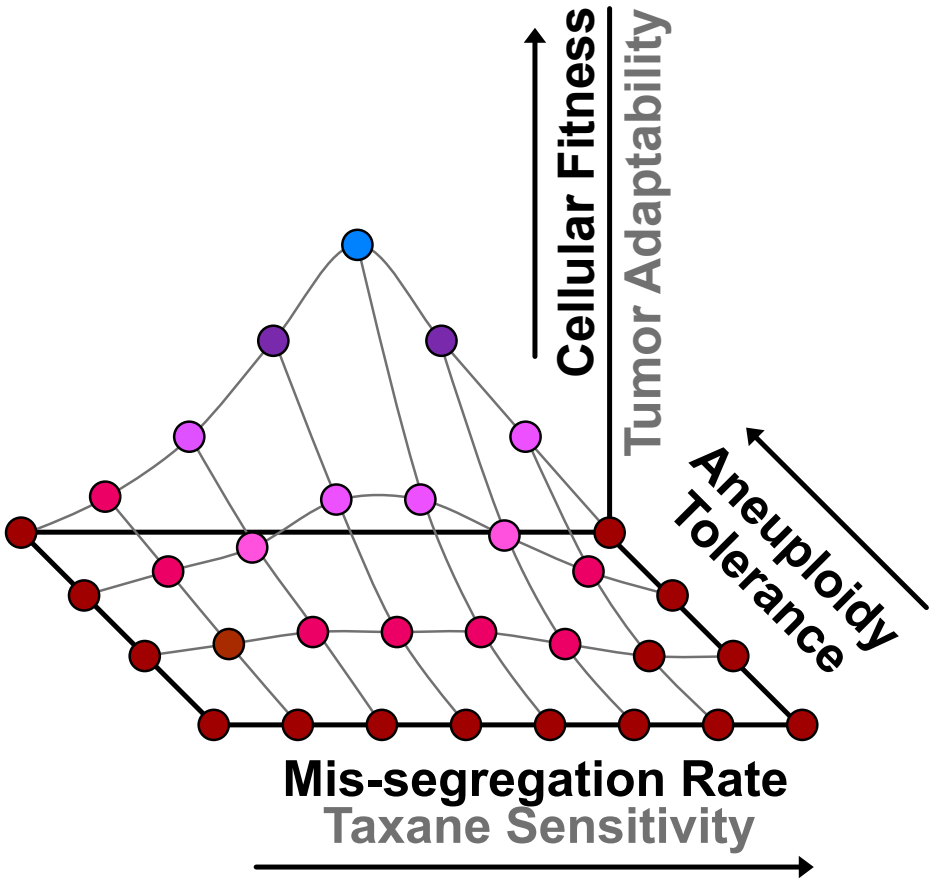

Figure 1.2 — The functional distribution of mis-segregation rates in cancer

Table 1.1 — Methods of CIN measurement

Modality	Method	Metric	Directly Observed	Selection Aware	Clinically Accessi-ble
Imaging	Microscopic readout of abnormal divisions.	% abnormal mitoses % abnormal anaphases % phase with defect # chromosomes with defect per cell # spindle poles per cell	✓	✗	✓
Imaging Flow Cytometry	Phenotypic reporter of mis-segregation	% cells w/wo reporter Mis-segregation rate (MDD)	✗	✗	✗
Cytogenetics	Chromosome spread counts	Standard deviation or variance of chromosome counts % of cells with non-modal chromosome counts	✗	✗	✗
Imaging Cytogenetics	Incidence of micronuclei	% of cells with micronuclei # micronuclei per cell	✗	✗	✓
Cytogenetics Sequencing Simulation	Karyotype diversity	Standard deviation or variance of chromosome counts # of non-modal whole or segmental chromosome alterations % of cells with non-modal chromosome alterations	✗	✗	✓
		Simulation-aided inference	✗	✓	✓
Cytogenetics	FISH probe diversity	Standard deviation or variance of probe counts % of cells with non-modal probe counts Mis-segregation rate (MDD)	✗	✗	✓

2

QUANTIFYING CHROMOSOMAL INSTABILITY FROM INTRATUMORAL KARYOTYPE DIVERSITY USING AGENT-BASED MODELING AND BAYESIAN INFERENCE

Adapted from Lynch et al. eLife. 2022. (Manuscript 4)

ABSTRACT

Chromosomal instability (CIN)—persistent chromosome gain or loss through abnormal mitotic segregation—is a hallmark of cancer that drives aneuploidy. Intrinsic chromosome mis-segregation rate, a measure of CIN, can inform prognosis and is a promising biomarker for response to anti-microtubule agents. However, existing methodologies to measure this rate are labor intensive, indirect, and confounded by selection against aneuploid cells, which reduces observable diversity. We developed a framework to measure CIN, accounting for karyotype selection, using simulations with various levels of CIN and models of selection. To identify the model parameters that best fit karyotype data from single-cell sequencing, we used approximate Bayesian computation to infer mis-segregation rates and karyotype selection. Experimental validation confirmed the extensive chromosome mis-segregation rates caused by the chemotherapy paclitaxel (18.5±0.5/division). Extending this approach to clinical samples revealed that inferred rates fell within

direct observations of cancer cell lines. This work provides the necessary framework to quantify CIN in human tumors and develop it as a predictive biomarker.

INTRODUCTION

Chromosomal instability (CIN) is characterized by persistent whole-chromosome gain and loss through mis-segregation during cell division. Genome instability is a hallmark of cancer (252) and one type, CIN, is the principal driver of aneuploidy, a feature of ~80% of solid tumors (253–255). CIN potentiates tumorigenesis (245, 256, 257) and associates with therapeutic resistance (200, 240, 258, 259), metastasis (238), and poor survival outcomes (182, 237, 260). Thus, CIN is an important characteristic of cancer biology. Despite its importance, CIN has not emerged as a clinical biomarker, in part because it is challenging to quantify.

Although CIN has classically been characterized as binary—tumors either have it or not—recent evidence highlights the importance of the rate of chromosome mis-segregation and the specific aneuploidies it produces. For example, clinical outcomes partially depend on aneuploidy of specific chromosomes (221, 261, 262). Further, higher levels of CIN suppress tumor growth when they surpass a critical threshold, thought to be due to lethal loss of essential genes and irregular expression due to imbalanced gene dosage (245, 249, 263, 264). Moreover, baseline CIN may predict chemotherapeutic response to paclitaxel (265, 266) and is proposed to both promote detection by or evasion from the immune system (267, 268). No single or standardized analytically valid measure of CIN has emerged and this gap has precluded its clinical validation as a prognostic or predictive biomarker.

Prior measures of CIN use various means to compare levels in tumors or populations, but do not establish a standardized quantitative rate. These prior measures include histologic analysis of mitotic defects (237, 269), fluorescence *in-situ* hybridization (FISH) with probes to detect individual chromosomes (122), and gene-expression methodologies like CIN scores (187). While these methods are readily accessible, they have significant drawbacks for clinical application. FISH and mitotic visualization approaches are laborious. Direct visualization of mitotic defects to measure CIN is only possible in the most proliferative tumors where enough cells are captured in short-lived mitosis. FISH typically quantifies only a subset of chromosomes, which will be misleading if there is bias toward specific chromosome gains/losses (270). While gene expression scores are proposed as indirect measures of CIN, they are not specific to CIN and correlate highly with proliferation and structural aneuploidy (187, 189).

Single-cell sequencing promises major advances in quantitative measures of CIN by displaying cell-cell variation for each chromosome across hundreds of cells (191, 194). However, selection poses another complication. To date, single-cell analyses have identified surprisingly low cell-cell karyotype variation, even when mitotic errors are directly observed by microscopy (138, 139, 194, 196, 271). These observations highlight the confounding role of selection against aneuploid karyotypes in measuring CIN in human tumors. Indeed, selection reduces karyotype variance in cancer cell populations that directly exhibit mitotic errors (258, 259, 272, 273). Here, we seek to overcome this gap by modeling chromosomal instability and explicitly considering the evolutionary selection of aneuploid cells, to derive a quantitative measure.

We describe a quantitative framework to measure CIN by sampling population structure and cell-cell karyotypic variance in human tumors, accounting for selection on aneuploid karyotypes. We built our framework on the use of phylogenetic topology measures to quantify underlying evolutionary processes (229); in this case to quantify CIN from both the diversity and the aneuploid phylogeny within a tumor. Using an agent-based model of CIN, we determine how distinct types and degrees of selective pressure shape the karyotype distribution and population structure of tumor cells at different rates of chromosome mis-segregation. We then use this *in silico* model as a foundation for parameter inference to provide a quantitative estimate of CIN as the numerical rate of chromosome mis-segregation per cell division. We apply this model to quantify CIN caused by the chemotherapeutic paclitaxel in culture. Next, using existing single-cell whole-genome sequencing data (scDNAseq), we measure CIN in cancer biopsy and organoid samples. As a whole, this work provides a framework to quantify CIN in human tumors, a first step towards developing CIN as a prognostic and predictive biomarker.

RESULTS

A framework for modeling CIN and karyotype selection

To assess intratumoral CIN via cell-cell karyotype heterogeneity, we considered how selection on aneuploid karyotypes impacts observed chromosomal heterogeneity within a tumor. By modeling fitness of aneuploid cells, we observe chromosomal variation in a population of surviving cells. The selective pressure of diverse and specific aneuploidies on human cells has not been, to our knowledge, directly measured. Therefore, we employ previously developed models of selection.

In models of CIN, fit karyotypes are selected while unfit aneuploid karyotypes are eliminated over time (243, 261, 262, 272). We use two previously proposed models of aneuploidy-associated cellular fitness, as well as hybrid and neutral selection models. The Gene Abundance model is based on the relatively low incidence of aneuploidy in normal tissues and assumes cellular fitness declines as the cell's karyotype diverges from a balanced euploid karyotype (226, 273). When an individual chromosome diverges from euploid balance (2N, 3N, 4N, for example), its contribution to cellular fitness is weighted by its abundance of genes (Figure 2.1A, left). Alternatively, the Driver Density model assumes that each chromosome's contribution to cellular fitness is weighted by its ratio of Tumor suppressor genes, Oncogenes, and Essential genes (TOEs)(221, 224). For example, Driver Density selection will favor loss of chromosomes with many tumor suppressors and favor gain of chromosomes replete with oncogenes and essential genes (Figure 2.1A, right). The hybrid averaged model accounts for both karyotypic balance and TOE densities (Figure 2.1A, middle). Using these fitness models, we assigned chromosome scores to reflect each chromosome's value to cellular fitness (Figure 2.1B, Table 2.1), the sum of which represent the total fitness value for the cell, relative to a value of 1 for a euploid cell. Further, we scaled the impact of cell fitness with a scaling factor, S, ranging from 0 (no selection) to 100 (high selection). While these models are approximations, they are nevertheless useful to estimate how mis-segregation and selective pressure cooperate to mold karyotypes in the cell population.

We employed these selection models in an agent-based model of exponential population growth wherein each cell has its own karyotype (Figure 2.1-2.2). Briefly, simulations started with 100 euploid cells and were run in discrete time steps with variable rates

of selective pressure, S, and rates of chromosome mis-segregation (P_{misseg}, see definitions in Table 2.2). The rate—or probability—of mis-segregation events, P_{misseg}, is the measure of CIN. During each time step, cells have a $P_{division}$ (=0.5 for euploid) chance of dividing. Each dividing cell has a P_{misseg} chance of improper segregation of each chromosome. Segmental chromosome breaks occur with a probability P_{break}, set at 0 or 0.5. After division, fitness (F) of each daughter is assessed. Cells are removed from the population if any given chromosome has copy number 0 or >6. The $P_{division}$ value of the remaining viable cells is adjusted by the cell's fitness under selection (F^S). Due to computational limitations, pseudo-Moran or Wright-Fisher models are employed to limit the modeled cell population (Figure 2.1C,D). These limits did not significantly affect the measures extracted from these populations (Figure 2.3). Thus, these models simulate an evolving population of aneuploid cells under given rates of CIN, P_{misseg}, and models and strength of selection.

Evolutionary dynamics imparted by CIN

To understand the interplay between CIN and selection, we simulated 100 steps of cell growth with CIN under each selection model. We varied the rate of CIN ($P_{misseg,c} \in [0, 0.001\ldots 0.05]$ per chromosome; or 0 – 2.3 chromosome mis-segregations per division) and selective pressure ranging from none to heavy selection ($S \in [0, 2\ldots 100]$). As expected the simulated cell number increases rapidly to the pseudo-Moran cap of 3000, where it remains (Figure 2.4A). As displayed in Figure 2.4B, diversity of the cell population, expressed as mean karyotypic variance increases over time, but also depends on mis-segregation rate, and selection levels (Figure 2.4B). As expected, high mis-segregation rates (P_{misseg}, Y axis) and low selection (S=0; top row) enhance the variance of the

population. Further, without selection (S=0; top row) all models returned comparable profiles over time, resembling neutral selection. However, when selective pressure is applied (S>0), the distinct profiles appear. The abundance model (first column) negatively selects against all aneuploid karyotypes and yields low heterogeneity that increases modestly with mis-segregation rate. With the Driver model (second column), there is a sharp increase in heterogeneity even at low mis-segregation rates, as this model favors specific aneuploid states that maximizes oncogenes and minimizes tumor suppressors. The Hybrid model falls between the other two. Results were not specific to the pseudo-Moran process of capping at 3000 cells—dynamics were similar in the constant-population Wright-Fisher model (Figure 2.5A,B). These data illustrate how CIN and selection operate together to shape the karyotype diversity in the cell population.

High levels of selection against aneuploid cells are expected to impede cell growth. To visualize this, we quantified the population of viable cells with distinct models (Figure 2.4C). As expected with the Abundance model at S=10 and S=100, cells proliferated more slowly with higher rates of mis-segregation. By contrast, the Driver model saw no growth defect as they favored specific aneuploid states that are easily reached with missegregation. As before, the Hybrid model, is intermediate, and findings are not impacted by pseudo-Moran or Wright-Fisher restrictions on cell number (Figure 2.5C).

To further assess model dynamics, we examined time-course of average cellular ploidy—the number of chromosomes divided by 23. In many cases, the mean ploidy of the populations tend to increase over time (Figure 2.4D, Figure 2.5D), particularly in the absence of selection (S=0; top). This is likely due to a higher permissiveness to chromosome gains than losses in our model (since cells ‘die’ with nullisomy or any chromosome

> 6, the optimum is 3.0). With selection (S=10; S=100 rows), the models diverge. In the abundance model, populations remain near diploid. With the Driver model, the average ploidy increases more rapidly due to favoring aneuploidy states that favor high oncogenes and low tumor suppressors, consistent with previous computational models built on chromosome-specific driver densities (221, 224). Under the Hybrid model, ploidy increases modestly. Similar effects are seen with the constant-population Wright-Fisher model (Figure 2.5D). In summary, selection and mis-segregation cooperate to shape the aneuploid karyotypes diversity, cell proliferation and average ploidy in a population of cells, or a human tumor. Further, sampling karyotypes in a cell population does not allow direct determination of mis-segregation rates, as their diversity is influenced by other factors such as selective pressure, selection modality, and time.

In some tumors, genome doubling occurs early in tumor initiation relative to other copy number changes (274, 275). Genome doubling is accomplished, for example, by endoreduplication, by failed cytokinesis, or by cell-cell fusion. Genome doubling buffers against loss of chromosomes and thereby favors aneuploidy. To determine how genome doubling impacts evolution in our model, we compared diploid and tetraploid founders (Figure 2.4E-G). Both diploids and tetraploids tend to converge towards the near-triploid state (ploidy ~ 3), as observed in many human cancers (276), though this is restrained to a degree with the Abundance and Hybrid models. Compared with diploid cells, tetraploidy buffered against the negative effects of cellular fitness in the Abundance model, despite generating similar levels of diversity over time (Figure 2.4F,G)— this is more pronounced when comparing P_{misseg} = 0.1 in tetraploids versus P_{misseg} = 0.2 in diploids to match the number of chromosome mis-segregations per division. This is consistent with the idea

that tetraploidy serves as an intermediate enabling a near-triploid karyotype that is common in many cancers (275, 277). By contrast, in the Driver model, tetraploidy did not provide a selective advantage to high-CIN tumors (Figure 2.4F). Similar fitness, karyotype diversities, and ploidy increases were obtained with a Wright-Fisher model of population growth (Figure 2.5E-G, Figure 2.6).

Taken together, the agent-based model recapitulates expected key aspects of tumor evolution, lending credence to our model. Further, they illustrate the difficulty of inferring mis-segregation rates directly from assessing variation in karyotypes in human cancer. Nevertheless, this model serves provides a framework to incorporate selection to measure CIN through quantitative inference from the observed karyotypes, as we will demonstrate.

Long-term karyotype diversity depends profoundly on selection modality

Some current measures of CIN are derived from karyotype diversity in the population. Yet, our model suggests that selection pressure will profoundly shape this diversity. To further understand the nature of karyotype diversity under selection, we evaluated their long-term dynamics, whether they exhibit clonality, and whether populations simulated under each model converge on a common karyotype.

We simulated diploid and tetraploid populations for 3000 time steps at a fixed mis-segregation rate, in an experimentally reported range, allowing for fragmentation of chromosome arms (P_{misseg} = 0.003, P_{break} = 0.5) (137, 138) and $S \in [1,25]$ (Figure 2.7A). We visualized copy-number heatmaps indicating karyotypes of sampled cells from the population. As expected, population diversity is limited under the Abundance model (Figure 2.7B). Even after 3000 time steps, only a small number of unique alterations and sub-

clonal alterations (+13p/-15p/-22p) existed, likely passenger alterations as they offer no fitness advantage in this model. Moreover, the karyotype average of 1500 cells across 5 replicates resembled a diploid karyotype (Figure 2.7C, row 1), indicating that the Abundance model provides stabilizing selection around the euploid karyotype. In fact, populations simulated under this model with elevated selection (S=25) quickly reache a low, steady-state level of karyotype diversity and fitness while those with the unmodified selection values (S=1) take a longer time to reach this steady-state and have similar levels of karyotype diversity and fitness as the other models (Figure 2.8B,C). To identify any contingencies that may affect these associations, we performed the same simulation using several variants of our model. We found this steady state to be consistent for tetraploid cells as well as when we eased the upper ploidy constraint from $n_c = 6$ to an extreme $n_c = 10$, when we imposed a severe, 90% fitness reduction for all cells with a haploidy, and when we simulated populations under the Wright-Fisher model (Figure 2.7C, rows 2-4).

The Driver Density and Hybrid models generate much more diversity (Figure 2.7B) but nevertheless converge by 3000 timesteps (2.8C). Without selection (neutral model), there is high diversity and no convergence over time. Taken together, these demonstrate a high dependence on the model of selection. However, the models are not highly dependent on ploidy constraints, haploid penalties, or on selection of Pseudo-Moran or Wright-Fisher restriction of cell numbers. Taken together, long-term populations are strongly shaped by the model of karyotype selection for a given P_{misseg}, but relatively insensitive to other particular features of the model. This justifies our approach henceforth of varying only the selection model, the degree of selection (S), and P_{misseg} to infer parameters from data via phylogenetic topology and Bayesian inference.

Topological features of simulated phylogenies delineate CIN rate and karyotype selection

Given a model capable of recapitulating diversity and selective pressures, next we wish to infer P_{misseg} as a measure of CIN from an observed population of cells. Phylogenetic trees provide insights into evolutionary processes of genetic diversification and selection. Moreover, the topology of the phylogenetic tree has been used as a quantitative measure of the underlying evolutionary processes (231, 232, 278–280).

Here, chromosome mis-segregation gives rise to karyotype heterogeneity, and the population of cells is then shaped by selection. To evaluate this, we use chromosome copy number-based phylogenetic reconstruction, since mutation rates are not high enough in tumors to reliably infer cellular relationships, particularly with low-copy sequencing. Once phylogenies are reconstructed from simulated and experimental populations, the topological features phylogenies can be compared. These features include 'cherries'—two tips that share a direct ancestor—and 'pitchforks—a clade with three tips (Figure 2.9A). Additionally, we considered a broader metric of topology, the Colless index, which measures the imbalance or asymmetry of the entire tree. To understand how these measures are affected by selection in simulated populations, we reconstructed phylogenies from 300 random cells from each population simulated with a range of selective pressures taken at 60 time steps (~30 divisions under Hybrid selection; Figure 2.9B). As seen previously, aneuploidy and mean karyotypic variance (MKV) decrease with selective pressure, a trend that is robust at high mis-segregation rates (Figure 2.9C). By contrast, Colless indices increase with mis-segregation rates and selective pressures, as the resulting variation and selection generate phylogenetic asymmetry. Accordingly, this

imbalance is apparent in phylogenetic reconstructions of simulated populations (Figure 2.9D). Cherries, by contrast, decrease with selection due to selection against many aneuploidies (Figure 2.9C). Pitchforks seemed less informative. Therefore, we tentatively selected 4 phylogenetic parameters that can retain information about chromosome mis-segregation—aneuploidy, MKV, Colless, and Cherries.

To characterize how well the four measures retain information about the simulation parameters, we performed dimensionality reduction with measures of karyotype heterogeneity alone (MKV and aneuploidy) alone and adding Colless and cherries—measures of phylogenetic topology (Figure 2.9E). This analysis indicates that when considering heterogeneity alone simulations performed under high CIN/high selection (yellow) and low CIN/low selection (red) associate closely, meaning these measures of heterogeneity are not sufficient to distinguish these disparate conditions (Figure 2.9E, left). These similarities arise because high selection can mask the heterogeneity expected from high CIN. By contrast, combining measures of heterogeneity with those of phylogenetic topology can discriminate between simulations with disparate levels of CIN and selection (Figure 2.9E, right). This provides further evidence that measures of heterogeneity alone are not sufficient to infer CIN due to the confounding effects of selection, particularly when the nature of selection is unclear or can vary. Together these results indicate that phylogenetic topology preserves information about underlying levels of selective pressure and rates of chromosome mis-segregation. Further, phylogenetic topology of single-cell populations may be a suitable way to correct for selective pressure when estimating the rate of chromosome mis-segregation from measures of karyotype diversity.

Experimental chromosome mis-segregation measured by Bayesian inference

To experimentally validate quantitative measures of CIN, we generated a high rate of chromosome mis-segregation with a clinically relevant concentration of paclitaxel (Taxol) over 48 hours (Figure 2.10A). We treated CAL51 breast cancer cells with either a DMSO control or 20 nM paclitaxel, which generates widespread aneuploidy due to chromosome mis-segregation on multipolar mitotic spindles (249), verified in this experiment (Figure 2.11A). At 48h cells will have undergone 1-2 mitoses and, consistent with abnormal chromosome segregation, we observe broadened DNA content distributions by flow cytometry (Figure 2.11B). Using low-coverage scDNAseq data, we characterized the karyotypes of 36 DMSO- and 134 paclitaxel-treated cells. As expected, virtually all cells had extensive aneuploidy after paclitaxel, in contrast with low variance in the control (Figure 2.10B). Additionally, the mean of the resultant aneuploid karyotypes for each chromosome still resembled those of bulk-sequenced cells, highlighting that bulk-sequencing is an ensemble average, and does not detect variation in population aneuploidy, particularly with balanced mis-segregation events (Figure 2.10B, single-cell mean and bulk). In quantifying the absolute deviation from the modal control karyotype in each cell, and assuming a single mitosis, cells exposed to 20 nM paclitaxel mis-segregate 18.5 ± 0.5—a P_{misseg} of ~0.42 considering the control's sub-diploid modal karyotype (Figure 2.10C). The majority of these appeared to be whole-chromosome mis-segregations (Figure 2.12).

In this instance, we were able to estimate mis-segregation rate by calculating absolute deviation from the modal karyotype after a single aberrant cell division. However, such an analysis would not be possible for long-term experiments, or real tumors, where new aneuploid cells may be subject to selection. Accordingly, we sought to infer the

parameters of this experiment—the mis-segregation rate of 18.5 chromosomes per division and low selection—using only measures of aneuploidy, variance, and phylogenetic topology. To display this, we used dimensionality reduction to ensure that observed measures from the paclitaxel-treated Cal51 population fell within the space of those observed from simulated populations over 2 steps under the Hybrid model. The experimental data mapped to those from simulations using high mis-segregation rates and relatively low selection (red point, Figure 2.10D). However, this comparison does not provide a quantitative measure of CIN. Instead, parameter inference via approximate Bayesian computation (ABC) is well suited for this purpose.

By deriving phylogeny metrics from simulated populations under a wide-range of distributions of evolutionary parameters, ABC identifies evolutionary parameters most consistent with the data—the posterior probability distribution. We used ABC with simulated data to infer the chromosome mis-segregation rate and selective pressure in the paclitaxel-treated cells (281). Importantly, this data has directly observed rates of mis-segregation, which provide a gold standard benchmark to optimize ABC inference.

One key aspect of ABC is the selection of optimal phylogenetic summary statistics. A small number of summary statistics is optimal and larger numbers impair the model (281). To address this, a common approach is to identify a small set of summary statistics that achieve the best inference. Here, we used the experimentally observed mis-segregation rate as a benchmark to optimally select a panel of measures for parameter inference (Figure 2.13) and selected the following four metrics to use concurrently in our ABC analysis: mean aneuploidy, MKV, the Colless index (a phylogenetic balance index) and number of cherries (normalized population size). In doing so, this analysis inferred a

chromosome mis-segregation rate of 0.396 ± 0.003 (or 17.4 ± 0.1 chromosomes; mean ± SE), which compares favorably with the experimentally observed rate of 18.5 ± 0.5 (Figure 2.10E; dashed line represents experimental rate, white '+' the inferred rate). The distribution of accepted values for selection was skewed toward lower pressure (21 ± 0.4; mean ± SE), meaning that karyotype selection had little bearing on the result at this time point, consistent with the absence of selection in a 48-hour experiment.

Interestingly, the incidence of nullisomy in the simulated population was higher than in the paclitaxel-treated populations at the observed mis-segregation rate (Figure 2.14A). This could be due to spindle pole clustering, a recovery mechanism often seen in paclitaxel treated cells that causes non-random chromosome mis-segregations. A posterior predictive check of the summary statistics demonstrates how each contributes to the inference of CIN rate (Figure 2.14B). In short, this experimental case validated ABC-derived mis-segregation rate as a measure of CIN, with an experimentally determined mis-segregation rate. Importantly, prior estimations of mis-segregation rate selective pressure were not required to develop this quantitative measure of CIN.

Together, these data indicate that combining simulated and observed metrics of population diversity and structure with a Bayesian framework for parameter inference is a flexible method of quantifying the evolutionary forces associated with CIN. Moreover, this method reveals the hitherto unreported potential extent of chromosome mis-segregation induced by a clinically relevant concentration of the successful chemotherapeutic paclitaxel consistent with the measured mis-segregation from non-pharmacologically induced multipolar divisions (282).

Minimum sampling of karyotype heterogeneity

The cost of high-throughput DNA sequencing of single cells is often cited as a limitation to clinical implementation (283). In part, the cost can be limited by low-coverage sequencing which is sufficient to estimate the density of reads across the genome. Further, it may be possible to minimize the number of cells that are sampled to get a robust estimate of CIN, though sampling too few cells may result in inaccurate measurements. Accordingly, we determined how sampling impacts measurement of mis-segregation rates using approximate Bayesian computation. We first took 5 random samples from the population of paclitaxel-treated cells each at various sample sizes (Figure 2.15A). We then inferred the mis-segregation rate in each sample and identified the sample size that surpasses an average of 90% accuracy and a low standard error of measurement. We found that even small sample sizes can accurately infer the mis-segregation rate, in this context, with a low standard error (Figure 2.15B-D). A sample size of 60 cells produced the most accurate measurement at 99.5% and a standard error of 0.008 (± 0.35 chromosomes). We repeated this analysis using simulated data from the Hybrid selection model and a range of mis-segregation rates spanning what is observed in cancer and non-cancer cultures ($P_{misseg} \leq 0.02$; see below). We again found a range of sample sizes whose inferred mis-segregation rates underestimate the known value from those simulations ($n \in [20, 40\ldots 180]$; Figure 2.15E,F). Across all mis-segregation rates and selective pressures, random samples of 200 cells had a median percent accuracy of 90% and median standard error of 0.0003 (± 0.0138 chromosomes per division). The difference in optimal sample sizes between the paclitaxel-treated population and the simulated population is notable and likely due to the presence of ‘clonal’ structures in the simulated population.

While the paclitaxel treatment resulted in a uniformly high degree of aneuploidy and little evidence of karyotype selection, the simulated populations after 60 steps (~30 generations) have discrete copy number clusters that may not be captured in each random sample. To verify this, we repeated the analysis using only data from the first time step, prior to the onset of karyotype selection (Figure 2.15H). In this case, we found that the sample size needed to achieve a median 90% accuracy over all simulations in this context is 100 cells, at which point the standard error for P_{misseg} is 0.0068 (placing measures within ± 0.31 chromosomes per division; Figure 2.15I,J). Thus, a larger number of cells is required in the context of long-term karyotype selection than a more acute time scale, such as we see with paclitaxel.

In conclusion, we recommend using 200 cells from a single sampled site which, at biologically relevant time scales and rates of mis-segregation, provides ≥90% accuracy. These data represent, to our knowledge, the first analysis of how sample size for single-cell sequencing affects the accuracy and measurement of chromosome mis-segregation rates.

Inferring chromosome mis-segregation rates in tumors and organoids

To determine if this framework is clinically applicable, we employed previously published scDNAseq datasets derived from tumor samples and patient-derived organoids (PDO) (138, 191). Importantly, the data from Bolhaqueiro et al. include sample-matched live cell imaging data in colorectal cancer PDOs, with direct observation of chromosome mis-segregation events to compare with inferred measures. We established our panel of measurements on these populations (Figure 2.16A) and used these to tune the prior distribution of time steps and the rejection threshold for ABC. In sensitivity analysis, 20 steps

or greater was sufficient to establish stable estimates of P_{misseg} and selection, S (Figure 2.17A,B)—we chose a window of 40-80 steps for further analysis. For rejection thresholds 0.05 and smaller, the inferred mis-segregation rates remained steady (Figure 2.17C). With these model parameters chosen, we evaluated the different selection models, and found that the Abundance model resulted in simulated data that best resembled experimental data, for both exponential and constant-population dynamics (Table 2.3). Given that the Abundance model is the most biologically relevant, we will use data simulated under this model in our prior dataset for inference.

Having confirmed the summary statistics from these samples were within the space of the simulation data with our chosen priors (Figure 2.16B), we performed ABC analysis on these datasets to infer rates of chromosome mis-segregation and levels of selection pressure and display the joint posterior distributions as 2D density plots (Figure 2.16C,D; Figure 2.18; Figure 2.19). Figure 6C illustrates the results for two individual colon organoid lines, showing the distribution of parameters used for simulations that gave the most similar results. With ABC, inferred parameters fall within rates of mis-segregation of about 0.001 to 0.006. Applied to a near-diploid cell, this translates to a range of about 5-38% of cell divisions having one chromosome mis-segregation. Importantly, these inferred rates of chromosome mis-segregation fall within the range of approximated *per chromosome* rates experimentally observed in cancer cell lines and human tumors (Figure 2.16E; Table 2.5) (122, 136, 137, 157, 237, 249, 284–286). Higher inferred mis-segregation rates tended to coincide with lower inferred selection experienced in these samples (Figure 2.16F). Posterior distributions in these samples were skewed toward high

selection (S) indicating the presence stabilizing selection in all cases, where the average of the distributions of some samples were slightly lower or higher (Figure 2.19).

To confirm the relevance of the inferred scalar exponent we performed our model selection scheme using only the simulation data with unmodified fitness values (S=1; Table 2.4). In this case we found that the inferred mis-segregation rates for most samples fell well below the expected range found in cancer cell lines (Figure 2.16E). Additionally, when we inferred mis-segregation rates and selection in the early timepoint of longitudinally sequenced organoid clones from Bolhaqueiro et al., 2019, the composition of the resultant populations simulated using these inferred characteristics better resembled the late-timepoint organoid data than those with unmodified selection values (S=1; Figure 2.20; Figure 2.21).

As further validation for mis-segregation rates, we compared these inferred rates from CRC PDOs with those directly measured in live imaging from Bolhaqueiro et al., 2019. Though mis-segregation cannot be directly inferred from microscopy, diversity should correlate with the observed rate of mitotic errors. There was a strong correlation but for two outliers—14T and U1T (Figure 2.16G). In fact, when adjusting to the same scale and correcting for cell ploidy, these data follow a strong positive linear trend with a slightly lower slope than a 1:1 correlation, which could reflect an overestimation of mis-segregation rates in the microscopy data (Figure 2.16H). Particularly with lagging chromosomes, despite a chromosome's involvement in an observed segregation defect, it may end up in the correct daughter cell. Overall, these results indicate that the inferred measures using approximate Bayesian computation and scDNAseq account for selection and provide a quantitative measure of CIN.

DISCUSSION

The clinical assessment of mutations, short indels, and microsatellite instability in human cancer determined by short-read sequencing currently guide clinical care. By contrast, CIN is highly prevalent, yet has remained largely intractable to clinical measures. Single-cell DNA sequencing now promises detailed karyotypic analysis across hundreds of cells, yet selective pressure suppresses the observed karyotype heterogeneity within a tumor. Optimal clinical measurement of CIN may be achieved with scDNAseq, but must additionally account for selective pressure, which reduces karyotype heterogeneity.

Despite the major limitations with current measures of CIN, emerging evidence hints at its utility as a biomarker to predict benefit to cancer therapy. For example, CIN measures appear to predict therapeutic response to paclitaxel (251, 265, 266). Nevertheless, existing measures of CIN have had significant limitations. FISH and histological analysis of mitotic abnormalities are limited in quantifying specific chromosomes or requiring highly proliferative tumor types, such as lymphomas and leukemia. Gene expression profiles are proposed to correlate with CIN among populations of tumor samples (187), though they happen to correlate better with tumor proliferation (189); in any case, they are correlations across populations of tumors, not suitable as an individualized diagnostic. We conclude that scDNAseq is the most complete and tractable measure of cellular karyotypes, and sampling at least 200 cells, coupled with computational models and ABC, promises to offer the best measure of tumor CIN.

Computational modeling of aneuploidy and CIN has been used to explore evolution in the context of numerical CIN and karyotype selection (196, 215, 223, 224, 287, 288). Gusev and Nowak lay the foundation for mathematical modeling of CIN. While

Gusev focused on the karyotypic outcomes of CIN, Nowak considered the effects of CIN-inducing mutations and the subsequent rate of LOH. Neither considered the individual fitness differences between specific karyotypes (215, 287, 288). This was improved in Laughney et al., 2015 and Elizalde et al., 2018 where the authors leveraged the chromosome scores derived in Davoli et al., 2013, which enable the inclusion of oncogenes and tumor suppressors in models of CIN as we have done. These studies have provided important insights such as the role of whole-genome doubling as an evolutionary bridge to optimized chromosome stoichiometry. Yet the populations derived in these studies tend to vary to a greater degree than observed with scDNAseq, as they do not model strong selection against aneuploidy. Further they do not attempt to use their models to measure CIN in biological samples. Here, we build on these models by considering, in addition to the selection on driver genes, the stabilizing selection wrought by chromosomal gene abundance. Further, we consider that the magnitude of selection pressure may not be a constant and implement a modifier to tune selection in our models. Lastly, we use our models as a quantitative measure of CIN that accounts for this selection.

Previous studies using single-cell sequencing identified surprisingly low karyotypic variance in human tumors including breast cancer (194, 196, 271) and colorectal and ovarian cancer organoids (138, 139). It has been difficult to understand these findings in the light of widespread CIN in human cancer (226, 245, 247, 262, 289). The best explanation of this apparent paradox is selection, which moderates karyotypic variance. Accounting for this, we can infer rates of chromosome mis-segregation in tumors or PDOs well within the range of rates observed microscopically in cancer cell lines. Additionally,

no previous work, to our knowledge, has estimated the required sample size to infer CIN from scDNAseq data.

As described by others (277, 284), and consistent with our findings, early emergence of polyploid cells can markedly reduce apparent selection, leading to an elevated karyotype diversity over time. While we do not explicitly induce chance of whole genome doubling (WGD) events in simulations, populations that begin either diploid or tetraploid converge on near-triploid karyotypes over time, consistent with the notion that WGD can act as an evolutionary bridge to highly aneuploid karyotypes. Notably, our analysis indicates the samples with apparent polyploidy experienced among the lowest levels of karyotype selection.

In some early studies, CIN is considered a binary process—present or absent. We assumed that CIN measures are scalar, not binary, and measure this by rate of chromosome mis-segregation per division. A scalar is appropriate if, for example, there was a consistent probability of chromosome mis-segregation per division. However, we recognize that some mechanisms may not well adhere to this simplified model of CIN. For example, tumors with centrosome amplification may at times undergo bipolar division without mis-segregation, or, at other times, a multipolar division with extensive mis-segregation. Further, it is possible that some mechanisms may have correlated mis-segregations such that a daughter cell that gains one chromosome is more likely to gain other chromosomes, rather than lose them. Another possibility is that CIN could result in the mis-regulation of genes that further modify the rate of CIN. Our model does not yet account for punctuated behavior or changing rates of CIN. Furthermore, while recent studies have reported non-random mis-segregation of chromosomes (157, 243), we did not

incorporate these biases into our models as these studies do not reach consensus on which chromosomes are more frequently mis-segregated, which may be model-dependent.

Our approach reconstructs phylogenetic trees via copy number variation (CNV) analysis. This approach may be suboptimal given the selection on aneuploid states and could be particularly problematic in the setting of convergent evolution. It is possible that this method results in low accuracy of the reconstructed phylogenies. Alternative approaches are possible but would likely require re-design of the scDNAseq assay to include spiked-in primers that span highly polymorphic regions on each chromosome. If this were done, these sequences could be read in all cells and single-nucleotide polymorphisms could track individual maternal and paternal chromosomes, allowing a means of reconstructing cell phylogeny independent of CNVs. Despite this limitation, our phylogenetic reconstructions did seem to allow inference of CIN measures consistent with directly observed rates of chromosome mis-segregation in our taxol-induced CIN model as well as several independent cancer PDO models and cell lines.

A final limitation of our approach is we used previous estimates of cellular selection in our agent-based model and used these selection models to infer quantitative measures of CIN. While this approach seems to perform well in estimates of mis-segregation rates, we recognize that the selection models do not necessarily represent the real selective pressures on distinct aneuploidies. Future investigations are necessary to measure the selective pressure of distinct aneuploidies—a project that is now within technological reach. Selective pressures could also be influenced by cell type (205, 290–292), tumor cell genetics (293–297), and the microenvironment (246).

In summation, we developed a theoretical and experimental framework for quantitative measure of chromosomal instability in human cancer. This framework accounts for selective pressure within tumors and employs Approximate Bayesian Computation, a commonly used analysis in evolutionary biology. Additionally, we determined that low-coverage single-cell DNA sequencing of at least 200 cells from a human tumor sample is sufficient to get an accurate (>90% accuracy) and reproducible measure of CIN. This work sets the stage for standardized quantitative measures of CIN that promise to clarify the underlying causes, consequences, and clinical utility of this nearly universal form of genomic instability.

MATERIALS AND METHODS

Agent-based modeling

Agent-based models were implemented using the agent-based platform, NetLogo 6.0.4 (298).

1. Underlying assumptions for models of CIN and karyotype selection

1.1. Chromosome mis-segregation rate is defined as the number of chromosome mis-segregation events that occur per cellular division.

1.2. Cell division always results in 2 daughter cells.

1.3. $P_{misseg,c}$ is assigned uniformly for each cell in a population and for each chromosome.

1.4. Cells die when the copy number of any chromosome is equal to 0 or exceeding 6 unless otherwise noted.

1.5. Steps are based on the rate of division of euploid cells. We assume a probability of division ($P_{division}$) of 0.5, or half of the population divides every step, for euploid populations. This probabilistic division is to mimic the asynchrony of

cellular proliferation and to allow for positive selection, where some cells may divide more rapidly than their euploid ancestors.

1.6. No chromosome is more likely to mis-segregate than any other.

2. Chromosome-arm scores

2.1. Gene Abundance Scores. The R package `biomaRt v.2.46.3` was used to pull the chromosome arm location for each gene in Ensembl's 'Human genes' dataset (GRCh38.p13). The number of genes on each chromosome arm were enumerated and Abundance scores were generated by normalizing the number of genes on each chromosome arm by the sum of all enumerated genes across chromosomes. Chromosome arms with no recorded genes were given a score of 0.

2.2. Driver Density Scores. Arm-level 'TSG-OG-Ess' scores derived in (221) were adapted for our purposes. These values were derived from a pan-cancer analysis (TCGA) of the frequency of mutation of these genes and their location in the genome. These scores correlate with the frequency with which chromosomes are found to be amplified in the genome. We adapted these scores by normalizing the published 'TSG-OG-Ess' score for each chromosome arm by the sum of all Charm scores. Chromosome arms with no published Charm score were given a score of 0. We refer to these as TOE scores for our purposes.

2.3. Hybrid Scores. Chromosome arm scores for the Hybrid selection model are the average of the chromosome arm's Gene Abundance and Driver Density scores.

3. Implementing karyotype selection

In each model, numerical scores are assigned to each chromosome, the sum of which represents the fitness of the karyotype (Figure 2.2B). At each simulation time step, fitness is re-calculated for each cell based on its updated karyotype. These fitness values determine if they undergo mitosis in the next round. However, the modality of selection changes how those karyotypes are assessed. Here, we implement 4 separate karyotype selection models 1) gene abundance, 2) driver density, 3) a hybrid gene abundance and driver density, and 4) neutral selection. The scores that are generated in each produce a fitness value (F) that can then be subjected to pressure (S) as described above.

3.1. Selection on Gene Abundance. The Gene Abundance selection model relies on the concept of gene dosage stoichiometry where the aneuploid karyotypes are selected against and that the extent of negative selection scales with the severity of aneuploidy and the identity and gene abundance on the aneuploid chromosomes (299). Chromosome arm fitness contribution scores (f_c) are taken as the chromosome arm scores derived above (section 2.1) and the sum of these scores is 1. These base values are then modified under the gene abundance model to generate a contextual fitness score ($CFS_{GA,c}$) at each time step such that…

$$\mathrm{CFS}_{\mathrm{GA,c}} = \mathrm{f_c} - \frac{\mathrm{f_c} \times |\mathrm{n_c} - \bar{\mathrm{x}}_\mathrm{p}|}{\bar{\mathrm{x}}_\mathrm{p}}$$

$$\mathrm{F} = \sum_{\mathrm{c}=1}^{46} \mathrm{CFS}_{\mathrm{GA,c}}$$

… where $\bar{x}_p$ is the average ploidy of the population and n_c is the chromosome copy number. In this model, the fitness contribution of a chromosome declines as its distance from the average ploidy increases and that the magnitude of this effect is dependent on the size of the chromosome.

3.2. Selection on Driver Density. The Driver Density modality relies on assigned fitness values to chromosomes based on their relative density of tumor suppressor genes, essential genes, and oncogenes. Chromosome arm fitness contribution scores (f_c) are taken as the chromosome arm scores derived above (section 2.2) and are employed such that…

$$\mathrm{CFS}_{\mathrm{TOE,c}} = \frac{\mathrm{n_c} \times \mathrm{TOE_c}}{\bar{\mathrm{x}}_{\mathrm{p}}}$$

$$\mathrm{F} = \sum_{\mathrm{c}=1}^{46} \mathrm{CFS}_{\mathrm{TOE,c}}$$

This selection model benefits cells that have maximized the density of oncogenes and essential genes to tumor suppressors through chromosome mis-segregation.

3.3. Hybrid Selection. The hybrid model relies on selection on both gene abundance and driver densities. $\mathrm{CFS}_{\mathrm{TOE,c}}$ and $\mathrm{CFS}_{\mathrm{GA,c}}$ are both calculated and averaged such that…

$$\mathrm{F} = \sum_{\mathrm{c}=1}^{46} \frac{\mathrm{CFS}_{\mathrm{GA,c}} + \mathrm{CFS}_{\mathrm{TOE,c}}}{2}$$

3.4. Neutral Selection. When populations are grown under neutral selection, the fitness of each cell is constitutively set to 1 regardless of the cells' individual karyotypes.

$$\mathrm{F} = 1$$

3.5. Scaling selection pressure. Within each model of karyotype selection, the magnitude of selective pressure upon any karyotype, with fitness F, can be scaled by applying the scalar exponent S to produce a modified fitness score F_M. Thus…

$$F_M = F^S$$

For example, in the Gene Abundance model of karyotype selection, an otherwise diploid cell with 3 copies of chromosome 1 in a diploid population will have a F value of 0.954. Under selection-null conditions (S=0)…

$$F_M = F^S = 0.954^0 = 1$$

… the fitness of the aneuploid cell is equivalent to that of a euploid cell. Under conditions of high selection (S=50)…

$$F_M = F^S = 0.954^{50} = 0.097$$

…fitness of the aneuploid cell is ~10% that of the euploid cell and thus divides ~10% as frequently.

4. Modeling growing and constant population dynamics

To accommodate different population size dynamics, we implemented our model using either growing, pseudo-Moran limited population dynamics and constant-size populations with approximated Wright-Fisher population dynamics.

4.1. Simulating CIN in exponentially growing populations with pseudo-Moran limits.

4.1.1. Populations begin with 100 founder cells with a euploid karyotype of integer value $\bar{x}_p$ and the simulation is initiated.

4.1.2. CFS values are calculated for each chromosome in a cell according to the chosen karyotype selection model.

4.1.3. Cellular fitness is calculated based on CFS values.

4.1.4. Selective pressure (S) is applied to fitness (F) values to modify cellular fitness (F_M).

4.1.5. Cells are checked to see if any death conditions are met and if the population limit is met. Cells die if any chromosome arm copy (n_c) is less than 1 or greater than 6 (unless otherwise indicated). We implemented population size limits in a pseudo-Moran fashion to reduce computational constraints. If the population size is 3000 cells or greater, a random half of the population is deleted.

4.1.6. Cells probabilistically divide if their fitness is greater than a random float (R) between 0 and 2. Thus…

$$\mathrm{R}\sim\mathrm{U}[0,2]$$

$$\mathrm{P}_{\mathrm{division}}=\mathrm{P}(\mathrm{F}_{\mathrm{M}}>\mathrm{R})$$

4.1.7. If a cell does not divide, it restarts the cycle from 4.1.2. If a cell divides, mis-segregations may occur.

4.1.8. Each copy (n_c) of each chromosome (c) has an opportunity to mis-segregate probabilistically. For each chromosome copy, a mis-segregation occurs if a random float (R) between 0 to 1 falls below P_{misseg}. Thus…

$$\mathrm{R}\sim\mathrm{U}[0,1]$$

Mis-segregate chromosome c if $\mathrm{P}_{\mathrm{misseg,c}}>\mathrm{R}$

4.1.9. If a chromosome copy is not mis-segregated, the next chromosome copy is tested. If a chromosome copy is mis-segregated, chromosome arms may be segregated separately (i.e. a reciprocal, arm-level CNA) if a random float (R) between 0 and 1 falls below P_{break}. Thus…

$$R \sim U[0,1]$$

Break chromosome c if $P_{misseg,c} > R$

4.1.10. The karyotype of the cell is modified according to the results of the mis-segregation sequence above. When the mis-segregation sequence is complete, a clone of the initial cell with any reciprocal copy number alterations to its karyotype is created.

4.1.11. The simulation ends if it reaches 100 steps and data are exported. Otherwise, the simulation continues from 4.1.2.

4.2. Simulating CIN in constant-size populations with approximated Wright-Fisher dynamics. We approximated constant-size Wright-Fisher dynamics in our model by re-initiating the population at each time step and randomly drawing from the previous generation's distribution of chromosome copy numbers for each chromosome in each cell of the new population. Because the exponential pseudo-Moran model relies on proliferation rates across over-lapping generations to enact karyotype selection, such a method would not be useful here. To accommodate karyotype selection in this model, we employed an additional baseline death rate of about 20% (180) that increases for cells with lower fitness and decreases for cells with higher fitness (see section 4.2.9). In this way, the karyotypes of the cells that die are removed from the pool of karyotypes that are drawn upon in the subsequent generation. CIN is simulated in this model as follows:

4.2.1. Populations begin with 4500 founder cells and the simulation is (re-)initiated. The population begins with a euploid karyotype of integer value $\bar{x}_p$ if the population is being created for the first time.

4.2.2. Cells divide every step, regardless of fitness.

4.2.3. Chromosomes are mis-segregated in the same fashion as the exponential pseudo-Moran model above (sections 4.1.8 – 4.1.10).

4.2.4. The simulation ends if it reaches 100 steps and data are exported. Otherwise, the simulation continues from 4.2.1.

4.2.5. CFS values are calculated for each chromosome in a cell according to the chosen karyotype selection model.

4.2.6. Cellular fitness is calculated based on CFS values.

4.2.7. Selective pressure (S) is applied to fitness (F) values to modify cellular fitness (F_M).

4.2.8. Cells are checked to see if any death conditions are met and if the population limit is met. Cells die if any chromosome arm copy (n_c) is less than 1 or greater than 6 (unless otherwise indicated).

4.2.9. Additionally, the cells' fitness values and a random float (R) between 0 and 5 are used to determine if they die. In this way, a cell with a fitness of 1 has a 20% baseline death rate. Thus, cells die if…

$$\frac{1}{F^S+0.001} > R \sim U[0,5]$$

4.2.10. After determining cell death, the copy number distributions of each cells' chromosome arm (c) are individually stored.

4.2.11. The cycle repeats from 4.2.1. However, the re-initated population will have its chromosome arm copy numbers drawn from the previous generation's stored chromosome arm copy number distributions.

Analysis of population diversity and topology in biological and simulated data

Phylogenetic trees were reconstructed from chromosome copy number profiles from live and simulated cells by calculating pairwise Euclidean distance matrices and performing complete-linkage clustering in R (Team, 2021). Phylogenetic tree topology measurements were performed in R using the package `phyloTop v2.1.1` (300). Sackin and Colless indices of tree imbalance were calculated, normalizing to the number of tree tips. Cherry and pitchfork number were also normalized to the size of the tree. MKV is taken as the variance of individual chromosomes taken across the population, averaged across all chromosomes, then normalized to the average ploidy of the population. Average aneuploidy is calculated as the variance within a single cell's karyotype averaged across the population.

Approximate Bayesian computation

Approximate Bayesian computation was used for parameter inference of experimental data from simulated data. For this we employed the the "abc" function in the R package `abc v2.1` (301). In short, a set of simulation parameters, θ_i, is sampled from the prior distribution. This set of parameters corresponds to a set of simulated summary statistics, $S(y_i)$, in this case phylogenetic tree shapes, which can be compared to the set of experimental summary statistics, $S(y_o)$. The Euclidean distance between the experimental and simulated summary statistics can then be calculated ($d(S(y_i),S(y_o))$. A threshold, T, is then selected—0.05 in our case—which rejects the lower 1-T sets of simulation parameters that correspond. The remaining parameters represent those that gave summary statistics with the highest similarity to the experimental summary statistics. These represent the posterior distribution of accepted parameters.

Bayesian model selection was performed using the “postpr” function in the same R package using tolerance threshold of 0.05 and rejection sampling method. This was used to calculate the posterior probability of each selection model *within* each growth model and the Bayes factor for each selection model with neutral selection as the null hypothesis. Bayes factors > 5 were considered substantial evidence of the alternative hypothesis.

Sliding window analysis to tune time-steps for approximate Bayesian computation

We chose which simulation time steps to use for approximate Bayesian computation on organoid and biopsy data by repeating the inference using a sliding window of prior datasets with a width of 11 time steps (i.e. parameters from steps $\in$ [0-10], [10-20], …, [91-100]) to see if the posterior distributions would stabilize over time. We then chose simulations from 40-80 time steps as our prior dataset as this range provided both a stable inference and is centered around 60 time steps (analogous to 30 generations, estimated to generate a 1 cm palpable mass of ~1 billion cells).

Cell cultivation procedures

Cal51 cells expressing stably integrated RFP-tagged histone H2B and GFP-tagged α-tubulin were generated as previously described (249). Cells were maintained at 37ºC and 5% CO_2 in a humidified, water-jacketed incubator and propagated in Dulbecco’s Modified Eagle’s Medium (DMEM) – High Glucose formulation (Cat #: 11965118) supplemented with 10% fetal bovine serum and 100 units/mL penicillin-streptomycin. Paclitaxel (Tocris Bioscience, Cat #: 1097/10) used for cell culture experiments was dissolved in DMSO. The Cal51 cells were obtained from the DSMZ-German Collection of Microorganisms and Cell Cultures and were free from mycoplasma contamination prior to study.

Karyotype analysis confirms the near-diploid characteristic of the cell line and the presence of both fluorescent markers suggests they are free of other contaminating cell lines.

Time-lapse fluorescence microscopy

Cal51 cells were transduced with lentivirus expressing mNeonGreen-tubulin-P2A-H2B-FusionRed. A monoclonal line was treated with 20 nM paclitaxel for 24, 48, or 72 hours before timelapse analysis at 37ºC and 10% CO_2. Five 2 µm z-plane images were acquired using a Nikon Ti-E inverted microscope with a cMos camera at 3-minute intervals using a 40X/0.75 NA objective lens and Nikon Elements software.

Flow cytometric analysis and cell sorting

Cells were harvested with trypsin, passed through a 35 µm mesh filter, and rinsed with PBS prior to fixation in ice cold 80% methanol. Fixed cells were stored at -80ºC until analysis and sorting at which point fixed cells were resuspended in PBS containing 10 µg/ml DAPI for cell cycle analysis.

Flow cytometric analysis.

Initial DNA content and cell cycle analyses were performed on a 5 laser BD LSR II. Doublets were excluded from analysis via standard FSC/SSC gating procedures. DNA content was analyzed via DAPI excitation at 355 nm and 450/50 emission using a 410 nm long pass dichroic filter.

Fluorescence activated cell sorting.

Cell sorting was performed using the same analysis procedures described above on a BD FACS AriaII cell sorter. In general, single cells were sorted through a 130-µm low-pressure deposition nozzle into each well of a 96-well PCR plate containing 10 µl Lysis and Fragmentation Buffer cooled to 4ºC on a Eppendorf PCR plate cooler. Immediately

after sorting PCR plates were centrifuged at 300 x g for 60 seconds. For comparison of single-cell sequencing to bulk sequencing, 1000 cells were sorted into each 'bulk' well. The index of sorted cells was retained allowing for the *post-hoc* estimation of DNA content for each cell.

Low-coverage single-cell whole genome sequencing

Initial library preparation for low-coverage scDNAseq was performed as previously described (302) and adapted for low coverage whole genome sequencing instead of high coverage targeted sequencing. Initial genome amplification was performed using the GenomePlex® Single Cell Whole Genome Amplification Kit and protocol (Sigma Aldrich, Cat #: WGA4). Cells were sorted into 10 µl pre-prepared Lysis and Fragmentation buffer containing Proteinase K. DNA was fragmented to an average of 1 kb in length prior to amplification. Single cell libraries were purified on a 96-well column plate (Promega, Cat #: A2271). Library fragment distribution was assessed via agarose gel electrophoresis and concentrations were measured on a Nanodrop 2000. Sequencing libraries were prepared using the QuantaBio sparQ DNA Frag and Library Prep Kit. Amplified single-cell DNA was enzymatically fragmented to ~250 bp, 5'-phosphorylated, and 3'-dA-tailed. Custom Illumina adapters with 96 unique 8 bp P7 index barcodes were ligated to individual libraries to enable multiplexed sequencing (302). Barcoded libraries were amplified following size selection via Axygen™AxyPrep Mag™ beads (Cat #: 14-223-152). Amplified library DNA concentration was quantified using the Quant-iT™ Broad-Range dsDNA Assay Kit (Thermo, Cat #: Q33130). Single-cell libraries were pooled to 15 nM and final concentration was measured via qPCR. Single-end 100bp sequencing was performed on an Illumina HiSeq2500.

Single-cell copy number sequencing data processing

Single-cell DNA sequence reads were demultiplexed using unique barcode index sequences and trimmed to remove adapter sequences. Reads were aligned to GRCh38 using Bowtie2. Aligned BAM files were then processed using Ginkgo to make binned copy number calls. Reads are aligned within 500kb bins and estimated DNA content for each cell, obtained by flow cytometric analysis, was used to calculate bin copy numbers based on the relative ratio of reads per bin (303). We modified and ran Ginkgo locally to allow for the analysis of highly variable karyotypes with low ploidy values (see Code and Data Availability). Whole-chromosome copy number calls were calculated as the modal binned copy number across an individual chromosome. Cells with fewer than 100,000 reads were filtered out to ensure accurate copy number calls (304). Cells whose predicted ploidy deviated more than 32% from the observed ploidy by FACS were also filtered out. The final coverage for the filtered dataset was 0.03. Single cell data extracted from Navin et al., 2011 were separated into their individual clones and depleted of euploid cells. Single cell data from Bolhaqueiro et al., 2019 were filtered to include only the aneuploid data that fell within the ploidies observed in the study (see Code and Data Availability).

Review and approximation of mis-segregation rates from published studies

We reviewed the literature to extract per chromosome rates of mis-segregation for cell lines and clinical samples. Some studies publish these rates. For those that did not, we estimated these rates by approximating the plotted incidence of segregation errors thusly:

$$\text{Approximate missegregration rate per chromosome} = \frac{\text{Observed \% frequency of errors per division}/100}{\text{Total \# modal chromosomes in sample}}$$

Modal chromosome numbers were either taken from ATCC where available or were assumed to equal 46. Observed % frequencies were approximated from published plots. Approximated rates assume that 1 chromosome is mis-segregated at a time.

ACKNOWLEDGMENTS

This study was supported by grants to M.E.B. and B.A.W. from the NCI (5R01CA234904). A.R.L. was supported by the UW Cellular and Molecular Pathology (5T32GM081061) and the UW Genomic Sciences Training Program (5T32HG002760) NIH training grants. Technical support comes from University of Wisconsin Carbone Cancer Center (UWCCC) Shared Resources funded by the UWCCC Support Grant P30 CA014520 – Flow Cytometry Core Facility (1S10RR025483-01), Cancer Informatics Shared Resource, Small Molecule Screening Facility. The authors thank the UW Biotechnology Center DNA Sequencing Facility for providing Illumina sequencing services. Special thanks go to Drs. Ana Bolhaqueiro, Bas Ponsioen, and Geert Kops for the provision of scDNAseq data for our analyses and to Dr. Caitlin Pepperell for valuable comments related to approximate Bayesian computation.

COMPETING INTERESTS

The authors declare no competing interests.

CODE AND DATA AVAILABILITY

DNA sequencing data from this study are deposited in NCBI Sequence Read Archive (Accession: PRJNA725515). Source code and data for modeling and analysis are available on the Open-Science Framework at (https://osf.io/snrg3/).

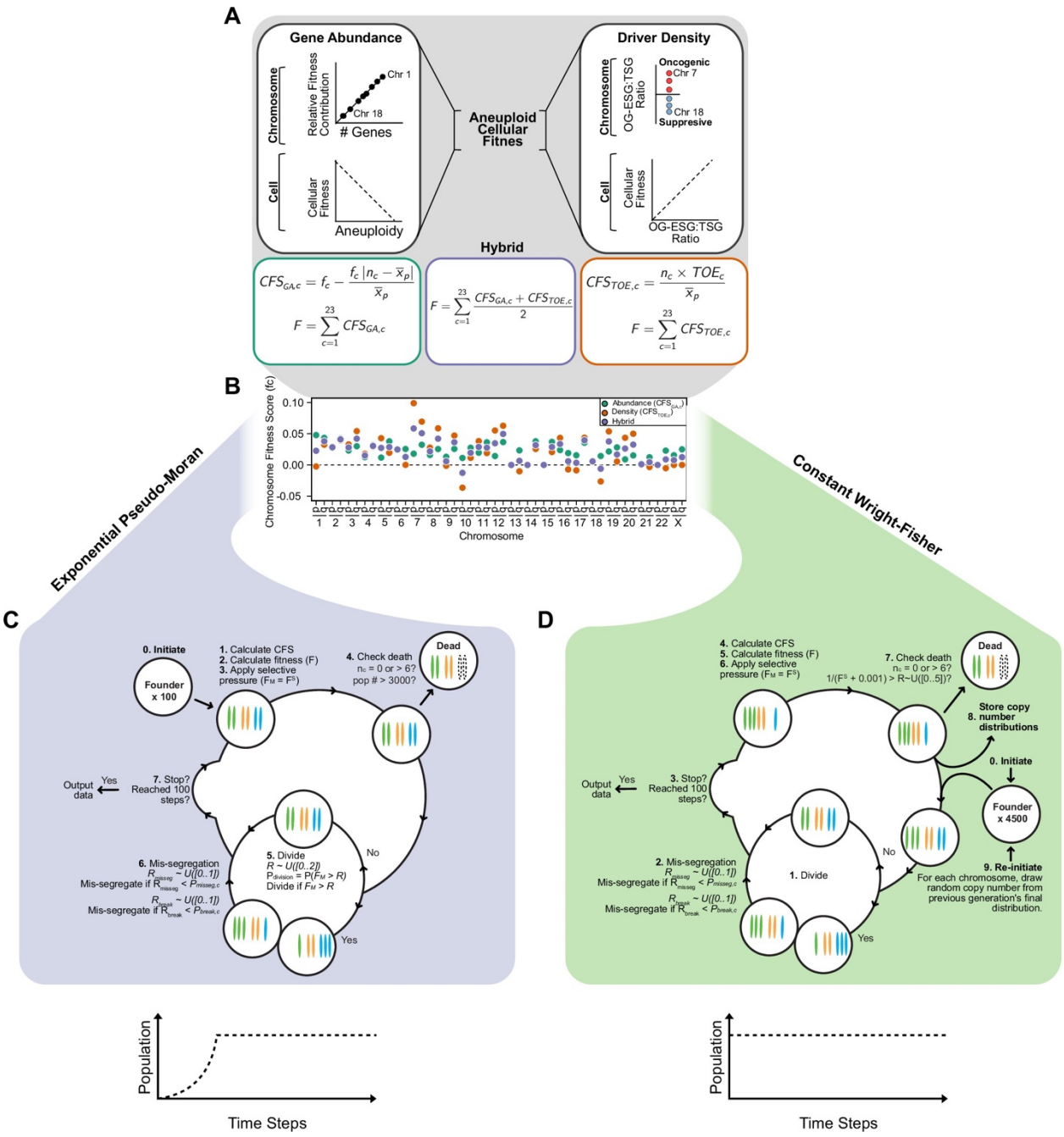

Figure 2.1 — Expanded model of chromosome mis-segregation and karyotype selection

Models of selection on aneuploid karyotypes. **Left**. In the Gene Abundance model, chromosomes that encode a larger number of genes contribute more to cellular fitness (F). Thus, large chromosomes have a higher fitness score (fc). Deviation from the average ploidy of the population results in a reduced Contextual Fitness Score (CFS) for each chromosome, the sum of which represents the fitness of the cell. **Right**. In the Driver Density Model, the fitness contribution of a chromosome depends on the ratio of oncogenes and

essential genes to tumor suppressors (OG-ESG:TSG). Gaining chromosomes with a higher OG-ESG:TSG ratio provides a fitness advantage while gaining more suppressive chromosomes invokes a fitness cost. These scores are still normalized to the ploidy of the average ploidy of the population to ensure that higher ploidy populations are not arbitrarily more fit. **Middle**. The Hybrid model takes the average of the fitness scores calculated in the other models. The neutral selection model (not shown) treats all karyotypes as equally fit. Base chromosome arm fitness scores for each model. Only the Hybrid and Driver Density model have negatively scored chromosomes, meaning their loss provides a fitness benefit. The neutral selection model does not require chromosome arm fitness scores. Simulating CIN in exponentially growing populations with pseudo-Moran limits. **(0)** Populations are founded by 100 founder cells and the simulation is initiated. **(1)** CFS values are calculated for each chromosome in a cell according to the chosen model. **(2)** Cellular fitness is calculated based on CFS values. **(3)** Selective pressure (S) is applied on cellular fitness values (F). **(4)** Cells are checked to see if any death conditions are met and if the population limit is met. **(5)** Cells probabilistically enter mitosis if their fitness value exceeds a random float (R) between 0 and 2. Thus Pdivision = P(FM >R). If a cell does not divide, it skips the next step. **(6)** If a cell enters mitosis, each chromosome has an opportunity to mis-segregate probabilistically. For each chromosome, a mis-segregation occurs if a random float (R), from 0 to 1, falls below Pmisseg. After a chromosome mis-segregation is determined, the chromosome arms may be individually segregated (i.e. reciprocal CNA) if a random float (R), from 0 to 1, falls below Pbreak. The cycle repeats and new CFS values are calculated, unless **(7)** stop conditions are met. When populations reach or exceed 3500 cells, a random half of the population is eliminated and the remaining cells continue the cycle. Simulating CIN in constant-size populations with Wright-Fisher dynamics. **(0)** Populations are initiated by 4500 euploid cells which **(1)** divide every step. **(2)** Chromosomes are mis-segregated as in the exponential pseudo-Moran model described above. **(3)** If stop conditions are met, the simulation ends and data are exported. If the cycle continues, **(4)** CFS values are calculated and used to **(5)** determine cellular fitness, after which, **(6)** selective pressure is applied. **(7)** Cells die if they lose both copies of a chromosome or exceed the upper limit of six. Additionally, to approximate Wright-Fisher dynamics, cells die if 1/(FS +0.001) exceeds a random float from 0 to 5. Thus, the baseline rate of cell death is ~0.2. **(8)** Each chromosome copy number is stored and the population is re-initiated

with 4500 new cells. The copy numbers for each of new cell's chromosomes are randomly and independently drawn from the copy number distributions of the previous generation. The cycle then repeats until the simulation ends **(step 3)**.

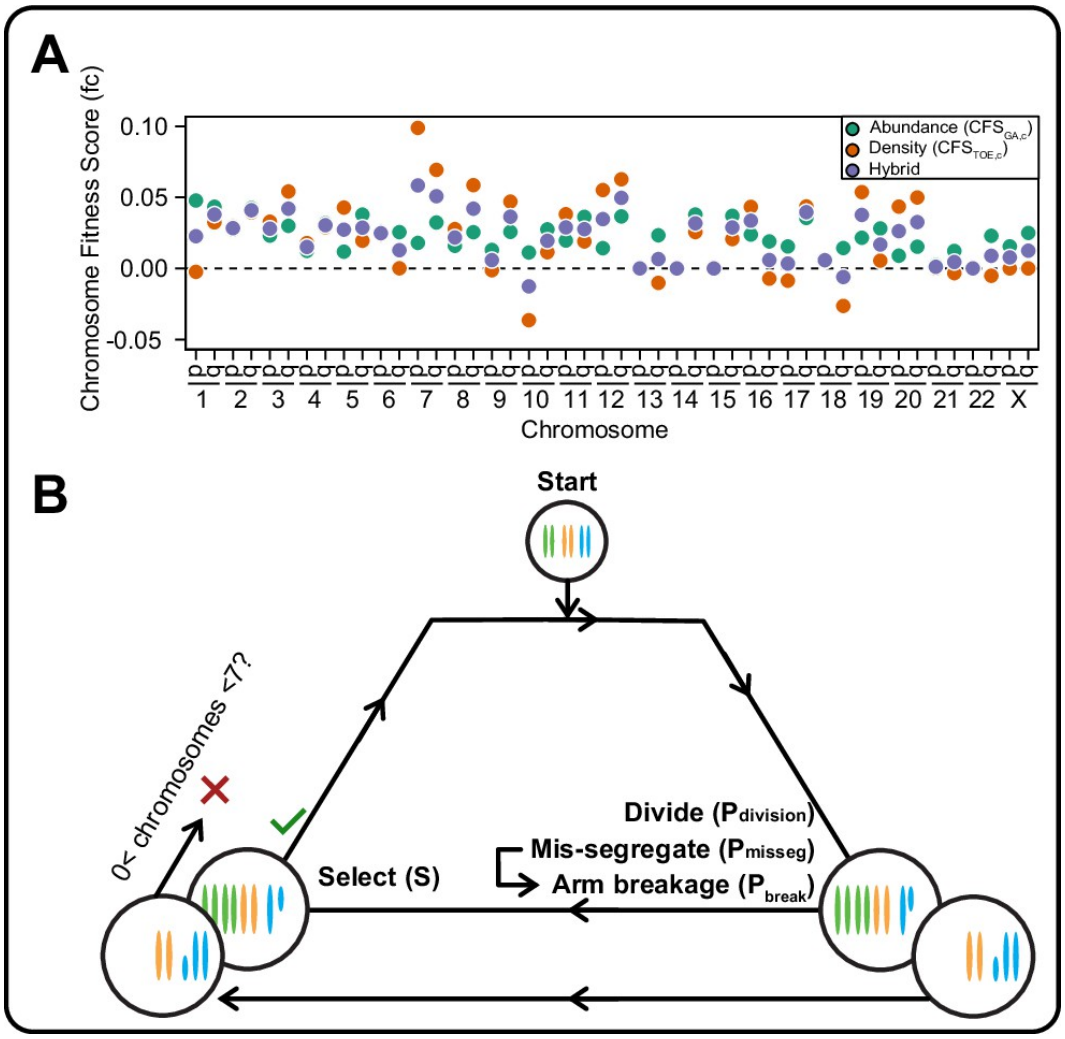

Figure 2.2 — A framework for modeling CIN and karyotype selection

(A) Chromosome arm scores for each model of karyotype selection. Gene Abundance scores are derived from the number of genes per chromosome arm normalized to the number of all genes. Chromosome arms 13 p and 15 p did not have an abundance score and were set to 0. Driver Density scores come from the pan-cancer chromosome arm scores derived in Davoli et al., 2013, and normalized to the sum of chromosome arm scores for chromosomes 1-22,X. Chromosome arms 13 p, 14 p, 15 p, 21 p, 22 p, and chromosome X did not have driver scores and were set to 0. Hybrid model scores are set to the average of the Driver and Abundance models. The neutral model (not displayed) is performed with all cell's fitness constitutively equal to 1 regardless of karyotype. **(B)** Framework for the simulation of and selection on cellular

populations with CIN. Cells divide (Pdivision starts at 0.5 in the exponential pseudo-Moran model and is constitutively equal to 1 for the constant Wright-Fisher model) and probabilistically mis-segregate chromosomes (Pmisseg $\in$ [0, 0.001… 0.05]). After, cells experience selection under one of the selection models, altering cellular fitness and the probability (Pdivision) a cell will divide again (green check). Additionally, cells wherein the copy number of any chromosome falls to zero or surpasses 6 are removed (red x). After this, the cycle repeats. See Materials and methods for further details.

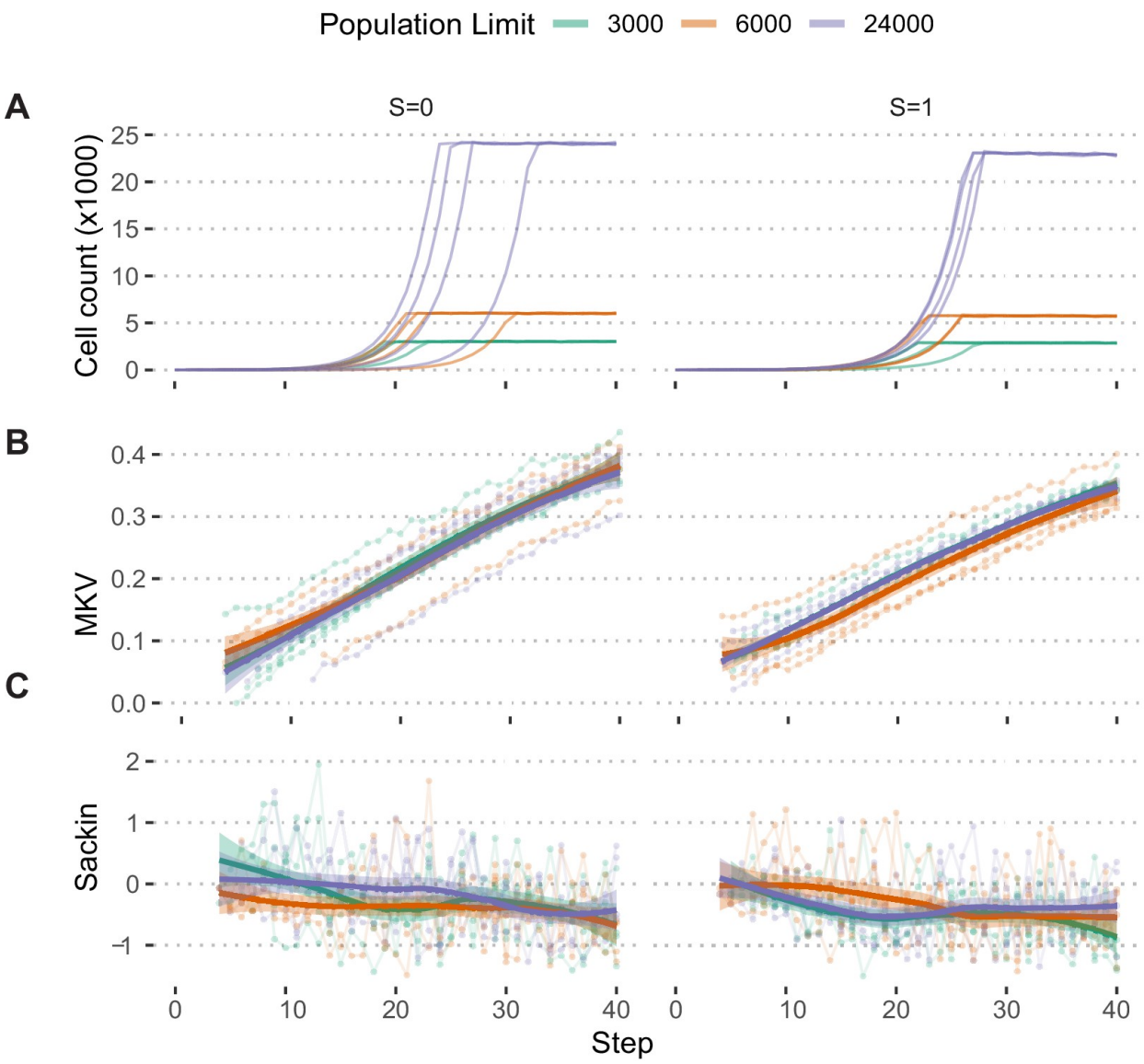

Figure 2.3 — Population growth limits do not bias population measures

(A) Growth curves of populations simulated under the Hybrid selection model and exponential pseudo-Moran growth model with S ∈[0,1] and Pmisseg misseg = 0.022 and limited to 3000, 6000, and 24,000 cells (n = 4 simulations each). **(B)** MKV (normalized to mean ploidy of the population) values steadily increase over time. **(C)** Loess regression curves show no significant deviations based on the population threshold, regardless of selection. Tree-tip-normalized Sackin index values for each population over time. No significant deviations based on the population threshold, regardless of selection.

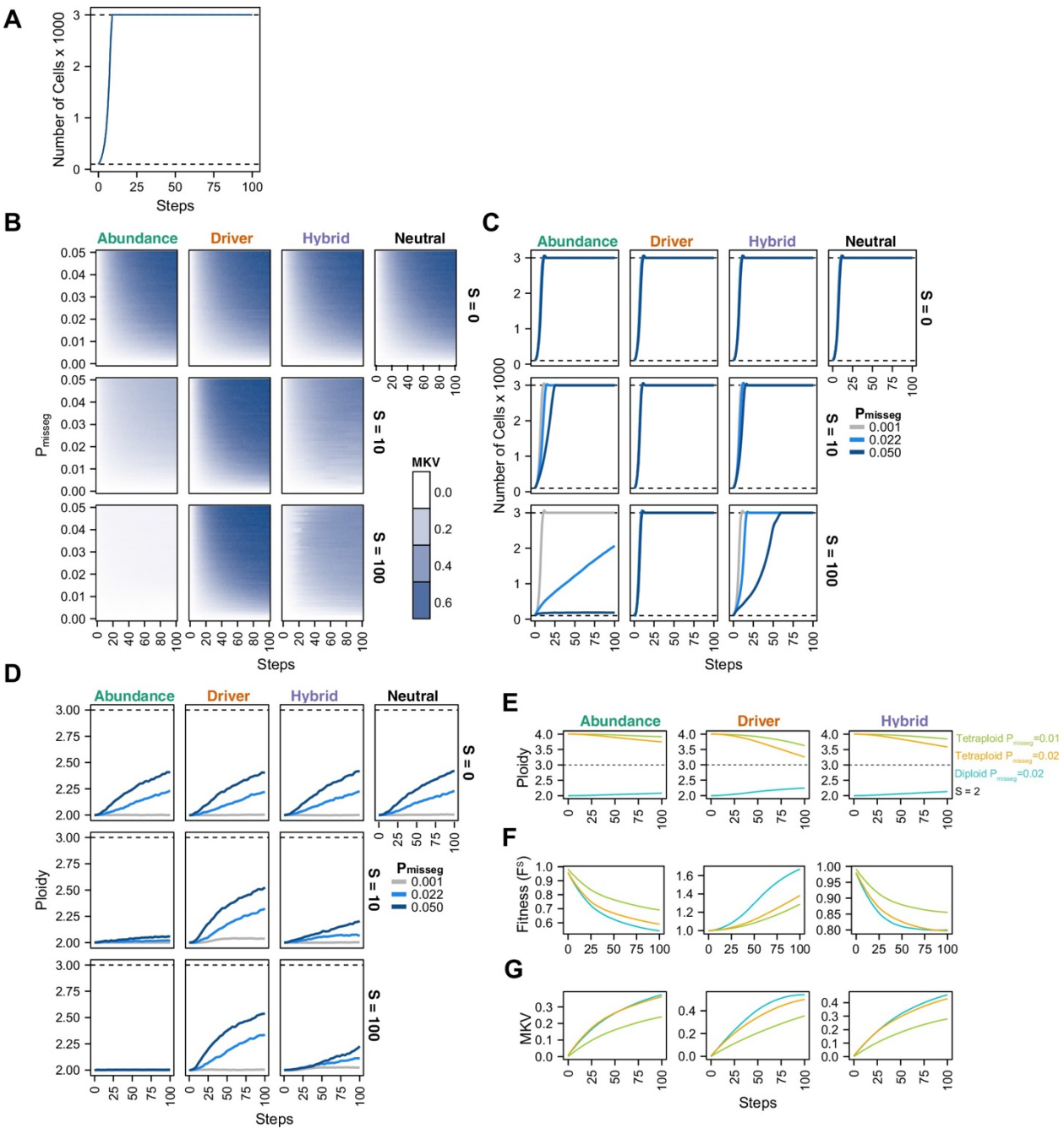

Figure 2.4 — Evolutionary dynamics imparted by CIN

(**A**) Population growth curve in the absence of selective pressure (P_{misseg} = 0.001, S = 0, n = 3 simulations). The steady state population in null selection conditions is 3000 cells. (**B**) Heatmaps depicting dynamics of karyotype diversity as a function of time (steps), mis-segregation rate (P_{misseg}), and selection (S) under each model of selection. Columns represent the same model; rows represent the same selection level. Mean karyotype diversity (MKV) is measured as the variance of each chromosome averaged across all

chromosomes 1–22, and chromosome X. Low and high MKV are shown in white and blue respectively (n = 3 simulations for every combination of parameters). (**C**) Population growth under each model, varying P_{misseg} and S. $P_{misseg} \in$ [0.001, 0.022, 0.050] translate to about 0.046, 1, and 2.3 mis-segregations per division respectively for diploid cells. (**D**) Dynamics of the average ploidy (total # chromosome arms / 46) of a population while varying P_{misseg} and S. (**E**) Dynamics of ploidy under each model for diploid and tetraploid founding populations. $P_{misseg} \in$ [0.01, 0.02] translate to about 0.46 and 0.92 mis-segregations for diploid cells and 0.92 and 1.84 mis-segregations for tetraploid cells. (**F**) Fitness (F^s) over time for diploid and tetraploid founding populations evolved under each model. (**G**) Karyotype diversity dynamics for diploid and tetraploid founding populations. MKV is normalized to the mean ploidy of the population at each time step. Plotted lines in C-G are local regressions of n = 3 simulations.

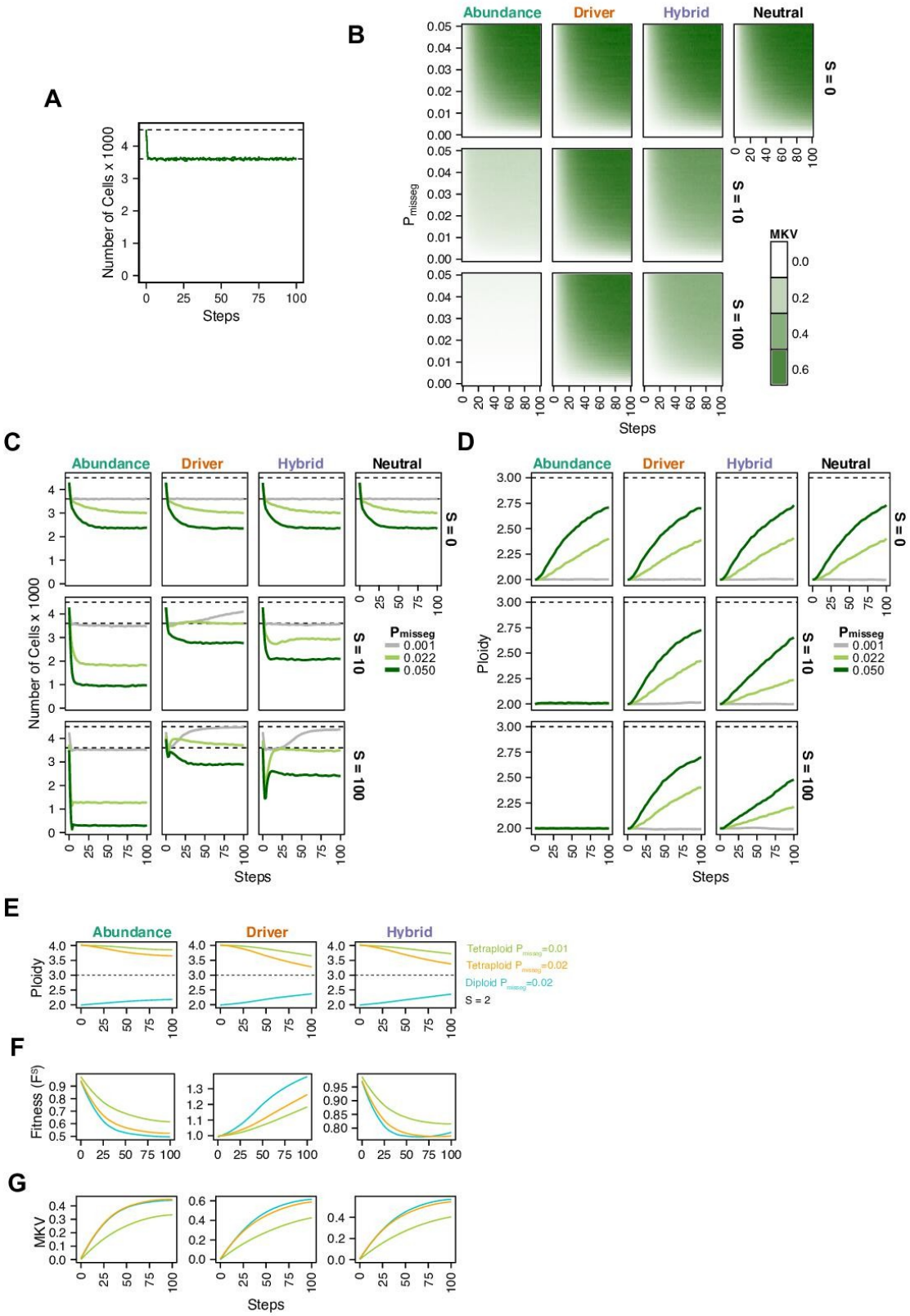

Legend on next page…

Figure 2.5 — Chromosomal instability and karyotype selection in constant-size populations approximating Wright-Fisher dynamics.

(**A**) Population size over time in the absence of selective pressure (P_{misseg} = 0.001, S = 0, n = 3 simulations). The steady state population in null selection conditions is ~3600 cells as data is exported before populations are re-initiated. Dashed line represents the population at (re-)initiation (4500 cells). (**B**) Heatmaps depicting dynamics of karyotype diversity as a function of time (steps), mis-segregation rate (P_{misseg}), and selection (S) under each model of selection. Columns represent the same model; rows represent the same selection level. Mean karyotype diversity (MKV) is measured as the variance of each chromosome averaged across all chromosomes 1–22, and chromosome X. Low and high MKV are shown in white and green respectively (n = 3 simulations for every combination of parameters). (**C**) Population growth under each model, varying P_{misseg} and S. $P_{misseg} \in$ [0.001, 0.022, 0.050] translate to about 0.046, 1, and 2.3 mis-segregations per division respectively for diploid cells. Top dashed line represents the population at (re-)initiation (4500 cells). Bottom dashed line represents the steady state population in selection-null conditions. (**D**) Dynamics of the average ploidy (total # chromosome arms / 46) of a population while varying P_{misseg} and S. (**E**) Dynamics of ploidy under each model for diploid and tetraploid founding populations. $P_{misseg} \in$ [0.01, 0.02] translate to about 0.46 and 0.92 mis-segregations for diploid cells and 0.92 and 1.84 mis-segregations for tetraploid cells. (**F**) Fitness (F^s) over time for diploid and tetraploid founding populations evolved under each model. (**G**) Karyotype diversity dynamics for diploid and tetraploid founding populations. MKV is normalized to the mean ploidy of the population at each time step. Plotted lines in C-G are local regressions of n = 3 simulations.

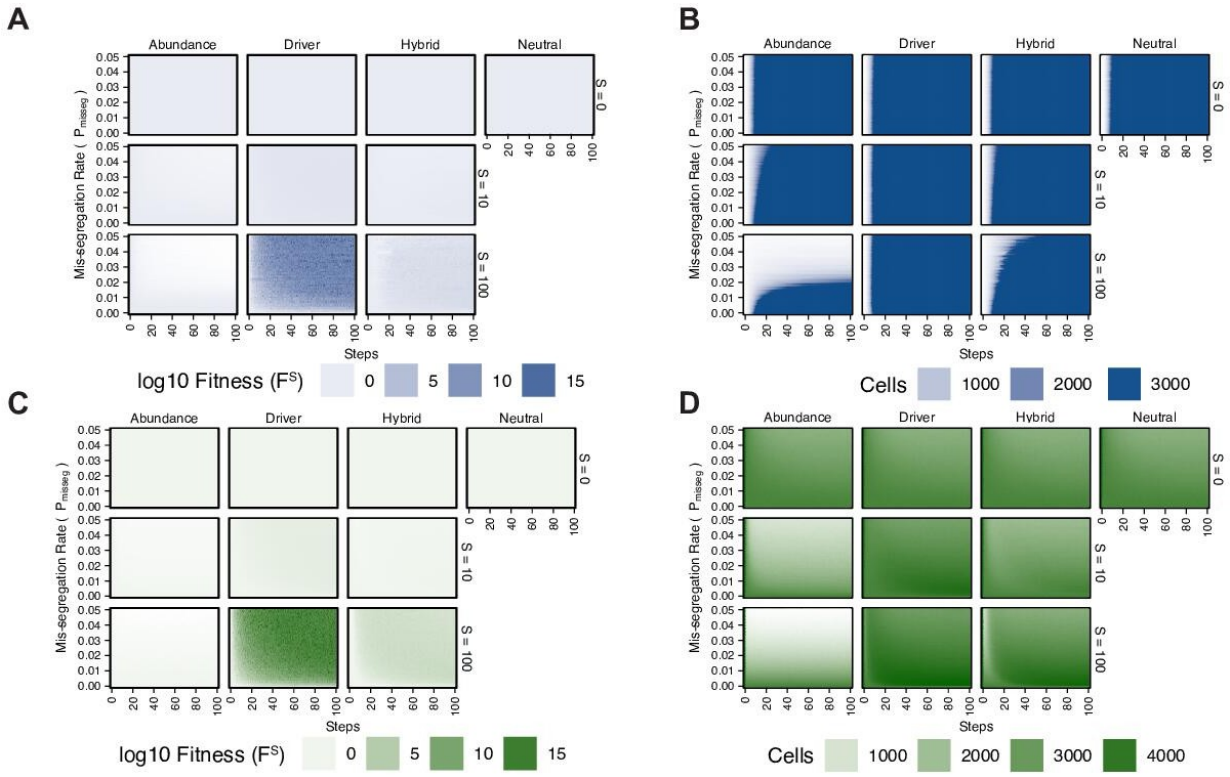

Tetraploid Founders

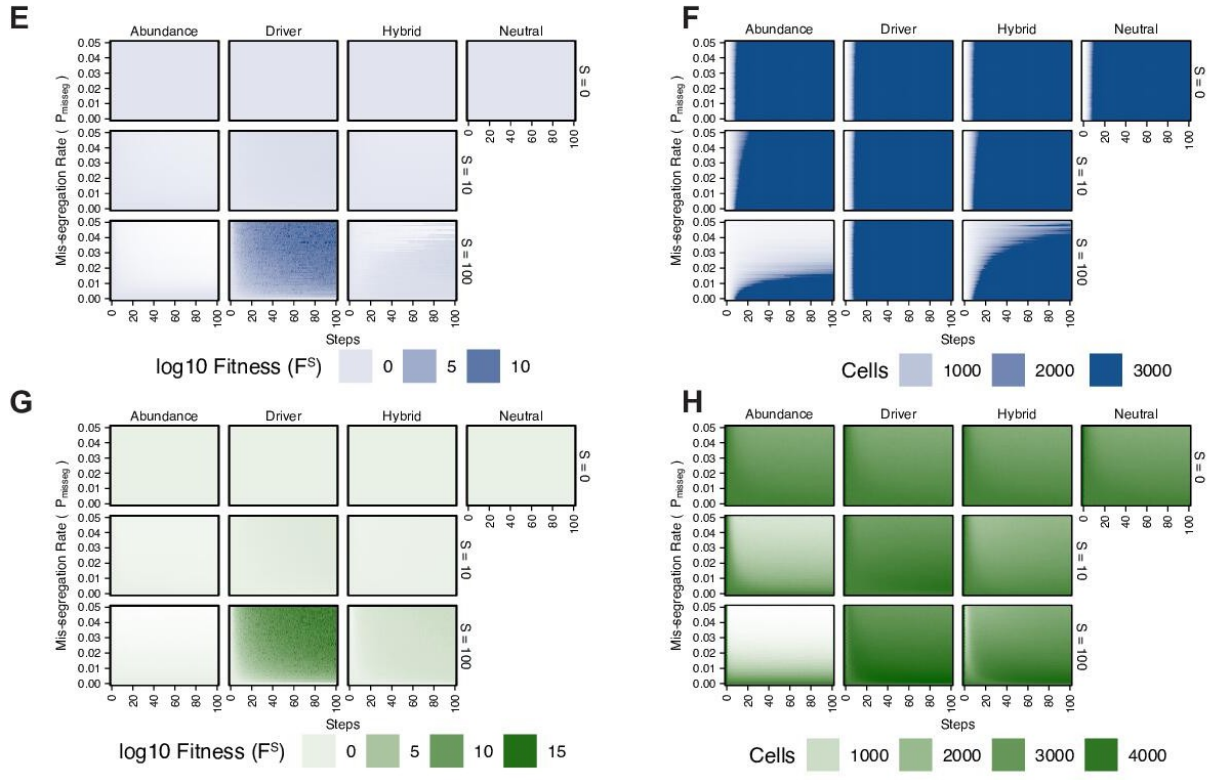

Legend on next page…

Figure 2.6 — Fitness of diploid and tetraploid CIN +populations.

(**A**) Fitness landscape of simulations founded by diploid cells under exponential pseudo-Moran growth dynamics. (**B**) Size of simulated populations founded by diploid cells under exponential pseudo-Moran growth dynamics. (**C**) Fitness landscape of simulations founded by diploid cells under constant Wright-Fisher growth dynamics. (**D**) Size of simulated populations founded by diploid cells under constant Wright-Fisher growth dynamics. (**E**) Fitness landscape of simulations founded by tetraploid cells under exponential pseudo-Moran growth dynamics. (**F**) Size of simulated populations founded by tetraploid cells under exponential pseudo-Moran growth dynamics. (**G**) Fitness landscape of simulations founded by tetraploid cells under constant Wright-Fisher growth dynamics. (**H**) Size of simulated populations founded by tetraploid cells under constant Wright-Fisher growth dynamics.

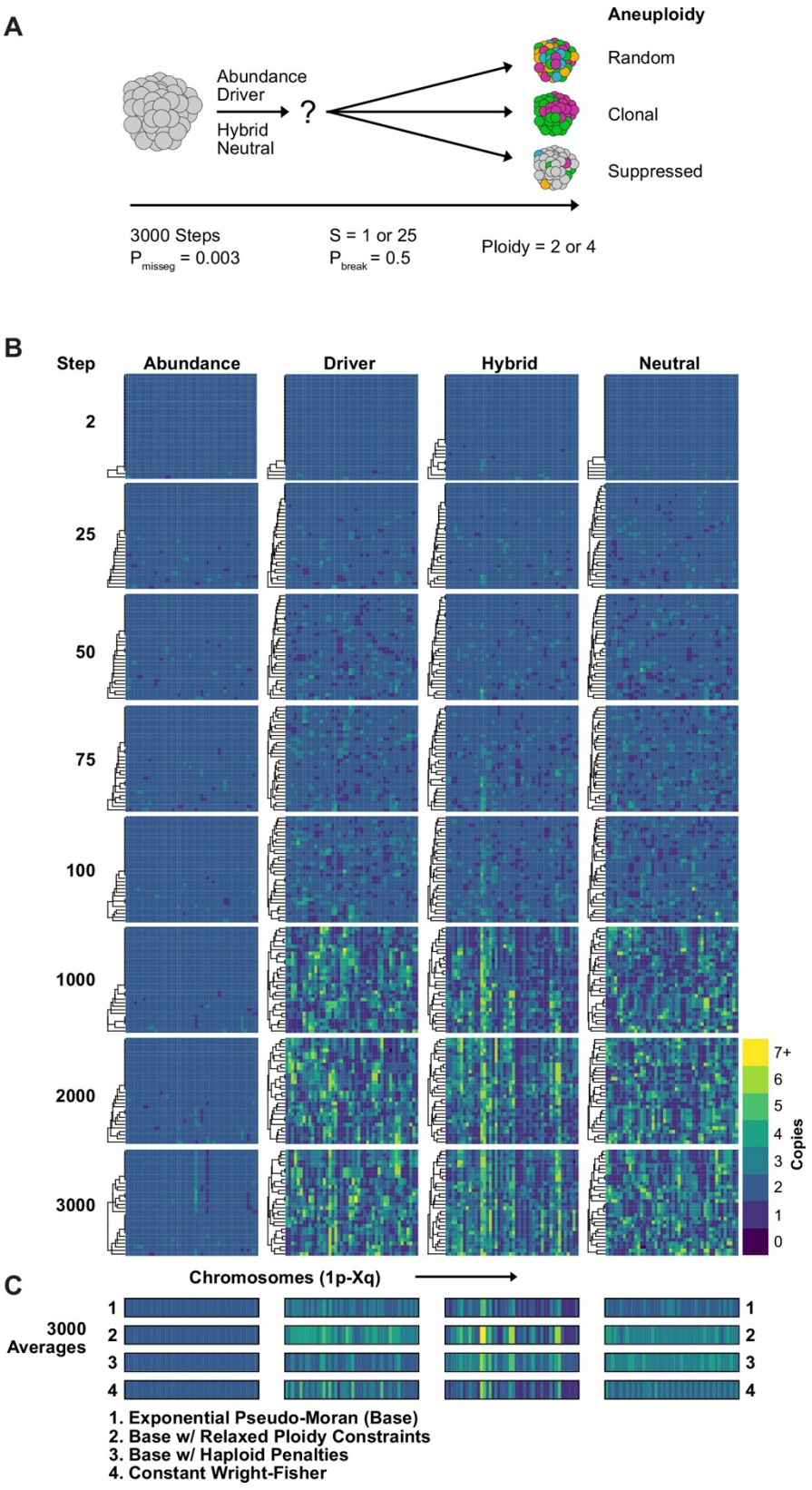

Legend on next page…

Figure 2.7 — Karyotype diversity depends profoundly on selection modality

(**A**) Simulation scheme to assess long-term dynamics of karyotype evolution and karyotype convergence. (**B**) Heatmaps depicting the chromosome copy number profiles of a subset (n = 30 out of 300 sampled cells) of the simulated population with early CIN over time under each model of karyotype selection. (**C**) Average heatmaps (lower) show the average copy number across the 5 replicates for (1) the Exponential Psuedo-Moran (Base), (2) the base model with the upper copy number limit set to 10, (3) the base model that invokes a F_M x 0.1 penalty for any cell with a haploid chromosome, (4) and the Constant Population-Size Wright-Fisher model. P_{misseg} = 0.003; S = 25 (except Neutral model; S = 0); ploidy = 2.

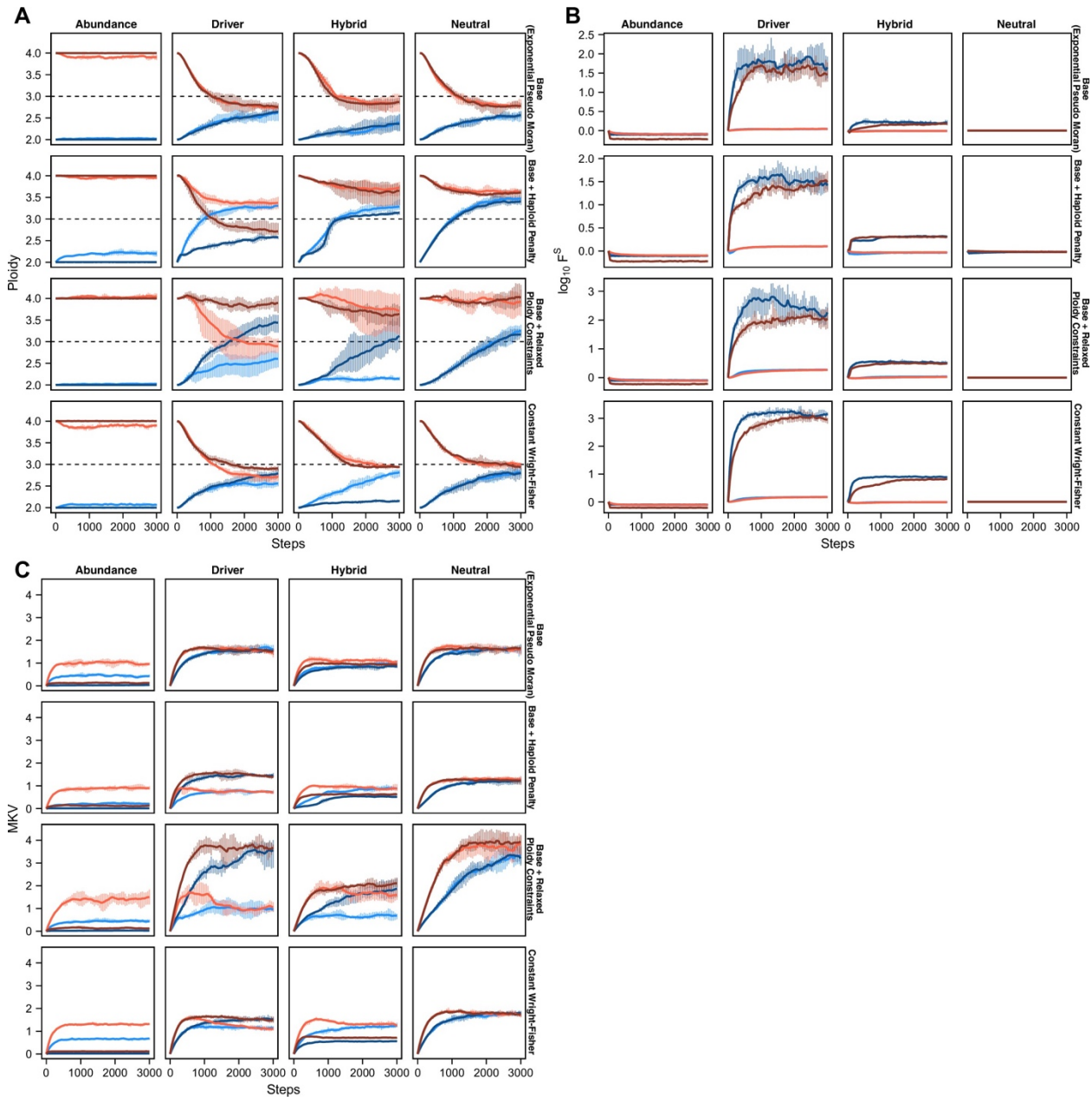

Figure 2.8 — Modeled population measures tracked over time.

(**A**) Average population ploidy over time for each selection model within each model variation. Data represent the mean and range (vertical lines) across five replicates for every 50 time steps in diploid populations with low selective pressure (light red) and high selective pressure (dark red) and tetraploid populations with low selective pressure (light blue) and high selective pressure (dark blue). (**B**) Average population fitness (log10) over time for each selection model within each model variation. Data represent the mean and range (vertical lines) across five replicates for every 50 time steps in diploid populations with low

selective pressure (light red) and high selective pressure (dark red) and tetraploid populations with low selective pressure (light blue) and high selective pressure (dark blue). (**C**) Mean karyotype variance over time for each selection model within each model variation. Data represent the mean and range (vertical lines) across five replicates for every 50 time steps in diploid populations with low selective pressure (light red) and high selective pressure (dark red) and tetraploid populations with low selective pressure (light blue) and high selective pressure (dark blue).

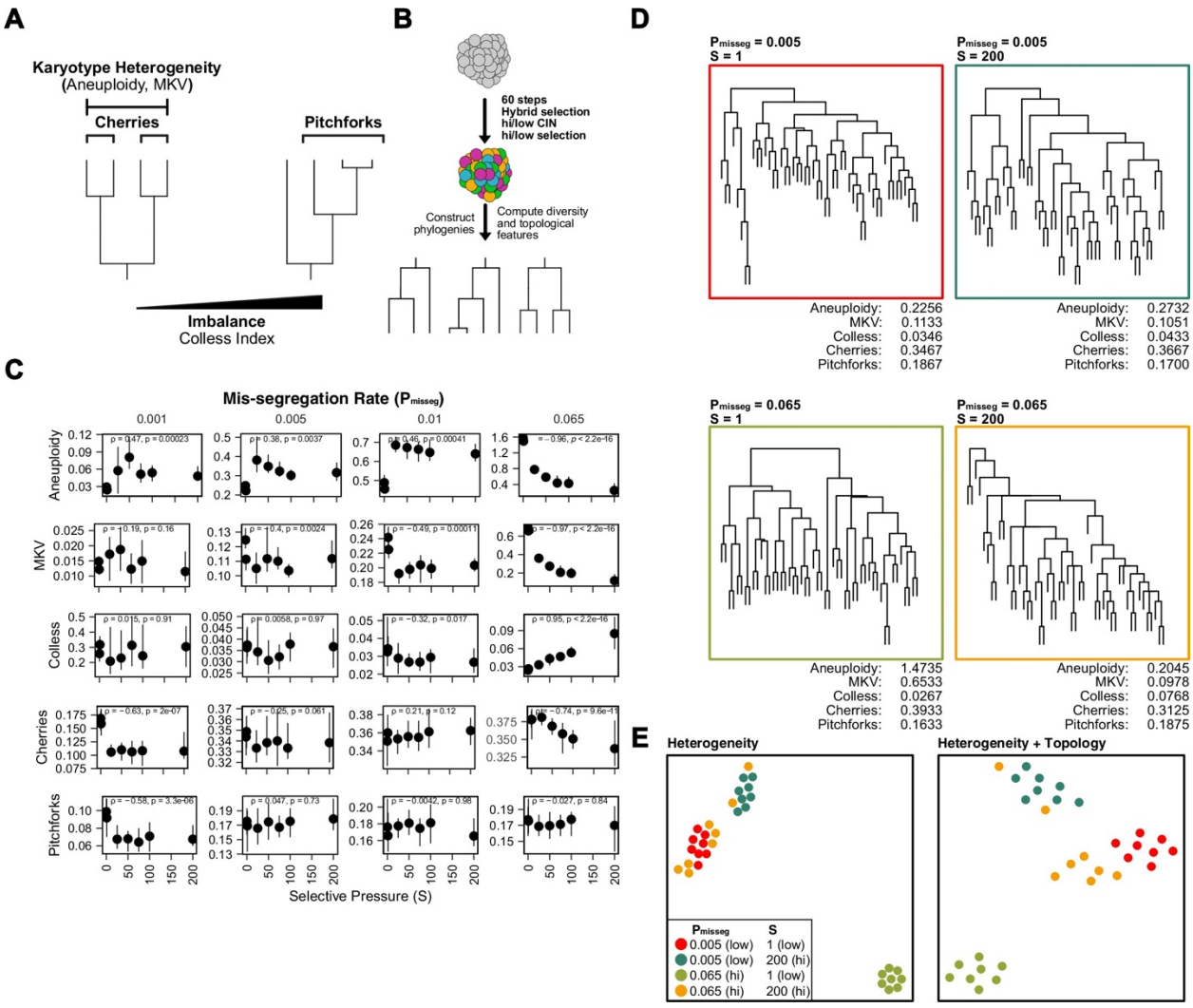

Figure 2.9 — Topological features of simulated phylogenies delineate CIN rate and karyotype selection.

(**A**) Quantifiable features of karyotypically diverse populations. Heterogeneity between and within karyotypes is described by MKV and aneuploidy (inter- and intra-karyotype variance, see Materials and methods). We also quantify discrete topological features of phylogenetic trees, such as cherries (tip pairs) and pitchforks (3-tip groups), and a whole-tree measure of imbalance (or asymmetry), the Colless index. (**B**) Scheme to test how CIN and selection influence the phylogenetic topology of simulated populations. (**C**) Computed heterogeneity (aneuploidy and MKV) and topology (Colless index, cherries, pitchforks) summary statistics under varying P_{misseg} and S values. MKV is normalized to the average ploidy of the population. Topological measures are normalized to population size. Spearman rank correlation coefficients (r) and p-values

are displayed (n = 8 simulations). (**D**) Representative phylogenies for each hi/low CIN, hi/low selection parameter combination and their computed summary statistics. Each phylogeny represents n = 50 out of 300 cells for each simulation. (**E**) Dimensionality reduction of all simulations for each hi/low CIN, hi/low selection parameter combination using measures of karyotype heterogeneity only (left; MKV and aneuploidy) or measures of karyotype heterogeneity and phylogenetic topology (right; MKV, aneuploidy, Colless index, cherries, and pitchforks).

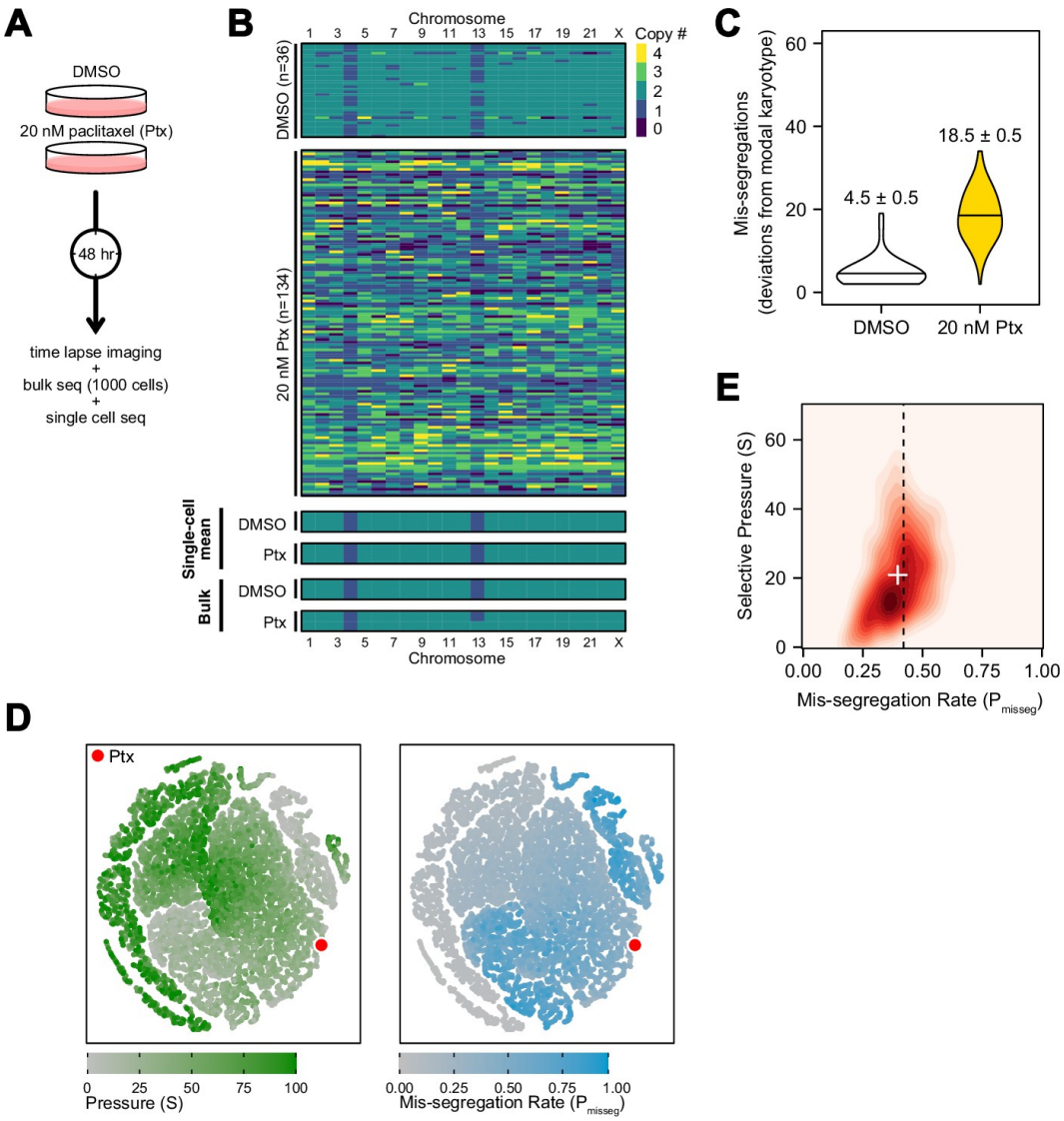

Figure 2.10 — Experimental chromosome mis-segregation measured by Bayesian inference

(**A**) Cal51 cells were treated with either DMSO or 20 nM paclitaxel for 48 hr prior to further analysis by time lapse imaging, bulk DNA sequencing, and scDNAseq. (**B**) Heatmaps showing copy number profiles derived from scDNAseq data, single-cell copy number averages, and bulk DNA sequencing. (**C**) Observed mis-segregations calculated as the absolute sum of deviations from the observed modal karyotype of the control. (**D**) Dimensionality reduction analysis of population summary statistics (aneuploidy, MKV, Colless index, cherries) from the first three time steps of all simulations performed under the Hybrid model. (**E**) 2D density plot showing joint posterior distributions from ABC analysis using population summary statistics computed from the paclitaxel-treated cells using the following priors and parameters: Growth Model =

‘exponential pseudo-Moran’, Selection Model = ‘Hybrid, initial ploidy = 2, 2 time steps, S ∈[0, 2… 100], P_{misseg}∈[0, 0.005… 1.00] and a tolerance threshold of 0.05 to reject dissimilar simulation results. (see Materials and Methods). Vertical dashed line represents the experimentally observed mis-segregation rate. White + represents the mean of inferred values.

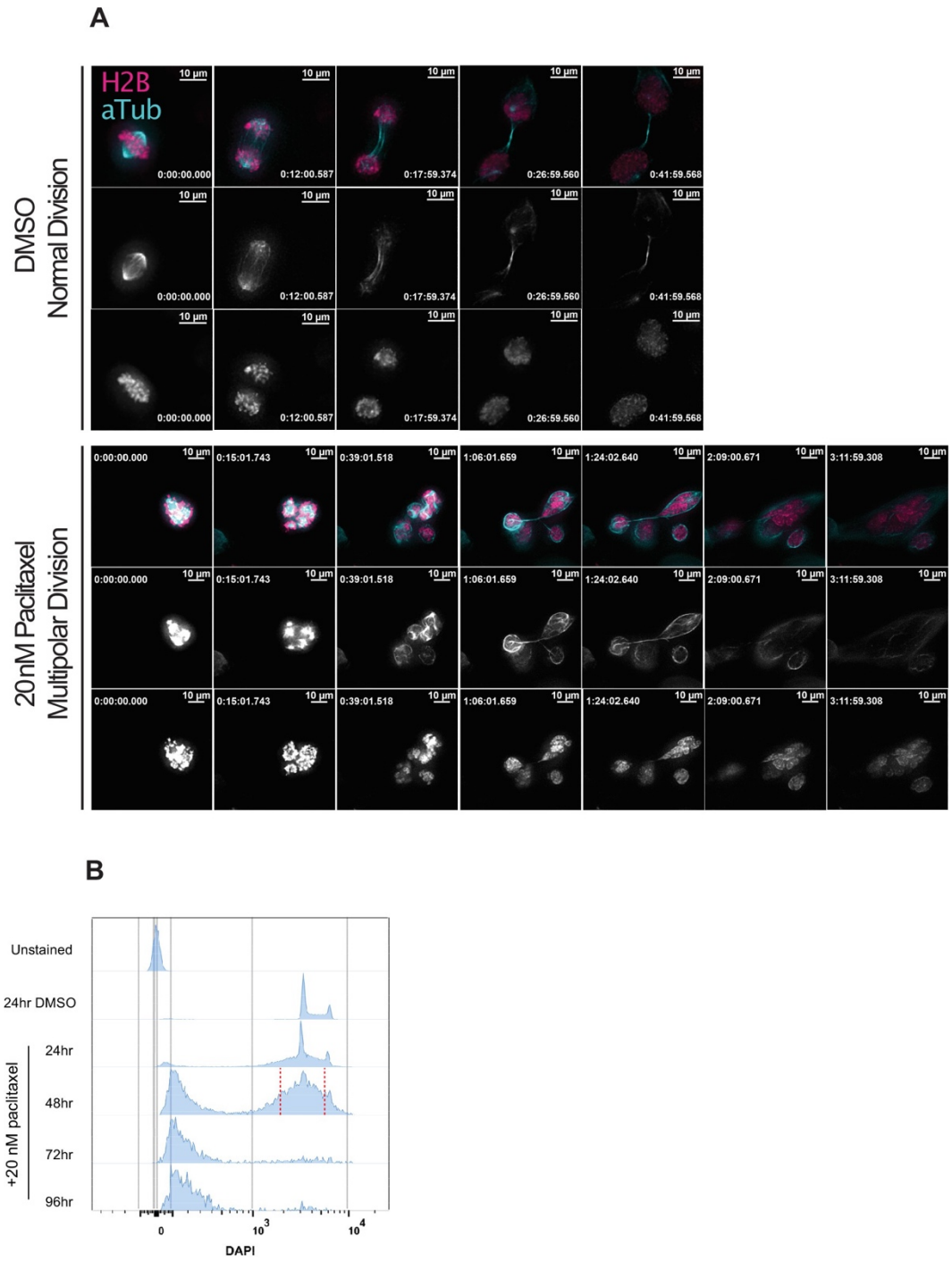

Figure 2.11 — Induction of extensive chromosome mis-segregation via paclitaxel.

(**A**) Immunofluorescence time lapse montage of control Cal51 cells undergoing normal mitosis (top) and paclitaxel-treated treated cells undergoing a multipolar anaphase (middle) and partial cytokinesis failure (bottom). (**B**) Cell cycle profiles from flow cytometric analysis of Cal51 cells treated with either DMSO (72

hr) or 20 nM paclitaxel for 24, 48, or 72 hr. For FACS, cells treated for 48 hr were sorted into individual wells of 96-well plates. Sorting gate is shown by the red, dashed line.

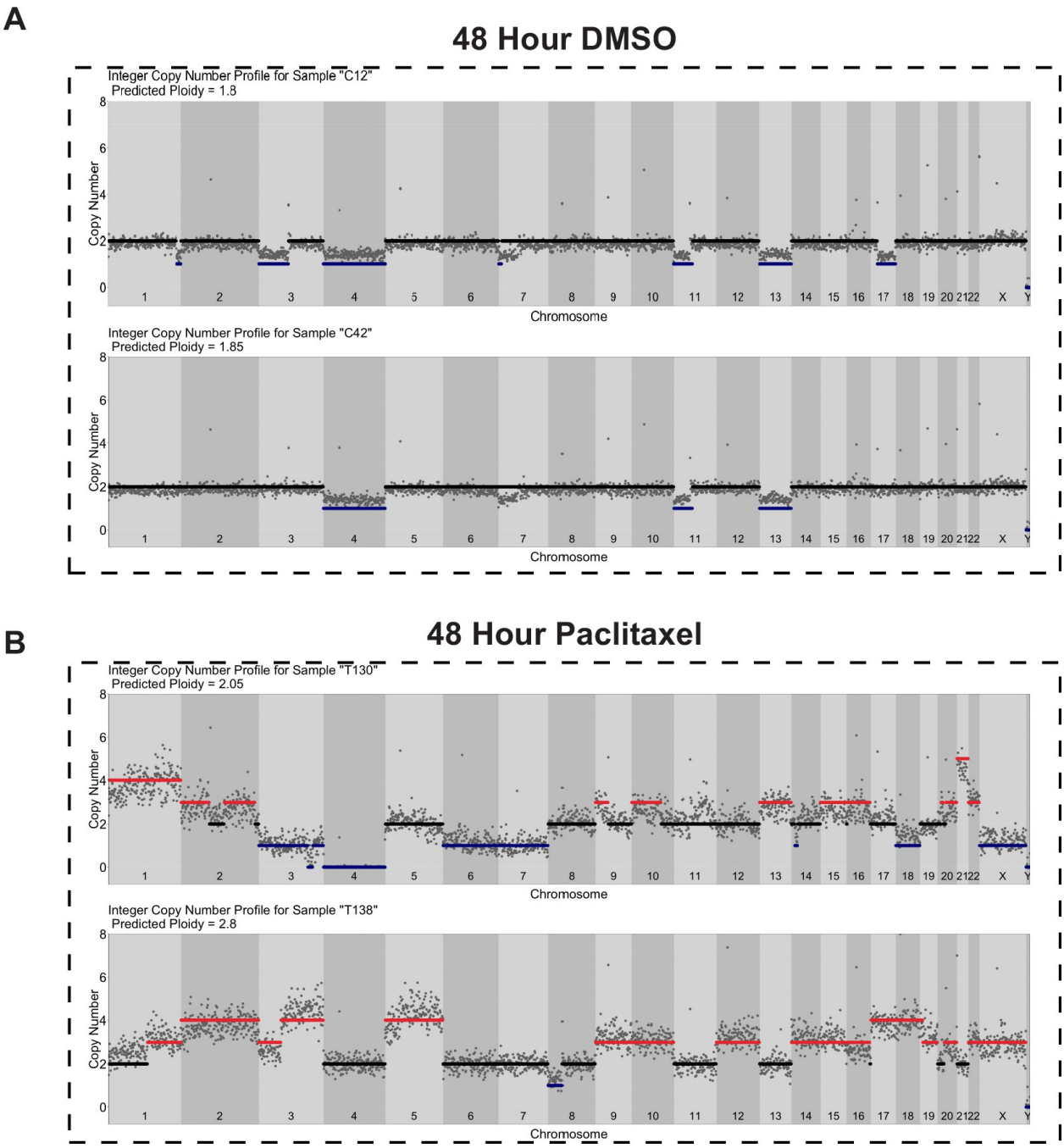

Figure 2.12 — Copy number profiles of DMSO- and paclitaxel-treated Cal51 cells.

Single-cell copy number profiles for single (**A**) DMSO- and (**B**) paclitaxel-treated cells. A total of 500 Kb genomic bins and DNA content from FACS were used for copy number calculations (see Materials and methods).

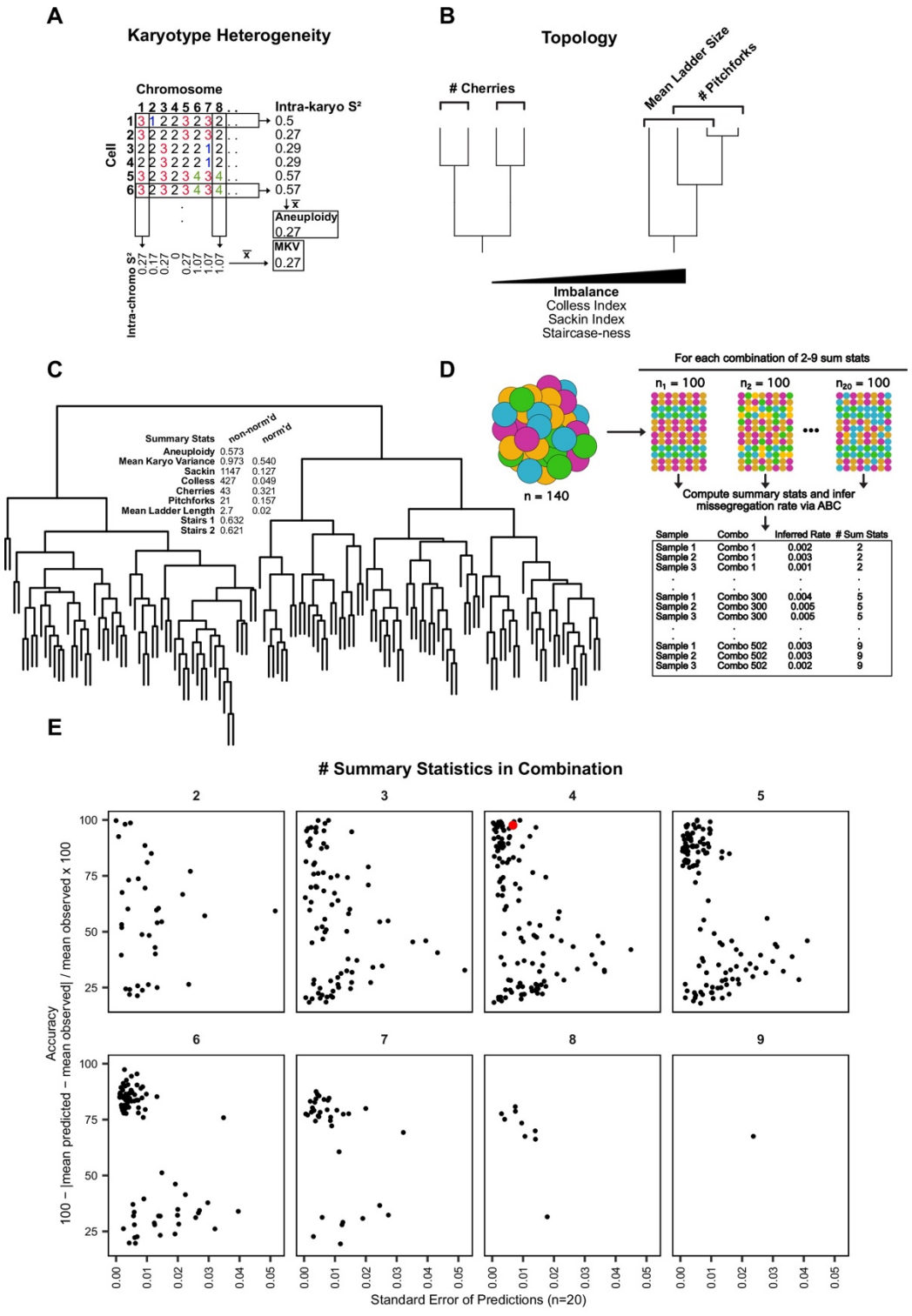

Figure 2.13 — Summary statistic optimization for ABC.

(**A**) Schematic showing calculation of aneuploidy and MKV. (**B**) Examples of phylogenetic topology metrics. (**C**) Phylogenetic reconstruction of a population of Cal51 cells treated with 20 nM paclitaxel for 48

hr and associated heterogeneity and topology metrics. Normalized and non-normalized summary statistics are displayed (see Materials and methods). (**D**) Analytical scheme to identify most accurate and least variable combinations of heterogeneity and topology metrics. For each combination of 2–9 metrics, we iteratively re-sampled and remeasured the rate of mis-segregation in 100 random cells, three times, from our original dataset of paclitaxel-treated Cal51 cells. The red data point denotes our chosen combination for future analyses—average aneuploidy, MKV, Colless Index, and Cherries. This combination both limits redundant measures (i.e. Colless and Sackin indices) and contains both heterogeneity and topology metrics. (**E**) Percent accuracy and standard error of the mean for three sampled measurements of 100 paclitaxel-treated cells from the original population, repeated for each combination of heterogeneity and topology measures.

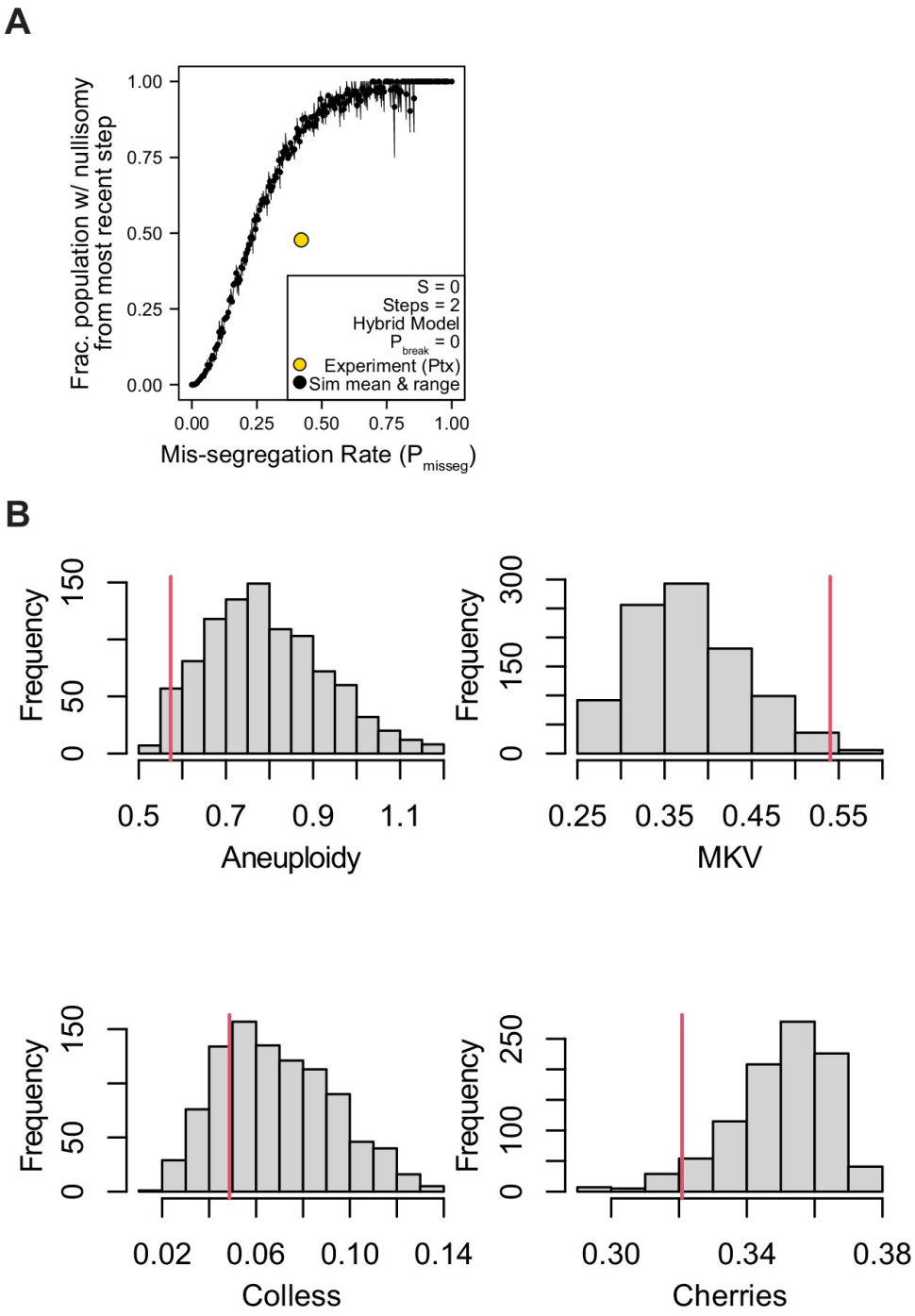

Figure 2.14 — Nullisomy and posterior predictive checks of summary statistics from paclitaxel-treated Cal51 cells.

(**A**) Observed incidence of nullisomy in paclitaxel-treated cells plotted against the observed mis-segregation rate ($P_{misseg,true}$ = 18.5/44 = 0.42) overlaid on simulated data from the second time step (2 generations) under the Hybrid model with S = 0 and P_{break} = 0 (n = 3 simulations). (**B**) Posterior distributions of summary

statistics from accepted simulations most similar to the paclitaxel-treated Cal51 cells (threshold = 0.05). The red line indicates the observed statistic in paclitaxel-treated cells. Colless index and cherry count is normalized to population size. MKV is normalized to the average ploidy of the population.

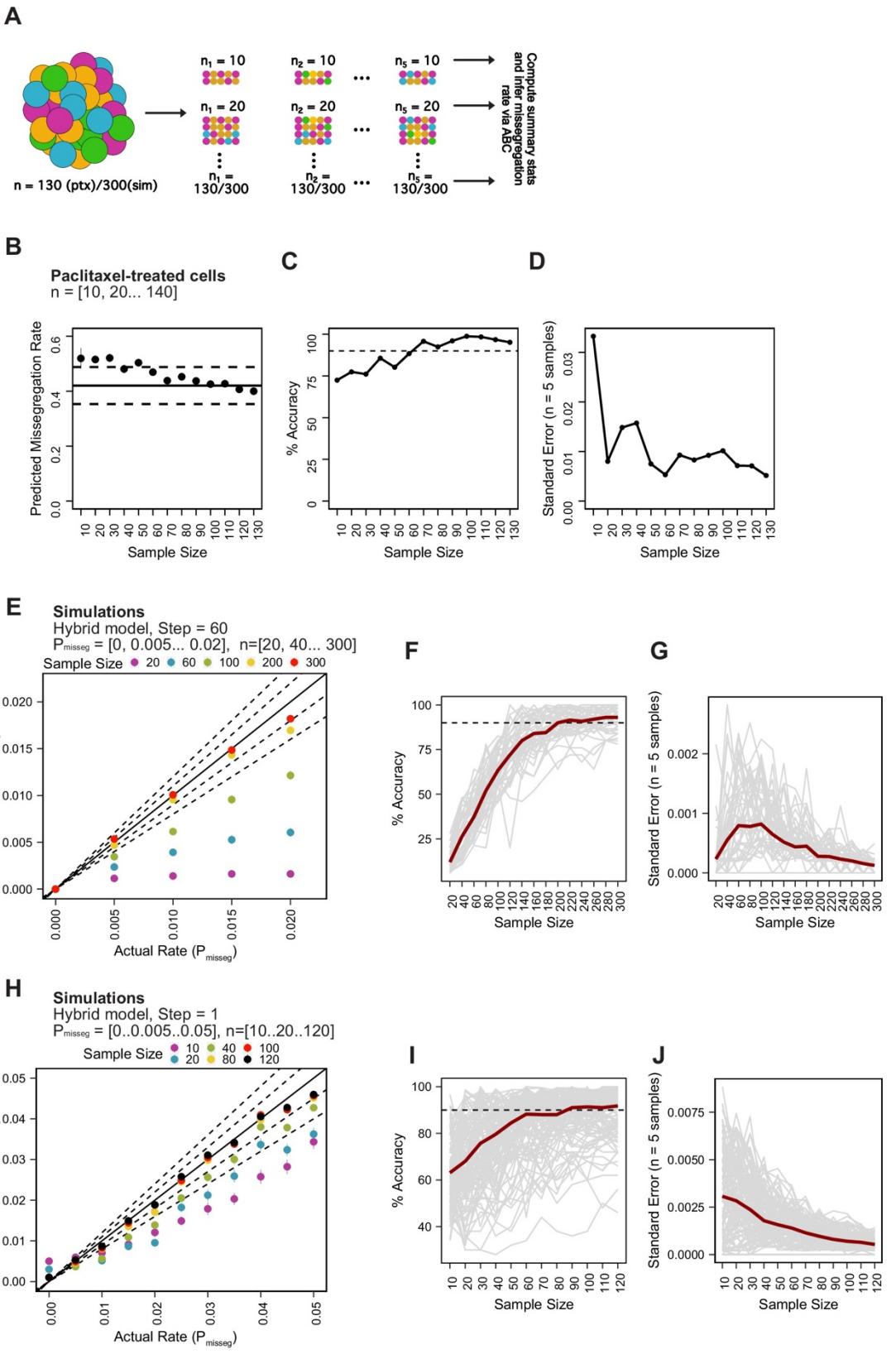

Legend on next page…

Figure 2.15 — Minimum sampling of karyotype heterogeneity.

(**A**) Analytical scheme to optimize the number of cells to sample for measuring mis-segregation rates from karyotype heterogeneity. We iteratively re-sampled and remeasured the rate of mis-segregation for a range of sample sizes (n = 5 random samples). (**B**) Predicted mis-segregation rates over a range of sample sizes (n = 5 samples). Points and error bars are the mean ± standard error. Black solid line denotes the mean observed rate of mis-segregation induced by 20 nM paclitaxel. Black dashed lines are half the standard deviation of observed mis-segregation rates per cell. (**C**) Mean percent accuracy of ABC-inferred rates of mis-segregation due to paclitaxel taken from each set of five random samples using the observed rate of mis-segregation as the 'true value'. Calculated as $\mathrm{mean}\ \%\ \mathrm{accuracy} = 100 - (\mathrm{true} - \mathrm{meaninferredtrue} \times 100)$. Dashed lines represent 90% accuracy. (**D**) Standard error of ABC-inferred rates of mis-segregation for each set of random samples from paclitaxel-treated cells. (**E**) ABC-inferred mis-segregation rates by sample size from simulations with known parameters (n = 5 samples). Points represent mean ± standard error across 5 samples for each of 11 selective pressure (S) values. Solid line represents a perfect correlation. Inner dashed line represent ±10% margin. Outer dashed line represents ±20% margin. Simulation parameters: $P_{misseg} \in$ [0, 0.005… 0.02], time steps = 60, Selection Model = 'Hybrid', Growth Model = 'exponential pseudo-Moran', S = [0, 10... 100], and a tolerance threshold of 0.05. (**F**) Mean percent accuracy of ABC-inferred rates of mis-segregation in simulations (parameters in **E**) taken at various sample sizes. Gray lines represent the mean percent accuracy of five random samples for each sample size for the same simulated population (n = 55 simulations). The dashed line represents 90% accuracy. Calculated as described above but taking the known simulation parameter as the 'true' value. (**G**) Standard error of ABC-inferred rates of mis-segregation in simulations (parameters in **E**) taken at various sample sizes. Gray lines represent the standard error of five random samples for each sample size for the same simulated population (n = 55 simulations). (**H**) ABC-inferred mis-segregation rates by sample size from simulations with known parameters (n = 5 samples). Points represent mean ± standard error across 5 samples for each of 11 selective pressure (S) values. Solid line represents a perfect correlation. Inner dashed line represent ±10% margin. Outer dashed line represents ±20% margin. ABC was performed with the following parameters and

priors: $P_{misseg} \in [0, 0.005 \ldots 0.05]$, time steps = 1, Selection Model = 'Hybrid', Growth Model = 'exponential pseudo-Moran', $S \in [0, 10 \ldots 100]$, and a tolerance threshold of 0.05. (**I**) Mean percent accuracy of ABC-inferred rates of mis-segregation in simulations (parameters in **H**) taken at various sample sizes. Gray lines represent the mean percent accuracy of five random samples for each sample size for the same simulated population (n = 121 simulations). The dashed line represents 90% accuracy. (**J**) Standard error of ABC-inferred rates of mis-segregation in simulations (parameters in **H**) taken at various sample sizes. Gray lines represent the standard error of five random samples for each sample size for the same simulated population (n = 121 simulations). Note: Red lines in **F**, **G**, **I**, and **J** represent the median.

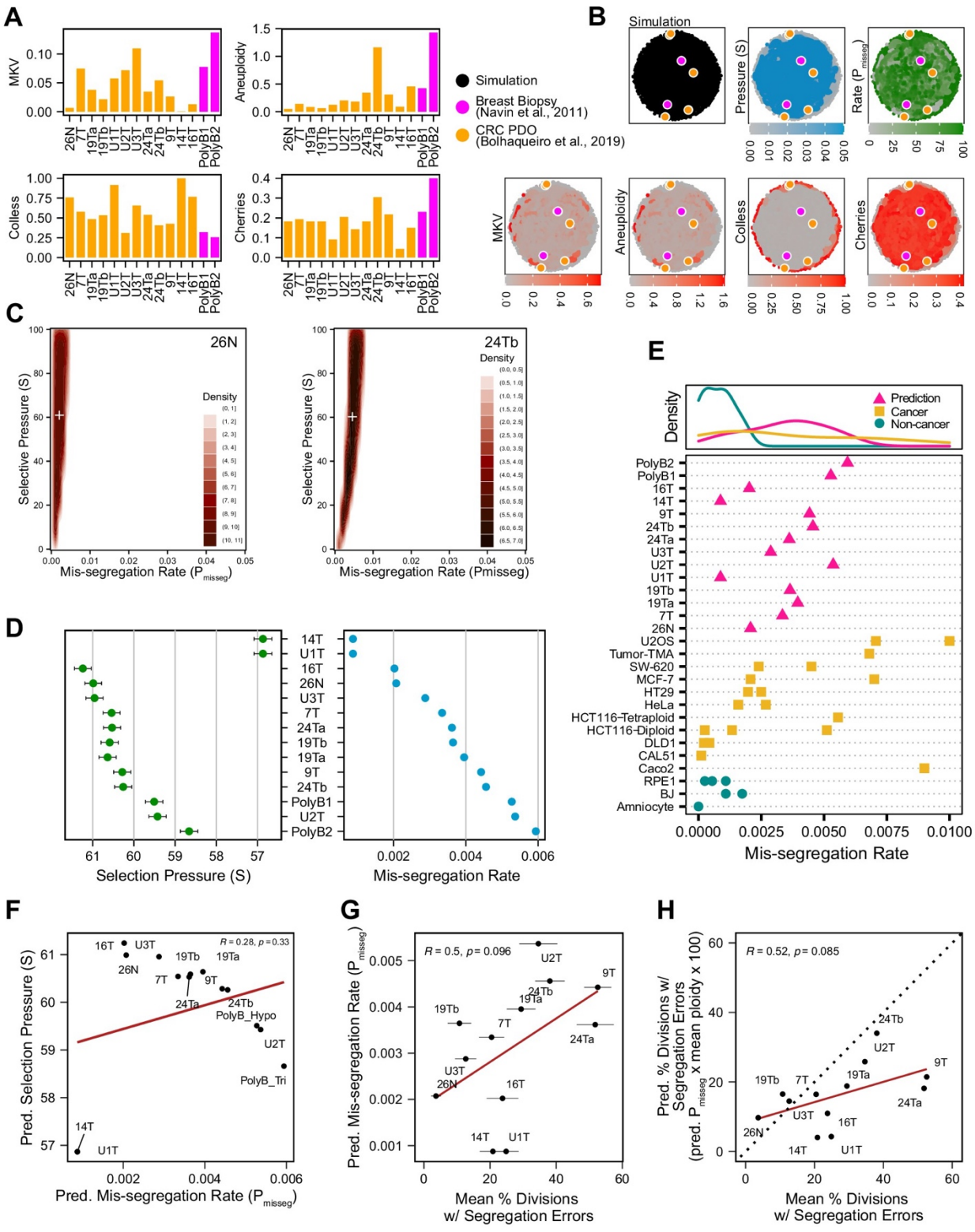

Figure 2.16 — Inferring chromosome mis-segregation rates in tumors and organoids from Bolhaqueiro et al. 2019 and Navin et al., 2011.

(**A**) Computed population summary statistics for colorectal cancer (CRC) patient-derived organoids (PDOs) and breast biopsy scDNAseq datasets from Bolhaqueiro et al., 2019 (gold) and Navin et al., 2011 (pink). (**B**) Dimensionality reduction analysis of population summary statistics showing biological observations overlaid on, and found within, the space of simulated observations. Point colors show the simulation parameters and summary statistics for all simulations using the following priors and parameters: Growth Model = 'exponential pseudo-Moran', Selection Model = 'Abundance', initial ploidy = 2, time steps $\in$[40, 41… 80], S $\in$[0,2… 100], $P_{misseg}\in$[0,0.001… 0.050] and a tolerance threshold of 0.05 to reject dissimilar simulation results. (see Materials and Methods). (**C**) 2D density plots showing joint posterior distributions of P_{misseg} and S values from the approximate Bayesian computation analysis of samples 26 N (left) and 24Tb (right) from Bolhaqueiro et al., 2019. White + represents the mean of inferred values. (**D**) Inferred selective pressures and mis-segregation rates from each scDNAseq dataset (mean and SEM of accepted values). (**E**) Predicted mis-segregation rates in CRC PDOs and a breast biopsy plotted with approximated mis-segregation rates observed in cancer (blue triangle) and non-cancer (red circle) models (primarily cell lines) from previous studies (Table 5; see Materials and methods). The predicted mis-segregation rates in these cancer-derived samples fall within those observed in cancer cell lines and above those of non-cancer cell lines. (**F**) Pearson correlation of predicted mis-segregation rates and predicted selective pressures in CRC PDOs from Bolhaqueiro et al., 2019. (**G**) Pearson correlation of predicted mis-segregation rates and the incidence of observed segregation errors in CRC PDOs from Bolhaqueiro et al., 2019. Error bars represent SEM values. (**H**) Pearson correlation of observed incidence of segregation errors in CRC PDOs from Bolhaqueiro et al., 2019 to the ploidy-corrected prediction of the observed incidence of segregation errors. These values assume the involvement of 1 chromosome per observed error and are calculated as the (predicted mis-segregation rate) x (mean number of chromosomes observed per cell) x 100. Dotted line = 1:1 reference.

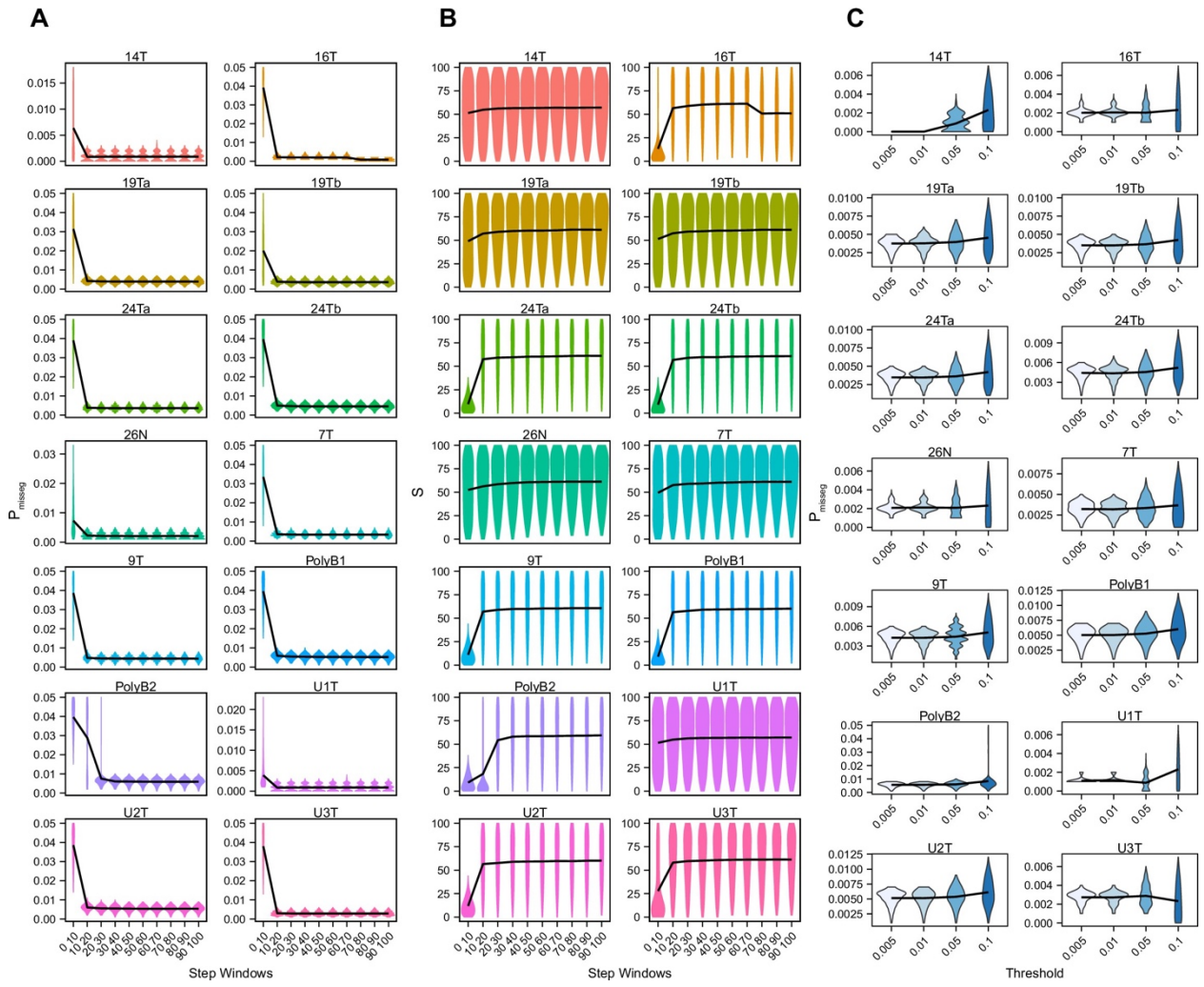

Figure 2.17 — ABC-inference threshold and step-window analysis.

Posterior distributions of mis-segregation rates (**A**) and selective pressure, S (**B**) inferred using ABC analysis of CRC organoids and a breast biopsy from Bolhaqueiro et al., 2019 and Navin et al., 2011 respectively using a sliding window prior distribution of time steps. ABC was performed for every interval of 10 steps between 0 and 100 using a tolerance threshold of 0.05. Schematic of analysis shown below. ABC was performed with the following parameters and priors: $P_{misseg} \in$ [0...0.001...0.05], S ∈ [0...2...100], indicated time step window, Selection Model = 'Abundance', Growth Model = 'exponential pseudo-Moran', and a tolerance threshold of 0.05. (**C**) Posterior distributions of mis-segregation rates inferred using ABC analysis on the same samples as in A using tolerance thresholds of 0.005, 0.01, 0.05, 0.1. ABC was performed with the following parameters and priors: $P_{misseg} \in$ [0, 0.001… 0.05], S ∈ [0, 2… 100], time steps ∈ [40, 41… 80],

Selection Model = ‘Abundance’, Growth Model = ‘exponential pseudo-Moran’, and the indicated tolerance threshold.

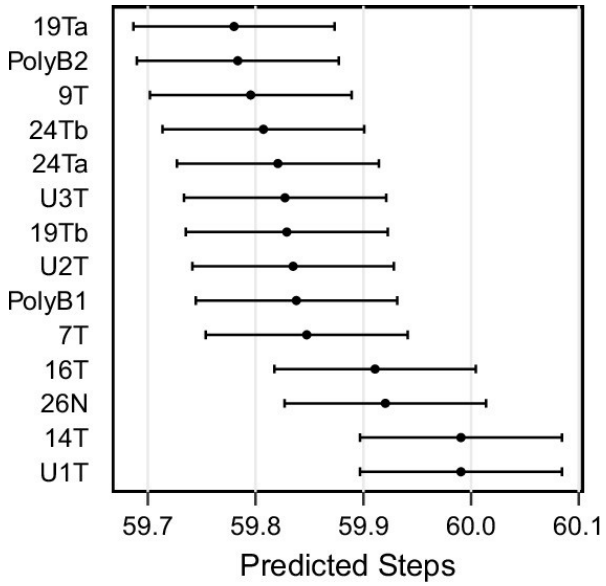

Figure 2.18 — ABC-inferred step count in patient-derived samples.

Mean and standard error for steps in each patient-derived sample (accompanying data in Figure 6), inferred via approximate Bayesian computation.

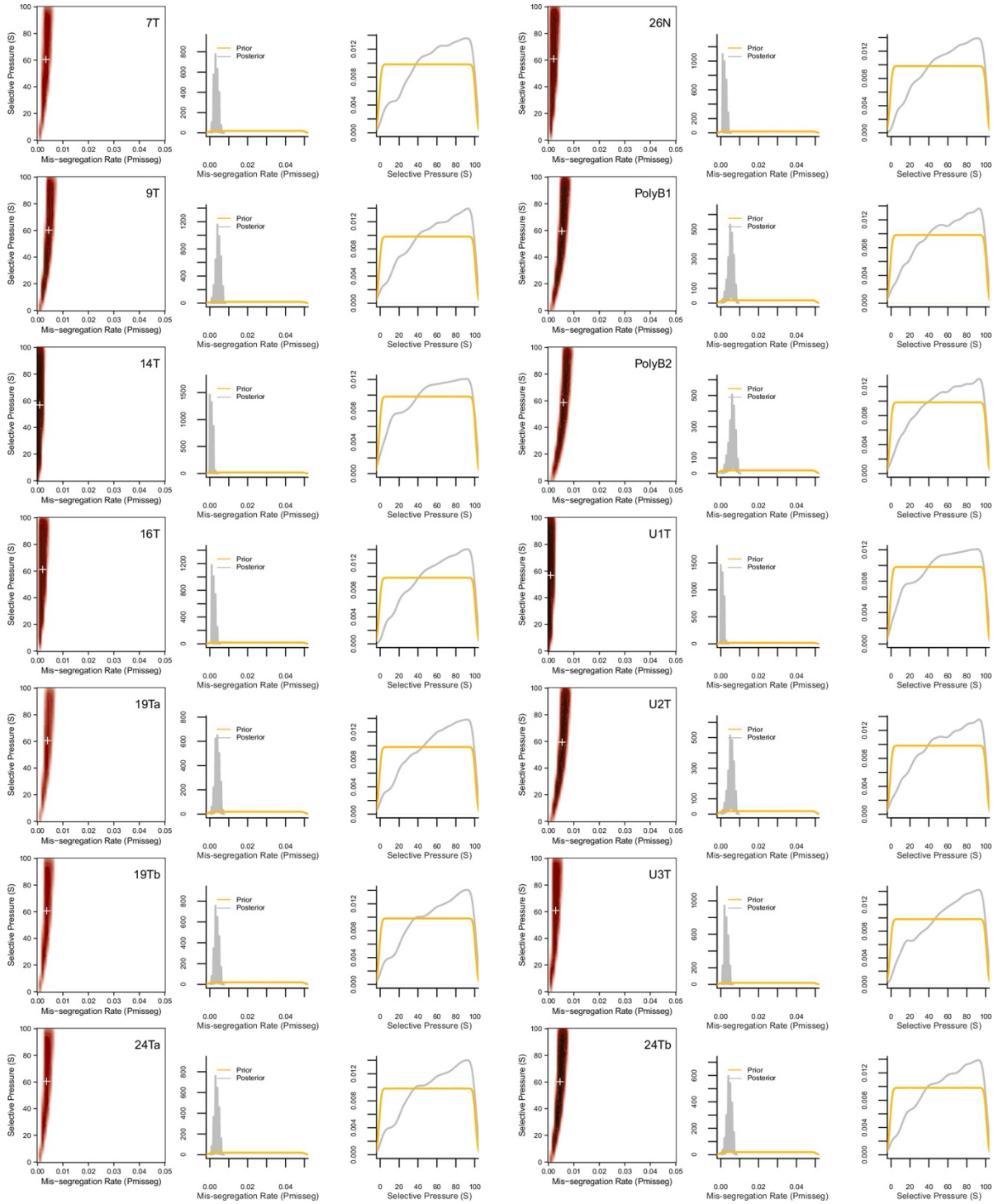

Figure 2.19 — ABC-inferred mis-segregation rates and selective pressures in patient-derived samples.

Joint (2D density plots) and individual (1D density plots) distributions of mis-segregation rates and selective pressures in patient-derived CRC organoids and a breast biopsy from Bolhaqueiro et al.,

2019 and Navin et al., 2011respectively (accompanying data in Figure 6). The prior (yellow) distribution represents the parameters used for simulation while the posterior (gray) distribution represents the parameters from simulations whose observed measurements were similar to the measurements taken from the patient-derived sample using a tolerance threshold of 0.05. White + signs on joint distributions represent the mean of both parameters.

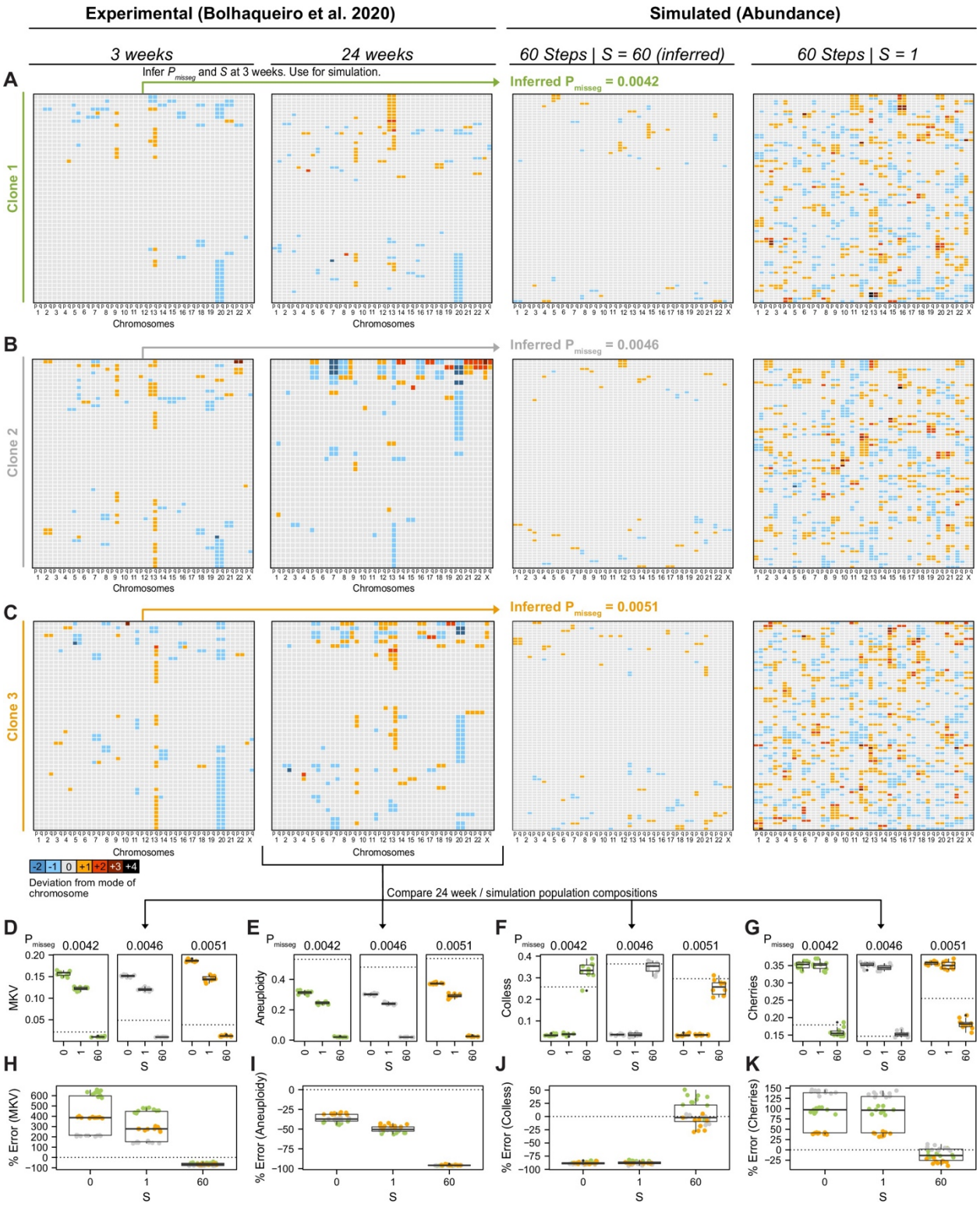

Legend on next page…

Figure 2.20 — Validation of selection in longitudinally sequenced CRC organoids.

(**A–C**) Copy number heatmaps showing the deviation from the mode of each chromosome derived from longitudinally sequenced clonal organoids from Bolhaqueiro et al., 2019. ABC was performed on scDNAseq data from three clones at 3 weeks of growth. The resulting inferred mis-segregation rate (P_{misseg}) and selective pressure (S) were used to simulate CIN and selection in these clones over 60 time steps, at which point the composition of the populations were compared to the scDNAseq data from each of the clones at 24 weeks of growth (**D–K**). Additional simulations using S = 0 (not shown) and S = 1 were also performed. Inferred P_{misseg} values for (**A**) clone 1, (**B**) clone 2, and (**C**) clone 3 were 0.0042, 0.0046, and 0.0051 respectively. S = 60 was inferred for each clone. ABC was performed on the 3 week data with the following parameters and priors: $P_{misseg} \in$ [0, 0.001... 0.05], S ∈ [0, 2… 100], time steps ∈ [40, 41... 80], Selection Model = 'Abundance', Growth Model = 'exponential pseudo-Moran', and a tolerance threshold of 0.05. (**D**) MKV values from n = 10 simulations per clone. Dotted line represents the MKV value observed in the scDNAseq data. (**E**) Aneuploidy values from n = 10 simulations per clone per S value. Dotted line represents the Aneuploidy value observed in the scDNAseq data. (**F**) Colless index values from n = 10 simulations per clone S value. Dotted line represents the Colless index value observed in the scDNAseq data. (**G**) Normalized cherry values from n = 10 simulations per clone S value. Dotted line represents the normalized cherry value observed in the scDNAseq data. (**H**) Percent error for MKV observations in n = 10 simulations per clone per S value. Dotted line represents 0% error. (**I**) Percent error for aneuploidy observations in n = 10 simulations per clone per S value. Dotted line represents 0% error. (**J**) Percent error for Colless observations in n = 10 simulations per clone per S value. Dotted line represents 0% error. (**K**) Percent error for normalized cherry observations in n = 10 simulations per clone per S value. Dotted line represents 0% error.

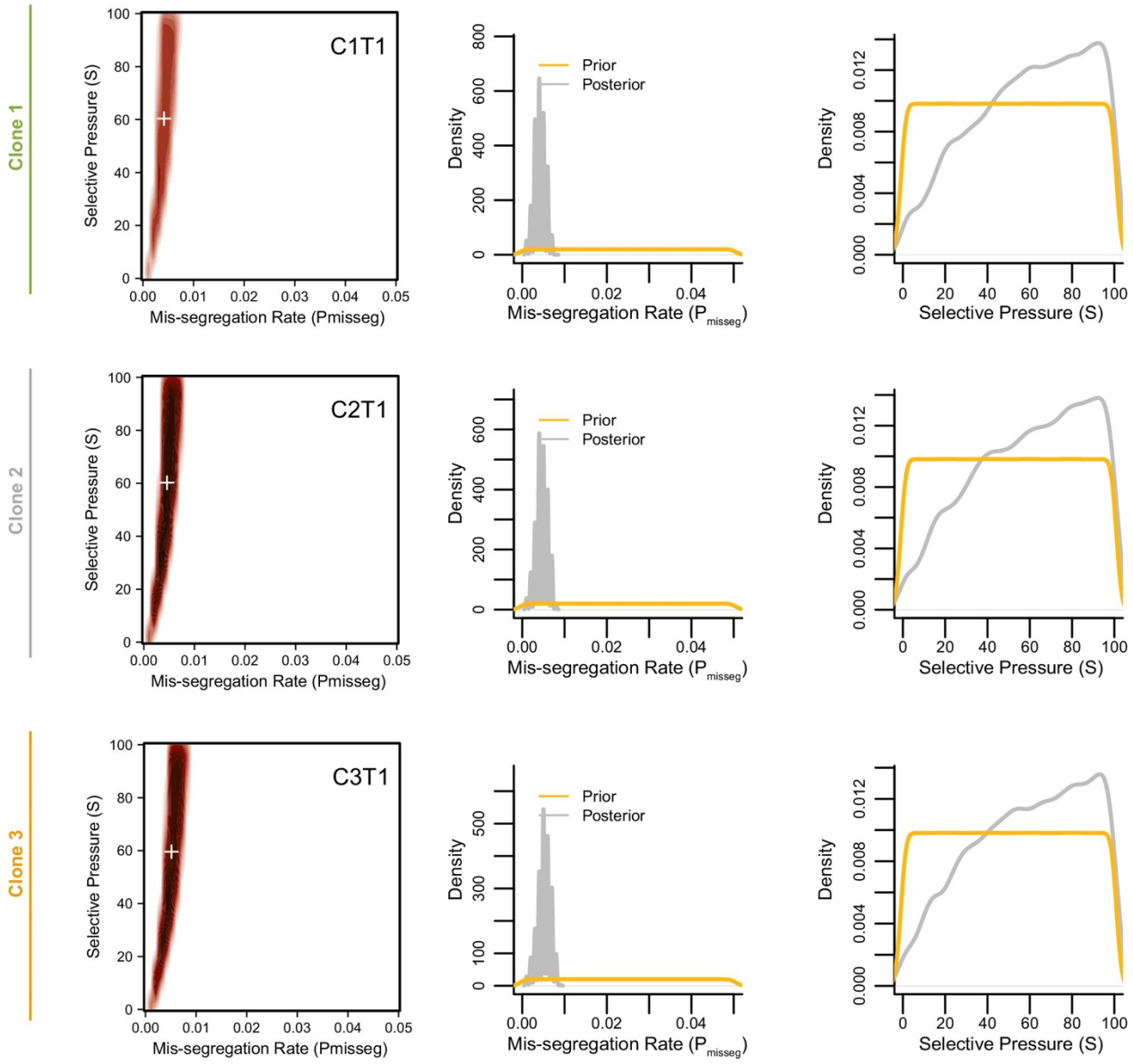

Figure 2.21 — Joint posterior distributions from CRC organoids at 3 weeks.

Joint (2D density plots) and individual (1D density plots) distributions of mis-segregation rates and selective pressures in individual clones of a patient-derived CRC organoid line from Bolhaqueiro et al., 2019 after 3 weeks of growth (accompanying data in Figure 6—figure supplement 4). The prior (yellow) distribution represents the parameters used for simulation while the posterior (gray) distribution represents the parameters from simulations whose observed measurements were similar to the measurements taken from the patient-derived sample using a tolerance threshold of 0.05. White + signs on joint distributions represent the mean of both parameters.

Table 2.1 — Base chromosome-specific fitness scores for individual karyotype selection models

	Selection Model		
Chr Arm	**Gene Abundance**	**Driver Density**	**Hybrid**
1p	0.04780162	-0.0024018	0.02269992
1q	0.04340321	0.03244362	0.03792341
2p	0.02733655	0.02935717	0.02834686
2q	0.04244054	0.03943267	0.0409366
3p	0.02310412	0.03289695	0.02800053
3q	0.0299756	0.05416736	0.04207148
4p	0.01238195	0.01784909	0.01511552
4q	0.03181796	0.02901324	0.0304156
5p	0.01178443	0.04281166	0.02729805
5q	0.03787615	0.01949934	0.02868775
6p	0.02557719	0.02398619	0.02478169
6q	0.02554399	0.00011625	0.01283012
7p	0.0179588	0.09889284	0.05842582
7q	0.03231589	0.06933314	0.05082451
8p	0.01591728	0.02769564	0.02180646
8q	0.0254942	0.05861427	0.04205423
9p	0.01301266	-0.0012941	0.00585929
9q	0.02572657	0.04702681	0.03637669
10p	0.0112201	-0.0364218	-0.0126008
10q	0.02750253	0.01142688	0.01946471
11p	0.01961858	0.03818621	0.0289024
11q	0.03629936	0.01898784	0.0276436
12p	0.0142575	0.0551551	0.0347063
12q	0.03659812	0.06273786	0.04966799
13p	0	0	0
13q	0.02333649	-0.0101539	0.00659128
14p	1.66E-05	0	8.2989E-06
14q	0.03792594	0.02557439	0.03175016
15p	0	0	0
15q	0.03701306	0.0206566	0.02883483
16p	0.02383442	0.04334736	0.03359089
16q	0.01900446	-0.0071444	0.00593005
17p	0.01548573	-0.0085975	0.00344414
17q	0.03553586	0.04363474	0.0395853
18p	0.00627396	0.00533697	0.00580547
18q	0.01434049	-0.0263632	-0.0060113
19p	0.02159372	0.05371416	0.03765394
19q	0.02813325	0.00550338	0.01681831
20p	0.0089628	0.04351025	0.02623653
20q	0.01526996	0.04993593	0.03260295
21p	0.00232369	0	0.00116185
21q	0.01233215	-0.0033092	0.00451147
22p	0.00013278	0	6.6391E-05
22q	0.02297134	-0.0051581	0.0089066
Xp	0.01555213	0	0.00777606

Xq	0.02499627	0	0.01249813

Table 2.2 — Parameters varied during agent-based modeling

Parameter	Description
P_{misseg}	Probability of mis-segregation per chromosome per division
P_{break}	Probability of chromosome breakage after mis-segregation
$P_{division}$	Probability of cellular division per time step
S	Magnitude of selective pressure on aneuploid karyotypes

Table 2.3 — Model selection

Sample	Growth Model	Selection Model	PP	BF (Ho Neutral)	Pmisseg	S	Steps
7T	exponential pseudo-Moran	Abun-dance	0.621	Inf	0.0033 ± 1e-05	60.5416 ± 0.2053	59.8475 ± 0.0937
7T	exponential pseudo-Moran	Driver	0.14	Inf	0.001 ± 1e-05	49.6557 ± 0.2389	58.7002 ± 0.0943
7T	exponential pseudo-Moran	Hybrid	0.239	Inf	8e-04 ± 1e-05	49.3428 ± 0.2377	58.5789 ± 0.0935
7T	exponential pseudo-Moran	Neutral	0	NA	9e-04 ± 5e-05	0 ± 0	57.7994 ± 0.6728
7T	constant Wright-Fisher	Abun-dance	0.985	Inf	0.0062 ± 2e-05	69.7026 ± 0.1724	59.9318 ± 0.0937
7T	constant Wright-Fisher	Driver	0	NA	0.0012 ± 1e-05	48.2881 ± 0.2384	57.5239 ± 0.0933
7T	constant Wright-Fisher	Hybrid	0.015	Inf	9e-04 ± 1e-05	50.7803 ± 0.2359	58.2514 ± 0.0941
7T	constant Wright-Fisher	Neutral	0	NA	9e-04 ± 5e-05	0 ± 0	58.7803 ± 0.6701
U1T	exponential pseudo-Moran	Abun-dance	0.582	199	9e-04 ± 1e-05	56.8672 ± 0.2168	59.9906 ± 0.0937
U1T	exponential pseudo-Moran	Driver	0.113	39	0.001 ± 1e-05	49.6611 ± 0.2389	58.6886 ± 0.0944
U1T	exponential pseudo-Moran	Hybrid	0.156	54	8e-04 ± 1e-05	49.3658 ± 0.2375	58.569 ± 0.0935
U1T	exponential pseudo-Moran	Neutral	0.149	1	9e-04 ± 5e-05	0 ± 0	57.7102 ± 0.67
U1T	constant Wright-Fisher	Abun-dance	0.654	290	0.001 ± 1e-05	61.4358 ± 0.2029	60.0021 ± 0.0937
U1T	constant Wright-Fisher	Driver	0.115	51	0.0012 ± 1e-05	48.2767 ± 0.2383	57.5267 ± 0.0934
U1T	constant Wright-Fisher	Hybrid	0.115	51	9e-04 ± 1e-05	50.8033 ± 0.2358	58.2507 ± 0.0941
U1T	constant Wright-Fisher	Neutral	0.115	1	9e-04 ± 5e-05	0 ± 0	58.7803 ± 0.6701
U2T	exponential pseudo-Moran	Abun-dance	0.628	251	0.0054 ± 1e-05	59.4269 ± 0.2108	59.8349 ± 0.0935
U2T	exponential pseudo-Moran	Driver	0.079	32	0.0027 ± 2e-05	50.1513 ± 0.2396	57.4538 ± 0.0934
U2T	exponential pseudo-Moran	Hybrid	0.166	66	0.0022 ± 2e-05	48.7779 ± 0.2413	57.7078 ± 0.0934
U2T	exponential pseudo-Moran	Neutral	0.127	1	0.0021 ± 7e-05	0 ± 0	56.8535 ± 0.6619
U2T	constant Wright-Fisher	Abun-dance	0.918	2817	0.0112 ± 3e-05	69.7222 ± 0.1703	60.0655 ± 0.0934
U2T	constant Wright-Fisher	Driver	0.001	4	0.0027 ± 2e-05	48.7794 ± 0.2389	56.4812 ± 0.0919
U2T	constant Wright-Fisher	Hybrid	0.064	196	0.0022 ± 1e-05	50.9564 ± 0.2379	57.1161 ± 0.0925
U2T	constant Wright-Fisher	Neutral	0.017	1	0.0022 ± 1e-04	0 ± 0	57.7898 ± 0.6841
U3T	exponential pseudo-Moran	Abun-dance	0.582	199	0.0029 ± 1e-05	60.9557 ± 0.2091	59.8273 ± 0.0938
U3T	exponential pseudo-Moran	Driver	0.113	39	0.001 ± 1e-05	49.6707 ± 0.2389	58.6986 ± 0.0944
U3T	exponential pseudo-Moran	Hybrid	0.156	54	8e-04 ± 1e-05	49.3754 ± 0.2376	58.5711 ± 0.0935

U3T	exponential pseudo-Moran	Neutral	0.149	1	9e-04 ± 5e-05	0 ± 0	57.7102 ± 0.67
U3T	constant Wright-Fisher	Abundance	0.736	Inf	0.0052 ± 2e-05	69.8357 ± 0.1713	59.932 ± 0.0934
U3T	constant Wright-Fisher	Driver	0.13	Inf	0.0012 ± 1e-05	48.2864 ± 0.2383	57.5385 ± 0.0934
U3T	constant Wright-Fisher	Hybrid	0.134	Inf	9e-04 ± 1e-05	50.8219 ± 0.2357	58.2482 ± 0.0941
U3T	constant Wright-Fisher	Neutral	0	NA	9e-04 ± 5e-05	0 ± 0	58.8567 ± 0.6676
14T	exponential pseudo-Moran	Abundance	0.582	199	9e-04 ± 1e-05	56.8672 ± 0.2168	59.9906 ± 0.0937
14T	exponential pseudo-Moran	Driver	0.113	39	0.001 ± 1e-05	49.6614 ± 0.239	58.695 ± 0.0944
14T	exponential pseudo-Moran	Hybrid	0.156	54	8e-04 ± 1e-05	49.3716 ± 0.2375	58.5632 ± 0.0935
14T	exponential pseudo-Moran	Neutral	0.149	1	9e-04 ± 5e-05	0 ± 0	57.7102 ± 0.67
14T	constant Wright-Fisher	Abundance	0.654	290	0.0011 ± 1e-05	62.8579 ± 0.2075	60.0029 ± 0.0936
14T	constant Wright-Fisher	Driver	0.115	51	0.0012 ± 1e-05	48.2967 ± 0.2383	57.5295 ± 0.0934
14T	constant Wright-Fisher	Hybrid	0.115	51	9e-04 ± 1e-05	50.8274 ± 0.2357	58.2478 ± 0.0941
14T	constant Wright-Fisher	Neutral	0.115	1	9e-04 ± 5e-05	0 ± 0	58.8567 ± 0.6676
16T	exponential pseudo-Moran	Abundance	0.582	199	0.002 ± 1e-05	61.2401 ± 0.2028	59.9109 ± 0.0935
16T	exponential pseudo-Moran	Driver	0.113	39	0.001 ± 1e-05	49.6539 ± 0.2389	58.7006 ± 0.0943
16T	exponential pseudo-Moran	Hybrid	0.156	54	8e-04 ± 1e-05	49.3611 ± 0.2376	58.574 ± 0.0935
16T	exponential pseudo-Moran	Neutral	0.149	1	9e-04 ± 5e-05	0 ± 0	57.7994 ± 0.6728
16T	constant Wright-Fisher	Abundance	0.654	290	0.0038 ± 1e-05	69.8456 ± 0.1701	59.9523 ± 0.0936
16T	constant Wright-Fisher	Driver	0.115	51	0.0012 ± 1e-05	48.261 ± 0.2384	57.5233 ± 0.0933
16T	constant Wright-Fisher	Hybrid	0.115	51	9e-04 ± 1e-05	50.7713 ± 0.2359	58.2554 ± 0.0941
16T	constant Wright-Fisher	Neutral	0.115	1	9e-04 ± 5e-05	0 ± 0	58.7803 ± 0.6701
19Ta	exponential pseudo-Moran	Abundance	0.711	313	0.004 ± 1e-05	60.6391 ± 0.2074	59.7801 ± 0.0934
19Ta	exponential pseudo-Moran	Driver	0.038	17	0.0028 ± 2e-05	50.2185 ± 0.2399	57.3764 ± 0.0934
19Ta	exponential pseudo-Moran	Hybrid	0.135	59	0.0022 ± 3e-05	48.3823 ± 0.242	57.5368 ± 0.0935
19Ta	exponential pseudo-Moran	Neutral	0.116	1	0.0022 ± 9e-05	0 ± 0	56.5955 ± 0.6549
19Ta	constant Wright-Fisher	Abundance	0.97	11760	0.0075 ± 2e-05	69.3863 ± 0.1735	59.956 ± 0.0938
19Ta	constant Wright-Fisher	Driver	0	0	0.0028 ± 2e-05	48.8413 ± 0.2392	56.4529 ± 0.0917
19Ta	constant Wright-Fisher	Hybrid	0.026	315	0.0023 ± 1e-05	50.8588 ± 0.2383	57.1031 ± 0.0925
19Ta	constant Wright-Fisher	Neutral	0.004	1	0.0023 ± 1e-04	0 ± 0	57.9522 ± 0.6869
19Tb	exponential pseudo-Moran	Abundance	0.727	320	0.0036 ± 1e-05	60.5885 ± 0.2085	59.829 ± 0.0938
19Tb	exponential pseudo-Moran	Driver	0.03	13	0.001 ± 1e-05	49.6622 ± 0.2389	58.6929 ± 0.0944
19Tb	exponential pseudo-Moran	Hybrid	0.127	56	8e-04 ± 1e-05	48.5237 ± 0.2322	58.9663 ± 0.0931

19Tb	exponential pseudo-Moran	Neutral	0.116	1	9e-04 ± 5e-05	0 ± 0	57.7102 ± 0.67
19Tb	constant Wright-Fisher	Abundance	0.979	47320	0.0068 ± 2e-05	69.5697 ± 0.173	59.9232 ± 0.0935
19Tb	constant Wright-Fisher	Driver	0	0	0.0012 ± 1e-05	48.2786 ± 0.2383	57.5433 ± 0.0934
19Tb	constant Wright-Fisher	Hybrid	0.02	982	9e-04 ± 1e-05	50.8162 ± 0.2357	58.2495 ± 0.0941
19Tb	constant Wright-Fisher	Neutral	0.001	1	9e-04 ± 5e-05	0 ± 0	58.8376 ± 0.669
24Ta	exponential pseudo-Moran	Abundance	0.731	321	0.0036 ± 1e-05	60.5303 ± 0.2082	59.8208 ± 0.0938
24Ta	exponential pseudo-Moran	Driver	0.029	13	0.001 ± 1e-05	49.6703 ± 0.2389	58.6938 ± 0.0944
24Ta	exponential pseudo-Moran	Hybrid	0.125	55	8e-04 ± 1e-05	49.3669 ± 0.2376	58.5778 ± 0.0935
24Ta	exponential pseudo-Moran	Neutral	0.116	1	9e-04 ± 5e-05	0 ± 0	57.7102 ± 0.67
24Ta	constant Wright-Fisher	Abundance	0.979	47346	0.0068 ± 2e-05	69.6173 ± 0.173	59.933 ± 0.0934
24Ta	constant Wright-Fisher	Driver	0	0	0.0012 ± 1e-05	48.2789 ± 0.2383	57.5377 ± 0.0934
24Ta	constant Wright-Fisher	Hybrid	0.02	956	9e-04 ± 1e-05	50.8229 ± 0.2357	58.2524 ± 0.0941
24Ta	constant Wright-Fisher	Neutral	0.001	1	9e-04 ± 5e-05	0 ± 0	58.8567 ± 0.6676
24Tb	exponential pseudo-Moran	Abundance	0.68	294	0.0046 ± 1e-05	60.2602 ± 0.2084	59.8073 ± 0.0936
24Tb	exponential pseudo-Moran	Driver	0.054	23	0.0031 ± 3e-05	50.2981 ± 0.2399	57.2927 ± 0.0934
24Tb	exponential pseudo-Moran	Hybrid	0.149	65	0.0025 ± 4e-05	48.3833 ± 0.244	57.4236 ± 0.0936
24Tb	exponential pseudo-Moran	Neutral	0.118	1	0.0025 ± 0.00013	0 ± 0	56.7229 ± 0.6579
24Tb	constant Wright-Fisher	Abundance	0.954	7730	0.0215 ± 0.00011	33.6703 ± 0.2962	59.9064 ± 0.0937
24Tb	constant Wright-Fisher	Driver	0	2	0.003 ± 2e-05	48.7528 ± 0.2393	56.4175 ± 0.0918
24Tb	constant Wright-Fisher	Hybrid	0.039	318	0.0024 ± 2e-05	50.7006 ± 0.2389	57.107 ± 0.0925
24Tb	constant Wright-Fisher	Neutral	0.006	1	0.0024 ± 0.00011	0 ± 0	58.0318 ± 0.6822
26N	exponential pseudo-Moran	Abundance	0.582	199	0.0021 ± 1e-05	60.9877 ± 0.2031	59.9205 ± 0.0934
26N	exponential pseudo-Moran	Driver	0.113	39	0.001 ± 1e-05	49.6389 ± 0.2389	58.7018 ± 0.0944
26N	exponential pseudo-Moran	Hybrid	0.156	54	8e-04 ± 1e-05	49.3389 ± 0.2377	58.5755 ± 0.0935
26N	exponential pseudo-Moran	Neutral	0.149	1	9e-04 ± 5e-05	0 ± 0	57.7994 ± 0.6728
26N	constant Wright-Fisher	Abundance	0.654	290	0.0039 ± 1e-05	69.794 ± 0.1704	59.9547 ± 0.0935
26N	constant Wright-Fisher	Driver	0.115	51	0.0012 ± 1e-05	48.2849 ± 0.2384	57.5175 ± 0.0933
26N	constant Wright-Fisher	Hybrid	0.115	51	9e-04 ± 1e-05	50.737 ± 0.2359	58.2609 ± 0.0941
26N	constant Wright-Fisher	Neutral	0.115	1	9e-04 ± 5e-05	0 ± 0	58.7803 ± 0.6701
9T	exponential pseudo-Moran	Abundance	0.685	299	0.0044 ± 1e-05	60.2829 ± 0.2086	59.7955 ± 0.0936
9T	exponential pseudo-Moran	Driver	0.052	23	0.0029 ± 2e-05	50.2323 ± 0.2398	57.3657 ± 0.0934
9T	exponential pseudo-Moran	Hybrid	0.147	64	0.0022 ± 3e-05	48.3829 ± 0.2422	57.5193 ± 0.0936

9T	exponential pseudo-Moran	Neutral	0.117	1	0.0023 ± 9e-05	0 ± 0	56.6083 ± 0.6581
9T	constant Wright-Fisher	Abundance	0.958	9299	0.0087 ± 2e-05	69.6836 ± 0.1724	59.926 ± 0.0937
9T	constant Wright-Fisher	Driver	0	1	0.0028 ± 2e-05	48.8394 ± 0.2392	56.4465 ± 0.0917
9T	constant Wright-Fisher	Hybrid	0.037	360	0.0023 ± 1e-05	50.8477 ± 0.2384	57.0952 ± 0.0925
9T	constant Wright-Fisher	Neutral	0.005	1	0.0023 ± 1e-04	0 ± 0	57.9427 ± 0.687
PolyB 1	exponential pseudo-Moran	Abundance	0.635	261	0.0053 ± 1e-05	59.5088 ± 0.2104	59.8379 ± 0.0935
PolyB 1	exponential pseudo-Moran	Driver	0.076	31	0.0028 ± 2e-05	50.2364 ± 0.2398	57.4025 ± 0.0934
PolyB 1	exponential pseudo-Moran	Hybrid	0.164	67	0.0022 ± 3e-05	48.6949 ± 0.2419	57.6322 ± 0.0934
PolyB 1	exponential pseudo-Moran	Neutral	0.124	1	0.0022 ± 9e-05	0 ± 0	56.5955 ± 0.6549
PolyB 1	constant Wright-Fisher	Abundance	0.925	3482	0.0111 ± 3e-05	70.2557 ± 0.169	60.042 ± 0.0936
PolyB 1	constant Wright-Fisher	Driver	0.001	4	0.0028 ± 2e-05	48.8194 ± 0.2391	56.4451 ± 0.0917
PolyB 1	constant Wright-Fisher	Hybrid	0.061	228	0.0023 ± 1e-05	50.895 ± 0.2381	57.1073 ± 0.0925
PolyB 1	constant Wright-Fisher	Neutral	0.014	1	0.0023 ± 1e-04	0 ± 0	57.9809 ± 0.6861
PolyB 2	exponential pseudo-Moran	Abundance	0.603	218	0.0059 ± 1e-05	58.6612 ± 0.212	59.7835 ± 0.0937
PolyB 2	exponential pseudo-Moran	Driver	0.086	31	0.0038 ± 4e-05	50.2948 ± 0.2394	57.0217 ± 0.093
PolyB 2	exponential pseudo-Moran	Hybrid	0.17	61	0.004 ± 7e-05	48.9466 ± 0.2472	57.28 ± 0.0942
PolyB 2	exponential pseudo-Moran	Neutral	0.141	1	0.0033 ± 0.00022	0 ± 0	56.5732 ± 0.6597
PolyB 2	constant Wright-Fisher	Abundance	0.893	1277	0.0301 ± 1e-04	3.0543 ± 0.0165	59.9142 ± 0.0936
PolyB 2	constant Wright-Fisher	Driver	0.003	4	0.0034 ± 3e-05	48.7328 ± 0.2396	56.3664 ± 0.0917
PolyB 2	constant Wright-Fisher	Hybrid	0.069	98	0.0027 ± 2e-05	50.3534 ± 0.2405	57.1445 ± 0.0928
PolyB 2	constant Wright-Fisher	Neutral	0.036	1	0.0026 ± 0.00014	0 ± 0	58.1592 ± 0.6741

Table 2.4 — Model selection with selective pressure constrained to S = 1

Sample	Growth Model	Selection Model	PP	BF (Ho Neutral)	Pmisseg	S	Steps
7T	exponential pseudo-Moran	Abundance	0.274	1	9e-04 ± 5e-05	1 ± 0	58.2452 ± 0.6646
7T	exponential pseudo-Moran	Driver	0.238	1	9e-04 ± 5e-05	1 ± 0	58.4745 ± 0.6725
7T	exponential pseudo-Moran	Hybrid	0.26	1	9e-04 ± 5e-05	1 ± 0	58.586 ± 0.6668
7T	exponential pseudo-Moran	Neutral	0.228	1	9e-04 ± 6e-05	1 ± 0	58.5446 ± 0.6791
7T	constant Wright-Fisher	Abundance	0.259	1	9e-04 ± 6e-05	1 ± 0	58.8089 ± 0.6627
7T	constant Wright-Fisher	Driver	0.24	1	9e-04 ± 6e-05	1 ± 0	58.1783 ± 0.6771
7T	constant Wright-Fisher	Hybrid	0.257	1	9e-04 ± 5e-05	1 ± 0	59.0924 ± 0.6742
7T	constant Wright-Fisher	Neutral	0.245	1	9e-04 ± 7e-05	1 ± 0	58.7516 ± 0.6787
U1T	exponential pseudo-Moran	Abundance	0.275	1	9e-04 ± 5e-05	1 ± 0	58.2452 ± 0.6646
U1T	exponential pseudo-Moran	Driver	0.239	1	9e-04 ± 5e-05	1 ± 0	58.4745 ± 0.6725
U1T	exponential pseudo-Moran	Hybrid	0.258	1	9e-04 ± 5e-05	1 ± 0	58.586 ± 0.6668
U1T	exponential pseudo-Moran	Neutral	0.228	1	9e-04 ± 6e-05	1 ± 0	58.5446 ± 0.6791
U1T	constant Wright-Fisher	Abundance	0.259	1	9e-04 ± 6e-05	1 ± 0	58.8089 ± 0.6627
U1T	constant Wright-Fisher	Driver	0.24	1	9e-04 ± 6e-05	1 ± 0	58.1783 ± 0.6771
U1T	constant Wright-Fisher	Hybrid	0.257	1	9e-04 ± 5e-05	1 ± 0	59.1592 ± 0.6715
U1T	constant Wright-Fisher	Neutral	0.245	1	9e-04 ± 7e-05	1 ± 0	58.7516 ± 0.6787
U2T	exponential pseudo-Moran	Abundance	0.276	1	0.0021 ± 8e-05	1 ± 0	57.3057 ± 0.653
U2T	exponential pseudo-Moran	Driver	0.235	1	0.0024 ± 0.00011	1 ± 0	57.7452 ± 0.6634
U2T	exponential pseudo-Moran	Hybrid	0.264	1	0.0021 ± 7e-05	1 ± 0	58.1274 ± 0.654
U2T	exponential pseudo-Moran	Neutral	0.225	1	0.0024 ± 0.00011	1 ± 0	57.8758 ± 0.6772
U2T	constant Wright-Fisher	Abundance	0.269	1	0.0023 ± 1e-04	1 ± 0	58.3439 ± 0.6532
U2T	constant Wright-Fisher	Driver	0.233	1	0.0023 ± 9e-05	1 ± 0	57.4777 ± 0.693
U2T	constant Wright-Fisher	Hybrid	0.263	1	0.0023 ± 1e-04	1 ± 0	57.8662 ± 0.6683
U2T	constant Wright-Fisher	Neutral	0.236	1	0.0025 ± 0.00012	1 ± 0	57.1433 ± 0.6655
U3T	exponential pseudo-Moran	Abundance	0.275	1	9e-04 ± 5e-05	1 ± 0	58.1624 ± 0.6643
U3T	exponential pseudo-Moran	Driver	0.239	1	9e-04 ± 5e-05	1 ± 0	58.4554 ± 0.6736
U3T	exponential pseudo-Moran	Hybrid	0.258	1	9e-04 ± 5e-05	1 ± 0	58.586 ± 0.6668
U3T	exponential pseudo-Moran	Neutral	0.228	1	9e-04 ± 6e-05	1 ± 0	58.6178 ± 0.6777
U3T	constant Wright-Fisher	Abundance	0.259	1	9e-04 ± 6e-05	1 ± 0	58.7611 ± 0.6614
U3T	constant Wright-Fisher	Driver	0.24	1	9e-04 ± 6e-05	1 ± 0	58.1783 ± 0.6771
U3T	constant Wright-Fisher	Hybrid	0.257	1	9e-04 ± 5e-05	1 ± 0	59.0955 ± 0.674
U3T	constant Wright-Fisher	Neutral	0.245	1	9e-04 ± 7e-05	1 ± 0	58.7516 ± 0.6787
14T	exponential pseudo-Moran	Abundance	0.275	1	9e-04 ± 5e-05	1 ± 0	58.1624 ± 0.6643
14T	exponential pseudo-Moran	Driver	0.239	1	9e-04 ± 5e-05	1 ± 0	58.4554 ± 0.6736
14T	exponential pseudo-Moran	Hybrid	0.258	1	9e-04 ± 5e-05	1 ± 0	58.586 ± 0.6668
14T	exponential pseudo-Moran	Neutral	0.228	1	9e-04 ± 6e-05	1 ± 0	58.5446 ± 0.6791
14T	constant Wright-Fisher	Abundance	0.259	1	9e-04 ± 6e-05	1 ± 0	58.8089 ± 0.6627
14T	constant Wright-Fisher	Driver	0.24	1	9e-04 ± 6e-05	1 ± 0	58.1783 ± 0.6771
14T	constant Wright-Fisher	Hybrid	0.257	1	9e-04 ± 5e-05	1 ± 0	59.0924 ± 0.6739
14T	constant Wright-Fisher	Neutral	0.245	1	9e-04 ± 7e-05	1 ± 0	58.7516 ± 0.6787
16T	exponential pseudo-Moran	Abundance	0.274	1	9e-04 ± 5e-05	1 ± 0	58.2452 ± 0.6646
16T	exponential pseudo-Moran	Driver	0.238	1	9e-04 ± 5e-05	1 ± 0	58.4745 ± 0.6725
16T	exponential pseudo-Moran	Hybrid	0.26	1	9e-04 ± 5e-05	1 ± 0	58.586 ± 0.6668
16T	exponential pseudo-Moran	Neutral	0.228	1	0.001 ± 6e-05	1 ± 0	58.6274 ± 0.6789
16T	constant Wright-Fisher	Abundance	0.259	1	9e-04 ± 6e-05	1 ± 0	58.8089 ± 0.6627
16T	constant Wright-Fisher	Driver	0.24	1	9e-04 ± 6e-05	1 ± 0	58.1783 ± 0.6771
16T	constant Wright-Fisher	Hybrid	0.257	1	9e-04 ± 5e-05	1 ± 0	59.1051 ± 0.6742
16T	constant Wright-Fisher	Neutral	0.245	1	9e-04 ± 7e-05	1 ± 0	58.7516 ± 0.6787
19Ta	exponential pseudo-Moran	Abundance	0.273	1	0.0021 ± 8e-05	1 ± 0	57.4045 ± 0.6565
19Ta	exponential pseudo-Moran	Driver	0.243	1	0.0024 ± 0.00011	1 ± 0	57.8025 ± 0.663
19Ta	exponential pseudo-Moran	Hybrid	0.261	1	0.0022 ± 8e-05	1 ± 0	57.9108 ± 0.65
19Ta	exponential pseudo-Moran	Neutral	0.222	1	0.0025 ± 0.00012	1 ± 0	57.9331 ± 0.6777
19Ta	constant Wright-Fisher	Abundance	0.27	1	0.0024 ± 0.00011	1 ± 0	58.2866 ± 0.6566
19Ta	constant Wright-Fisher	Driver	0.233	1	0.0023 ± 1e-04	1 ± 0	57.8185 ± 0.6927
19Ta	constant Wright-Fisher	Hybrid	0.261	1	0.0023 ± 1e-04	1 ± 0	58.0478 ± 0.6705

19Ta	constant Wright-Fisher	Neutral	0.237	1	0.0025 ± 0.00012	1 ± 0	57.2261 ± 0.6669
19Tb	exponential pseudo-Moran	Abundance	0.275	1	9e-04 ± 5e-05	1 ± 0	58.1624 ± 0.6643
19Tb	exponential pseudo-Moran	Driver	0.239	1	9e-04 ± 5e-05	1 ± 0	58.4554 ± 0.6736
19Tb	exponential pseudo-Moran	Hybrid	0.258	1	9e-04 ± 5e-05	1 ± 0	58.586 ± 0.6668
19Tb	exponential pseudo-Moran	Neutral	0.228	1	9e-04 ± 6e-05	1 ± 0	58.5796 ± 0.6796
19Tb	constant Wright-Fisher	Abundance	0.259	1	9e-04 ± 6e-05	1 ± 0	58.7611 ± 0.6614
19Tb	constant Wright-Fisher	Driver	0.24	1	9e-04 ± 6e-05	1 ± 0	58.1178 ± 0.679
19Tb	constant Wright-Fisher	Hybrid	0.257	1	9e-04 ± 5e-05	1 ± 0	59.1592 ± 0.6715
19Tb	constant Wright-Fisher	Neutral	0.245	1	9e-04 ± 7e-05	1 ± 0	58.7516 ± 0.6787
24Ta	exponential pseudo-Moran	Abundance	0.275	1	9e-04 ± 5e-05	1 ± 0	58.1624 ± 0.6643
24Ta	exponential pseudo-Moran	Driver	0.239	1	9e-04 ± 5e-05	1 ± 0	58.4554 ± 0.6736
24Ta	exponential pseudo-Moran	Hybrid	0.258	1	9e-04 ± 5e-05	1 ± 0	58.586 ± 0.6668
24Ta	exponential pseudo-Moran	Neutral	0.228	1	9e-04 ± 6e-05	1 ± 0	58.6656 ± 0.6783
24Ta	constant Wright-Fisher	Abundance	0.259	1	9e-04 ± 6e-05	1 ± 0	58.7611 ± 0.6614
24Ta	constant Wright-Fisher	Driver	0.24	1	9e-04 ± 6e-05	1 ± 0	58.1783 ± 0.6771
24Ta	constant Wright-Fisher	Hybrid	0.257	1	9e-04 ± 5e-05	1 ± 0	59.1592 ± 0.6715
24Ta	constant Wright-Fisher	Neutral	0.245	1	9e-04 ± 7e-05	1 ± 0	58.7516 ± 0.6787
24Tb	exponential pseudo-Moran	Abundance	0.273	1	0.0023 ± 0.00011	1 ± 0	57.0446 ± 0.6526
24Tb	exponential pseudo-Moran	Driver	0.242	1	0.0025 ± 0.00012	1 ± 0	57.551 ± 0.6661
24Tb	exponential pseudo-Moran	Hybrid	0.264	1	0.0022 ± 9e-05	1 ± 0	57.9108 ± 0.6512
24Tb	exponential pseudo-Moran	Neutral	0.222	1	0.0026 ± 0.00013	1 ± 0	57.7516 ± 0.6758
24Tb	constant Wright-Fisher	Abundance	0.267	1	0.0024 ± 0.00013	1 ± 0	58.379 ± 0.6601
24Tb	constant Wright-Fisher	Driver	0.237	1	0.0024 ± 1e-04	1 ± 0	57.7357 ± 0.6922
24Tb	constant Wright-Fisher	Hybrid	0.257	1	0.0023 ± 1e-04	1 ± 0	57.9045 ± 0.6718
24Tb	constant Wright-Fisher	Neutral	0.239	1	0.0025 ± 0.00012	1 ± 0	57.2643 ± 0.6726
26N	exponential pseudo-Moran	Abundance	0.274	1	9e-04 ± 5e-05	1 ± 0	58.2452 ± 0.6646
26N	exponential pseudo-Moran	Driver	0.239	1	9e-04 ± 5e-05	1 ± 0	58.4045 ± 0.6706
26N	exponential pseudo-Moran	Hybrid	0.26	1	9e-04 ± 5e-05	1 ± 0	58.586 ± 0.6668
26N	exponential pseudo-Moran	Neutral	0.227	1	0.001 ± 7e-05	1 ± 0	58.6815 ± 0.6776
26N	constant Wright-Fisher	Abundance	0.259	1	9e-04 ± 6e-05	1 ± 0	58.8089 ± 0.6627
26N	constant Wright-Fisher	Driver	0.239	1	9e-04 ± 6e-05	1 ± 0	58.1783 ± 0.6771
26N	constant Wright-Fisher	Hybrid	0.257	1	9e-04 ± 5e-05	1 ± 0	59.1178 ± 0.6745
26N	constant Wright-Fisher	Neutral	0.245	1	0.001 ± 7e-05	1 ± 0	58.6879 ± 0.6762
9T	exponential pseudo-Moran	Abundance	0.274	1	0.0021 ± 8e-05	1 ± 0	57.3854 ± 0.6574
9T	exponential pseudo-Moran	Driver	0.242	1	0.0024 ± 0.00011	1 ± 0	57.8025 ± 0.663
9T	exponential pseudo-Moran	Hybrid	0.261	1	0.0022 ± 8e-05	1 ± 0	57.9108 ± 0.65
9T	exponential pseudo-Moran	Neutral	0.222	1	0.0025 ± 0.00012	1 ± 0	57.9522 ± 0.6787
9T	constant Wright-Fisher	Abundance	0.269	1	0.0024 ± 0.00011	1 ± 0	58.2866 ± 0.6566
9T	constant Wright-Fisher	Driver	0.233	1	0.0023 ± 1e-04	1 ± 0	57.9076 ± 0.6927
9T	constant Wright-Fisher	Hybrid	0.261	1	0.0023 ± 1e-04	1 ± 0	58.1115 ± 0.6708
9T	constant Wright-Fisher	Neutral	0.236	1	0.0025 ± 0.00012	1 ± 0	57.2261 ± 0.6669
PolyB1	exponential pseudo-Moran	Abundance	0.274	1	0.0021 ± 8e-05	1 ± 0	57.4045 ± 0.6565
PolyB1	exponential pseudo-Moran	Driver	0.243	1	0.0024 ± 0.00011	1 ± 0	57.7102 ± 0.6622
PolyB1	exponential pseudo-Moran	Hybrid	0.261	1	0.0022 ± 8e-05	1 ± 0	57.9459 ± 0.6512
PolyB1	exponential pseudo-Moran	Neutral	0.222	1	0.0025 ± 0.00011	1 ± 0	57.9522 ± 0.6776
PolyB1	constant Wright-Fisher	Abundance	0.271	1	0.0023 ± 0.00011	1 ± 0	58.2834 ± 0.6575
PolyB1	constant Wright-Fisher	Driver	0.231	1	0.0023 ± 9e-05	1 ± 0	57.6656 ± 0.6949
PolyB1	constant Wright-Fisher	Hybrid	0.261	1	0.0023 ± 1e-04	1 ± 0	57.9713 ± 0.6668
PolyB1	constant Wright-Fisher	Neutral	0.237	1	0.0025 ± 0.00012	1 ± 0	57.207 ± 0.6674
PolyB2	exponential pseudo-Moran	Abundance	0.272	1	0.0027 ± 2e-04	1 ± 0	56.8471 ± 0.6544
PolyB2	exponential pseudo-Moran	Driver	0.245	1	0.0029 ± 0.00021	1 ± 0	57.3312 ± 0.6609
PolyB2	exponential pseudo-Moran	Hybrid	0.263	1	0.0024 ± 0.00011	1 ± 0	57.9204 ± 0.6466
PolyB2	exponential pseudo-Moran	Neutral	0.221	1	0.0029 ± 0.00017	1 ± 0	57.4236 ± 0.6784
PolyB2	constant Wright-Fisher	Abundance	0.268	1	0.0025 ± 0.00013	1 ± 0	58.2484 ± 0.6616
PolyB2	constant Wright-Fisher	Driver	0.235	1	0.0026 ± 0.00014	1 ± 0	57.5796 ± 0.6897
PolyB2	constant Wright-Fisher	Hybrid	0.257	1	0.0026 ± 0.00015	1 ± 0	58.1115 ± 0.6741
PolyB2	constant Wright-Fisher	Neutral	0.24	1	0.0027 ± 0.00014	1 ± 0	57.379 ± 0.6701

Table 2.5 — Approximate reported per chromosome mis-segregation rates

1st Author	DOI	Model	Sample Type	Statistic	Assessment	Approximate observed frequency %	Aprrox modal chromosome # (ATCC)	Approximate mis-segregation rate (per chromosome)
Bakhoum	https://doi.org/10.1158/1078-0432.CCR-11-2049	Tumor-TMA	Tumor	Reported	Lagging/Bridging	31.3	46	0.00680
Orr	https://doi.org/10.1016/j.celrep.2016.10.030	U2OS	Tumor	Approx. Mean	Lagging	32.5	46	0.00707
Orr	https://doi.org/10.1016/j.celrep.2016.10.030	HeLa	Tumor	Approx. Mean	Lagging	22	82	0.00268
Orr	https://doi.org/10.1016/j.celrep.2016.10.030	SW-620	Tumor	Approx. Mean	Lagging	22.5	50	0.00450
Orr	https://doi.org/10.1016/j.celrep.2016.10.030	RPE1	Non-tumor	Approx. Mean	Lagging	2.5	46	0.00054
Orr	https://doi.org/10.1016/j.celrep.2016.10.030	BJ	Non-tumor	Approx. Mean	Lagging	8	46	0.00174
Nicholson	https://doi.org/10.7554/eLife.05068	Amniocyte	Non-tumor	Approx. Mean	Lagging	0	46	0.00000
Nicholson	https://doi.org/10.7554/eLife.05068	DLD1	Tumor	Approx. Mean	Lagging	1	46	0.00022
Dewhurst	https://doi.org/10.1158/2159-8290.CD-13-0285	HCT116-Diploid	Tumor	Approx. Mean	Lagging/Bridging	23	45	0.00511
Dewhurst	https://doi.org/10.1158/2159-8290.CD-13-0285	HCT116-Tetraploid	Tumor	Approx. Mean	Lagging/Bridging	50	90	0.00556
Bakhoum	https://doi.org/10.1038/ncb1809	U2OS	Tumor	Reported	Lagging		46	0.01000
Zasadil	https://doi.org/10.1126/scitranslmed.3007965	CAL51	Tumor	Approx. Mean	Lagging	0.5	44	0.00011
Thompson	https://doi.org/10.1083/jcb.200712029	RPE1	Non-tumor	Approx. Mean	Acute aneuploidy via FISH		46	0.00025
Thompson	https://doi.org/10.1083/jcb.200712029	HCT116-Diploid	Tumor	Approx. Mean	Acute aneuploidy via FISH		45	0.00025
Thompson	https://doi.org/10.1083/jcb.200712029	HT29	Tumor	Approx. Mean	Acute aneuploidy via FISH		71	0.00250
Thompson	https://doi.org/10.1083/jcb.200712029	Caco2	Tumor	Approx. Mean	Acute aneuploidy via FISH		96	0.00900
Thompson	https://doi.org/10.1083/jcb.200712029	MCF-7	Tumor	Approx. Mean	Acute aneuploidy via FISH		82	0.00700
Bakhoum	https://doi.org/10.1016/j.cub.2014.01.019	HCT116-Diploid	Tumor	Approx. Mean	Lagging	6	45	0.00133
Bakhoum	https://doi.org/10.1016/j.cub.2014.01.019	DLD1	Tumor	Approx. Mean	Lagging	2	46	0.00043
Bakhoum	https://doi.org/10.1016/j.cub.2014.01.019	HT29	Tumor	Approx. Mean	Lagging	14	71	0.00197
Bakhoum	https://doi.org/10.1016/j.cub.2014.01.019	SW-620	Tumor	Approx. Mean	Lagging	12	50	0.00240
Bakhoum	https://doi.org/10.1016/j.cub.2014.01.019	MCF-7	Tumor	Approx. Mean	Lagging	17	82	0.00207
Bakhoum	https://doi.org/10.1016/j.cub.2014.01.019	HeLa	Tumor	Approx. Mean	Lagging	13	82	0.00159
Worrall	https://doi.org/10.1016/j.celrep.2018.05.047	BJ	Non-tumor	Approx. Mean	Unspecified Error	5	46	0.00109

Worrall	https://doi.org/10.1016/j.celrep.2018.05.047	RPE1	Non-tumor	Approx. Mean	Unspecified Error	5	46	0.00109

3

A SURVEY OF CHROMOSOMAL INSTABILITY MEASURES ACROSS INDUCIBLE MECHANISTIC MODELS

Adapted from Lynch et al. (Manuscript 3). In preparation.

ABSTRACT

Chromosomal instability (CIN) is the persistent reshuffling of cancer karyotypes via chromo-some mis-segregation during cell division. In cancer, CIN exists at varying levels that have dif-ferential effects on tumor progression. However, mis-segregation rates re-main challenging to assess in human cancer despite an array of proposed measurement methods. To evaluate measures of CIN, we compared quantitative methods using specific, inducible phenotypic models of CIN including chromosome bridges, pseudobipolar spin-dles, multipolar spindles, and polar chromosomes. For each, we measured CIN using mul-tiple approaches: fixed and timelapse fluorescence microscopy, chromosome spreads, 6-centromere FISH, bulk tran-scriptomics, and single cell DNA sequencing (scDNAseq). While direct microscopy of tumor cells in live and fixed samples correlated well correlated well ($R = 0.77$; $p < 0.01$) and sensitively detected CIN, fixed imaging often underestimated transient causes of CIN. Commonly used cytogenetics approaches include chromosome spreads and 6-centromere FISH, which also correlated well ($R = 0.77$; $p < 0.01$) but had limited sensitivity for lower rates of CIN. Turning to genomics, inducible CIN is not

detected with bulk genomic DNA signatures and bulk tran-scriptomic scores, CIN70 and HET70. By contrast, single cell DNA sequencing (scDNAseq) de-tects CIN with high sensitivity, and correlates very well with imaging methods ($R = 0.83$; $p < 0.01$). scDNAseq is further enhanced by accounting for cellular selection using approximate Bayesian computation (ABC). We conclude that single-cell methods such as imaging, cytoge-netics, and scDNAseq can measure CIN, and that scDNAseq is the most comprehensive method accessible to clinical samples. To facilitate comparison of CIN rates between groups and methods, we propose a standardized unit of measure of CIN: Mis-segregations per Diploid Division (MDD). This systematic analysis of common CIN measures highlights the superiority of single-cell methods and provides guidance for measuring CIN in the clinical setting.

INTRODUCTION

David von Hansemann and Theodor Boveri described chromosomal instability (CIN) and proposed its role in human cancer over 100 years ago (305, 306). Indeed, CIN accelerates tumor evolution, and portends increased metastasis (238, 262), therapeutic resistance (240, 241, 243), and worse prognosis (182, 237, 260). Importantly, tumors' CIN levels vary considerably. While moderate CIN levels promote these advanced clinical features, and while high CIN levels are tumor-inhibiting in mouse models(245, 246, 263), it is unclear whether high CIN levels improve (188, 251, 307–309) or impair (182, 237, 310, 311) patient survival outcomes in human cancer. This discrepancy is due in large part to poorly defined levels of CIN, highlighting the need for accurate, quantitative CIN measures that are amenable to clinical use.

Since Hansemann and Boveri, several methods of quantifying CIN have been used in basic and translational studies. However, these methods vary in accuracy as well as how comprehensively and directly they assess CIN, leading to disagreement among measures (157, 270). It is important to compare and judge the analytic validity of these approaches to optimize CIN measures for human cancer.

Among cell biologists, direct observation of mitotic abnormalities is a common measure of CIN. Fixed and time-lapse microscopy rely on the visual identification of abnormal mitotic phenotypes such as lagging, polar, and bridging chromosomes as well as spindle multipolarity. This direct observation of mitotic defects is considered the 'gold standard'. However, the identity of the missegregated chromosome(s) remains unclear and, in some cases, even direct observation requires assumptions to infer chromosome mis-segregation, such as whether a lagging chromosome segregates to the correct or incorrect daughter cell (135, 240, 241, 243). Further, these methods are not readily applicable to human tumors.

Cytogenetic methods can be used to infer CIN by cell-to-cell variation in chromosome numbers or karyotypes. Actively cycling cells can be captured in mitosis for chromosome counts and karyotypes. However, the reliance on mitotic cells may bias the sample, particularly as *de novo* aneuploidy may may delay progression through interphase (198, 201, 268). By contrast, centromeric fluorescence *in situ* hybridization (cenFISH) identifies abnormal complements of chromosomes in fixed cells without bias for cycling cells. However, *interphase* FISH is limited to a small number of chromosomes and may

suffer from other limitations such as sectioning artifacts. Further, any analysis of living cells in a tumor is biased by cellular selection (138, 147, 228, 241).

Genomics promises more comprehensive measures of genomic heterogeneity, and a variety of genomic methods have been proposed to assess CIN. Bulk transcriptional data (bRNAseq) has been used to assign CIN scores to tumor samples. Expression scores such as CIN70 (187), meant to reflect the level of CIN, are derived from an inferred level of aneuploidy and correlate with proliferation and structural aneuploidy. Thus, they may correlate with CIN but do not directly measure it. The HET70 score correlates with high karyotype heterogeneity in the NCI60 panel without correlating with PCNA, suggesting it is independent of proliferation (312). However, it is unclear if bulk transcriptional scores can discriminate ongoing CIN or merely correlate with it in cancer models. Similarly, bulk DNA sequencing (bDNAseq) CIN signatures are proposed to quantify and identify initial cause of CIN, by inferring mechanisms that could produce an observed cell-averaged DNA copy number profile. Whether bulk sequencing measures detect ongoing CIN has not been tested.

Single-cell genomic measures of cell-to-cell variation in copy number analysis are less commonly used in clinical samples but have an advantage over bulk methods as they are not averaged across cells, allowing for direct evaluation of cell-to-cell variation (147). Low-coverage single cell DNA sequencing (scDNAseq) can determine numerical copy numbers of all chromosomes in single cells in experimental models and patient tumors (191, 313). Like FISH, this information can be used to measure CIN by quantifying cell-to-cell heterogeneity in genomics-inferred karyotypes. scDNAseq can be further improved

by accounting for cellular selection against highly aneuploid cells using computational modeling and approximate Bayesian computation (ABC) (147).

Here, we directly compare these various measures of CIN in well-defined inducible cell-based models. The results reveal the pre-eminence of single-cell measures (microscopic analysis of mitosis, cytogenetic methods, scDNAseq) in measuring ongoing CIN and the inability of bulk molecular sequencing (transcriptional profiles and bulk DNA sequencing) to detect CIN. Among single-cell measures, those that survey all chromosomes across hundreds of cells are most sensitive. The data collected here are made available to investigators who seek to establish novel measures of CIN and are an important touchstone to establish their directness for ongoing CIN. We anticipate that this comprehensive comparison will allow the most accurate CIN measures to be employed in clinical samples to advance mechanistic insight, as well as clinical significance and to facilitate use of CIN as a predictive biomarker, such as for microtubule-targeted therapies (251).

RESULTS

Design and validation of CIN models with distinct mechanisms

We developed 4 phenotypic models of CIN induced by distinct mechanisms (Figure 3.1): 1) Bridging chromosomes (Br, red) in CAL51 cells via tetracycline-inducible expression of a dominant negative mutant of telomeric repeat binding factor (*TERF2*-DN) lacking both its basic domain and Myb-binding box (314), 2) pseudobipolar spindles (Pb, blue) in MCF10A cells via induction of centrosome amplification and subsequent spindle pole focusing after tetracycline-inducible expression of polo-like kinase 4 (*PLK4*), 3) multipolar spindles (Mp, green) in MCF10A cells by inhibition of HSET to prevent focusing in

the Pb model (251), and 4) polar chromosomes (Po, orange) in MCF10A cells by mitotic enrichment and sequential inhibition of CENP-E then MPS1. This sequential chemical treatment induces anaphase onset with multiple polar chromosomes with high penetrance (315). After induction of each CIN model, we performed imaging (fixed immunofluorescence and 4–12-hour time lapse fluorescence microscopy), cytogenetic (mitotic chromosome counts and cenFISH), and sequence-based assays (bRNAseq, bDNAseq, scDNAseq) to measure CIN.

We first verified that our models induced CIN by microscopy. Using fixed and time lapse imaging, we found the expected CIN phenotypes for each model, indicating successful induction (Figure 3.2). As expected, the Br model induced ~30-40% anaphase bridges after doxycycline, visible on fixed and live analysis (Figure 3.2A,E). For the Pb model, we often observed multipolar spindles that focus to pseudobipolar spindles by anaphase onset such that a single spindle pole often has two pericentric foci (Figure 2B). The Pb model displayed pseudobipolar anaphases in 40-50% of cells (Figure 3.2B,F), though about 5-15% of cells exhibited multipolar anaphase (Figure 3.2C,G). The Mp model induced ~25% multipolar anaphases after doxycycline + CW-069. The Po model induced high penetrance of CIN with polar chromosomes found in virtually all cells (Figure 3.2D-H).

To evaluate measures of CIN, we quantified the total mitotic aberrations by microscopy using fixed and time lapse imaging (Figure 3.2I,J). As expected, all had statistically elevated CIN over controls and the two methods were closely correlated (Figure 3.2K). To directly compare the relative levels of CIN imparted by each model, we quantified a

standardized measure of CIN, mis-segregations per diploid division (MDD), which we previously described (316). This measure accounts for the relative mis-segregation rates produced by different CIN phenotypes, the relative penetrance of these phenotypes, and the ploidy of the cell. In short, we assume that pseudobipolar spindles produce no mis-segregations, bridging and lagging chromosomes each produce 1 mis-segregation, polar chromosomes produce 7.8 mis-segregations based on quantitative immunofluorescence imaging of polar centromere foci (Figure 3.3A) and multipolar spindles produce 18 mis-segregations based on Lynch et al. 2022 (Table 3.1, Materials & Methods). By this approximation, the mis-segregation rates (MDD) observed for each model are 0.22 ± 0.1 for CtrlC, 0.61 ± 0.04 for Br, 0.28 ± 0.06 for CtrlM, 1.21 ± 0.37 for Pb, 4.59 ± 0.56 for Mp, and 7.77 ± 0.15 for Po by fixed imaging (Figure 2L). By time lapse imaging, these approximations are 1.32 ± 0.63 for CtrlC, 1.45 ± 0.22 for Br, 0.65 ± 0.62 for CtrlM, 2.91 ± 0.56 for Pb, 4.63 ± 0.7 for Mp, and 8.04 ± 0.37 for Po (Figure 3.2M).

In summary, these findings validate our CIN models and demonstrate low levels of CIN with Br and Pb, intermediate levels with Mp, and very high levels with Po. These distinct models and mechanisms of CIN confirm they are suitable models to compare quantitative measures of CIN.

Short-lived CIN phenotypes are underestimated in fixed imaging

While the two imaging methods correlated well (Figure 3.2K), time lapse imaging appeared more sensitive to certain CIN phenotypes. For example, we detected significantly more multipolar metaphases and anaphases with lagging chromosomes using time lapse imaging. Anaphase polar chromosomes were more readily detected using time

lapse imaging as well. These differentially detected defects are transient in nature, suggesting that the differences are not an artifact of live imaging alone. For example, multipolar spindles can be clustered rapidly throughout mitosis while lagging and polar chromosomes are often incorporated into the segregating chromosome mass during anaphase (Figure 3.3B). Together, these results indicate that measurement of CIN phenotypes using fixed imaging, as is common in retrospective clinical analyses of CIN, may underestimate the incidence of some mitotic defects.

Cytogenetic methods exhibit low sensitivity to ongoing CIN

Mitotic chromosome counts and centromeric FISH are commonly used cytogenetic approaches to measure CIN (89, 121, 249, 251). Chromosome counts detected variation around the modal chromosome count (46 for CAL51s and 47 for MCF10As) in all CIN models and their controls (Figure 3.4A). In several models, in addition to near-diploid aneuploidy there were small fractions of counts consistent with triploid (n=69) or tetraploid (n=92) cells. The variation in chromosome counts only significantly differs from control for the highest rate of CIN generated, the Po condition, in which nearly all cells were affected (Figure 3B). FISH probe counts also had low sensitivity for CIN (Figure 3.4C,D). Nonmodal probe counts were seen at similar levels to control for Br and Pb. Though nonmodal counts were elevated two-fold and three-fold for Mp and Po, the models with the highest level of CIN (based on approximated MDD values), FISH only significantly detected a difference in Mp (Figure 3.4D). In fact, the fraction of non-modal counts was much less than with chromosome spreads, likely because this method only surveys 3 of 23 unique chromosomes, making single chromosome alterations harder to detect. This could be

improved by increasing the number of probes or cells counted. Recent data also suggest a bias in mis-segregation of larger chromosomes (270, 317) which might make it important to survey chromosomes more broadly than possible with interphase FISH. These data suggest that cytogenetics methods are less sensitive than inspection of mitosis at detecting ongoing CIN.

Published bulk transcriptomic and genomic CIN signatures do not reflect ongoing CIN

Transcriptional signatures of CIN such as CIN70 and HET70 (to a lesser extent) are commonly used as a proxy measure to assess CIN from bulk transcriptomic data in tumor samples (189, 318). These are derived indirectly by identifying gene expression that correlates with aneuploidy in tumor samples (CIN70)(187) and karyotype heterogeneity in cell lines (HET70)(189). CIN70 is known to be confounded by proliferation-associated transcription and neither CIN70 nor HET70, to our knowledge, have been tested in inducible models of CIN. To determine if these directly measure induced CIN, we employed these transcriptional measures with our models of ongoing CIN. We performed bulk RNA sequencing and measured CIN70 and HET70 signatures in our models (Table 3.2). To validate our results, we verified that doxycycline addition caused a 4-fold increase of TERF2 expression in the Br condition and a 32-fold increase in PLK4 expression in Pb and MP. In each case, these were among the top differentially expressed genes (Figure 3.5). Turning to CIN scores, we plotted the distribution of all 70 genes in violin plots (Figure 3.6A,B) with the mean representing the score. As illustrated, neither CIN70 nor HET70 was increased in any of the CIN models. In fact, CIN70 decreased slightly in Pb and Mp

models (Figure 3.6A), likely due to a decrease in cell proliferation after centrosome amplification (319). This suggests that these bulk transcriptional scores do not detect ongoing CIN.

In addition to RNA, bulk genomic DNA measures of CIN are proposed to detect characteristic signatures of copy number variation (CNV) from SNP array and genome sequencing data—essentially measuring patterns of aneuploidy (186). These measures characterize the final state of the tumor, which could either arise from an early event in oncogenesis, or through continuous CIN with selection for certain aneuploid clones. In the latter circumstance, bulk DNA would potentially measure CIN. Whole-genome sequencing (~10x coverage) and copy number calling in our models revealed nearly identical copy number profiles between control and CIN-induced groups (Figure 3.6C). We next analyzed recently published CIN signatures (186) in each replicate and clustered the models and controls by signature (Figure 3.6D). CX1 is the predominant CIN signature in all groups. Importantly, it also appeared in control cells. CX1 corresponds to large scale copy number alterations consistent with whole chromosome or chromosome arm mis-segregation, though is only slightly higher in Pb and Po models than in control cells. Surprisingly, CX6 did not differ between controls and induced CIN models, other than Pb, even though it similarly represents whole chromosome and chromosome arm mis-segregation. CX2, which corresponds to impaired homologous recombination (IHR), is modestly elevated with in Pb, Mp, and Po models, though it is also elevated in control MCF10a cells. (Figure 3.6E). CX3 was only elevated in MCF10a control cells. Since our models of CIN are induced over 8-72h, they do not provide sufficient time for extensive cellular

selection, a process that is likely required for these signatures to appear as they are based on the averaged CNVs of the population. Nevertheless, we conclude that the DNA genomic signatures of CIN do not directly measure ongoing CIN of samples. In sum, we find that bulk genomic measures of CIN, whether transcriptomic or genomic, do not directly measure ongoing CIN, even in an ideal context where tumor purity is not at issue.

scDNAseq detects ongoing numerical CIN and enables inference of mis-segregation rates

The analyses above highlight characteristics of optimal CIN measures—they (i) detect all chromosomes, (ii) directly detect CNV variation across cells, and (iii) have high throughput. Single cell DNA sequencing (scDNAseq) meets these characteristics. Even low coverage of reads across the genomes are sufficient to infer copy numbers across all chromosomes. Thus, scDNAseq has been employed to measure cell-cell variation in chromosome copy number and to infer CIN (147, 233). We therefore evaluated scDNAseq as a sensitive measure of CIN in our models.

To evaluate scDNAseq, we sampled 32 single cells per replicate by FACS (Figure 3.7) and included a bulk sample of 500 cells to infer average karyotype. We filtered for quality and inferred large-scale chromosome copy number alterations at 1Mb resolution, resulting in 378 high-quality single-cell copy number profiles (Figure 3.8A). Bulk analyses reveal CAL51 as diploid with a focal 8q amplification; MCF10A cells also had 8q plus gains of 1q, 5q, and recurring sub-clonal gains of Xq. To quantify chromosomal deviations, we evaluated the absolute difference between each single-cell karyotype and the modal karyotype inferred from bulk samples. Both controls—CAL51 and MCF10A—had a small

number of deviations from modal karyotype (Figure 3.8B). We did not detect a clear increase in chromosomal deviations in the Br model. This could be due to 1) resolution of chromatin bridges, 2) chromosome breakages resulting in structural variation, but conserved copy number, which would be undetectable by low coverage scDNAseq, or 3) segmental copy number changes smaller than 50% of the chromosome. However, we ruled out the latter possibility using an alternative analysis to detect telomere proximal breaks resulting from breakage of bridging chromosomes, which produced no significant results (Figure 3.9). We found a modest increase in non-modal chromosomes with the Pb model and significant increases in the Mp and Po models, which average about 5-6 deviations per cell respectively (Figure 3.8B). The percentage of cells with deviations from the mode followed a similar trend, though also detects a small increase in the Br model that is not statistically significance (Figure 3.8C). As expected, the Mp model displayed a significant bias of chromosome losses over gains (Figure 3.8D)—this is expected since division of duplicated chromosomes into 3+ daughter cells reduces chromosome number. Other models showed no such bias with gains/losses being roughly equal. Taken as a whole, these data support scDNAseq as a sensitive method for detecting CIN.

Single-cell resolution may enable detection of CIN signatures (186), so we repeated our previous analysis using the single cell copy number profiles. Again, the proposed whole/arm mis-segregation signature, CX1, was the predominant among the groups (Figure 3.10). However, this relative activity of this signature between groups did not correspond to CIN as observed by microscopy or by directly measuring whole-chromosome copy number alterations. CX6, the other proposed whole/arm mis-segregation

signature had much lower activity among groups and did not correspond to observed CIN. Interestingly, despite their low activity, the only signatures that seemed to reflect the observed trend were decreasing CX4 and increasing CX8, proposed signatures of whole genome doubling and replication stress respectively. This analysis suggests that these measures of CNV at single cell resolution do not well characterize ongoing CIN (Figure 3.10).

Because the fitness levels imparted by different karyotypes can be acted on over time by natural selection, the absolute number of chromosomal deviations in a population may not capture CIN in its entirety. We recently addressed this issue and developed a computational framework to infer mis-segregation rates from scDNAseq datasets using approximate Bayesian computation (ABC), a method to statistically relate biological and simulated data (147). This relies on establishing a phylogenetic tree of single cells and measurements of indexes describing this tree from experimental and simulated data. ABC infers biological parameters from the simulation parameters that produce similar phylogeny.

To employ ABC, we characterized the populations with summary indexes: aneuploidy (average sub-clonal variance within karyotypes), mean karyotype variance (MKV; average variance within chromosomes across the population), and the Colless index, a metric of the imbalance of phylogenetic trees reconstructed from cells' copy number profiles, an indication of ongoing selection (229, 230) (Figure 3.8E-G). As expected, our CIN models increased aneuploidy and all but Br increased MKV compared with controls (Figure 3.8E,G). Further, Colless index decreased indicating a low level of selection is at place

after CIN induction (Figure 3.8F). This likely reflects the lack of selection over the short-time of the experiment (8-72h); by contrast, the control population has been under long-term selection and has higher Colless. Together, the summary statistics enable inference of mis-segregation rates by ABC.

We next applied ABC to infer chromosome mis-segregation rates. First, we performed dimensionality reduction, which verified that the biological data falls within the 'summary space' of the simulated data (Figure 3.8H). Inferring mis-segregation rates (taken as the average of the posterior rate distributions) revealed a wide range across models from 0.3-11.5 MDD (316, 320). There was only a 2-fold increase in mis-segregation rate in the Br model of bridging chromosomes: CtrlC and Br showed mis-segregation rates of 0.12±0.07 and 0.28±0.02 MDD respectively**.** CtrlM cells had inferred mis-segregation rates at about 0.83±0.64 MDD while the Pb, Mp, and Po models had much higher mis-segregation rates of about 5.37±0.46, 6.53±1.27, and 11.30±1.83 MDD respectively (Figure 3.8I). In comparison, the approximated mis-segregation rates of in RPE1 cells is 0.01-0.05 MDD and for U2OS, 0.33-0.46 MDD (316). These rates compare favorably with the number of deviations measured directly from whole chromosome copy number data, particularly when accounting for the partial induction of CIN over 8 hours with the Po model (Figure 3.8B). They similarly compare with MDD values approximated for each model by imaging methods (Figure 3.8L,M). Further, joint posterior distributions reflect lower apparent evidence of ongoing selection in the Po model, as compared to the other models, in concordance with the short timespan of CIN induction (Figure 3.8J). The mis-segregation rate observed in the Mp model, when taking into account the penetrance of

the phenotype, agrees with previously observed mis-segregation rates caused by multipolar divisions (147).

We conclude that CIN can be measured several ways using single cell copy number profiles. Copy number alterations can be calculated directly, particularly if the period of CIN is relatively short, in which case karyotype selection is not a significant factor. Inferring chromosome mis-segregation rates by comparing to simulated data works in both short and long time periods, though it is ideal for long time periods when karyotype selection becomes a strong confounder.

Concordance and performance of CIN measures

To assess and summarize the performance of CIN measures, we performed standardized effect size and pairwise correlation analyses. As expected, fixed immunofluorescence, time lapse, non-modal mitotic chromosome, and centromeric probe counts were significantly correlated ($\alpha = 0.01$), excepting the pair of fixed imaging and chromosome counts (Figure 3.11A). By contrast, bulk transcriptional CIN signatures (CIN70, HET70) did not correlate to imaging, nor cytogenetics, nor between themselves. Considering genomic signatures on bulk (CX1, CX6 bDNAseq), and with single cell data (CX1 scDNAseq; CX6 scDNAseq), these also correlated poorly with one another with the exception of single-cell CX1 and CX6. Interestingly, the CIN signature CX1, when measured in bDNAseq data, did modestly correlate with time-lapse imaging, but not fixed imaging. HET70 negatively correlated with the CX1 and CX6 signatures in single cells. This seemed to be a cell line-dependent effect as MCF10A cells had relatively high HET70 expression and low CX1 and CX6 signature activity than CAL51, regardless of CIN model (Figure 3.12). scDNAseq

chromosomal analyses performed well whether they considered whole-chromosome deviations from mode or inferred MDD from ABC—not only do these correlate with each other, but also with fixed and time lapse imaging quantifications of defect rate and approximate mis-segregation rates, and with FISH analyses. We conclude that the single cell analyses perform well for measuring rates of ongoing CIN.

We next turned to effect size, Hedge's *g*, which allows us to compare sensitivity of different measures (Figure 3.11B). Average standardized effect sizes across all CIN phenotypes were high among the imaging methods, followed closely by inferred MDD using scDNAseq and ABC. CX1 measured by bDNAseq was similarly high, though, as noted previously, these scores do not reflect observed CIN levels by imaging or single-cell sequencing. The average effect sizes for whole chromosome deviations measured by scDNAseq and non-modal centromeric FISH measurements were similar while those for putative CIN signatures CX6 as measured by bulk or single cell DNAseq and CX1 as measured by single cell DNAseq were middling. Transcriptional measures of CIN (CIN70 and HET70) and CIN measured by mitotic chromosome counts exhibited the lowest effect sizes. We conclude that highly sensitive quantitative measures of CIN can be achieved by direct microscopy or by scDNAseq combined with inference of rates by ABC.

In summary, our data compare proposed and widely used measures of CIN on simplified models where CIN is induced. Paradoxically these exhibit vastly different capabilities in detecting CIN. Direct observation of CIN by imaging is the most sensitive and reliable followed by scDNAseq measures and cenFISH. By contrast, transcriptional CIN scores, mitotic chromosome counts, and statistically derived CIN signatures, regardless of bulk

or single cell resolution, were far less capable in measuring ongoing CIN terms of effect size and correlation with other measures.

DISCUSSION

Ongoing CIN is defined by an elevated rate of chromosome mis-segregation, which varies across tumors and depends on the penetrance and error frequency of specific CIN mechanisms. The intrinsic rate of mis-segregation in a cell population produces functional consequences for tumorigenesis, cancer progression, and treatment response. Low mis-segregation rates limit tumorigenesis, presumably due to reduced adaptive potential, while high mis-segregation rates have the same effect through loss of necessary genetic material. Moderate mis-segregation rates promote tumorigenesis. Once a tumor has formed, patients whose tumors exhibit moderate to high intrinsic rates of mis-segregation tend to have poorer clinical outcomes. Though, breast cancer patients whose tumors exhibit high mis-segregation rates tend to have a more durable response to paclitaxel due a reduced capacity for correcting attachment errors and multipolar mitotic spindles produced by the drug. Despite the clinical significance of CIN and its relative severity across tumors, its measurement is not currently used to guide patient care (235, 237, 245, 246, 251).

The reason CIN is not measured for clinical use is ultimately due to three factors: accessibility, scalability, and sensitivity. In reviewing the CIN measures tested in this study, we find varying levels of accessibility and scalability (Table 3.3). Some measures are clinically accessible in terms of necessary equipment and reagents, but they do not easily scale in time required for sample preparation or data acquisition. For example, fixed

imaging is commonplace for pathological assessment of tumors. In this study, fixed immunofluorescence imaging was among the most sensitive methods to detect ongoing CIN. However, the quantification of CIN phenotypes in these samples is not scalable as data acquisition requires substantial time commitments and sampling a sufficient number of mitoses requires highly proliferative tumors, such as diffuse large B-cell lymphoma (237). Karyotypes and chromosome counts are not readily possible in patient tissues, as they require a large number of mitotic cells, not easily obtained by culturing tumor tissues. Likewise, time lapse imaging is not possible directly in patient tumors, and is laborious, time-consuming, and expensive even with *ex vivo* culture, fluorescent labeling, and imaging of patient organoids.

Measures of CIN based on bulk genomic and transcriptomic sequencing are attractive due to the wide availability of shared high-throughput sequencing data, and because they are already in routine clinical use. However, bulk sequencing failed to detect ongoing CIN in any of our phenotypic models. This is likely because, despite the misleading nomenclature, bulk sequencing measures detect RNA or DNA levels averaged across many cells and thus establish an average aneuploid state, without the ability to detect cell-to-cell differences in chromosome copy numbers. One fundamental problem in the field of genomic integrity is that CIN and aneuploidy are often conflated. To be fair, aneuploidy is a product of prior mis-segregation events, providing a rationale to infer a degree of CIN from the current degree of aneuploidy in a tumor. We can describe this as *historical CIN*, which represents an accumulation of prior chromosome gains/losses and cellular selection. However, this does not permit inference of ongoing chromosome gains or

losses because any degree of aneuploidy could, in fact, be a product of a single event that was not repeated. By contrast, *ongoing CIN*, described here, is a process in which there are ongoing aberrations over multiple cell divisions, which is associated with metastasis and response to microtubule-targeted therapies (235, 237, 245, 246, 251).

The *de novo* karyotype heterogeneity in cell populations with ongoing CIN does not significantly alter the predominant karyotype and is not detected by bulk genomic CIN signatures (e.g., CX1 and CX6). This demonstrates that these signatures detect historical aneuploidy rather than ongoing CIN. Nor do the gene expression states of new aneuploid clones significantly alter the predominant transcriptional phenotype with respect to previously established transcriptomic CIN scores (CIN70 and HET70). As for the CIN70 score, this result was unsurprising for two reasons — 1) the derivation of CIN70 was based on the fundamental assumption that aneuploidy is derived by CIN and 2) CIN70 is confounded by upregulation of proliferative genes, as aneuploidy, proliferation, and advanced tumor grade are all co-variates. Further this result comports with previous findings (189, 321). MCF10A cells scored slightly higher on HET70 than CAL51. While this may represent cell line specific gene expression, we note that the scDNAseq data shows MCF10A cells exhibiting higher karyotype heterogeneity than CAL51 at baseline, despite exhibiting similar rates of mitotic errors during imaging. Thus, while HET70 scores did not respond to induced CIN and karyotype heterogeneity, we cannot rule out that HET70 detects a pre-existing transcriptional phenotype that is tolerant of aneuploidy and increased karyotype heterogeneity. However, while HET70 did not detect induced, ongoing CIN in any of our models, MCF10A cells did score higher on HET70 than CAL51. While this may

represent cell line specific gene expression, we note that the scDNAseq data shows MCF10A cells exhibiting higher karyotype heterogeneity than CAL51 at baseline, despite exhibiting similar, if somewhat lower rates of mitotic errors during imaging. Although HET70 scores did not increase with induced CIN and karyotype heterogeneity, we cannot rule out that HET70 detects a transcriptional phenotype that correlates with aneuploidy tolerance.

As a clinically accessible alternative to imaging, scDNAseq provides the best measure of CIN in terms of sensitivity and correlation to both fixed and time lapse imaging. CIN can be measured by quantifying the absolute number of chromosomal deviations from the modal (i.e., clonal) karyotype of a population. Additionally, the rate of mis-segregation resulting in a given population of single cell copy number profiles can be measured by pairing computational modeling and statistical inference. Both analysis methods performed well in measures of ongoing induced CIN over relatively few cell divisions. However, we have previously found that the latter, inference of CIN, performs better in the context of longer time scales, such as the growth of a tumor (147). While single-cell sequencing is not currently used in clinical care, major advances in ultra-high-throughput sequencing will likely make low-coverage scDNAseq accessible at clinical capacity (220, 322, 323). Toward this end, we estimated that ~200 cells are needed for accurate measurement of CIN (147). Although we did not detect increased segmental copy number alterations caused by bridging chromosomes in our inducible model, further advancement of sequencing technology and scDNAseq methods may enable more robust detection of copy-neutral structural variation in single cells. Importantly, the measurement of structural

CIN using scDNAseq would require relatively uniform coverage of the entire genome, which is not provided by mutation panels. For intact tumors, it would be important to distinguish the genome structures of tumor cells from stromal cells, which could be accomplished by simultaneously detecting cancer-specific mutations.

One limitation of this study is that we measured CIN in cell-line models a short time after inducing CIN. This approach is ideal to ensure ongoing CIN, but we cannot rule out that methods that failed in these models would correlate with ongoing CIN after cellular selection or would indicate a permissive cellular context for ongoing CIN. For example, although we found that cenFISH only detects the highest levels of CIN in our system, we cannot rule out that this method becomes more sensitive over several generations with elevated CIN, which would increase the probability that one of a limited set of probes would detect an alteration. Further, in this study, we did not evaluate single cell RNAseq (scRNAseq) as a method of measuring CIN. Currently, there are no widely used scRNAseq-based measures of CIN and we did not seek new methods of CIN measurement. However, given the preponderance of evidence of the transcriptional consequences of CIN and aneuploidy (200, 201, 204, 324–326), it is conceivable that robust transcriptional CIN signatures could be derived at single cell resolution. Whether these would reflect gene dosage, a general response to CIN or would be phenotype/mechanism-dependent is unclear. In any case, the reliability of these measures could be limited by dosage compensation (327–331). Although we could select specific genes unaffected by compensation, the sparse data with current scRNAseq platforms remains a challenge. On the other hand, large-scale DNA copy number alterations can be inferred from

scRNAseq data (209, 210), which would provide an additional dimension of single cell genomic data and perhaps increase the reliability of a measure of CIN based on single cell chromosome copy number data.

This work provides a thorough empirical analysis of the relative capability of current CIN measures to detect ongoing CIN across specific, inducible phenotypic models of CIN. We find current measures differ in their ability to detect ongoing CIN and that some fail to reliably detect CIN at all. Imaging approaches are the most sensitive and reliable. Cytogenetic approaches have low sensitivity, only significantly detecting the model which had among the highest mis-segregation rates. Bulk genomic and transcriptomic measures do not reflect ongoing CIN while single cell genomic methods, particularly the inference of mis-segregation rates, offer both sensitivity and potential for clinical accessibility. In light of these conclusions, we recommend single-cell genomics with Bayesian inference as the best method for further development of a clinically accessible measure of CIN. Importantly, the models and data generated here serve as a resource for investigators seeking to validate innovative measures of ongoing CIN from bulk and single-cell sequencing.

MATERIALS AND METHODS

Cell line derivation and cultivation conditions

MCF10A-PLK4-WT-tetOn cells were kindly provided by the laboratory of Dr. David Pellman (332). We used lentiviral transduction to stably express H2B-mNeonGren and mScarlet-α-Tubulin. CAL51 cells were obtained from DSMZ-German Collection of Microorganisms and Cell Cultures and CAL51-TERF2-DN-tetOn was generated using retroviral transduction of pCMV Retro TetO into which we cloned the TERF2-DN mutant sequence

(Addgene, 16069) and an mScarlet reporter. To make retrovirus, we transfected 293T cells then transduced CAL51 cells expressing TetR for ~18 hours with 4 ug/mL polybrene. We selected with puromycin (2 ug/mL) and sub-cloned in 96-wells to generate monoclonal lines. All cell lines were tested and free from mycoplasma contamination prior to study.

Cells were maintained at 37°C and 5% CO_2 in a humidified, water-jacked incubator and propagated in either Dulbecco's Modified Eagle's Medium (DMEM)/High Glucose (Cytiva Hyclone, SH3024301) for CAL51 cells or mammary epithelial basal media for MCF10A cells, consisting of DMEM/F12 (Cytiva Hyclone, SH3026101), 5% horse serum (Gibco, 16050122), 20 ng/mL EGF (Peptrotech, AF-100-15), 0.5 mg/ml hydrocortisone (MP Biomedicals, 0219456901), 100 ng/ml cholera toxin (Enzo Life Sciences, BMLG1170001), and 10 ug/ml insulin (Millipore Sigma, I9278). All growth media is supplemented with 10% fetal bovine serum (GeminiBio, 900-108),100 units/mL penicillin-streptomycin (Gibco, 15070063), and plasmocin prophylactic (Invivogen, ant-mpp) to a final concentration of 5 ug/mL.

Statistical Analyses

Statistical analysis was completed in R/Rstudio (v4.2.3/v1.2.5019) (333, 333). Unless otherwise specified, statistical significance between group means is determined using two-tailed, two-sample Student's *t*-tests and $\alpha = 0.05$ over at least 3 biological replicates.

Fixed immunofluorescence microscopy

Cells were re-seeded on sterile glass #1.5 cover slips (Fisher, 12-545-81P) at 40% and grown to ~70-80% over 18-24 hours. Coverslips are rinsed in warmed (37°C) PBS (x1) before fixation in warmed 4% paraformaldehyde (PFA) in PHEM buffer (120 mM PIPES,

50 mM HEPES, 20 mM EGTA, 4 mM $MgSO_4$ in pure water, pH 7.0) for 10 minutes. Coverslips are rinsed of fixative (x3), extracted with 1% NP40 in PHEM buffer for 15 minutes, and blocked with 3% bovine surum albumin (BSA)(Millipore Sigma, A2153) and 0.1% Triton X-100 in PBS (BSA + PBSTx) for 30 minutes. Primary and secondary antibodies were pooled separately in BSA + PBSTx. Coverslips were incubated with primary antibodies for 1 hour at room temperature, rinsed (x3) in PBSTx, then incubated with secondary antibodies for 30 minutes, and rinsed (x3) again in PBSTx. Coverslips were counterstained with 10 ug/mL DAPI (Sigma-Aldrich, 62248), mounted on glass slides with Prolong Dimaond anti-fade medium (Molecular Probes, P36970), and cured for 48 hours. Cells were immunostained to visualize α-tubulin (Primary — 1:1000 mouse (γ1) anti-α-tubulin (DM1A)(Invitrogen, 14-4502-82, RRID: AB_1210456; Secondary — 1:350 goat anti-mouse (γ1) + Alexa Fluor 750 (Invitrogen, A-21037, RRID: AB_2535708) for CAL51 cells or goat anti-mouse (H+L) + Alexa Fluor 555 (Invitrogen, A-11001, RRID: AB_2534069) for MCF10A cells) and pericentrin (Primary — 1:1000 rabbit anti-pericentrin (Abcam, ab4448); Secondary — 1:350 chicken anti-rabbit (H+L) + Alexa Fluor 647 (Invitrogen, A-21443, RRID: AB_2535861) for CAL51 cells or goat anti-rabbit (H+L) + Alexa Fluor 488 (Invitrogen, A-11008, RRID: AB_143165) for MCF10A cells)

Image acquisition was performed on a Nikon Eclipse Ti inverted microscope equipped with motorized stage, LED epifluorescence light source (Spectra X), 60x/1.4NA (Plan Apo) DIC oil immersion objective, and ORCA Flash4.0 V2+ digital sCMOS camera (Hamamatsu). Optical sections were taken at 200-nm intervals and deconvolved using the LIM 3D

Deconvolution module in Nikon Elements. Micrograph montages were prepared in Affinity Designer.

For analysis, mitotic phenotypes of all mitotic cells observed in metaphase, anaphase, or telophase were recorded until at least 50 metaphase cells were counted or until all four coverslips were expended. Exceptions are replicate 2 of Po, with 10 metaphase cells and 137 anaphase and telophase cells, replicate 3 of CtrlM with 30 metaphase cells and 21 anaphase and telophase cells, and replicate 3 of Pb, with 11 metaphase cells and 3 anaphase and telophase cells. Data from these replicates were retained and reported as the alternative measures of the replicate provided sufficient information.

Time lapse fluorescence microscopy

Cells were re-seeded in 4- or 8-well chamber slides (Ibidi, 80426) at 40% and grown to ~70-80% over 18-24 hours. At the time of re-plating, CAL51-TERF2-DN-mCherry-TetOn cells were transduced with adenovirus to express β-tubulin-mScarlet + P2A-H2B-NeonGreen to visualize mitotic spindles and DNA. They were then imaged on a Nikon Ti-E2 inverted fluorescence microscope outfitted with a Yokogawa CSU-W1 spinning disk confocal scanning unit. Images were collected every 2.5 minutes for 4-12 hours with a 20x/0.5NA (P Fluotar) objective and an ORCA Flash 4 digital sCMOS camera (Hamamatsu). Environmental control was maintained by a humidified, stage-top chamber (Tokei Hit) set to 37°C and 5% CO_2. Micrograph montages were prepared in Affinity Designer.

For analysis, at least 20 cells for each replicate and each CIN model were tracked from nuclear envelope breakdown through to cytokinesis and mitotic phenotypes were recorded for metaphase, anaphase, and telophase. Exceptions are replicate 1 of CtrlC,

with 17 cells, and replicate 5 of Pb, with 18 cells. Data from these replicates were retained and reported as the alternative measures of the replicate provided sufficient information.

Imaging-based approximation of mis-segregations per diploid division (MDD)

MDD was approximated using fixed immunofluorescence and time lapse fluorescence imaging data as well as the formula $\mathrm{MDD} = (\frac{\text{Errors per Defect} \times \text{Defect Rate} \times \text{Penetrance}}{\text{Modal Chromosomes}}) \times 46$, as previously described (316).

To derive the values for this formula, we made the following assumptions: 1) Lagging and bridging chromosomes are assumed to produce 1 mis-segregation; 2) Polar chromosomes are assumed to produce 7.8 mis-segregations as we observed cells treated under the Po model (prior to anaphase onset) had an average of 15.6 polar ACA foci (Figure 3.3A); 3) Pseudobipolar spindles do not produce mis-segregation events; 4) Multipolar spindles are assumed to produce 18 mis-segregations based on Lynch et al. 2022; 5) CAL51 cells have 46 chromosomes and MCF10A cells have 47 chromosomes; 6) The penetrance of each observed CIN phenotype is 100% (i.e., 100% chance the defect results in mis-segregation). The fraction of cells with polar chromosomes represents metaphase cells wherein they are most readily detectable. All other CIN phenotypes are taken from anaphase or telophase cells.

Cytogenetics

Cells were re-seeded in T75 flasks at 40% and grown to ~70-80% density over 18-24 hours prior to harvest. For Po, AZ3146 was washed out at T-0 hours and harvest performed at T+24 hours. Colcemid (Millipore Sigma, 234109) was added to a final concentration of 50 ng/mL and incubated for 2 hours to enrich mitotic cells. We retained the

media and trypsinized cells, rinsing once in warm PBS. Cells were resuspended and swelled for 5 minutes in 75 mM KCl with 10 drops of Carnoy fixative (3:1 methanol:glacial acetic acid). This was followed by three successive resuspensions in Carnoy fixative, after which, samples were stored at -30°C then cells were dropped onto slides and dried in a drying chamber. For analysis, at least 50 mitotic chromosome spreads were counted for each replicate of each model with the exception of a replicate of CtrlC, with 2 biological replicates, the Mp model, which exhibited a relatively few mitotic cells in each biological replicate (18, 32, and 35 mitotic chromosome spreads). Data from these replicates were retained and reported as the alternative measures of the replicate provided sufficient information.

Fluorescence in situ hybridization (FISH) enumeration of chromosomes 3, 4, 7, 9, 10, and 17 was completed using the following 2 probe mixes: Vysis CEP 3 (D3Z1) labeled SpectrumOrange (Vysis, 06J3613) localizing to 3p11.1-q11.1, Vysis CEP 7 (D7Z1) labeled SpectrumAqua (Vysis, 06J5427) localizing to 7p11.1-q11.1, Vysis CEP 9 labeled SpectrumGreen (Vysis, 06J3719) localizing to 9p11-q11 in IntelliFISH hybridization buffer (Vysis, 08N8701), and Vysis CEP 4 labeled SpectrumGreen (Vysis, 06J3714) localizing to 4p11-q11, Vysis CEP 10 labeled SpectrumAqua (Vysis, 06J5420) localizing to 10p11.1-q11.1 and Vysis CEP 17 (D17Z1) labeled SpectrumOrange (Vysis, 06J3697) localizing to 17p11.1-q11.1 in IntelliFISH hybridization buffer (Abbott Molecular, Des Plaines, IL). Slides were aged for 2 minutes in 2xSSC at 74°C and put through a dehydration ethanol series (70%, 85%, and 95%). Slides and probe were codenatured by heating at 80°C for 2 minutes using a ThermoBrite instrument (Abbott Molecular). Hybridization was

performed overnight at 37°C. Finally, the slides were mounted with Vectashield containing DAPI (Vector Laboratories). Localization of the probes was confirmed on pooled cytogenetically normal blood controls. For analysis, at least 100 interphase cells were counted per 3-probe set.

Single-cell DNA sequencing and analysis

Single cell DNA sample preparation

Cells were re-seeded in 6-well plates at 40% and grown to ~70-80% density over 18-24 hours prior to harvest. Cells were washed with HBSS, trypsinized, pelleted, and washed by resuspension in wash buffer (2% FBS in 1x PBS). Pelleting once more, cells were resuspended in 500 µL wash buffer and fixed by dropwise addition to 4.5 mL 80% ethanol. Samples were stored at -30°C.

Flow cytometry and fluorescence activated cell sorting

Fixed cell suspensions were pelleted and resuspended in wash buffer containing 10 µg/mL DAPI. Single cells or bulk samples (500 cells) were sorted by FACS (BD FACS AriaII), gating on 0.5-1.5x the DAPI signal intensity of the G1 peak, through a 130 µm low-pressure deposition nozzle into 96 well PCR plates containing 10 µL 1x prepared Cell Lysis and Fragmentation Buffer Mix (Millipore Sigma, WGA4). Doublets were excluded from analysis via standard FSC/SSC gating procedures. DNA content was analyzed via DAPI excitation at 355 nm and 450/50 emission using a 410 nm long pass dichroic filter. Gating for cell sorting was defined by 0.5x/1.5x (lower/upper) the DAPI intensity of the G1 peak. After sorting, the PCR plates were immediately centrifuged at 100 x g for 1 minute before library preparation. Plates were kept at 4°C when not on the cell sorter.

Single cell DNA library preparation

Initial cell lysis, genomic fragmentation, and genomic amplification reactions were done with the GenomePlex® Single Cell Whole Genome Amplification Kit (Millipore Sigma, WGA4). Initial genomic library distributions were assessed on a 1.5% agarose gel and purified using a ZR-96 Genomic DNA Clean & Concentrator-5 Kit (Zymo Research, D4067). Library concentrations were quantified using the Quant-iT™ dsDNA Broad Range Assay Kit (Invitrogen, Q33130) and normalized before additional preparation. Genomic libraries were enzymatically fragmented to ~250 bp, 5'-phosphorylated, 3'-dA-tailed, and index adaptor-ligated with the sparQ DNA Frag & Library Prep Kit (Quantabio, 95194). Ligated adaptors were standard P5 and custom uniquely indexed P7 illumina adaptors described previously (302). Indexed libraries underwent eight additional amplification cycles, purification with Axygen® AxyPrep MAG PCR Clean-Up beads (Corning, MAG-PCR-CL), and DNA concentration quantification as above. Up to 96 libraries with unique indices were pooled in equimolar concentrations. Library quality was validated on an Agilent TapeStation and concentration was measured via Qubit 2.0 fluorometer and qPCR.

Single cell sequencing and data pre-processing

Paired-end bulk RNA sequencing (2x150bp) was performed on an Illumina HiSeq sequencer and demultiplexed using Illumina bcl2fastq (v2.20). Reads were trimmed of adaptor sequences, quality filtered, and de-duplicated in fastp (v0.23.2) and aligned to reference sequence hg19 with bowtie2 (v2.3.5). Format conversions were performed with samtools (v1.9) and bedtools (v2.29.2).

Single cell copy number calling

Copy number calls were performed in a local installation of Ginkgo (303) with a variable bin size of ~2.5 Mb using global segmentation. Minimum ploidy was set to 1.35 and maximum ploidy to 3 to reflect our flow cytometric gating strategy for FACS. Whole chromosome copy numbers were estimated by taking the mode of copy numbers across genomic bins for each chromosome. Thus, even sub-chromosomal gains and losses of greater than 50% of a chromosome should remain detectable.

Quantification of single cell CIN signatures

We quantified previously published putative CIN signatures from Drews et al. 2022 using resources made publicly available in a github repository by the authors (https://web.archive.org/web/20220615195321/https://github.com/markowetzlab/CIN-SignatureQuantification). We used the function 'quantifyCNSignatures' in the available R package CINSignatureQuantification (186) to call signatures from unrounded segment copy number matrices derived using Ginkgo, as described above and report the normalized, unscaled signature activity levels to avoid masking the relative activity of each signature.

Inference of mis-segregation rates

We used agent-based simulation and approximate Bayesian computation to infer mis-segregation rates from scDNAseq data. Agent-based simulation of CIN and karyotype selection in growing populations was performed in NetLogo (v6.0.4) (298) and approximate Bayesian computation was performed using the R (v4.2.2) (333) using the abc package (v2.1)(281) as previously described (147).

Agent based simulation. We initiated simulated populations with 100 diploid cells and evolved exponentially growing populations using a pseudo-Moran process to reduce computational demands (a random 50% of cells are culled when the population surpasses 3000 cells). Euploid cells had a 50% chance to divide at every step, a probability that is modified according to a cell's fitness level. We used a karyotype selection scheme that emulates stabilizing selection by negatively selecting genetically unbalanced karyotypes. The contribution of each chromosome to karyotype selection is dependent on the abundance of genes it encodes. We simulated populations using the following parameters: MDD = [0, 0.046, 0.092, …, 46], S = [0, 1, 2, …, 200], Time Steps = [0, 1, 2, …, 100]. We assumed whole-chromosome mis-segregation and that chromosome copy numbers below 1 and above 7 would result in cell death. Accordingly, as cells divide and mis-segregate chromosomes, more aneuploid cells with more unbalanced karyotypic stoichiometries are less likely to continue division. A random selection of 300 karyotypes is exported to measure summary statistics at each time step. Each combination was repeated 3 times for a total of 1,006,005 independent simulations. See Lynch et al. 2022 for additional details.

Population summary statistics. To summarize the characteristics of karyotypes from simulated populations and scDNAseq data, we quantified three features: aneuploidy, mean karyotype variance (MKV), and Colless index. Aneuploidy was quantified as the mean variance of copy numbers within each cell's sub-clonal karyotype (normalized to the modal karyotype). MKV was quantified as the mean variance of copy numbers for each chromosome across the population. Colless index was measured using the R

package phyloTop (v2.1.1)(300) and was normalized to the number of leaf tips. Phylogenetic trees for measuring the Colless index were reconstructed from chromosome copy numbers by computing Euclidean distance matrices and hierarchical clustering using complete linkage, both in the R stats package (v.4.2.3)(333). Hierarchical clustering may not produce the same results every time, and rare, highly different dis-similar observations can drastically skew Colless indices, both of which result in measurement noise. To reduce this noise we, we permute the copy numbers of individual homologous chromosomes (i.e., a population's copy numbers for chromosome 1 are permuted separately from those of chromosome 2) across the population and repeat this Colless index measurement, taking the average of 200 iterations. This preserves phylogenetic imbalance for populations with sub-clonal alterations but reduces imbalance for those with a rare highly dissimilar karyotype, resulting in a stable and reproducible measure. Also, because hierarchical clustering requires at least 3 observations, we removed all simulated datasets that failed to maintain at least 3 cells, which could occur when high mis-segregation rates force cells past the pre-defined lethal chromosome copy number thresholds (1 to 7), promoting population collapse.

Approximate Bayesian computation. Parameter inference of mis-segregation rates and selection pressure from scDNAseq data was performed with approximate Bayesian computation using our simulated dataset as a prior dataset. We used the R package abc (v2.1) (281) to complete the analysis with rejection sampling and a tolerance threshold of 0.01. We chose independent prior datasets that best matched each control and experimental group. For example, we assigned control groups a prior dataset that encompassed 30-50

time steps (i.e., 15-25 generations) to reflect the number of passages after mono-clonal culture. Groups with doxycycline-induced CIN were assigned a prior dataset with ≤ 4 time steps (2 generations) to encompass about 48 hours of growth with fully penetrant CIN induction (this assumes induction of the tetOn constructs takes about 24 hours to become fully induced). The polar chromosome model (Po), which was induced using sequential chemical treatments and enrichment of about 50% of the population, was assigned a prior dataset with ≤ 2 time steps (1 generation).

Bulk DNA sequencing and analysis

Bulk sample and library preparation

Sample preparation, sorting, and bulk DNA library preparation were prepared in parallel with and in the same manner as single-cell DNA samples. 500 cells were sorted for each bulk DNA sample.

Bulk DNA sequencing and data pre-processing

Paired-end bulk DNA sequencing (2x150bp) was performed on an Illumina HiSeq to ~10x coverage and demultiplexed using Illumina bcl2fastq (v2.20). Sequencing reads were adaptor-trimmed, filtered, de-duplicated, and aligned to hg19 with the Illumina DRAGEN Bio-IT Platform using default settings.

Bulk copy number calling

Bulk DNA copy numbers were called in R using QDNAseq (v1.34.0) (334) and a bin size of 30 Kb. Segment copy numbers were called using bin copy numbers smoothed over 2 bins and Anscombe transformed (transformFun = “sqrt” in the ‘segmentBins’ function).

Quantification of CIN signatures

Putative CIN signatures were derived from bulk copy number profiles and reported in the same manner as for single cell DNA copy number profiles as described above.

Bulk RNA sequencing

Bulk RNA sample preparation

Cells were re-seeded in 6-well plates at 40% and grown to ~70-80% density over 18-24 hours prior to harvest. Media was removed from cells and immediately lysed with TRI Reagent (ThermoFisher Scientific, AM9738) to preserve RNA, which was stored at -80°C. Total RNA was isolated using Zymo Direct-zol RNA MiniPrep kit (Zymo Research, R2050) and the concentration and quality were assessed with a Qubit 2.0 fluorometer and Agilent TapeStation respectively.

Bulk RNA library preparation

RNA libraries were prepared using the NEBNext Ultra II RNA Illumina Library Prep Kit (New England Biolabs, E7775) and mRNAs were enriched with oligo-d(T) beads then fragmented for 15 minutes at 94°C prior to first and second strand cDNA synthesis. cDNAs were end-repaired, 3'-adenylated, ligated with universal Illumina adapters and unique index sequences, then enriched by PCR. Library quality was validated on an Agilent TapeStation and concentration was measured via Qubit 2.0 fluorometer and qPCR.

Bulk RNA sequencing, data pre-processing, and analysis

Paired-end bulk RNA sequencing (2x150bp) was performed on an Illumina HiSeq sequencer and demultiplexed using Illumina bcl2fastq (v2.20). Demultiplexed reads were trimmed of universal Illumina index sequences with BBMap's bbduk (v38.95) (335). We

aligned trimmed reads to reference sequence hg19 and generated fragment count matrices in R/Rstudio (v4.2.3/v1.2.5019) (333, 336) using Rsubread (v2.4.3) (337). Library size normalization and dispersion estimation was performed in edgeR (v.3.32.1) (338) while linear modeling and differential expression analysis was performed in limma (v3.46) (339, 340).

ACKNOWLEDGMENTS

We thank the University of Wisconsin Carbone Cancer Center (UWCCC) Shared Resources funded by the UWCCC Support Grant P30 CA014520 – Flow Cytometry Core Facility (1S10RR025483-01), Cancer Informatics Shared Resource, Small Molecule Screening Facility. Thanks also go to the Wisconsin State Laboratory of Hygiene for cytogenetic expertise and support, Dr. Rob Lera for microscopy assistance, and members of the laboratories of Drs. Mark Burkard, Beth Weaver and Aussie Suzuki for many productive discussions.

COMPETING INTEREST STATEMENT

MEB declares all interests without adjudicating relationship to the published work. He is on the medical advisory board of Strata Oncology, receives research funding from Abbvie, Genentech, Puma, Arcus, Apollomics, Loxo Oncology/Lilly, and Elevation Oncology, and holds patents on a microfluidic device for drug testing and for homologous recombination and super-resolution microscopy technologies.

All other authors report no conflicts of interest.

CODE AND DATA AVAILABILITY

Scripts and data used for data analysis and visualization will be freely available on Open Science Framework and sequence data will be deposited to NCBI SRA and GEO prior to final publication.

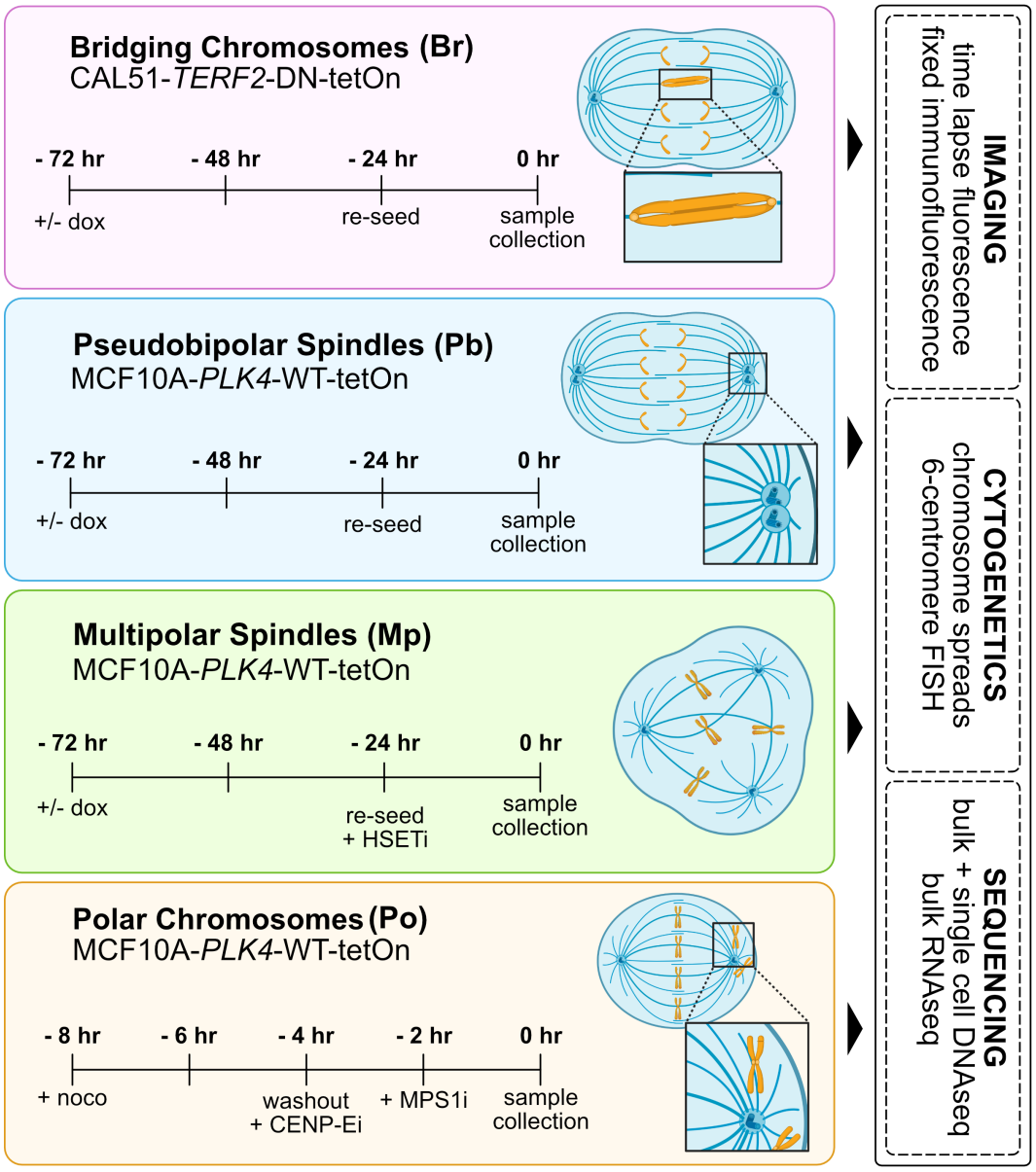

Figure 3.1 — Multimodal analysis of specific and inducible CIN phenotypes

Schematic showing genetically and chemically inducible models of CIN phenotypes and subsequent CIN measures employed. Bridging chromosomes (Br) are produced by tetracycline-controlled expression of a dominant negative TERF2 mutant in CAL51 cells. Pseudobipolar spindles (Pb) are produced by tetracycline-controlled expression of WT PLK4 in MCF10A cells. Multipolar spindles (Mp) are produced by further perturbation of Plk4 inducible cells with a chemical inhibitor of HSET (25 μM CW-069). Polar chromosomes (Po) are produced by enrichment of mitotic cells with nocodazole (1 μg/mL), washout into a CENP-

E inhibitor (1.5 μM GSK923295) followed by an inhibitor of MPS1 (2 μM AZ3146). All tetracycline-controlled systems were constitutively activated for 72 hours (2 μg/mL doxycycline) before harvest. Po cells used for mitotic chromosome spreads and centromeric cenFISH were washed out at T-0 and harvested 24 hours later after a 2 hour 50 ng/mL colcemid treatment.

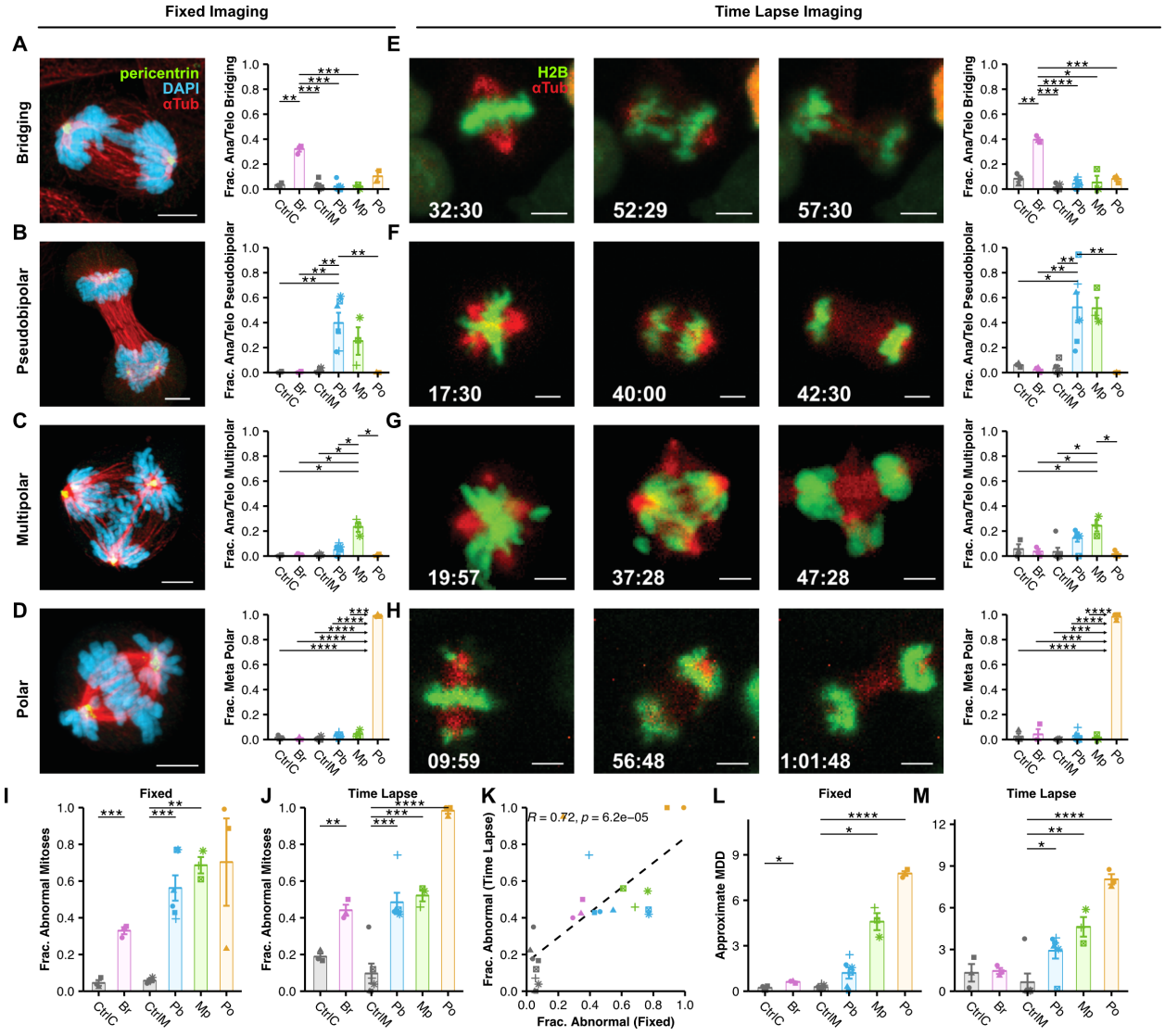

Figure 3.2 — Incidence and specificity of CIN phenotypes via imaging

(A-D) Representative images of specific CIN phenotypes in their respective cell line model and quantifications of their observed incidence using fixed immunofluorescence or **(E-H)** time lapse fluorescence imaging. **(I)** Quantification of the fraction of mitoses with any abnormality across phenotypic CIN models for

fixed immunofluorescence or **(J)** time lapse fluorescence imaging. Symbolic significance thresholds are 0.05 (*), 0.01 (**), 0.001 (***), and 0.0001 (****). **(K)** Correlation between fixed immunofluorescence and fluorescence time lapse imaging with Pearson correlation coefficient. **(L)** MDD values approximated from fixed imaging. **(M)** MDD values approximated from time lapse fluorescence imaging. MDD values were approximated as the sum of phenotype specific MDD values for each condition (Table 3.1). Colors of individual points indicate the biological replicate. Bars and error bars indicate mean and standard error. Significance values above data are from a two-tailed, two-sample Student's t-tests. For time lapse imaging, $N \geq 20$ cells for each of ≥ 3 biological replicates. (Exceptions are single replicates of CtrlC and Pb. See Materials and Methods.) For fixed imaging, $N \geq 50$ metaphase and $\geq$ anaphase/telophase cells for each of $\geq$ biological replicates. (Exceptions are single replicates of CtrlM, Pb, and Po. See Materials and Methods.)

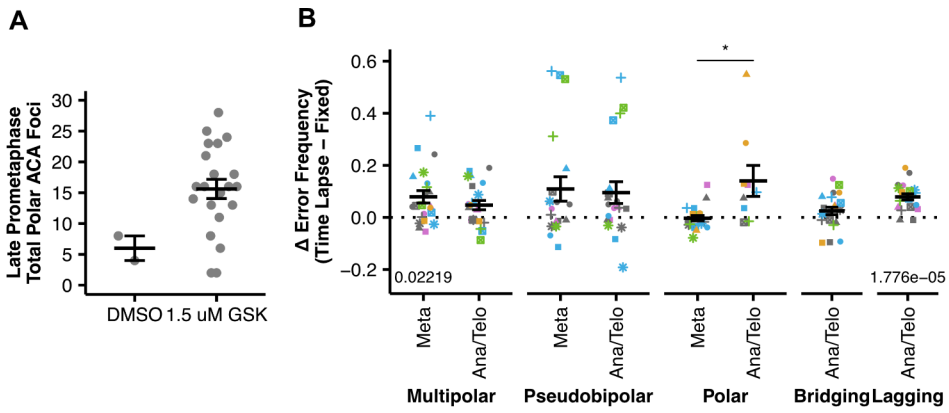

Figure 3.3 — Supplemental Imaging Data

(A) Number of anticentromere antibody (ACA) foci at or behind the spindle pole in late prometaphase (i.e., discernable metaphase plates) MCF10A cells treated under the Po condition but prior to anaphase induction. **(B)** Differences in observed frequencies of mitotic defects between fixed immunofluorescence and time lapse fluorescence imaging in metaphase or anaphase/telophase. Significance values beneath data are from two-tailed, one-sample Student's *t*-tests where H_o: $\mu = 0$. Colors of individual points indicate the biological replicate. Bars and error bars indicate mean and standard error. Significance values above data are from a two-tailed, two-sample Student's *t*-tests.

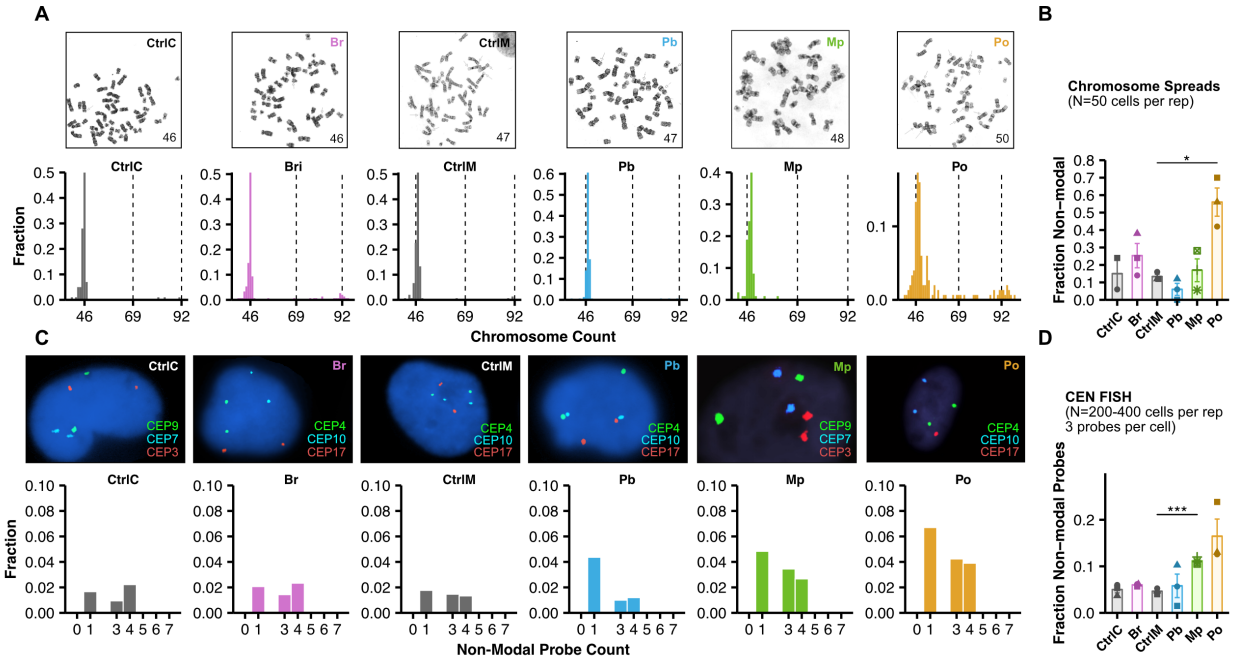

Figure 3.4 — Cytogenetics methods exhibit low sensitivity to ongoing CIN

(A) Representative images of mitotic chromosome spreads from each phenotypic CIN model with corresponding histograms of mitotic chromosome counts per spread. **(B)** Quantification of the fraction of mitotic chromosome spreads whose chromosome counts differ from the mode +/- 1. N ≥ 50 mitotic spreads for each of 3 biological replicates. (Exceptions being CtrlC, with 2 biological replicates, and Mp model, which had a low mitotic index in all 3 replicates (see Materials and Methods).) **(C)** Representative centromeric FISH images from each phenotypic CIN model with corresponding histograms of centromeric probe counts per cell. Diploid counts are excluded from histograms to emphasize aneuploid counts. **(D)** Quantification of the fraction of cells whose cenFISH probe counts differ from the mode. Shapes of individual points indicate the biological replicate. N ≥ 200 cells for each of 3 biological replicates. Bars and error bars indicate mean and standard error. Significance values above data are from a two-tailed, two-sample Student's t-tests. Symbolic significance thresholds are 0.05 (*).

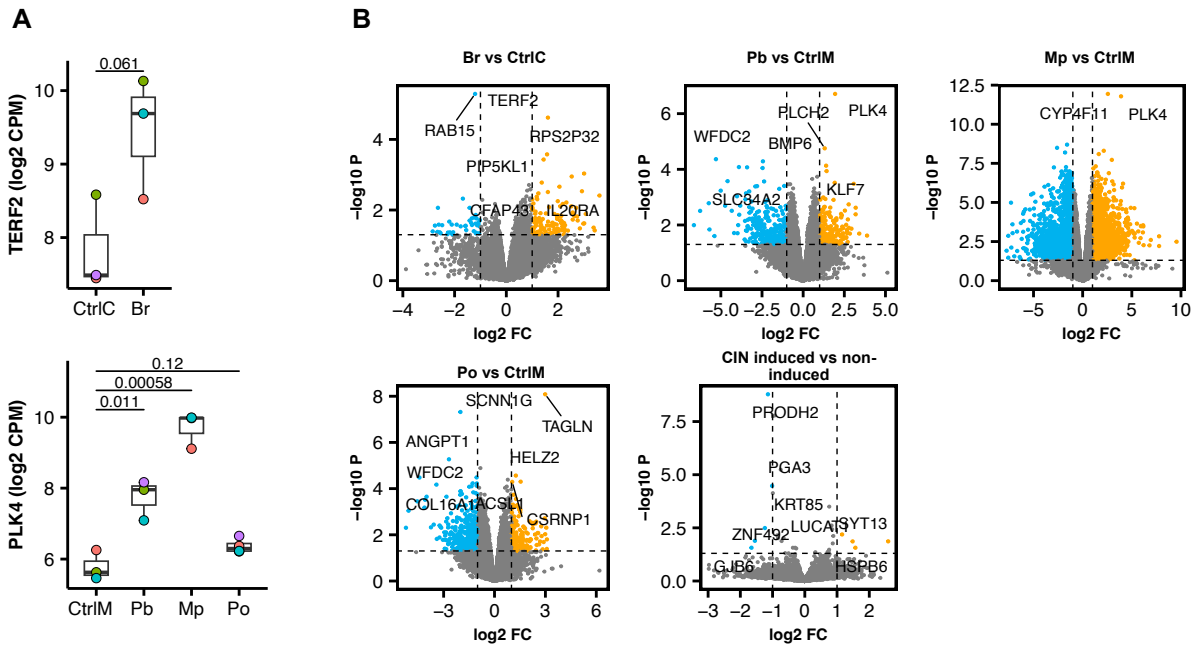

Figure 3.5 — Gene expression in inducible phenotypic models of CIN

(A) Expression levels (log2 counts per million (CPM)) of *TERF2* and *PLK4* in CAL51-TERF2-DN-tetOn and MCF10A-PLK4-WT-tetOn cells respectively. Two-tailed, two-sample Student's *t*-tests are shown above data. N ≥ 3 biological replicates. **(B)** Volcano plots of differential gene expression in each CIN-induced model compared to its uninduced control and a pooled analysis of all CIN-induced groups compared to all non-induced groups. Dashed lines indicate log2 fold-change thresholds of -1/1 and unadjusted P value of 0.05.

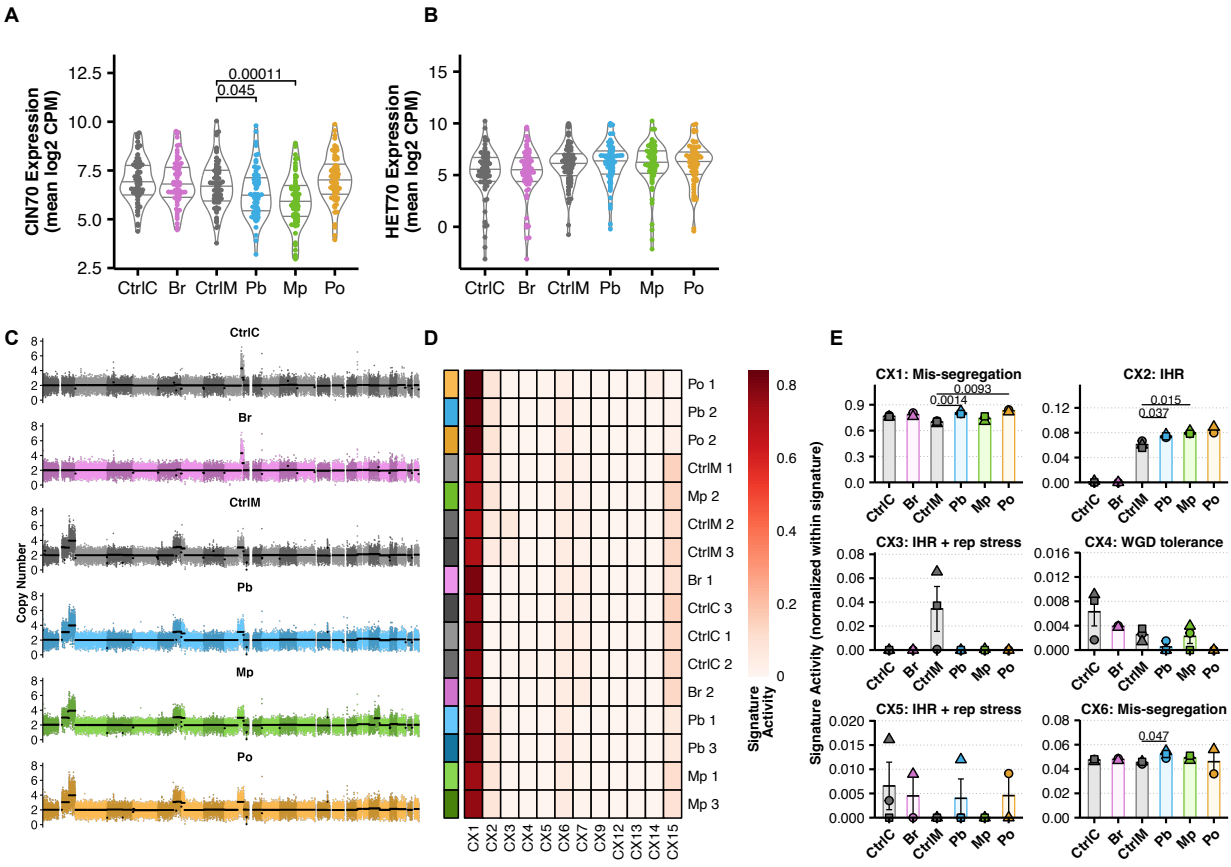

Figure 3.6 — Previously published bulk transcriptomic and genomic CIN signatures do not reflect ongoing CIN

(A) Expression levels (mean log2 counts per million (CPM)) of CIN70 and **(B)** HET70 genes from bRNAseq data from each phenotypic CIN model. Each point indicates the average expression level across 3 biological replicates. **(C)** Representative whole-genome copy number profiles of 500 cells from each phenotypic CIN model sequenced together to ~10x depth. Points indicate copy number of 30 Kb bins. Black lines indicate segment copy number. Alternating shades indicate chromosomes. **(D)** Normalized CIN signature activities of all putative signatures defined in Drews et al. 2022 which provided signal for at least one sample. Color annotations on left of heatmap indicate models and

shades indicate replicates. Rows are clustered by similarity of CIN signatures. **(E)** Normalized signature activities of all putative CIN signatures whose mechanistic etiologies are classified as ‘high confidence’ in Drews et al. 2022. CIN signatures for a given sample are normalized to sum to 1. Shapes of individual points indicate the biological replicate. Bars and error bars indicate mean and standard error. Significance values above data are from a two-tailed, two-sample Student’s *t*-tests.

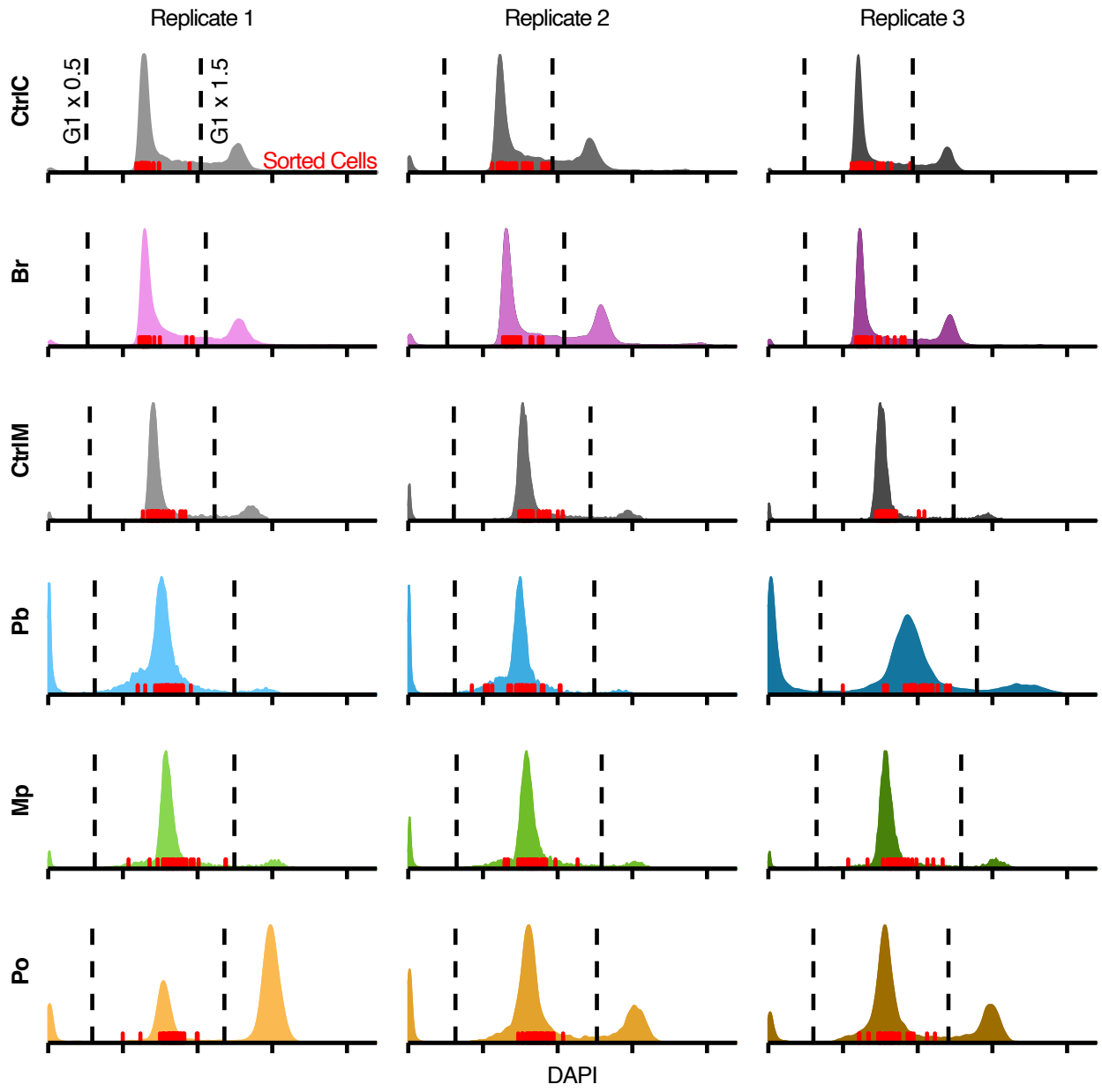

Figure 3.7 — DNA content analysis and gating for pre-scDNAseq FACS

Cell cycle profiles (measured by flow cytometric analysis of DAPI intensity) for each replicate of each phenotypic model of CIN. Dashed lines indicate gating strategy for FACS of cells for scDNAseq and were determined by 50% and 150% of the intensity of the G1 peak. Red ticks indicate the DAPI intensity of cells sorted for scDNAseq. Note the broader G1 peaks of CIN-induced models Pb, Mp, and Po, indicative of extensive aneuploidy.

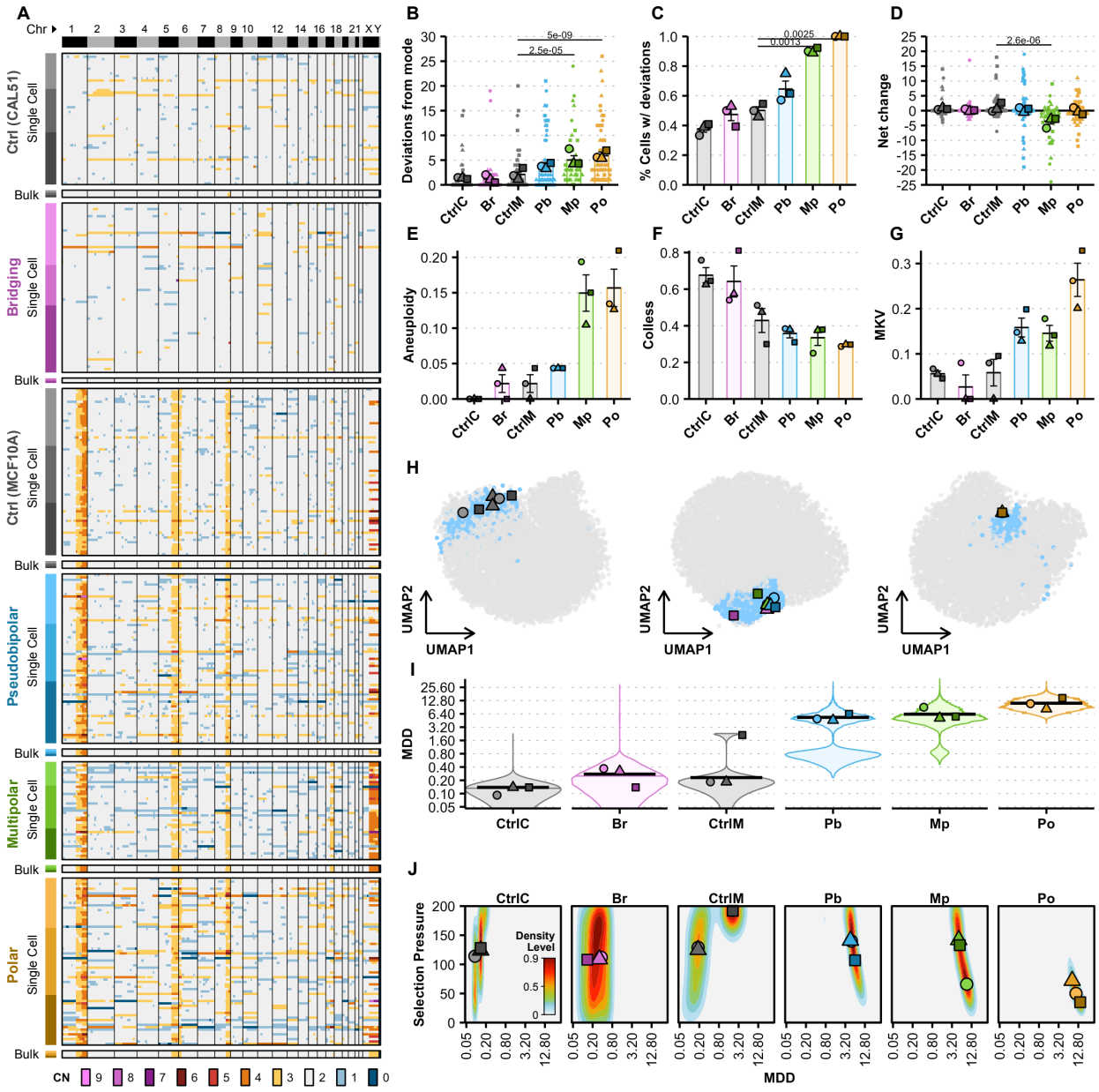

Figure 3.8 — scDNAseq detects ongoing numerical CIN and enables inference of mis-segregation rates

(A) Heatmaps of unsorted single cell and bulk (500 cells) copy number profiles low coverage scDNAseq of each phenotypic CIN model. Copy numbers were called using 2.5 Mb genomic bins. Color annotations on left of heatmap indicate models and shades indicate replicates. Color annotations on top of heatmap and vertical lines indicate chromosomes. Heatmap colors indicate copy number. Whole chromosome copy

numbers are derived as the mode of bin copy numbers across each chromosome and used to quantify, for each phenotypic model, **(B)** the absolute number of whole chromosome deviations from its modal karyotype, **(C)** the percentage of cells with whole chromosome deviations, and **(D)** the net change of total chromosomes in each cell. Quantified **(E)** aneuploidy (the sub-clonal mean variance within karyotypes), **(F)** Colless indices (i.e., phylogenetic imbalance), and **(G)** mean karyotype variance (MKV, the mean variance of each chromosome) were used as summary statistics for approximate Bayesian computation (ABC). **(H)** Space of summary statistics of independent prior simulation datasets used for ABC projected (small data points) with summary statistics measured in each phenotypic CIN model (large data points) using uniform manifold approximation and projection (UMAP). Blue points indicate accepted simulations for at least one model and replicate, whereas grey were rejected. **(I)** Posterior distributions (violin plots) of mis-segregation rates (mis-segregations per diploid division, MDD) across all replicates for each phenotypic CIN model (individual points) inferred using ABC. A log2 scale is used to better illustrate the data. **(J)** Joint posterior density distributions of accepted mis-segregation rates and selective pressure values from ABC for all replicates of each phenotypic CIN model. Data points are mean values for each replicate. Parameter values for prior simulation datasets are as follows: CtrlC and CtrlM — MDD = [0 … 2.3], S = [0 … 200], Time Steps = [30 … 50]; Br, Pb, and Mp — MDD = [0 … 46], S = [0 … 200], Time Steps = [0 … 4]; Po — MDD = [0 … 46], S = [0 … 200], Time Steps = [0 … 2]. See Materials and Methods for further detail. Shapes of individual points indicate the biological replicate. Bars and error bars indicate mean and standard error. Significance values above data are from a two-tailed, two-sample Student's *t*-tests.

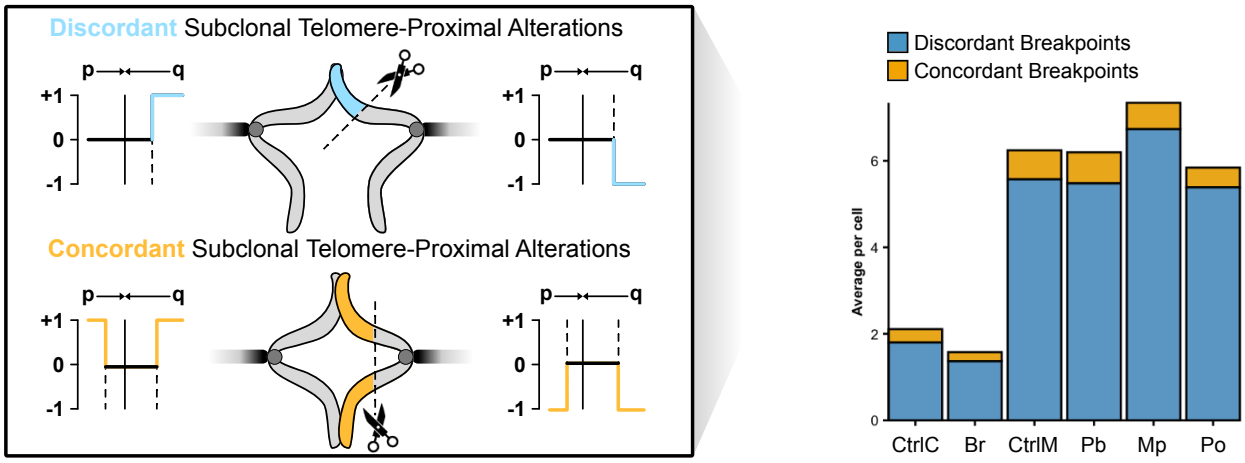

Figure 3.9 — Breakpoint analysis in scDNAseq data

Breakpoint analysis of discordant and concordant telomere-proximal copy number alterations. Copy numbers are normalized relative to those of the modal karyotype of each phenotypic CIN model to uncover subclonal or relatively recent alterations. Only segments with copy number alteration consensus across the 4 telomere-proximal genomic bins (10 Mb), but which terminate at or before the centromere, are considered. Discordant subclonal telomere-proximal alterations are defined as those that are not matched by an alteration on the opposite chromosome arm. Concordant alterations are those that are matched on the opposite chromosome arm. The quantification shows the average number of each alteration per cell for each model.

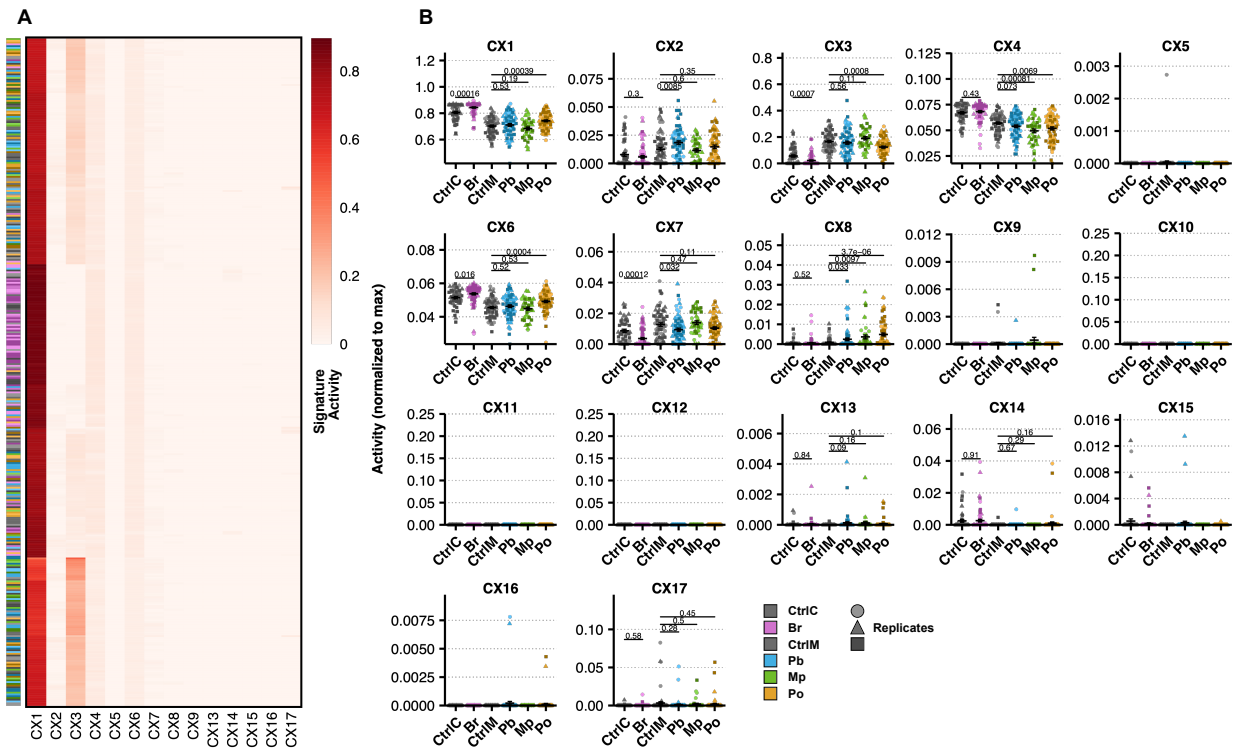

Figure 3.10 — Putative CIN signatures in inducible phenotypic models of CIN at single cell resolution

(A) Heatmap of all normalized putative CIN signature measurements in single cells showing with rows clustered by similarity. Colorized annotation on the left indicates phenotypic CIN model and shade indicates biological replicate. **(B)** Normalized putative CIN signature measurements in single cells grouped by model. Results from two-tailed, two-sample Student's *t*-tests are shown above data using all cells across 3 biological replicates. Shape and shade of data points indicate biological replicate.

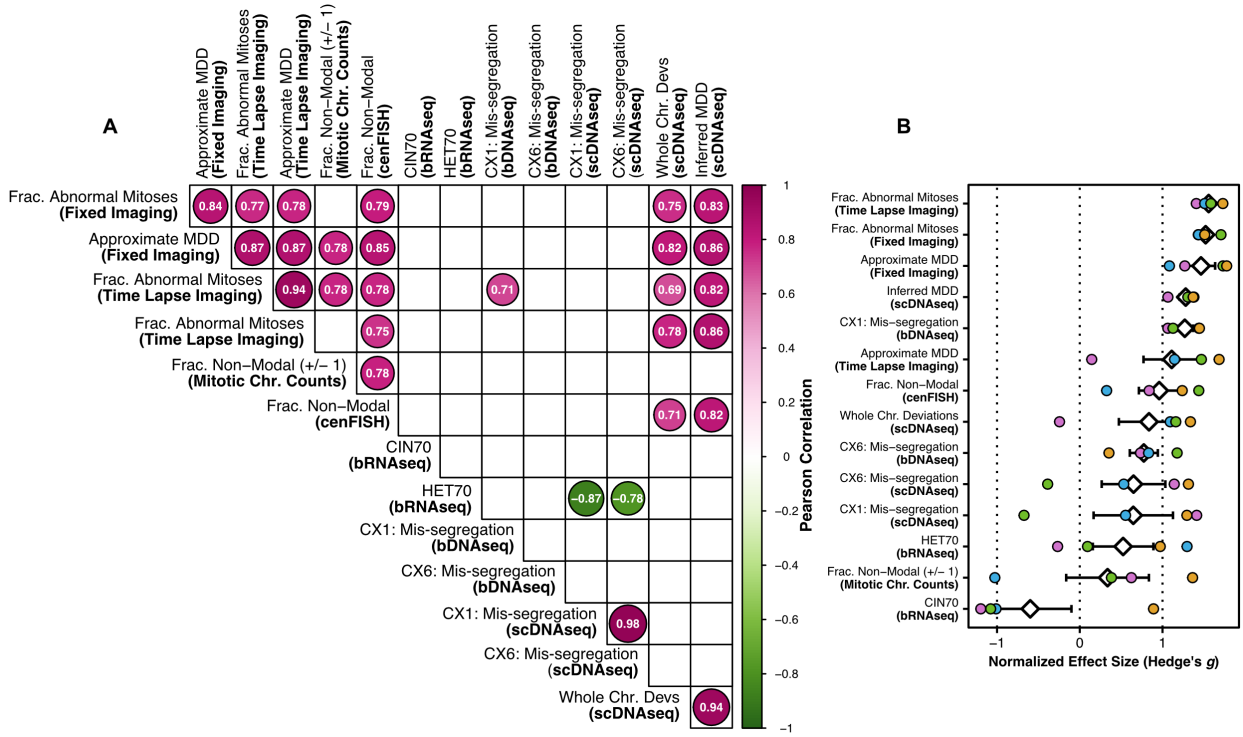

Figure 3.11 — Concordance and performance of CIN measures

(A) Pairwise correlations of CIN measurements. Only statistically significant Pearson correlation coefficients (α = 0.01) are shown. Size of circles represents degree of correlation. **(B)** Effect sizes (Hedge's *g*) of CIN measurements for each model compared to its control. White diamond and error bars indicate mean and standard error.

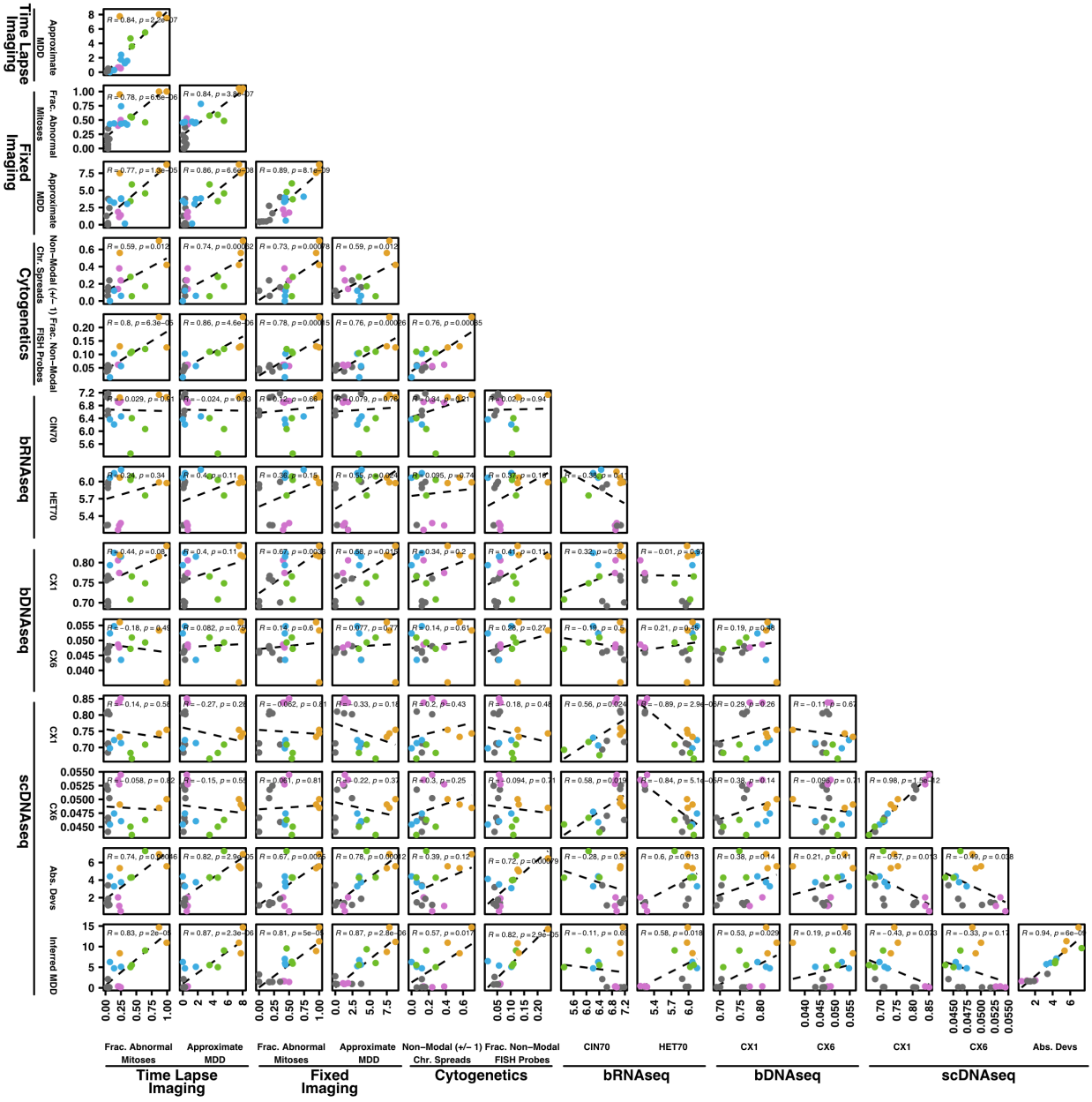

Figure 3.12 — Extended pairwise correlations of CIN measurements

Pairwise correlations between each CIN measurement. Colors of data points indicate the phenotypic model of CIN. Pearson correlation coefficients and p-values of regression are shown.

Table 3.1 — MDD by phenotype approximated by imaging

Group	Phenotype	Fraction w/ Phenotype	Pheno-type SE	Approximate MDD	MDD SE
			Fixed Imaging		
CtrlC	Multipolar	0	0	0.09	0.09
	Polar	0.02	0.01	0.13	0.08
	Bridging	0.03	0.01	0.03	0.01
	Lagging	0	0	0	0
Br	Multipolar	0.01	0	0.24	0.06
	Polar	0.01	0.01	0.07	0.07
	Bridging	0.32	0.02	0.32	0.02
	Lagging	0.01	0.01	0.01	0.01
CtrlM	Multipolar	0.01	0	0.21	0.04
	Polar	0.02	0.01	0.14	0.05
	Bridging	0.03	0.01	0.03	0.01
	Lagging	0.01	0.01	0.01	0.01
Pb	Multipolar	0.05	0.02	0.92	0.32
	Polar	0.03	0.01	0.26	0.06
	Bridging	0.03	0.02	0.03	0.02
	Lagging	0.04	0.01	0.04	0.01
Mp	Multipolar	0.23	0.04	4.21	0.71
	Polar	0.05	0.02	0.35	0.13
	Bridging	0.03	0	0.03	0
	Lagging	0.11	0.03	0.11	0.03
Po	Multipolar	0.01	0.01	0.13	0.13
	Polar	0.99	0	7.72	0.04
	Bridging	0.07	0.04	0.07	0.04
	Lagging	0.06	0.03	0.06	0.03
			Time Lapse Imaging		
CtrlC	Multipolar	0.08	0.05	1.51	0.84
	Polar	0.02	0.02	0.19	0.19
	Bridging	0.08	0.03	0.08	0.03
	Lagging	0.06	0.06	0.06	0.06
Br	Multipolar	0.04	0.02	0.66	0.37
	Polar	0.06	0.06	0.49	0.49
	Bridging	0.4	0.02	0.4	0.02
	Lagging	0.07	0.03	0.07	0.03
CtrlM	Multipolar	0.04	0.04	0.72	0.72
	Polar	0	0	0	0
	Bridging	0.01	0.01	0.01	0.01
	Lagging	0.07	0.04	0.07	0.04
Pb	Multipolar	0.14	0.03	2.6	0.54
	Polar	0.03	0.02	0.22	0.12
	Bridging	0.05	0.02	0.05	0.02
	Lagging	0.12	0.02	0.12	0.02
Mp	Multipolar	0.24	0.05	4.37	0.82
	Polar	0.01	0.01	0.1	0.1
	Bridging	0.08	0.08	0.08	0.08
	Lagging	0.2	0.04	0.2	0.04
Po	Multipolar	0.02	0.02	0.43	0.43

	Polar	0.98	0.02	7.67	0.13
	Bridging	0.08	0.02	0.08	0.02
	Lagging	0.18	0.02	0.18	0.02

Approximated MDD for each CIN phenotype in each model. MDD was calculated using $MDD = \left(\frac{Errors\ per\ Defect \times Defect\ Rate \times Penetrance}{Modal\ Chromosomes}\right) \times 46$ and assumptions of the number of chromosomes mis-segregated for each defect (see Materials and Methods). The fraction of cells with polar chromosomes represents metaphase cells wherein they are most readily detectable. All other CIN phenotypes are taken from anaphase or telophase cells.

Table 3.2 — CIN70 and HET70 genes

CIN70		HET70	
TPX2	MSH6	AHCYL1	LPP
PRC1	EZH2	AKT3	MED8
FOXM1	CTPS1	ANO10	MMP2
CDK1	DKC1	ANTXR1	MUL1
TGIF2	OIP5	ATP6V0E1	MYO10
MCM2	CDCA8	ATXN1	NAGK
H2AZ1	PTTG1	B4GALT2	NR1D2
TOP2A	CEP55	BASP1	NRIP3
PCNA	H2AX	BHLHE40	P4HA2
UBE2C	CMAS	BLVRA	PKIG
MELK	NCAPH	CALU	PLOD2
TRIP13	MCM10	CAP1	PMP22
NCAPD2	LSM4	CAST	POFUT2
MCM7	NCAPG2	CAV1	POMGNT1
RNASEH2A	ASF1B	CLIC4	PRKAR2A
RAD51AP1	ZWINT	CTSL	MOK
KIF20A	PBK	CYB5R3	RHOC
CDC45	ZWILCH	ELOVL1	RRAGC
MAD2L1	CDCA3	EMP3	SEC22B
ESPL1	ECT2	FKBP14	SERPINB8
CCNB2	CDC6	FN1	SPAG9
FEN1	UNG	FST	SQSTM1
TTK	MTCH2	GNA12	TIMP2
CCT5	RAD21	GOLT1B	EMC3
RFC4	ACTL6A	HECTD3	TRIM16
ATAD2	GPI	HEG1	TRIO
CKAP5	SRSF2	HOMER3	TUBB2A
NUP205	HDGF	IGFBP3	VEGFC
CDC20	NXT1	IL6ST	VIM
CKS2	NEK2	ITCH	WASL
RRM2	DHCR7	P3H1	YIPF5
ELAVL1	AURKA	P3H2	YKT6
CCNB1	NDUFAB1	LEPROT	ZBTB38
RRM1	NEMP1	LGALS1	ZCCHC24
AURKB	KIF4A	LIMA1	ZMPSTE24

Table 3.3 — Characteristics of CIN measurement methods

Method	Accessibility	Scalability	Sensitivity	Imaging Concord-ance
fixed imaging	+++	no	(4/4) bridges / pseudobipolar / multi-polar / polar	-
time lapse im-aging	-	no	(4/4) bridges / pseudobipolar / multi-polar / polar	-
chromosome spread	-	no	(1/4) polar	no
6-centromere FISH	+++	yes	(1/4) multipolar	yes
bulk RNA seq	++	yes	(0/4)	no
bulk DNA seq	+++	yes	(0/4)	no
scDNAseq	+	yes	(3/4) pseudobipolar / multipolar / polar	yes

Categories for clinical accessibility are (-) insurmountable barriers, (+) requires special equipment and/or reagents **and** time-consuming and/or laborious, (++) requires special equipment and/or reagents **or** time-consuming and/or laborious, or (+++) commonly performed clinical assays use the same equipment and reagents. Scalability is determined by the pre-existence of established protocols and/or platforms for high throughput sample preparation and data acquisition in a clinical or non-clinical setting. Sensitivity to a specific mechanism is determined by a significant difference between the control and CIN-induced groups. Imaging concordance is determined by significant correlation to both imaging methods.

4

CINFER: AN INTERACTIVE WEB-PLATFORM FOR INFERRING ONGOING CHROMOSOME MIS-SEGREGATION RATES FROM SINGLE CELL DNA SEQUENCING DATA

Adapted from Lynch et al. (Manuscript 2). In preparation.

ABSTRACT

Chromosomal instability (CIN), persistent gain and loss of chromosomes, contributes to cancer progression and therapeutic response in a mis-segregation rate-dependent manner. However, the difficulty of measuring these rates has hindered the study of its origin in cancer and its clinical use as a prognostic and predictive biomarker. Here we present CINFER, a user-friendly and interactive web-based platform to infer ongoing chromosome mis-segregation rates from single-cell DNA sequencing datasets. CINFER enables users to perform approximate Bayesian computation (ABC) using an extensive database of agent-based simulations of CIN and karyotype selection in cell populations. This resource can be accessed at https://andrewrlynch.shinyapps.io/CINFER/.

MAIN

Chromosomal instability (CIN) promotes aneuploidy and intratumor heterogeneity through the mis-segregation of chromosomes during abnormal mitoses. The pervasive aneuploidy observed in tumors (80-90%) suggests that CIN occurs in most tumors (253–255). CIN was previously considered a binary feature of tumors and mutually exclusive

with microsatellite instability (121). We now know the severity of CIN — the rate of chromosome mis-segregation — varies from tumor to tumor and likely varies over time and between clones in the same tumor (138, 191, 194, 196, 220, 237). Further, the ongoing rate of mis-segregation influences the CIN's roles in tumorigenesis (246, 341, 342), progression (182, 237, 245, 260, 343), and therapeutic response (249, 251, 265, 266). Knowing the severity of CIN in patients' tumors would be advantageous for prognoses and personalized medicine. However, quantification of ongoing chromosome mis-segregation rates in tumors has proved challenging as methods for which are clinically intractable and because these measurements are confounded by ongoing karyotype selection (138, 241, 243). For example, the observed cell-to-cell variation of karyotypes at a single timepoint (e.g., the time of biopsy) may underestimate a high mis-segregation rate via the death of unfit cells such as those that lose too many chromosomes. In addition to precluding any clinical benefit, the difficulty of measuring CIN in cancer patients' tumors has hindered fundamental research into the molecular causes of CIN and determinants of patient-to-patient severity. While CIN can be induced in an experimental setting by manipulation of genes involved in mitosis (e.g., spindle-assembly, chromosome alignment, error correction), these genes are rarely mutated in cancer. Therefore, uncovering the mechanisms that generate CIN in cancer requires further study in patients' tumors.

We previously developed a framework to account for the confounding effects of karyotype selection to enable the rapid, accurate measurement of CIN from single-cell DNA sequencing data (scDNAseq) (147). We validated this approach experimentally and used it to infer mis-segregation rates in clinically derived tumor samples. This confirmed

the expected range of mis-segregation rates in tumors and supported a role for stabilizing selection in limiting the diversity of cancer cell populations with ongoing CIN.

Expanding on this work, we now present CINFER, a user-friendly, web-based platform for inference of ongoing mis-segregation rates. CINFER uses chromosome copy numbers inferred from shallow (<1x) scDNAseq data to infer ongoing mis-segregation rates in the sequenced sample (Figure 4.1). These analyses are based on thousands of agent-based simulations of CIN and karyotype selection over a physiologically relevant timescale, which sweep through a parameter space from low to high rates of chromosome mis-segregation and low to high selective pressure. Measurements taken from these simulations are stored in a database (CINFERdb) which CINFER uses to as a prior dataset for parameter inference of mis-segregation rates using approximate Bayesian computation.

The simulated data in CINFERdb consists of over 5 million measurements across 50 thousand independent simulated cell populations grown over 100 time steps (~50 generations). This encompasses the physiological time required to form an approximately 1 cm, palpable tumor made of around 1 billion cells, which can develop in about 30 generations. Across these simulations, we sweep through uniform parameter space using mis-segregation rates (MDD) from 0 to 4.6 and karyotype selection pressures from 0 to 100 (Table 4.1, Figure 4.2A). Most evidence points to stabilizing selection as the predominant mode of ongoing karyotype selection (147, 218, 225, 226, 228). While karyotypic drift occurs through chromosome mis-segregation, most single cell karyotypes resemble that of the ensemble population. The simulations in CINFERdb emulate this process by negatively selecting aneuploid cells that stray from the average ploidy of the population. Each

chromosome affects this to a different extent according to the number of genes it encodes. While karyotypic drift can occur, the karyotypes of individual simulated cells are constrained depending on the strength of the selective pressure parameter (S).

The seven summary statistics in CINFERdb are measured at each time step for each independent simulation (Figure 4.2B). These measurements summarize the karyotypic diversity and phylogenetic shape at each point in time.

CINFERdb's three karyotype diversity measures are quantifications of subclonal aneuploidy, mean karyotype diversity, and fraction of unique clones in the population. While aneuploidy itself is not indicative of CIN as some aneuploid clones can be chromosomally stable, the subclonal aneuploidy metric measures the extent to which each individual cell differs from the clonal population. For example, if all cells but one share the same karyotype, this measure would differentiate whether the outlier bears a single chromosomal alteration, which could result from a lagging chromosome, or fifteen, which could result from a multipolar spindle. Mean karyotype diversity (MKV) is a transposed quantification of aneuploidy. Instead of measuring *intra*-karyotype variance and taking the mean across all cells, it measures the *trans*-karyotype variance for each chromosome and takes the mean across all chromosomes. In this way, population with the single outlier would score low on MKV. However, if each cell differs slightly, it will score higher. The fraction of the population consisting of unique clones (based on karyotype) is similarly indicative of ongoing chromosome mis-segregation, though with a smaller dynamic range.

CINFERdb's four phylotopology measures are quantifications of the shape of phylogenetic trees reconstructed from each cells karyotype. Phylogenetic shape is indicative

of the evolutionary processes that shape them (229, 230, 232, 344). Thus, these measures aid the inference of mis-segregation rates by correcting for the degree of ongoing karyotype selection. To do this, phylogenetic trees of each simulated population at each time step are reconstructed from single cell karyotypes using hierarchical clustering. Sackin and Colless indices measure the imbalance (i.e. asymmetry) of these reconstructed phylogenetic trees, with greater imbalance indicative of greater ongoing karyotype selection. In some cases, a rare, highly aneuploid cell, such as a daughter cell resulting from a recent multipolar division, can heavily skew phylogenetic tree reconstructions. We also implemented a measure of the Colless index where copy numbers for each chromosome (e.g., chromosome 1) are permuted across the population. The permuted Colless index preserves repetitive karyotype alterations indicative of ongoing selection, but minimizes the outsized effects of rare, highly dissimilar cells. And while Colless and Sackin indices are whole-tree measures of imbalance, the number of ‘cherries’ (i.e., clades consisting of single pairs of tree tips), offers a measure of more discrete structures within a given tree. While the number of cherries is inversely correlated to the imbalance of the tree, they are informative as an orthogonal method to counter outsized effects of small numbers of cells on overall tree shape. Further, each phylotopology measure is normalized to the size of the population to accommodate any number of cells in a scDNAseq dataset.

Measuring these same statistics using scDNAseq-derived copy numbers enables the use of ABC, a statistical method for parameter inference by comparing simulated and biological data (301, 345–347). Thus, mis-segregation rates can be inferred by identifying

the simulation parameters (MDD, S, and time steps) that produced sets of summary statistics in CINFERdb that most closely resemble the biological data.

We previously validated this approach by recalling experimentally observed mis-segregation rates caused by the chemotherapeutic drug, paclitaxel, and by demonstrating that mis-segregation rates inferred from patient-derived colorectal cancer organoids associate with rates observed by microscopy. We validated the stabilizing selection model by demonstrating that simulations using inferred mis-segregation rates with karyotype selection more closely resemble biological data than those inferred without this selection. Further, we confirmed stabilizing selection as the predominant mode of ongoing karyotype selection through model selection against other proposed selection models (147). We also found that this method of measuring mis-segregation rates performs better than any other measure of CIN, excluding direct imaging, when performed in tandem across inducible cell culture models of several CIN phenotypes (Lynch et al., *in submission*).

We developed CINFER with several built-in user-defined settings to allow users to tailor analyses to their experimental requirements. To demonstrate, we have measured ongoing chromosome mis-segregation rates in the high-grade serous ovarian cancer cell line, OV2295 (Figure 4.3). After retrieving previously published scDNAseq-derived absolute copy number data (322), we filtered out poor-quality cells using the authors' predefined quality metrics. We then took the mode of copy numbers for each chromosome as whole-chromosome copy numbers, performed hierarchical clustering on karyotypes, and k-means clustering of 4 major 'clones' within the population as determined by within-cluster sums of squares. We extracted the copy numbers for one of these clones as a

data matrix with chromosomes as columns and single cells as rows. Importing this matrix into CINFER, population summary statistics for karyotype diversity and phylotopology are automatically measured. We selected prior parameter distributions relevant to the population of cells (in particular, a long timescale since, to our knowledge, these cells had not recently been sub-cloned) and which was encompassed by the space of our selected summary statistics (aneuploidy, MKV, and the permuted Colless index) using UMAP dimensionality reduction. To handle ABC in CINFER, we implemented a previously published package designed specifically for running this analysis on pre-simulated data (281), in our case, CINFERdb. Accordingly, we allow users to select from the four ABC strategies defined in this implementation. For computational simplicity, we selected 'Rejection' sampling, which simply takes the median parameter value across all accepted simulations within a given tolerance threshold as the inferred value. For the tolerance threshold, we chose 0.05 to include only the most similar 5% of prior simulations in the posterior distribution. After running parameter inference, CINFER outputs the joint posterior distribution of mis-segregation rate and selection pressure. CINFER also outputs clear values for each inferred parameter. In our case, we find that the inferred values for mis-segregation rate, selection pressure, and time steps are MDD = 0.23 ± 0.119, S = 13 ± 5.379, and Steps = 95 ± 3.167 respectively (median ± standard deviation). This means that, given the assumption of our chosen prior parameter distributions, the mis-segregation rate that most likely resulted in the observed scDNAseq data is 0.23 mis-segregations per diploid division, or about 1 mis-segregation every 4 divisions. CINFER then prompts users to check the predictive power of these inferences against the null hypothesis that no karyotype

selection has occurred. Here, CINFER takes the inferred values and re-initializes a limited number of additional simulations, re-measures the selected summary statistics, and compares them to the observed measures and to those from simulations without karyotype selection. In this case, we find that summary statistics from the posterior prediction fall relatively close to those measured in the OV2295 cells and outperform those from simulations use the null hypothesis of no karyotype selection.

This analysis can be extended to scDNAseq from other longitudinal samples from other cell culture experiments, tumor-derived organoids, and even tumor biopsies. Moreover, CINFER is flexible in accommodating shorter time periods and higher mis-segregation rates characteristic of acute molecular or chemical perturbations used to induce CIN, such as inhibition of the spindle assembly checkpoint protein, MPS1. Though, because the data in CINFERdb was simulated under the assumption of whole-chromosome mis-segregation, CINFER is not suitable for inferring rates of chromosome arm-level copy number alterations characteristic of ongoing structural CIN or mis-segregation of whole albeit highly re-arranged chromosomes. While this could be achieved using additional simulation data, CINFER is currently computationally constrained to smaller datasets.

In summary, CINFER is a computational platform for inference of chromosome mis-segregation rates. It guides users through the steps necessary to perform a robust analysis including user-defined prior parameter distributions and population summary statistics, a configurable inference framework, and the option to perform additional simulations to assess the posterior predictive power of one’s results. This user-friendly platform is backed by CINFERdb, which contains over 5 million measurements taken simulated

populations grown over a physiologically relevant timescale using a broad and uniform set of CIN and selection parameters. Prior to developing CINFER, we previously validated this approach to measure CIN in several cases. We then used CINFER to measure ongoing mis-segregation rates in the OV2295 HGSOC cell line. However, relative levels of CIN are challenging to measure, particularly when microscopic observation is not a viable option, such as in a clinical setting. CINFER is a leap forward in making the karyotype selection-aware measurement of CIN easier in both clinical and experimental samples.

MATERIALS AND METHODS

Data requirements for end-users

CINFER currently requires pre-formatted absolute chromosome copy number data in CSV format with chromosomes in columns and cells in rows. Cell IDs should be included as row names, rather than in the matrix, while chromosome IDs can remain in the matrix. Users may exclude any chromosome they wish, such as the sex chromosomes.

Agent-based modeling

CINFERdb was created using simulations developed and performed in NetLogo (see Table 4.2 for package versions) as previously described (147). In short, we initiated simulated populations with 100 diploid cells and evolved exponentially growing populations using a pseudo-Moran process to reduce computational demands (a random 50% of cells are culled when the population surpasses 3000 cells). Euploid cells had a 50% chance to divide at every step, a probability that is modified according to a cell's fitness level. We used a karyotype selection scheme that emulates stabilizing selection by negatively selecting genetically unbalanced karyotypes. The contribution of each chromosome

to karyotype selection is dependent on the abundance of genes it encodes. We simulated populations using the following parameters: MDD = [0, 0.046, 0.092, …, 4.6], S = [0, 1, 2, …, 100], Time Steps = [0, 1, 2, …, 100]. We assumed whole-chromosome mis-segregation and that chromosome copy numbers below 1 and above 7 would r7esult in cell death. Accordingly, as cells divide and mis-segregate chromosomes, more aneuploid cells with more unbalanced karyotypic stoichiometries are less likely to continue division. A random selection of 300 karyotypes is exported to measure summary statistics at each time step. See Lynch et al. 2022 for additional details.

Hierarchical clustering

Complete-linkage clustering of chromosome copy number data was performed in R using Euclidean distance matrices for both heatmap visualization and derivation of phylotopology measurements (described below). Heatmaps were constructed using ComplexHeatmap. We determined the optimal number of OV2295 clusters, or clones, using the ‘elbow’ method by plotting the total within sum of squares for 1 to 10 clusters with locally estimated scatterplot smoothing (loess) (span = 1) and selecting the number of clusters closest to the estimated inflection point.

Population summary statistics

CINFERdb contains seven quantitative measures of karyotype diversity and phylotopology, all of which are measured in R.

Aneuploidy is measured by calculating the modal karyotype of the population, then subtracting the modal karyotype from each cell’s own karyotype. This masks clonal aneuploidies that are less likely to associate with ongoing CIN. The variance within each cell’s

karyotype is calculated and the mean of all cell's intra-karyotype variance represents the aneuploidy of the population.

Mean Karyotype Variance (MKV) is similar to the quantification of aneuploidy, though it measures the dissimilarity between karyotypes instead of the variance within karyotypes. It does not require subtraction of the modal karyotype and the variance and mean calculations are transposed. The variance of each individual chromosome (e.g., chromosome 1) is calculated, then the average of these variance values across the 24 chromosomes (23 if the Y chromosome is excluded, for example) represents the MKV of the population.

The fraction of the population consisting of unique subclones is measured simply by consolidating all cells to their unique karyotypes to get the number of unique subclones and normalizing to the size of the population.

Phylotopology measures, in our case, require hierarchically clustering the population on whole chromosome copy number values as described above. This results in a cluster object which can be interpreted as a binary, mid-point rooted tree. Then, each measurement is made using the phyloTop package in R.

The Colless index, a broad measure of tree imbalance, is measured by calculating the sum of absolute values of differences in the number of leaf tips between each pair of clades joined by each node in the tree. Thus, more imbalanced, or asymmetric trees, have a higher Colless index. The Sackin index, another measure of tree imbalance, is measured similarly. Here, the sum of the number of ancestor nodes for each leaf tip is calculated. Thus, more imbalanced trees have a higher Sackin index. Both indices are normalized by

the number of tip pairs in the tree. Additionally, we implemented a variant of the Colless index that takes a tree constructed after randomly permuting the copy number values within each chromosome (e.g., chromosome 1) and is averaged over 100 permutations. In some cases, a rare cell with a vastly different may be present in the copy number data, particularly if the input data are not clustered and selected prior to analysis. In these cases, these rare cells can have an outsized effect on the imbalance indices as the they would appear to have far fewer ancestor nodes or far fewer cells in its respective clade. Permuting the copy number data distributes the variance of the outlier throughout the tree, minimizing the effect of these rare outliers while preserving the broad topological structure of the rest of the population.

In a phylogenetic tree, cherries are pairs of adjacent leaf tips connect by a common ancestor node and are local measures of tree balance inversely correlated to the Sackin and Colless indices. We quantify cherries simply by normalizing their number to the number of tip pairs in the tree.

Uniform manifold approximation and projection (UMAP)

UMAPs are performed using the uwot package in R and a matrix of summary statistics measured from simulated data and scDNAseq data. In CINFER, UMAPs are generated using a random sub-sample of 2500 data points from user-selected distributions of simulated data and summary statistics. (UMAP parameters: n_neighbors = 5, bandwidth = 0.33, fast_sgd = TRUE). For UMAPs in Figure 4.2 of this manuscript, we used a random subsample of 100,000 data points from CINFERdb in its entirety and include all 7 summary statistics. (UMAP parameters: n_neighbors = 8, bandwidth = 0.5)

Approximate Bayesian computation

In CINFER, we implement ‘abc’, a previously published R package designed to perform ABC on pre-simulated datasets (281). We do not change its underlying framework and three of its features include for configuration and cross-validation within CINFER:

1. Choice of 1 of 4 methods for ABC, rejection sampling, rejection with local linear regression, rejection with ridge regression, and a neural network for non-linear regression of inferred values.
2. Choice of tolerance threshold to control the proportion of the prior distribution of simulated data that is accepted.
3. Cross-validation of tolerance thresholds to evaluate how one’s chosen tolerance threshold affects the parameter inference within the selected prior distributions.

Posterior predictive checks

The median of posterior distributions for each parameter are passed into nlrx, an R package used as a wrapper for running NetLogo simulations. This initializes 10 new simulations in the same manner as previously described. However, 5 of these simulations use the inferred parameters for simulating new populations and 5 use the inferred rate and time parameter, but neutral selection as a null hypothesis to assess the choice of a selective pressure distribution. Summary statistics from these populations are measured identically to those measured in the imported scDNAseq data and in CINFERdb.

Application architecture and hosting

CINFER was built in R and shiny and hosted on shinyapps.io.

Code Availability

The source code for CINFER and scripts for analyses in this manuscript are available on GitHub (https://github.com/andrewrlynch/CINFER).

ACKNOWLEDGMENTS

Special thanks to the UW – Madison Social Science Computing Cooperative for computational support and to the laboratories of Drs. Sohrab Shah and Samuel Aparicio for making available the copy number data for OV2295 cells.

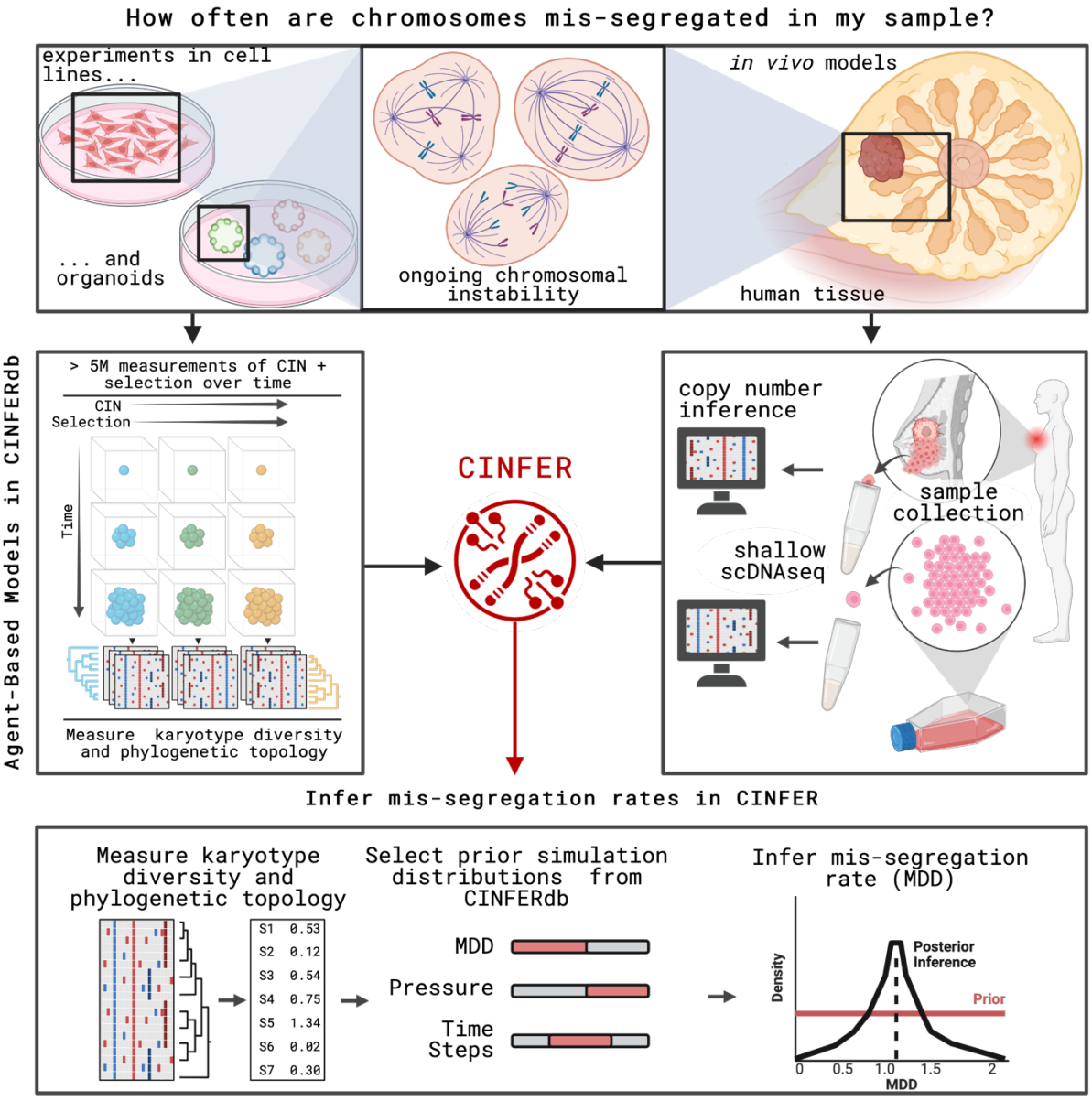

Figure 4.1 — CINFER: a web-platform for inferring chromosome mis-segregation rates from scDNAseq data

CINFER is backed by a database (CINFERdb) of over 5 million measurements of karyotype diversity and phylotopology from agent-based simulations of CIN and karyotype selection over time. Inferring mis-segregation rates requires only a few steps: (1) Users upload chromosome copy number matrices inferred from shallow scDNAseq to CINFER to measure the relevant summary statistics from their data. (2) Selection of relevant prior parameters to pull down data from CINFERdb. (3) Configuring and running approximate

Bayesian computation to compare user's data to the CINFERdb prior. (4) Check the posterior predictive power of the inference and cross-validate the users selected tolerance threshold.

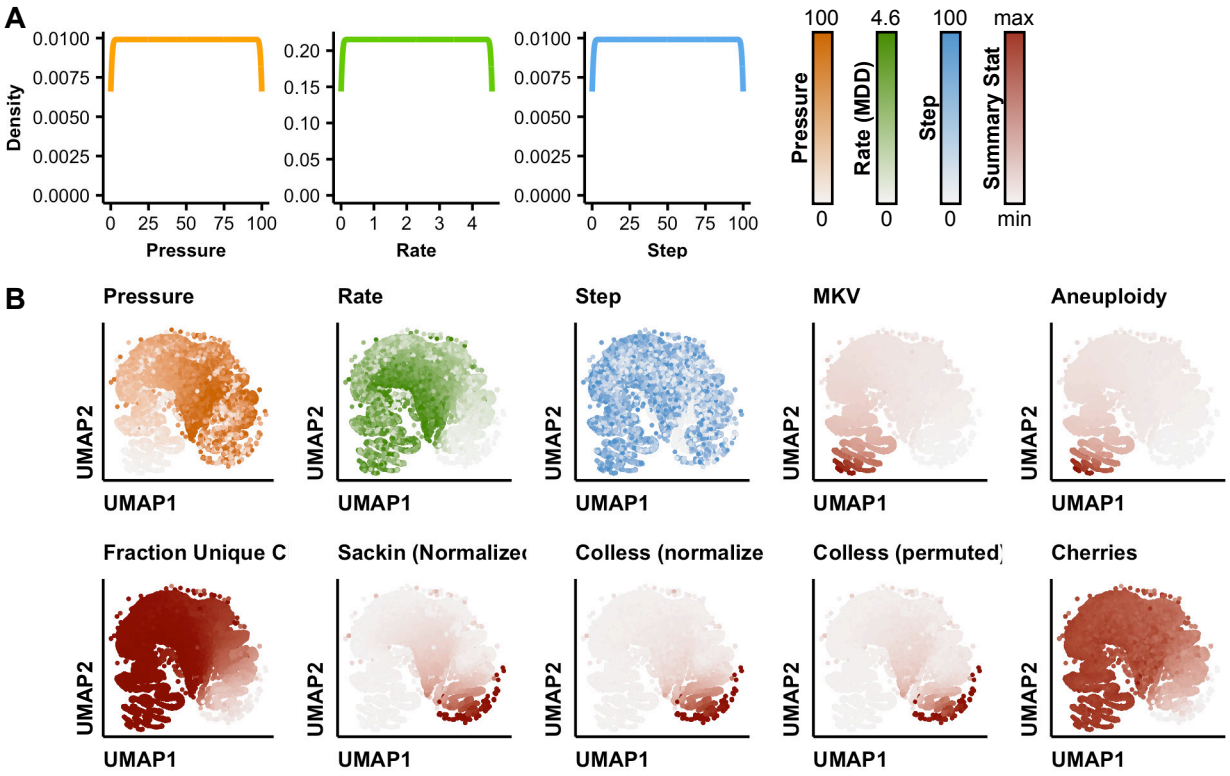

Figure 4.2 — Characteristics of the CINFERdb dataset

(A) Uniform prior parameter distributions for simulated data in CINFERdb. Resolution of distributions is shown in Table 1. **(B)** Dimensionality reduction projections (uniform manifold approximation and projection, UMAP) which show the relationships between simulation parameters and measured summary statistics from simulated data in CINFERdb. UMAP projections are randomly down-sampled to 100,000 data points.

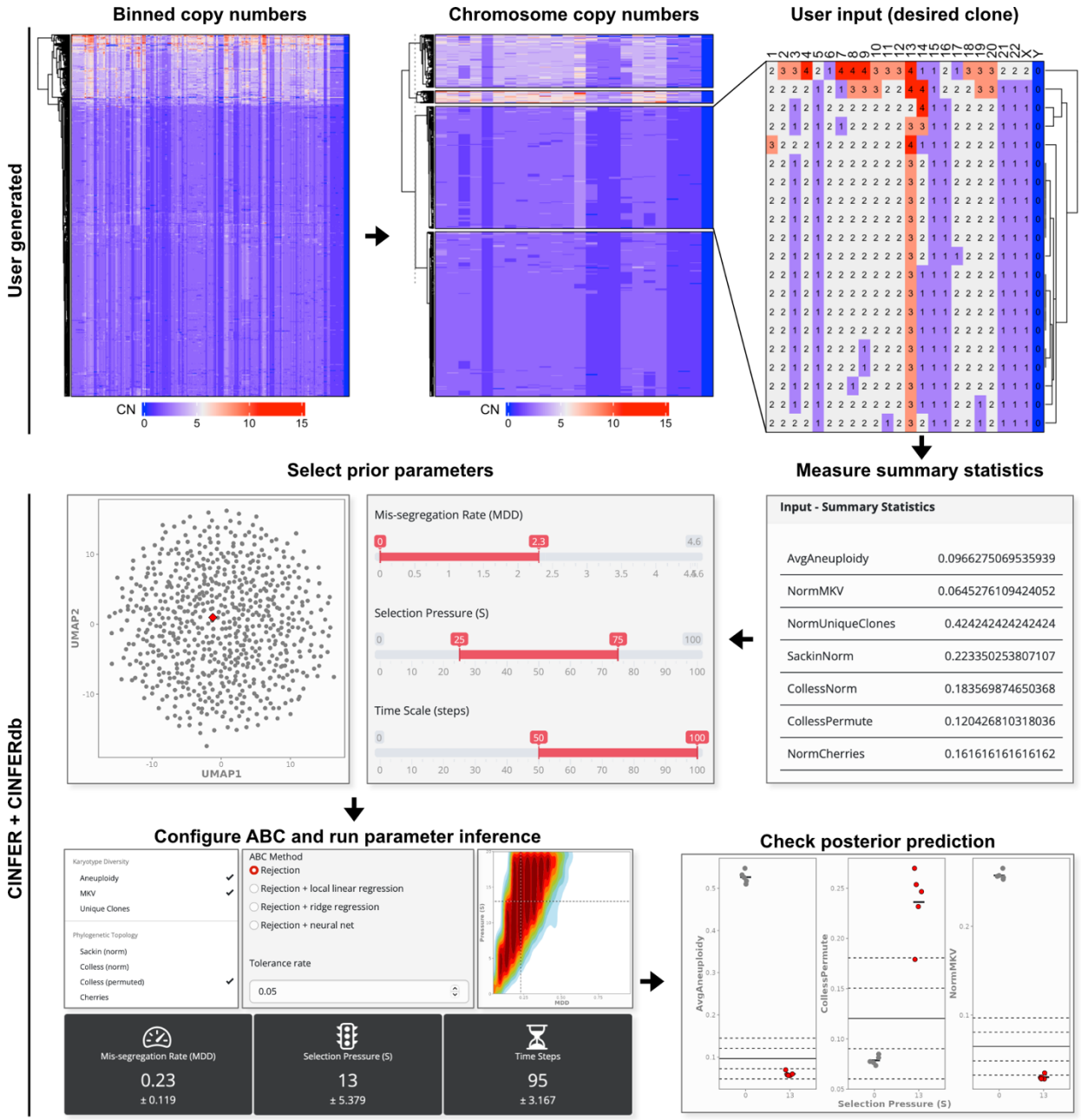

Figure 4.3 — Inference of mis-segregation rates in OV2295

Representative workflow of mis-segregation rate inference. Shallow scDNAseq data of OV2295 cells were retrieved from Laks, McPherson, Zahn et al. 2019 and filtered according to the authors' quality metrics (quality ≥ 0.6). Modal chromosome copy numbers were taken for each chromosome and imported into CINFER, from which each population summary statistic was measured. Prior parameters of MDD = [0,0.046, …, 1], S = [0, 1, …, 100], and Steps = [90, 91, 100] w5/24/23 11:53:00 AMere selected and the

population measurements of the scDNAseq data were projected onto the space of summary statistics to ensure goodness of fit. Aneuploidy, MKV, and a permuted Colless index were used as summary statistics for ABC, as well as rejection sampling and a tolerance threshold of 0.05. A joint posterior distribution shows the parameter density of accepted simulations and the median MDD, S, and steps is taken as the inferred values. These are used to perform additional posterior predictive simulations and compared to a null hypothesis of S = 0. Measurements from these simulations are then compared to those taken from the scDNAseq data (solid horizontal line). Dashed lines represent ± 25% and ± 50% error.

Table 4.1 – Characteristics of the CINFERdb dataset

Simulation Parameters	
Rate (MDD)	0 – 4.6 by 0.046
Pressure (S)	0 – 100 by 1
Time steps	0 – 100 by 1
Database Statistics	
Replicates per combination	5
Total simulations	51005
Total measurements	5151429

Table 4.2 – Critical software packages

Software	**Version**	**Reference**
NetLogo	6.1.1	(298)
R	4.2.3	(333)
RStudio	2022.7.0.548	(336)
R Packages		
abc	2.2.1	(281)
nlrx	0.4.3	(348)
phyloTop	2.1.2	(300)
RSQLite	2.3.0	(349)
shiny	1.7.4	(350)
tidyverse	2.0.0	(351)
uwot	0.1.14	(352)

5

PERSPECTIVES

Adapted from Lynch, Bradford, and Burkard (Manuscript 1). Under review.

CONCLUSIONS IN SUMMARY

1. Karyotype diversity depends on the primary mode of karyotype selection.
2. Low CIN populations under low karyotype selection can produce similar levels of karyotype diversity to high CIN populations under high karyotype selection, which confounds the inference of CIN from karyotype heterogeneity.
3. The topology of phylogenies reconstructed from chromosome copy numbers detect ongoing karyotype selection and delineate CIN and karyotype selection in otherwise confounded scenarios.
4. Bayesian inference using simulated populations with chromosomal instability and karyotype selection can recover experimentally observed mis-segregation rates.
5. Paclitaxel induces an average of 18 chromosome mis-segregations in a single cell division, confirming predicted baseline mis-segregation rates caused by multipolar spindles.
6. Ongoing mis-segregation rates in cancer samples (breast biopsy, colorectal cancer organoids) fall between 0.05 and 0.4 mis-segregations per diploid

division (MDD). This implies the dynamic range of mis-segregation rates, and their relative effects in tumor progression fall within one order of magnitude.

7. The primary mode of ongoing karyotype selection in tumors is stabilizing selection around the clonal karyotype.
8. A widely used transcriptional measures of CIN, the CIN70 gene panel, fails to detect ongoing, genetically and chemically induced CIN.
9. Selection-aware inference of mis-segregation rates is clinically accessible and outperforms most current methods of measuring CIN.
10. Induction of nullisomy as a strategy to induce cell death requires extensive chromosome mis-segregation rates (about 16 mis-segregations to achieve nullisomy in 50% of a diploid population.
11. Prior chromosome loss sensitizes cells to mis-segregation through nullisomy.
12. Spindle pole clustering and partial cytokinesis failure can rescue cells from nullisomy-mediated cell death.

TOWARD THE CLINICAL APPLICATION OF CIN MEASUREMENTS

The clinical significance of CIN is well established and has been thoroughly reviewed here and elsewhere (116, 353, 354). To summarize, experimental, pre-clinical, and *post hoc* clinical studies have shown that the level of CIN in cancer cell populations drives malignancy in a non-linear fashion. Low levels of CIN limit the evolvability of tumors. Moderate levels of CIN promote tumorigenesis and drive cancer progression by increasing adaptability, promoting increased fitness, LOH of tumor suppressors, amplification of activated oncogenes, metastasis, and therapeutic resistance. High levels of CIN promote

unsustainable genomic catastrophe such as nullisomy (138, 182, 237, 240, 245, 246, 248, 343). Further, the intrinsic level of CIN in a tumor has long been thought, and recently been demonstrated, to predict sensitivity to drugs that further increase CIN (248, 249, 265, 266, 355). Paclitaxel, for instance, is widely used and very effective in about half the patients who receive it (356). The other half receive no benefit and there is no clinical biomarker to inform who should receive paclitaxel. Thus, if CIN were measured in the clinic, it may be viable as a predictive biomarker for paclitaxel treatment. Indeed, despite the clinical significance of CIN levels, and unlike microsatellite instability (MIN), tumors' CIN status is not used in any clinical capacity to inform patient prognosis or treatment strategies.

Why? As we've established thus far, the widely used measures of CIN each suffer barriers to clinical accessibility. Fixed microscopy is direct, but slow and imprecise as chromosome fate is unknown. Time lapse microscopy is, of course, only available *ex vivo*. Cytogenetics methods display cell-cell karyotype resolution and can, with the exception of FISH and simple chromosome counts, detect structural CIN. Yet, these are also slow and may suffer the effects of karyotype selection masking. Bulk transcriptomic CIN signatures have been shown to be uninformative of ongoing CIN. Bulk genomic sequencing can detect aneuploidy and, to a limited extent, subclonal and allelic alterations indicative of CIN, but are insufficient to establish rates of mis-segregation. Further, for the time being, most clinical sequencing relies on panel or exome sequencing, which are less robust in calling large-scale CNAs induced by CIN. Single cell genomics and transcriptomics, if CNAs can reliably be inferred from the latter, offer the necessary sensitivity and

completeness of cell-cell variation and potential for the necessary throughput to capture recently acquired, yet-unselected, CNAs. These methods remain costly and require additional computational methods to account for selection and infer mis-segregation rates. Nevertheless, the combination of single cell and computational technologies will likely be the fastest route to benefit patients through robust, clinically accessible measures of CIN.

The pace of basic research into CIN's function is also impeded by the lack of clinical CIN measurements. The wealth of CIN research in model systems and *post hoc* clinical analysis up to this point has allowed us to make broad hypotheses regarding its broad roles in cancer progression. Yet the lack of a clinically established CIN measure prevents some key questions from being addressed.

QUESTIONS REMAINING

How does CIN contribute to advanced disease? We know that high-grade, aggressive cancers are associated with elevated levels of CIN. It is generally thought that the increased karyotype diversification provides a richer substrate for natural selection of ever-more optimal gene combinations in tumors. Is the shuffling of large genomic regions like whole chromosomes or chromosome arms sufficient to promote aggressive clinical phenotypes without further structural CIN and focal alterations? Or does numerical CIN only serve to enrich the substrate for subsequent structural CIN and focal alteration of specific genes? Similarly, as CIN promotes chromothripsis and extrachromosomal DNA formation, do cancers with higher or earlier CIN have a greater diversity of extrachromosomal DNA?

Alternatively, to what extent is CIN's role in cancer progression an epi- or extra-genomic effect? For instance, cells with higher CIN may be less differentiated (238, 357–359). Does CIN cause cancer cell dedifferentiation or does dedifferentiation increase tolerance to CIN through altered transcriptional plasticity, for example. Further, CIN can purportedly induce metastasis by inducing an inflammatory cytosolic DNA response secondary to mis-segregation and rupture-prone micronucleation of chromosomes (238). What level of CIN is sufficient to promote this in tumors?

How does CIN develop? Perhaps a more fundamental challenge than determining CIN's role in cancer, is determining its origin. In laboratory experiments, CIN can be triggered by manipulation of genes associated with DNA damage repair and synthesis, cell cycle progression, mitotic spindle assembly, kinetochore-micotubule attachment error correction, and chromosome congression. However, these genes are rarely mutated or differentially transcribed in cancer. The combination of this low 'signal' and the high 'noise' of insufficient and ineffective CIN measures has stymied the identification of CIN's etiology in cancer.

How is CIN tolerated? Inactivation of p53 is commonly cited as a potent driver of CIN tolerance (297, 360, 361). However, p53 is mutated in ~60% of tumors while aneuploidy is present in 80-90% (254, 255). Though, other alterations of the p53 pathway, such as MDM2 amplification, could produce similar tolerance. Nevertheless, multiple additional mechanisms could be responsible in addition to the p53 pathway — unfolded protein response, endoplasmic reticulum stress response, and transcriptional, translational, and post-translational mechanisms of dosage compensation to name a few (327–329, 331).

The measure of CIN levels in patients would help us understand the ways in which CIN is tolerated.

Does CIN or CIN tolerance come first? Low levels of somatic aneuploidy in normal tissue (313) could be due to intolerance to CIN or exceedingly low rates of mis-segregation. Does increased CIN tolerance allow subsequent outgrowth of rare cells that have developed CIN early in neoplasia? Do cells develop CIN first and subsequently develop tolerance mechanisms to support it?

What is the critical threshold of tolerable CIN in tumors? Mathematical modeling suggests the boundary conditions that should be universal to all cells, not just cancer and selection-aware models further refine these models. For example, most cells are not likely to enjoy mis-segregating a quarter of their chromosomes in a single division. However, different cancers could have varying levels of CIN tolerance. For example, ovarian cancers tend to exhibit a high burden of CNAs, which could (though not definitive evidence) portend greater levels of CIN in ovarian cancer than hematological cancers, for example. This may suggest that the typical developmental trajectory of ovarian cancers promote and/or tolerate higher CIN whereas hematological cancers would be more sensitive to that very same level. Accordingly, the interactions between canonical cancer driver pathways, CIN promoting pathways, and CIN tolerance mechanisms would be of interest once sufficient data are available.

What is low CIN vs high CIN? It is common to refer to different rates of chromosome mis-segregation, subjectively, as ‘low’, ‘moderate’, or ‘high’, when discussing its role in cancer. This is because, up to this point, methods of CIN measurement have not

been amenable to the quantification of a rate. Therefore we don't know what the relevant mis-segregation rates are as they pertain to a functional role in cancer. The consequence of this is conflicting definitions of CIN levels depending on the context. For example, most *post hoc* clinical studies that have measured CIN in various ways, refer to the highest levels of CIN they observe as 'high', understandably. In this context, the range of mis-segregation rates seems to fall between 0-0.5 MDD (Table A2.2). However, observational clinical trials have examined the strategy of using chemotherapeutics like paclitaxel to elevate CIN as a mechanism of action. In these studies the same levels would be considered 'low' or 'moderate' compared to the 'high' rate of mis-segregation that can cause cell death, which are not common in cancer without therapeutic challenge. For example, paclitaxel treatment of cultured cells can induce CIN in excess of ~18 MDD. A widely used, quantitative measure of CIN would unify these paths of investigation, provide a scale of what is truly 'low' and 'high' CIN, and clarify the range of CIN's consequences related to mis-segregation rate.

NEXT GENERATION CIN MEASURES

The measure of CIN has advanced greatly since its discovery, a progress catalyzed by technological and methodological advancements and evidence of its importance in cancer over nearly two centuries. However, further advancements are required to use measures of CIN to benefit cancer patients and answer some fundamental questions about the biology of CIN. Fifteen years ago, Geigl et al. introduced criteria for a definition of CIN and some recommendations for its measure (362). With advancements in single-

cell sequencing technologies since then, we update these recommendations and provide a set of criteria, some aspirational, for a next generation of CIN measures.

Do not conflate CIN with aneuploidy. First and foremost, recall the adage “CIN is a rate, aneuploidy is a state.” While the extent of subclonal aneuploidy in a population can be a helpful metric to infer CIN, aneuploidy itself is not sufficient evidence of CIN. Therefore, refrain from making conclusions about CIN when only measuring a level of aneuploidy, particularly clonal aneuploidy.

Provide single-cell resolution. In lieu of direct observation, the measure of CIN relies on cell-to-cell karyotypic variation. Even with multiregion sampling and subclonal inference, a great deal of heterogeneity can be masked through bulk measures. Single cell measures are required.

High throughput and information rich. The accurate measure of the extent of CIN in a population requires the full karyotypes of hundreds to thousands of cells from the same sample. Small sample sizes will be more sensitive to sampling bias and the inherent stochasticity of CIN.

Comprehensively measure numerical and structural CIN. While the inference of structural variation from most single cell sequencing data is challenging, this will likely not always be the case. Efforts to quantify the rate of whole-chromosome mis-segregation as well as chromosomal rearrangements should be made.

Clinically accessible. The clinical measurement of CIN requires rapid sampling, preparation, and analysis as well as relatively cost-effective strategies. One way this could

be achieved is by combining the measurement of CIN with other clinical assays like mutation panel sequencing, though on a high-throughput, single cell platform.

Account for empirically-derived selection dynamics. Measures of CIN should incorporate known, empirically-derived selection dynamics. The observable degree of karyotype heterogeneity is not the full story as other cells may not survive mis-segregation or are otherwise outcompeted. Therefore, further characterization of karyotype selection dynamics will benefit the inference of CIN.

Use a standard metric — mis-segregations per diploid division (MDD). Subjective 'levels' of CIN become unnecessary when the rate of mis-segregation can be quantified. Several factors need to be accounted for in a singular CIN measure: time, background ploidy, and penetrance. Time can be expressed as the number of divisions that have occurred in a population. We propose that background ploidy should be normalized to the typical diploid human karyotype rather than per chromosome to correlate with direct imaging, rather than per cell to relate to the rate per chromosome at risk. For a given MDD, a tetraploid cell mis-segregates 2x the chromosomes as a diploid one. Penetrance can be thought of as the fraction of a population that mis-segregates *n* chromosomes per division. To illustrate this latter point, cell population *A* might mis-segregate 1 chromosome every division through a lagging phenotype while cell population *B* might mis-segregate 10 chromosomes every 10 divisions through a multipolar division phenotype. The penetrance of CIN differs between populations *A* and *B*, but the total CIN in the population can be considered equal (Table A2.3). We propose measuring CIN using a standard metric — **mis-segregations per diploid division (MDD)** — which accounts for each of these

factors. Importantly MDD can be measured using sequencing-based inference methods discussed above or estimated from microscopy-based mitotic analyses.

CLOSING

In the end, I hope the findings of these studies and other perspectives herein are of use. The study of CIN is challenging, in no small part because it has been a challenge to measure. The major goal of this work has been to improve the measure of CIN so as to improve our understanding of the relevant rates of mis-segregation that occur in patients' tumors. This improved understanding will serve both basic and clinical purposes. By understanding rates of chromosome mis-segregation that occur in tumors, we can delineate levels of CIN in patient samples and understand the molecular determinants of CIN severity and perhaps even its origin. Further, understanding these rates will improve our understanding of how CIN contributes to cancer progression, not just 'in general', but in individual patients, and will improve clinicians' prognostication and confidence in prescribing effective therapies.

To conclude, I return to the words of Theodor Boveri who recognized the importance of experimental and methodological development:

> *There are still many other facts to be gleaned from the histological and experimental study of malignant tumours and from clinical and statistical evidence that could provide criteria for the validation of our point of view… For in this field, as in any other, many important phenomena remain unobserved despite the most assiduous investigation because they are not*

anticipated by any of our current concepts and must therefore appear to be adventitious concomitants.

APPENDIX 1: ALGORITHMIC FIRST PRINCIPLES OF CHROMOSOMAL INSTABILITY

Adapted from Lynch (Manuscript 2). In progress.

0 ABSTRACT

Chromosome mis-segregation commonly occurs in tumors and works to remodel cancer cell karyotypes. However, the extent to which to karyotypes are remodeled as a function of mis-segregation rates and specific CIN phenotypes has not been thoroughly examined. Here I introduce a series of deterministic and stochastic models aimed at exploring the karyotypic consequences of mis-segregation rates and various aspects of multipolar divisions over single divisions. I find that induction of nullisomy requires extensive mis-segregation rates most readily achievable by multipolar division, which appear to induce a high baseline mis-segregation rate of about 15 chromosomes (in diploid cells undergoing tripolar divisions). Conversely, clustering of multipolar spindles can otherwise rescue daughter cells from nullisomy. These results comport with scDNAseq data from CAL51 cells treated with paclitaxel which showed a best-fit with simulations performed with a high degree of clustering and a moderate level of spindle asymmetry. Altogether, these data lay a theoretical foundation for the extent to which chromosome mis-segregation can remodel a cell's karyotype.

1 INTRODUCTION

Mitosis is strictly regulated to ensure faithful bi-directional segregation of bioriented sister chromatids on a bipolar mitotic spindle. However, this process can fail in several

ways, ultimately leading to chromosome mis-segregation with varying phenotypes and severity. Chromosomal instability (CIN) is characterized by the persistence of these failed mitoses, leading to losses and gains of chromosomes over time, which is commonly observed in cancer cells. In this way, CIN is a powerful driver of intratumoral heterogeneity by increasing aneuploidy, altering the copy number of hundreds to thousands of genes(201, 363) and triggering additional secondary mutational processes like chromothripsis (104, 105). Further, the severity of CIN, or rate at which chromosome mis-segregations occur, has its own spectrum of consequences in the context of cancer. Low rates of chromosome mis-segregation hamper tumorigenesis and, perhaps, the progression of cancer by limiting the evolutionary potential. However, high rates of chromosome mis-segregation can cause cell death (245, 246, 249). While there is relatively little research on chromosome mis-segregation-mediated cell death, it could occur due to the traversal of an intolerable threshold of gene dosage imbalance or acute DNA damage or by induction of nullisomy, the complete loss of a set of homologous chromosomes. The basis of the latter putative cause of cell death is relatively more certain. Nullisomy is not observed in human cells with the exception of chromosome Y and some cases of acute, high levels of chromosome mis-segregation. For example, in a cell line model, high rates of chromosome mis-segregation through multipolar divisions induced by the chemotherapeutic drug paclitaxel produced nullisomy in about 50% of cells (147). Indeed, chromosome mis-segregation on multipolar spindles is the clinical mechanism of action of paclitaxel (249). This finding confirmed previous hypotheses that significant elevation of CIN in a tumor could produce a therapeutic response in cancer patients (248, 265) and

increased interest in other CIN-increasing drugs that could have the same effect. Many of these have failed in clinical trials (364, 365). It is currently unclear if paclitaxel represents an extreme example of an agent that is particularly effective at inducing CIN, if multipolar spindles are always a potent phenotype of CIN, or what would be required for other mechanisms of CIN to produce the same effect. This is because the baseline numerical consequences of mis-segregation rates over single divisions have not been closely examined. Here, I model several facets of chromosome mis-segregation to determine the theoretical numerical consequences of mis-segregation rate and mechanism. In exploring how these variables interact, I lay a theoretical foundation to determine the fates of daughter cell genomes resulting from abnormal divisions.

2 MODELING NULLISOMY ACROSS MIS-SEGREGATION RATES

There are two ways to define mis-segregation rate which depend on whether the mis-segregation is quantified in the mother cell or the daughter cells. For example, a mis-segregation rate of 18 chromosomes is derived when the karyotype of a daughter cell deviates from diploid (46 chromosomes) by 18 chromosomes. However, if the number of chromosomes is quantified in the mother cell, 36 mis-segregated chromatids would result in the same 18 deviations in the daughter cell. It will be important to note that I take the former perspective to frame the investigation on consequences of mis-segregation for daughter cells rather than as a characteristic of a single division.

2.1 Initial Assumptions

1) The probability of mis-segregation is applied across all cells uniformly.

2) The probability of mis-segregation is applied across all chromosomes uniformly.
3) Cells are euploid unless otherwise stated.
4) Sex chromosomes are equivalent. Thus, cells are considered to have 23 sets homologous chromosomes.

2.2 A deterministic model of nullisomy after a single division with mis-segregation

2.2.1 Mis-segregation with independence

Consider the probability of mis-segregating both copies, in the case of diploidy, of a homologous chromosome pair during the same division with given mis-segregation rate m. Under the additional assumption that mis-segregation events are independent, we can first calculate the probability of any two chromosomes being mis-segregated in a daughter cell as

$$\left(\frac{\mathrm{m}}{46}\right)^2, \tag{1}$$

which can also be extended to other ploidy levels, where p is the ploidy of mother cell M, as

$$\left(\frac{\mathrm{m}}{23\mathrm{p}}\right)^{\mathrm{p}}. \tag{2}$$

Because this also represents the probability of two homologous chromosomes both mis-segregating, and because there is a $1:2^{\mathrm{p}}$ chance that these mis-segregations result as two losses for daughter cell D (Figure A1.1A), we can write the probability that chromosome set C will achieve nullisomy as

$$\mathrm{C}_{\mathrm{nullisomy}} = \left(\frac{\mathrm{m}}{23\mathrm{p}}\right)^2 \times \frac{1}{2^{\mathrm{p}}}. \tag{3}$$

Applying this to calculate the number of the 23 homologous chromosomes that are affected by nullisomy across mis-segregations rates in daughter cell D gives

$$\mathrm{D}_{\mathrm{nullisomies}} = \left(\frac{\mathrm{m}}{23\mathrm{p}}\right)^2 \times \frac{23}{2^{\mathrm{p}}}. \tag{4}$$

2.2.2 Mis-segregation with dependence

The previous model assumes that mis-segregation events are independent of each other. Thus, the probability for a chromosome to mis-segregate does not change as a set number of chromosomes are mis-segregated. We may consider an alternative model where these mis-segregations are dependent wherein the mis-segregation of one chromosome affects the probability of another. Under this framework we can adapt Eqn. 3 to include n, which controls the dependency of chromosome mis-segregation events on preceding events, the maximum value of which is equal to p. The probability of a chromosome being nullisomic is then

$$\mathrm{C}_{\mathrm{nullisomy}} = \frac{1}{2^{\mathrm{p}}} \times \prod_{\mathrm{n}=0}^{\mathrm{p}-1} \frac{\mathrm{m}-\mathrm{n}}{23\mathrm{p}-\mathrm{n}}. \tag{5}$$

Likewise, as in Eqn. 4, the number of nullisomic chromosomes after mis-segregation can be shown as

$$\mathrm{D}_{\mathrm{nullisomies}} = \frac{23}{2^{\mathrm{p}}} \times \prod_{\mathrm{n}=0}^{\mathrm{p}-1} \frac{\mathrm{m}-\mathrm{n}}{23\mathrm{p}-\mathrm{n}}. \tag{6}$$

2.2.3 A stochastic model of uniform mis-segregation over single divisions

To orthogonally validate the mathematical models proposed above, I wrote a stochastic simulation of single division chromosome mis-segregation (Algorithm 1). In this simulation, a random sample of chromosomes, with sample size equal to mis-segregation

rate m, are mis-segregated and the number of resulting nullisomies in each cell is calculated.

2.2.4 Modeling populations' nullisomic fraction across mis-segregation rates

The number of nullisomies is a cell's karyotype must be 0 or greater. Thus, $\mathrm{D}_{\mathrm{nullisomies}}$ should follow a Poisson distribution and can be equated to λ in the Poisson probability mass function

$$P(x) = \frac{e^{-\lambda}\lambda^{x}}{x!}. \tag{7}$$

Accordingly, the probability of inducing nullisomy with a given mis-segregation rate m and ploidy p can be written as

$$\begin{aligned} D_{nullisomy} &= P(\mathrm{D}_{\mathrm{nullisomies}} > 0) = 1 - P(\mathrm{D}_{\mathrm{nullisomies}} = 0) \\ &= 1 - \frac{\left(e^{-\left(\frac{m}{23p}\right)^{p} \times \frac{23}{2^{p}}}\right)\left(\frac{m}{23p}^{p} \times \frac{23}{2^{p}}\right)^{0}}{0!} \\ &= 1 - e^{-\left(\frac{m}{23p}\right)^{p} \times \left(\frac{23}{2^{p}}\right)}. \end{aligned} \tag{8}$$

2.2.5 Incorporating prior aneuploidy

The previous models explore nullisomy as a function of mis-segregation rate in euploid cells. However, euploid cancer cells are very rare. Therefore, we must consider how pre-existing aneuploidy affects the rate of nullisomy after mis-segregation. Instead of using a euploid ploidy p, we can define a karyotype set $K = \{n_1, n_2, \ldots, n_{23}\}$ where $n \in K$ is the copy number of each chromosome (for a G1 mother cell). Thus, the probability of nullisomy is calculate for each set of homolog9us chromosomes independently. Accordingly, Eqns. 4 and 6 can be modified to

$$\mathrm{C}_{\mathrm{nullisomy}} = \left(\frac{\mathrm{m}}{\sum \mathrm{K}}\right)^{\mathrm{n}} \times \left(\frac{1}{2^{\mathrm{n}}}\right) \tag{9}$$

for a given set of homologous chromosomes and

$$\mathrm{D}_{\mathrm{nullisomies}} = \sum_{\mathrm{n}\in\mathrm{K}} \left(\frac{\mathrm{m}}{\Sigma \mathrm{K}}\right)^{\mathrm{n}} \times \left(\frac{1}{2^{\mathrm{n}}}\right) \tag{10}$$

as the frequency of nullisomy within the daughter cell karyotype. Thus, the incidence of nullisomy in a population with modal karyotype K, the incidence of cells with nullisomy in the population (as in Eqn 8), is

$$\mathrm{D}_{\mathrm{nullisomy}} = 1 - \mathrm{e}^{-\sum_{\mathrm{n}\in\mathrm{K}}\left(\frac{\mathrm{m}}{\sum \mathrm{K}}\right)^{\mathrm{n}} \times \left(\frac{1}{2^{\mathrm{n}}}\right)}. \tag{11}$$

2.3 Results

2.3.1 Interdependence of discrete mis-segregation events does not have a significant impact on the incidence of nullisomy.

I find that the functions of nullisomy incidence with respect to mis-segregation rate produce similar results regardless of whether mis-segregations are independent or dependent events. (Figure A1.1B-D). While it is possible these models may reflect different phenotypic expressions of chromosome mis-segregation — for example, attachment errors alone vs combined attachment and congression errors — the functional difference between them in terms of the incidence of nullisomy appears to be negligible over a large range of mis-segregation rates (Figure A1.1E). Either appear to be suitable to estimate this incidence for a given phenotypic expression of CIN. Therefore, going forward, independence of mis-segregation rates will be assumed unless otherwise noted.

2.3.2 Nullisomy is a rare event at biologically relevant mis-segregation rates, particularly in polyploid cells

As expected, the probability of nullisomy for a given set of homologous chromosomes increases with mis-segregation to 0.25 for diploid cells. Even in the extreme event where all chromosomes are mis-segregated, the probability of nullisomy remained quite low, particularly in triploid and tetraploid cells. This is true even at mis-segregation rates that are much higher than what is commonly observed in cancer cell culture ($\mathrm{m} < 1$; Figure A1.1B-E). This supports polyploidization as a buffer against nullisomy and may permit increased mis-segregation rates, as recent studies suggest. Accordingly, the frequency of nullisomy within a daughter cell after mis-segregation increased with mis-segregation (Figure A1.1G). Interestingly, to reliably induce a single nullisomy in all diploid cells in a single division, one would have to induce mis-segregation of ~20 chromosomes, though even this is low incidence is markedly decreased in triploid and tetraploid cells. Notably, we recently found that paclitaxel, on average, induces 18 chromosome mis-segregations, which would appear to satisfy the requirement for extensive mis-segregation to cause cell death via nullisomy. This finding also raises the bar on how effective a CIN-inducing drug must be to cause cell death in this manner. Raising the rate of mis-segregation in a tumor to 1-2 mis-segregations per division is unlikely to cause significant levels of nullisomy in tumors, at least over a single division.

2.3.3 The incidence of nullisomy in a population follows a Poisson distribution.

Stochastic modeling of nullisomy as a function of mis-segregation rate also confirmed that the frequency of nullisomic cells in a population follows a Poisson distribution (Figure A1.1H). Although I found that the mis-segregation rate that produced an average of 1 nullisomy per cell was ~20, I also found that only ~75% of the population appeared

nullisomic at this rate (Figure A1.1I). This result is useful because if we consider induction of nullisomy to be the primary mechanism of action of a CIN-inducing drug, then we can calculate the number of mis-segregations required to produce an EC50. In this case, where I used euploid cells, the EC50s for diploid and triploid cells were about 16 and 42 mis-segregations respectively (dashed lines), while the EC50 for tetraploid was not achieved between within the 0-46 chromosome mis-segregations considered. This raises the possibility of targeting CIN-inducing drugs to those tumors exhibiting hypodiploidy.

2.3.4 Prior chromosome losses potentiate nullisomy after mis-segregation

Because the EC50s of euploid cells were high relative to what is biologically relevant (excluding the chemical induction of CIN), I asked if chromosome losses in an otherwise euploid context substantially changes this result. Applying Eqn. 11 to accommodate prior aneuploidies and updating my stochastic model, I find that chromosome losses seem to have a greater impact on the incidence of nullisomy than chromosome gains. Prior loss of 5 random chromosomes in a diploid background reduced the EC50 from 16 to 9 chromosome mis-segregations whereas 5 gains increased it to 20 chromosome mis-segregations. In a triploid background, 5 losses reduced the EC50 to about 32 chromosome mis-segregations and 5 gains increased it to about 45 chromosome mis-segregations. Again, the EC50 of tetraploid cells was not achieved between the 0-40 chromosome mis-segregations used here.

2.3.5 Summary

In total, these results provide a framework for how nullisomy can be achieved through mis-segregation and reveal that nullisomy may be harder to achieve than

previously thought. This could explain the relatively poor performance of several CIN-inducing drugs in clinical trials as compared to taxanes.

3 MODELING MIS-SEGREGATION RATES WITH RESPECT TO MULTIPOLAR SPINDLE ARCHITECTURE

3.1 Initial Assumptions

1) Mis-segregation occurs solely by nature of distributing two amphitelically attached chromatids (t_1, t_2) over 3+ spindle poles. Accordingly, each chromatid of a pair must attach one spindle pole with mutual exclusion. Erroneous attachments will be explored later.
2) Each existing pole has a non-zero probability of attaching a chromatid.
3) Each spindle pole will ultimately produce a single daughter cell. Alternatives will be explored later.
4) The attachment of each chromatid at a given pole are dependent events such that that they form and attachment matrix (A) where

$$A = t_1 \begin{array}{c|cccc} & t_2 & & & \\ & \Pi_1 & \Pi_2 & \bullet & \Pi_n \\ \hline \Pi_1 & 0 & \frac{\pi_2\pi_1}{1-\pi_1} & \bullet & \frac{\pi_n\pi_1}{1-\pi_1} \\ \Pi_2 & \frac{\pi_1\pi_2}{1-\pi_2} & 0 & \bullet & \frac{\pi_n\pi_2}{1-\pi_2} \\ \bullet & \bullet & \bullet & 0 & \bullet \\ \Pi_i & \frac{\pi_1\pi_n}{1-\pi_n} & \frac{\pi_2\pi_n}{1-\pi_n} & \bullet & 0 \end{array} \tag{12}$$

3.2 A deterministic model of mis-segregation on multipolar spindles

3.2.1 A basic model of spindle multipolarity

Consider a mitotic mother cell M with a set of spindle poles $\Pi = \{\Pi_{\{i\}} \mid i \in I\}$ and spindle pole symmetry $\pi = \{\pi_i \mid i \in I\}$ where I is the index set $I = \{1,2 \ldots, n\}$ that defines each pole and n the total number of poles in the cell. The probability that a given pole (and resultant daughter cell D) will not receive either chromatid of a pair, resulting in mis-segregation through loss, is

$$\alpha = \left(\sum_{j \in I \setminus i} \sum_{k \in I \setminus i; k \neq j} \frac{\pi_j \pi_k}{1 - \pi_k} \right) - \frac{2}{|\pi|} \tag{13}$$

where j, k are pairwise poles of the index set $I \setminus i$. Here $\frac{2}{|\pi|}$ represents the probability of distributing correctly attached toward a given pole and resultant daughter cell while the numerator, 2, is a corrective factor to account for the impossibility of amphitelic mis-segregation occurring on bipolar spindles.

If spindle attachments are dependent events and each pole has an equal probability of forming an attachment to a given chromatid ($\pi_1 = \pi_2 = \ldots = \pi_i$) — spindle symmetry, in other words — then mis-segregation occurs solely by nature of unequal distribution of the genome into the incorrect number of daughter cells. Thus, the mis-segregation rate m for any daughter cell D from mother cell M with euploid ploidy p in this case is

$$m = 23p\alpha \tag{14}$$

3.2.2 Incorporating spindle asymmetry

The above case can easily be adapted to accommodate asymmetric spindles which segregate unequal fractions of the genome. While these cannot necessarily be predicted *a priori* at this time, they are frequently observed after anaphase onset (148). Therefore, they are worth considering.

Assuming all poles receive a non-zero share of the genome, the sum of all pole symmetry values (π) should equal 1. Thus, a symmetric tripole could be represented as $\pi_i \in \{0.\overline{33}, 0.\overline{33}, 0.\overline{33}\}$ and an asymmetric tripole, for example, as $\pi_i \in \{0.45, 0.25, 0.30\}$. In the latter case, Π_1 would have a greater chance of receiving a given chromatid than would Π_2 or Π_3. This would give rise to daughter cells $D_i \in \{1, 2, 3\}$ with an average mis-segregation rate m of 15.3 chromosomes. With the assumption of correct, dependent attachments, these would all yield copy number losses.

3.3 A stochastic model of multipolar divisions

3.3.1 The basic model – multipolar mis-segregation via amphitelic attachment

To stochastically simulate the segregation of chromosomes symmetrically into three daughter cells, I constructed a simple nested 'for' loop to iterate through and distribute homologous sets of sister chromatids to two poles per sister chromatid pair (Algorithm 2, lines 16 and 61-67). This alone, assuming one daughter cell forms from a single spindle pole, would simulate the theoretical scenario where sister chromatids are segregated on proper amphitelic attachments into two daughter cells despite the presence of three spindle poles and in the absence of any additional attachment errors. Thus, this represents the most basic instance in which chromosomes may be mis-segregated.

3.3.2 Clustering: spindle focusing and partial cytokinesis failure

One complicating variable often seen during ongoing multipolar division is the occurrence of partial cytokinesis failure and spindle pole focusing, which I will collectively call ‘clustering’. Partial cytokinesis failure can occur when at least two daughter cells of a multipolar division fail to completely transit mitosis, resulting in the collapse of the would-be daughter cells into one, often forming a binucleated cell. Spindle pole focusing can occur any time prior to cytokinesis and is characterized by the coalescence of two or more discrete spindle poles into one ‘pseudo-pole’. This often results in a ‘pseudo-bipolar’ spindle. For my purposes here, I will consider partial cytokinesis failure and spindle pole focusing to be analogous. To accommodate these phenomena, I include chance for random pairs of ‘poles’ or ‘daughter cells’ to combine to produce a set number of daughter cells from the initial number of spindle poles. This is an iterative process where a random pair of poles is combined to create a new pseudo-pole prior to the next round of clustering (Algorithm 2, lines 68-74). For example, if a cell with 4 poles is made to cluster to 2 daughter cells, there would be 2 rounds of clustering which may either result in 2 pseudo-poles consisting of pairs of the initial 4 poles, or 1 pseudo-pole consisting of 3 of the initial poles, with 1 of the initial poles remaining.

3.3.3 Spindle pole asymmetry

Another complicating variable for the genomic fate of daughter cells resulting from multipolar divisions is the occurrence of asymmetric segregation. The simulation as outlined thus far assumes that each of the daughter cells are equally likely to inherit chromosomes. However, in practice, the chromosome masses in transit to the three or more nascent daughter cells may differ in genomic content. To accommodate this

phenomenon, in several instances in Algorithm 2, I invoke a weighted probability that chromosomes are segregated to individual poles equal to its pre-defined spindle symmetry π_i.

3.3.4 Additional mis-segregation via erroneous attachment

Finally, to accommodate mis-segregation through additional attachment errors in combination with those caused by amphitelic attachment on multipolar spindles, I incorporated probabilities for different types of attachment errors as well as the rate at which these attachment errors are corrected (Algorithm 2, lines 23-60). In this case, the sequential order of attachment error mis-segregations relative to multipolar mis-segregations matters, as attachment errors effectively limit the number of chromosomes which can be mis-segregated amphitelically on multipolar spindles. Likewise, the relative order of attachment errors is meaningful in that atelic attachment errors (unattached chromosomes) effectively limit monotelic attachments and so on. Therefore, the order in which mis-segregations are determined are decided is as follows: atelic, monotelic, syntelic, merotelic, amphitelic (multipolar). Importantly, atelic, monotelic, and syntelic mis-segregations all result in mis-segregation toward the pole that nucleated their erroneous attachments, whereas merotelic attachments may still result in correct segregation.

Once established, I apply these procedures to any number of cell divisions and measure nullisomies, mis-segregation rates, total chromosome numbers, aneuploidy to understand how spindle architecture affects the karyotypes of daughter cells.

3.4 Results

3.4.1 Division on multipolar spindles produces high average baseline rates of mis-segregation, irrespective of spindle symmetry or clustering

To explore the models defined above, I first consider two cases of multipolar spindles: a spindle with three poles and perfect spindle symmetry $\pi_i \in \{0.\overline{33}, 0.\overline{33}, 0.\overline{33}\}$, and one with four poles and asymmetry $\pi_i \in \{0.2, 0.3, 0.1, 0.4\}$, which produce the following attachment matrices (also shown in Figure A1.2A,B).

	Π_1	Π_2	Π_3
Π_1	0	0.17	0.17
Π_2	0.17	0	0.17
Π_3	0.17	0.17	0

	Π_1	Π_2	Π_3	Π_4
Π_1	0	0.08	0.03	0.10
Π_2	0.08	0	0.04	0.17
Π_3	0.03	0.04	0	0.04
Π_4	0.10	0.17	0.04	0

Applying Eqn. 14 across diploid, triploid, and tetraploid cells, I find, as expected, that the average mis-segregation rate in symmetrical tripolar divisions, regardless of ploidy, is about 1/3rd of the total ploidy of the cell: ~15, 23, and 31 chromosomes for diploids, triploids, and tetraploids respectively. On the other hand, average mis-segregation rates for tetrapolar cells were ½ the total ploidy of the cell.

To determine the extent to which the degree of symmetry affects average mis-segregation rate among daughter cells of multipolar divisions, I ran instances of the stochastic model using 500 randomly drawn symmetry vectors for tripolar and tetrapolar spindles and diploid, triploid, and tetraploid cells. I find that the degree of asymmetry, as measured by the variance between symmetry values, has little bearing on the average

mis-segregation rate in daughter cells (Figure A1.2D). Because karyotypes can be considered a closed system when all daughter cells are tracked, no chromosomes are lost or gained. Instead, cells that lose more chromosomes are reciprocated by cells which gain more chromosomes.

This is clear when returning to our pre-defined spindle pole symmetries and track the number of mis-segregations caused in each case. Symmetrical tripolar divisions produce monomodal distributions of mis-segregated chromosomes for all ploidy levels, meaning mis-segregation rates were relatively consistent across daughter cells. However, asymmetric tetrapolar divisions resulted in multimodal distributions that reflect the number of mis-segregations that occurred in each daughter cell. In general, the 'minor' daughter cells with lower spindle symmetry values mis-segregate more chromosomes than 'major' daughter cells. However, the average mis-segregation rate in each case is recapitulated by the deterministic model defined in Eqn. 14 (Figure A1.2E).

Spindle clustering seems to have a similarly small effect on average mis-segregation rates after multipolar division. Stochastic simulations using the same parameters, except forcing spindle clustering down to 2 daughter cells results in very similar mis-segregation rate distributions and averages (Figure A1.2G). This makes the same intuitive sense as before. Mis-segregation is a reciprocal process in a closed system.

3.4.2 Partial spindle clustering following multipolar division results in near-triploid and near-tetraploid karyotypes.

When plotting copy number profiles from the same dataset as in 3.4.1 as heatmaps I found differences in distributions of total ploidy between cells resulting from symmetric

or un-clustered divisions and those from asymmetric and clustered divisions (Figure A1.2F,H). Symmetric un-clustered divisions (Figure A1.2F; heatmaps 4-6 from the left) resulted in populations with a relatively uniform level of karyotype heterogeneity, whereas asymmetric un-clustered divisions (Figure A1.2F; heatmaps 1-3 from the left) resulted in a gradient of total ploidy levels across cells, reflecting their individual ability to capture and inherit chromosomes according to their symmetry value. Likewise symmetric, clustered divisions (Figure A1.2H; heatmaps 4-6 from the left) resulted in a bifurcated population wherein the relative levels of karyotype heterogeneity and ploidy are uniform and where one falls beneath the background ploidy while the other supersedes. Asymmetric clustered divisions gave a similar, if more well-defined gradient as compared to asymmetric un-clustered divisions (Figure A1.2H; heatmaps 1-3 from the left). This suggests that multipolar spindles, while often producing cells with nullisomy, can produce near-triploid and near-tetraploid cells that are often observed in tumors by the same token.

To further understand how total ploidy are affected by spindle clustering and the other CIN factors I simulated additional populations across the gamut of CIN factors discussed thus far as a supplement to analyses moving forward (Figure A1.3). These additional datasets support the role of spindle clustering in producing near-triploid and near-tetraploid cells. Whereas mis-segregation via attachment errors alone was able to produce similar mis-segregation rates as multipolar spindles when pushed high enough (Figure A1.3; rows 1, 10; columns F-J), it did not cause most cells to significantly alter their background ploidy (Figure A1.3; rows1, 10; columns K-O) as compared to spindle clustering, which did. Instead, cells which only experienced attachment errors without

multipolar division exhibited a broadened the distribution of their ploidy around a mean equal to their background ploidy.

Combined, these results indicate that the production of near-triploid and near-tetraploid cells within a single division is a unique feature of multipolar division with asymmetric and/or clustered spindle poles.

3.4.3 Partial spindle clustering can rescue multipolar daughters from nullisomy

As we've seen, multipolar divisions in diploid cells can result in a substantial fraction of sub-haploid cells, particularly in the context of asymmetric genome distributions. Given the certainty that nullisomy occurs in these cells as well as well as the deleterious effect it exerts on real cells, I sought to understand the interaction between multipolar spindle architecture and the incidence of nullisomy in a population.

Simulated symmetric tripolar divisions in diploid populations resulted in an average of about 3 nullisomies per cells when allowed to proceed unclustered (Figure A1.3; row 5; column A) with about 5% of cells exhibiting no nullisomy. Clustering cells in an otherwise identical simulation resulted in about 50% of cells exhibiting no nullisomy. Additional spindly asymmetry in tripolar spindles works to polarize this effect (Figure A1.3; row 3; column A). On one hand, should the two major daughters cluster, the likelihood they experience nullisomy is lower than would be seen in a symmetric division, as would any major daughter alone as it inherits a greater fraction of the genome. However, the minor daughter and any daughter resulting from a clustering event between a major and minor daughter are increasingly likely to experience nullisomy. Nevertheless, clustered populations remain over 50% non-nullisomic. This is amplified in cases of extreme asymmetry

and larger initial pole numbers (Figure A1.3; rows 7, 9). Further, while the numbers of nullisomy per cell are reduced overall, the dynamics of these spindle architectural effects on nullisomy are conserved for tetraploid cells (Figure A1.3; rows 10-18).

As an aside, the karyotypic consequences of multipolar divisions appear to be more extensive than those produced by attachment errors alone (Figure A1.3; rows 1, 10) across total nullisomies, total mis-segregations, and total chromosome number. In each simulated daughter cell population, the addition of attachment errors to multipolar divisions only seems to broaden the extant distribution that is present without attachment errors (Figure A1.3).

These results show that clustering, whether it be through partial cytokinesis failure or spindle pole focusing, can rescue daughter cells of multipolar divisions from nullisomy.

3.4.4 CAL51 daughter cell genomes treated with paclitaxel meet expectations for asymmetric divisions with a high penetrance of partial cytokinesis failure

Lastly, I sought to determine whether these results comport with the previously mentioned biological ground-truth scenario using paclitaxel in CAL51 cells. To do this I used a Kolmogorov-Smirnov test to compare distributions of karyotype characteristics from stochastically simulated populations (diploid background, no additional attachment errors, tripolar spindles, spindle symmetries = {0.333, 0.333, 0.333} or {0.4, 0.4, 0.2} or {0.45, 0.45, 0.1}, 0% clustering, 50% clustering, or 100% clustering) to those from the paclitaxel-treated population (Figures A1.4A-C, red-outlined plots). The Kolmogorov-Smirnof distances between distributions of absolute deviations were most sensitive to genome distribution symmetric and were lowest among the simulations with {0.2, 0.4, 0.4}

symmetries among daughter cells indicating a moderately asymmetric distribution is prevalent in the biological data (Figure A1.4D, left). For the prevalence of nullisomy in the population, simulations where 100 percent of divisions resulted in partial cytokinesis failure exhibited the lowest KSD (Figure A1.4D, right). Together, these results comport with the observed biological circumstances where multipolar spindles are induced by paclitaxel and often experience partial cytokinesis failure. Though, whether these also co-occur with a high degree of asymmetric genomic distribution is yet to be established.

4 DISCUSSION

Multipolar divisions are a relatively infrequent (140), but potent driver of chromosome mis-segregation during tumor progression. Whether the daughter cells that arise from multipolar divisions continue to proliferate has not been fully examined and is likely dependent on other factors like the fraction of the genome received by the daughter cells, and the co-occurrence of partial cytokinesis failure. Though a recent study, which adopted the concept of spindle pole symmetry described here, shows that cells which form from spindle poles that segregated less genomic content are more likely to die (148). Additionally, whole genome doubled cells, which are more likely to undergo multipolar division due to the presence of supernumerary centrosomes, may be more likely to sustain the significant karyotypic insult caused by multipolar division (145, 275, 277, 284, 332). However, the use of paclitaxel to cause cell death by induction of multipolar spindles calls this into question. The relative likelihood of these outcomes is uncertain because the karyotypic consequences of multipolar divisions have not been thoroughly examined.

While paclitaxel is effective for about 50% of patients, the reason for the remaining patients' lack of response is unknown (250, 356). One hypothesis is that non-responding tumors have a lower baseline rate of chromosome mis-segregation and that the added chromosomal instability induced by paclitaxel remains at a tolerable level (249, 265, 266). Another is that a cancer cells' ability to 'cluster' their spindle poles prior to division mediates tolerance to paclitaxel (251). This work lends quantitative credence to the latter hypothesis as simulations of pole clustering significantly reduced the incidence of nullisomy in the population. Moreover, this supports the hypothesis that inhibiting pole clustering may increase the efficacy paclitaxel.

On the other hand, recent work has proposed that multipolar divisions produce 'hopeful monsters', cells whose karyotypes have become highly aneuploid (282). In rare instances, these cells may continue to proliferate with the adaptive advantages of its highly aneuploid karyotype. Spindle clustering drastically reduces the likelihood of nullisomy in daughter cells of multipolar division. Thus, this phenomenon may be a frequent and more parsimonious method of producing viable 'monsters' by inducing significant aneuploidy as well as a whole genome doubled-like state in one of the daughter cells in the same division, a phenomenon which is often observed to occur early in tumor development (196, 274, 277).

A limitation of these simulation experiments is the assumption that all cells will follow the same general rules of division. However, biological systems likely exhibit heterogeneity in these phenotypes, even within the same population. For example, the symmetry

of genomic distributions into daughter cells certainly does not always follow a {20, 40, 40} arrangement; there is a spectrum of symmetry commonly seen in multipolar divisions.

While nullisomy is presumably lethal, more work is needed to determine the viability of cells arising from abnormal divisions that do not produce nullisomy, but a high degree of aneuploidy, nevertheless. This work may well serve as a theoretical baseline against which hypotheses regarding the viability of such cells can be tested.

5 STOCHASTIC ALGORITHMS

Algorithm 1 — Stochastic simulation of chromosome mis-segregation

```
INPUT VARIABLES:
i: iterations
m: mis-segregation rate
p: ploidy

START
 Create k (a G1 karyotype vector with ploidy p)
 FOR i iterations
    Randomly sample m terms from k, without replacement
    Let h be the total number of homologous chromosome sets sampled p times
    Randomly sample a vector 1 to 2^p, h times, with replacement
    Let n (number of nullisomies) be the number of samples = 1
ENDFOR
    Export all n
    Export | Compute average n
END
```

Algorithm 2 — Stochastic simulation of mis-segregation with respect to spindle architecture and attachment.

```
INPUT VARIABLES:
 i: iterations
 poles: the number of spindle poles
 daughters: the number of daughter cells
 symmetries: the symmetry values of all poles
 ζ: probability of atelic attachment error
 ζ’: probability of atelic attachment penetrance
 μ: probability of monotelic attachment error
 μ’: probability of monotelic attachment penetrance
σ: probability of syntelic attachment error
σ’: probability of monotelic attachment penetrance
ψ: probability of merotelic attachment error
ψ’: probability of monotelic attachment penetrance

START
FOR i iterations
   IF poles < daughters
   BREAK
   IF poles ≠ symmetries
   BREAK
   Create k
   Create cells, a matrix with poles rows and 23 columns
   START AtelicMisseg
       FOR chromosome in k
           IF random float (0-1) ≤ ζ x ζ’
               Let selected = 1 random sample of poles, weighted by symmetries
               Let cells[selected, chromosome] = cells[selected, chromosome] + 2
               Remove chromosome from k
           ENDIF
       ENDFOR
   END AtelicMisseg
   START MonotelicMisseg
       FOR chromosome in k
           IF random float (0-1) ≤ μ x μ’
               Let selected = 1 random sample of poles, weighted by symmetries
               Let cells[selected, chromosome] = cells[selected, chromosome] + 2
               Remove chromosome from k
           ENDIF
       ENDFOR
   END MonotelicMisseg
   START SyntelicMisseg
       FOR chromosome in k
           IF random float (0-1) ≤ σ x σ’
               Let selected = 1 random sample of poles, weighted by symmetries
               Let cells[selected, chromosome] = cells[selected, chromosome] + 2
               Remove chromosome from k
           ENDIF
       ENDFOR
   END SyntelicMisseg
   START MerotelicMisseg
       FOR chromosome in k
           IF random float (0-1) ≤ ψ x ψ’
               Let combo = 1 random pole combo, weighted by mean of symmetries
```

```
54              Let selected = 2 random samples combo, weighted by symmetries of combo,
   with replacement
55              Let cells[selected[1], chromosome] = cells[selected[1], chromosome] + 1
56              Let cells[selected[2], chromosome] = cells[selected[1], chromosome] + 1
57              Remove chromosome from k
58          ENDIF
59       ENDFOR
60    END MerotelicMisseg
61 START Segregation
62    FOR chromosomes in k
63       Let selected = 2 random samples of poles, weighted by symmetries
64       Let cells[selected[1], chromosome] = Let cells[selected, chromosome] + 1
65       Let cells[selected[2], chromosome] = Let cells[selected, chromosome] + 1
66    ENDFOR
67 END Segregation
68 IF poles > daughters
69    START Clustering
70       FOR u in 1 to (poles-daughters)
71          Let selected = 2 random rows from cells
72          Let cells = cells where cells[selected] are additively merged
73       ENDFOR
74    END Clustering
75 ENDIF
76    Export | Compute sum k as TotalChromosomes
77    Export | Compute average k as TotalPloidy
78    Export | Compute total chromosomes = 0 as TotalNullisomies
79    Export | Compute abs(k-p) as TotalMissegs
80END
```

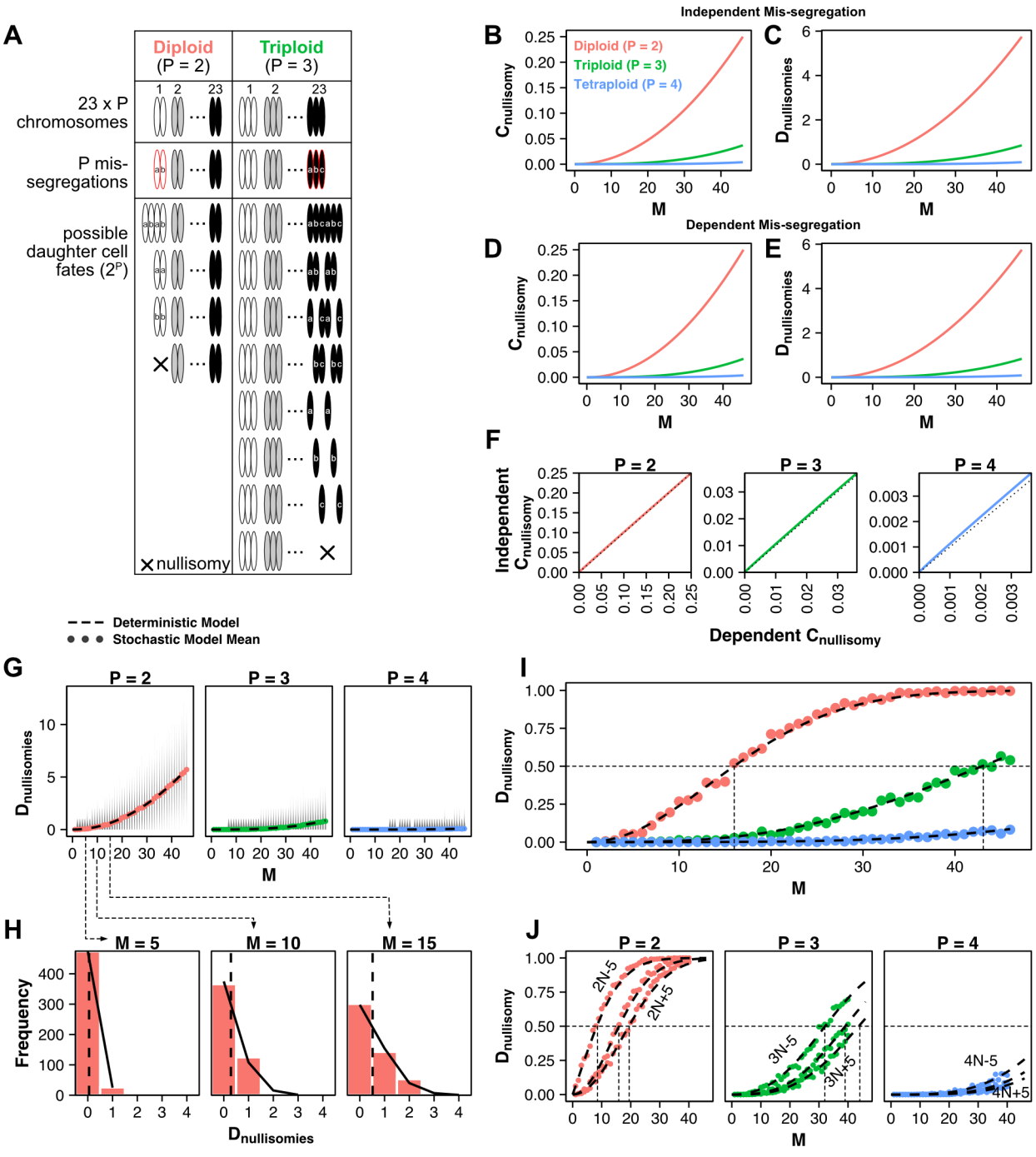

Figure A1.1 — Modeling nullisomy across mis-segregation rates

(A) Schematic of the number of ways in which homologous chromosomes can be mis-segregated in diploid and triploid cells. **(B-E)** probability of nullisomy per homologous chromosome ($C_{nullisomy}$) and frequency of nullisomy with daughter cells ($D_{nullisomies}$) as a function of independent or dependent chromosome mis-segregations in diploid, triploid, and tetraploid cells. **(F)** Correlation of $C_{nullisomy}$ between independent

and dependent chromosome mis-segregation rates across ploidy. **(G)** $D_{nullisomies}$ observed in a stochastic model of mis-segregation in a single division. Distributions of $D_{nullisomies}$ per mis-segregation rate are shown as grey violin plots, average of stochastic model observations shown as solid line, with the deterministic function (Eqn 10) overlaid as a dashed line. **(H)** Histograms of $D_{nullisomies}$ caused by mis-segregation rates of 5, 10, and 15 chromosomes. Average of histogram shown dashed line. Poisson distribution with λ = mean of distribution overlaid as solid line. **(I)** $D_{nullisomy}$ of stochastically simulated populations across ploidies. Averages shown as data points with the deterministic function (Eqn 11) overlaid as a dashed line. (J) Effect of prior chromosome losses or gains on $D_{nullisomy}$ as a function of mis-segregation rate. Data points are means of stochastic simulations. Dashed curves are overlays of the deterministic function (Eqn 11) and straight dashed lines show the EC50 of nullisomy as a function of mis-segregation rate. 250 divisions were simulated for each stochastic simulation.

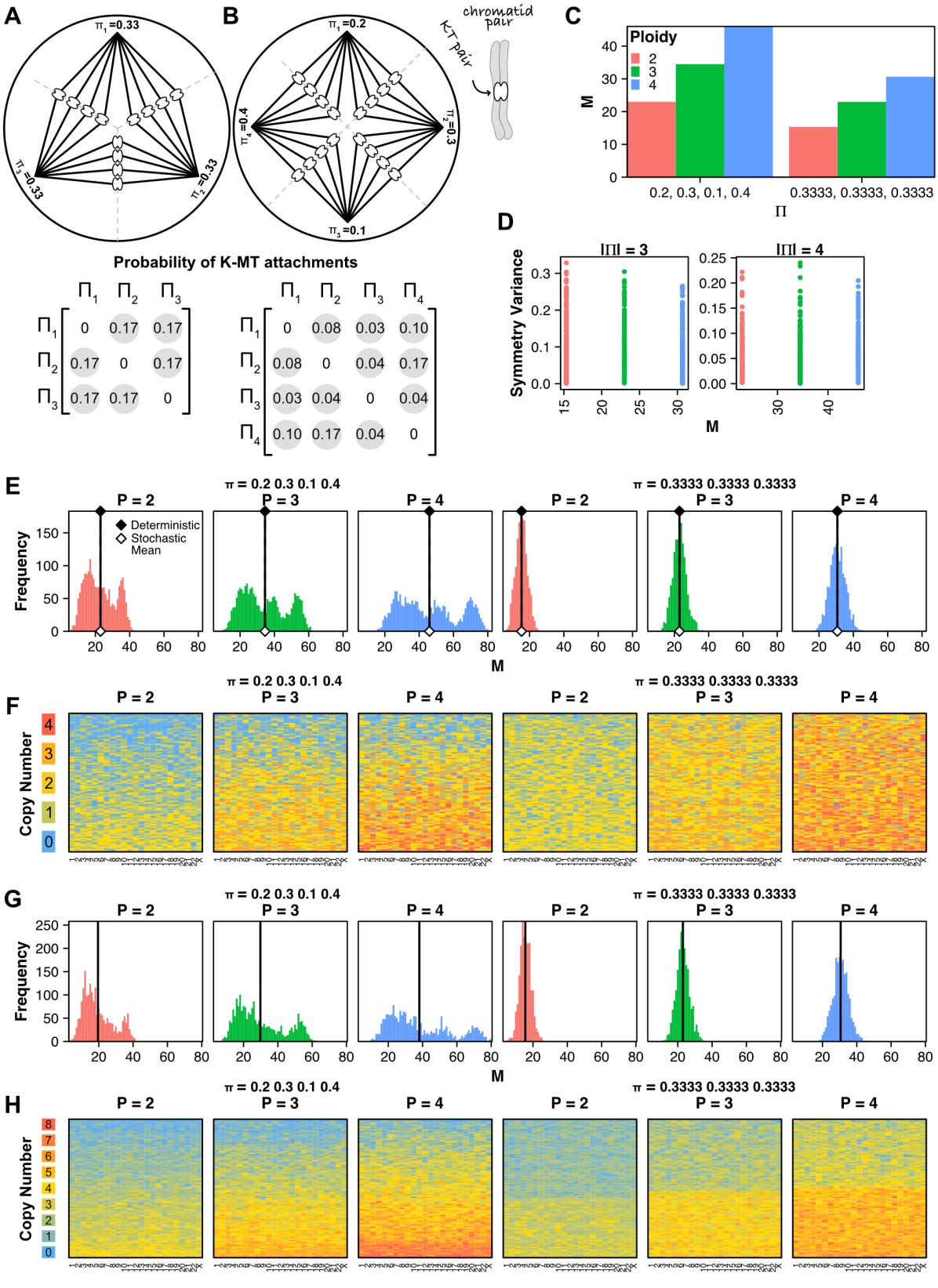

Legend on next page…

Figure A1.2 — Modeling mis-segregation rates with respect to multipolar spindle architecture

(A-B) Schematics and attachment matrices for **(A)** a symmetric tripolar spindle and **(B)** asymmetric tetrapolar spindle. **(C)** Mis-segregation rates calculated from the deterministic model (Eqns 13 and 14). **(D)** Mis-segregation rates variance of symmetry values randomly generated for the stochastic model derived in section 3.3. **(E)** Distribution of mis-segregation rates and **(F)** chromosome copy number heatmaps of daughter cells from multipolar divisions without spindle clustering. **(G)** Distribution of mis-segregation rates and **(H)** chromosome copy number heatmaps of daughter cells from multipolar divisions without spindle clustering. 1000 divisions were simulated for each stochastic simulation. Heatmaps show random sub-samples of 100 cells.

Continued on next page…

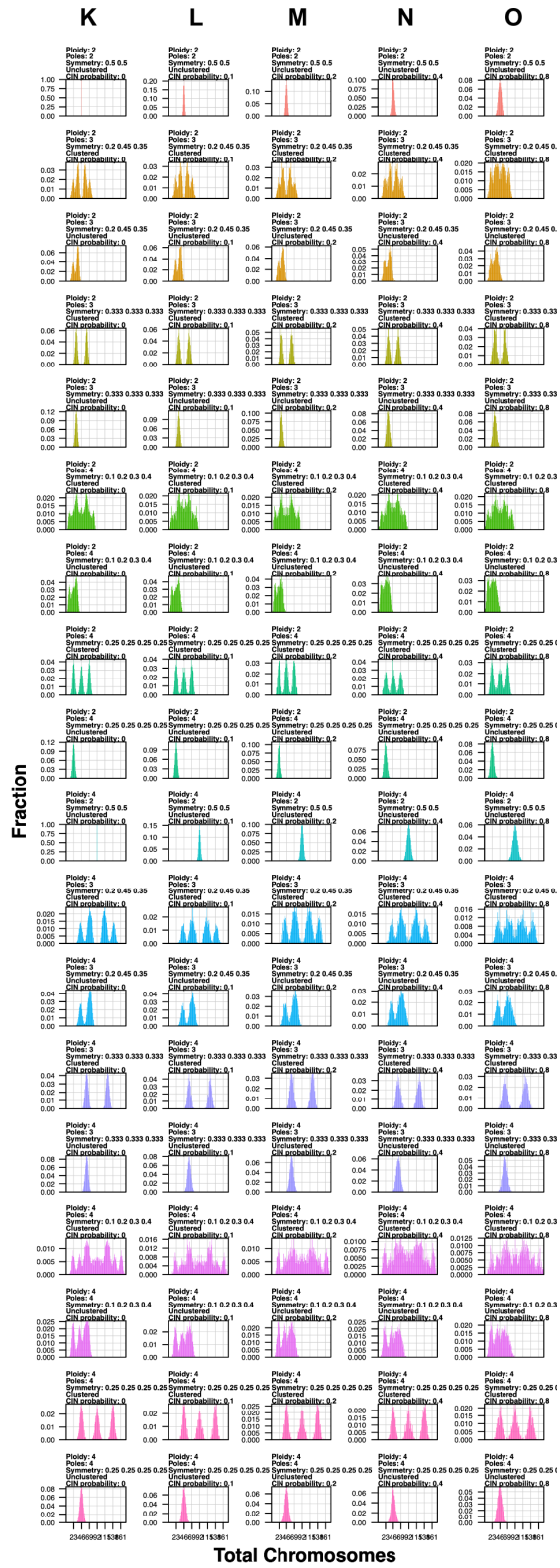

Legend on next page…

Figure A1.3 — Karyotypic features of daughter cells across the CIN gamut

(A-E) Distributions of nullisomic chromosomes, (F-J) distributions of mis-segregated chromosomes, and (K-O) distributions of total chromosome number across 90 configurations of parameters for the stochastic model defined in section 3.3. Rows 1-9 are simulated in a diploid background while rows 10-18 are simulated in a tetraploid background. Colors of distributions define the unique combination of ploidy, pole number, and symmetry values. Columns within each metric (e.g., columns A-E) are defined by the total CIN probability. Total CIN probability represents the sum of all probabilities for each attachment error (i.e., $(\zeta \times \zeta') + (\mu \times \mu') + (\sigma \times \sigma') + (\psi \times \psi')$. These were produced by iterating through the model with attachment error probabilities in {0, 0.05, 0.2} and attachment error penetrance rates in {0, 0.5, 1}.

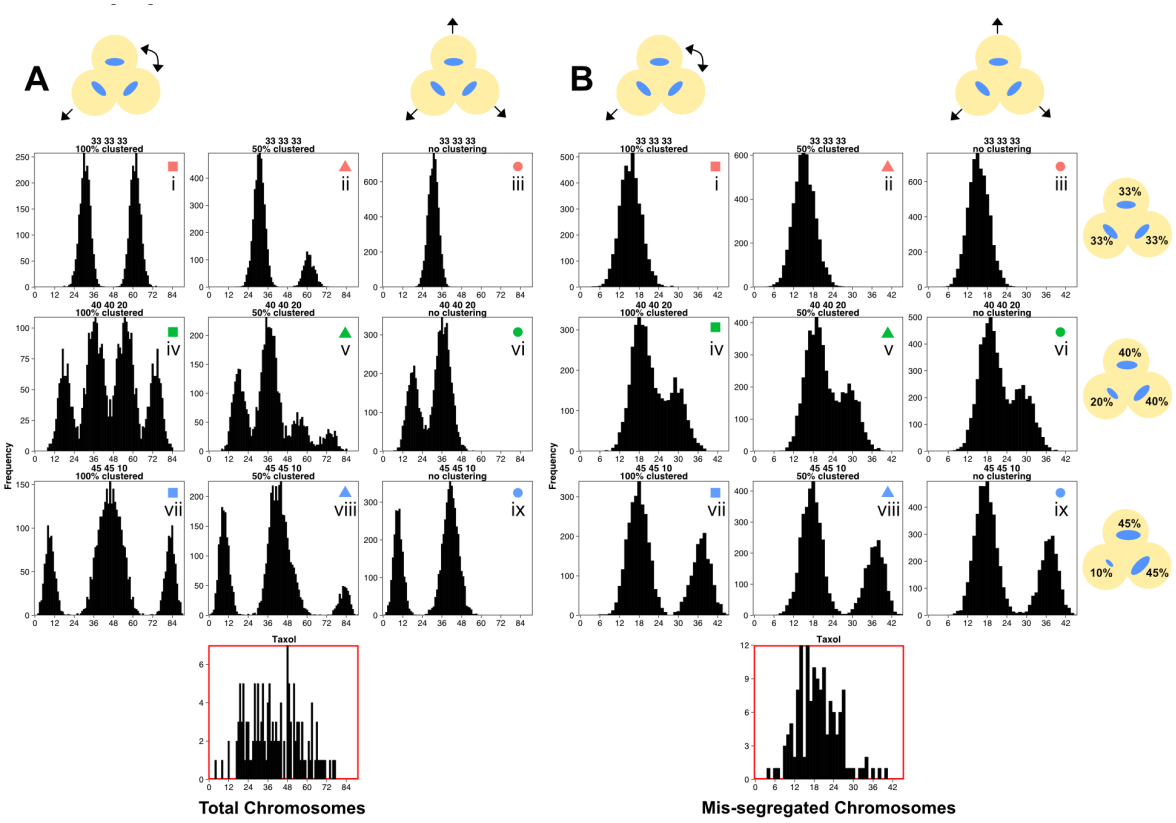

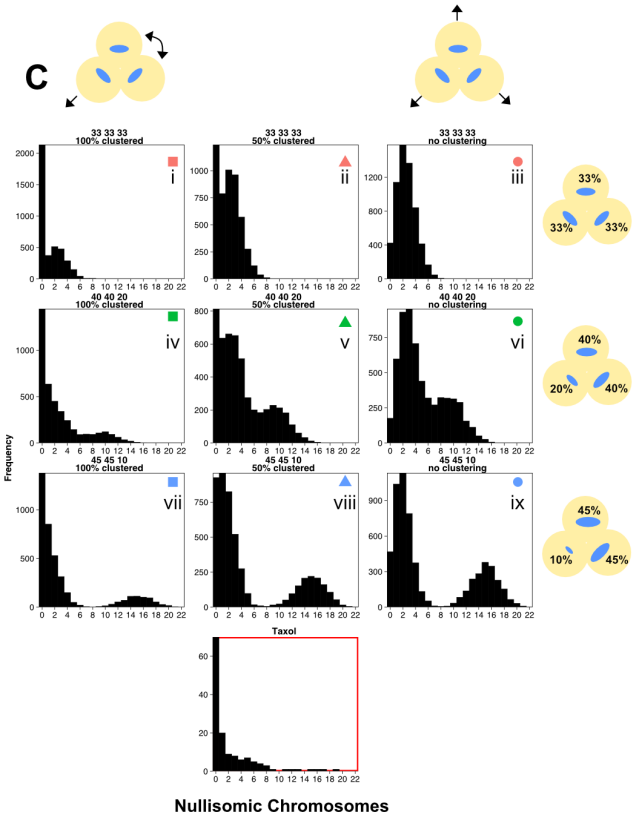

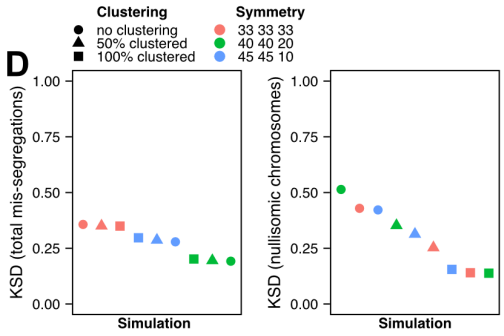

Legend on next page…

Figure A1.4 — CAL51 daughter cell genomes treated with paclitaxel meet expectations for asymmetric divisions with a high penetrance of clustering

(A-C) Distributions of total chromosome number **(A)**, mis-segregated chromosomes **(B)**, and nullisomic chromosomes **(C)** in simulated daughter cell populations after tripolar division with pole symmetries {0.33, 0.33, 0.33}, {0.4, 0.4, 0.2}, and {0.45, 0.45, 0.1} (rows). These divisions involved pole clustering either 100% of the time (left column) , 50% of the time (middle column), or went unclustered (right column). Distributions outlined in red show karyotype charactersitics derived from CAL51 cells treated with 20 nM paclitaxel over 48 hours (from Lynch et al. 2022) **(D)** Kolmogorov-Smirnov distances between mis-segregation and nullisomy distributions from each simulation configuration and the distribution observed in paclitaxel-treated cells. Lower values indicate a better fit. Data points correspond to those indicated in the upper-right corner of each distribution's panel.

APPENDIX 2: MIS-SEGREGATIONS PER DIPLOID DIVISION (MDD)

Table A2.1 — MDD: a standardized measure of mis-segregation rates

Chromosome mis-segregation rates are affected by multiple factors:

1. The number of apparent attachment errors (e.g., lagging chromosomes) per abnormal division.
2. The rate of abnormal division (i.e. penetrance of CIN).
3. The rate of resolved attachment errors (i.e., resolution rate).
4. The number of chromosomes in a cell (i.e., ploidy).

Cells can present with mis-segregations in several ways. Some cell lines may mis-segregate a chromosome every other division. Others may undergo multipolar division every 10 divisions, mis-segregating many chromosomes in a punctuated burst. Further, the appearance of attachment errors does not guarantee a chromosome mis-segregation. In some instances, the chromosome defect will ultimately resolve and segregate to the correct daughter cell. Even if any given chromosome in a cell line mis-segregates at the same rate, the background ploidy of a cell may change the apparent magnitude of a defect by nature of a higher chromosome number.

We propose a standardized measure of CIN that accounts for the above factors to accurately convey the number of mis-segregations per diploid division (MDD).

Observed errors → Mis-segregation per chromosome per division (MCD)

$$\boldsymbol{MCD} = \frac{(\boldsymbol{Errors\ per\ Abnormal\ Division} \times \boldsymbol{Abnormal\ Division\ Rate}) \times (\mathbf{1} - \boldsymbol{Resolution\ Rate})}{\boldsymbol{\#\ Modal\ Chromosomes}}$$

MCD → Mis-segregations per diploid division (MDD)

$$\boldsymbol{MDD} = \boldsymbol{MCD} \times \mathbf{46}$$

Example 1: HCT116 cells with 45 chromosomes where 23% of divisions present 1 lagging chromosome, but a resolution rate is unknown.

$$\boldsymbol{MDD} = \left(\frac{(\mathbf{1} \times \mathbf{0.23})}{\mathbf{45}}\right) \times \mathbf{46}$$

$$\boldsymbol{MDD} = \mathbf{0.235}$$

Example 2: HCT116 cells with 45 chromosomes where 23% of divisions present 1 lagging chromosome, and a resolution rate of 70%.

$$\boldsymbol{MDD} = \left(\frac{(\mathbf{1} \times \mathbf{0.23}) \times (\mathbf{1} - \mathbf{0.7})}{\mathbf{45}}\right) \times \mathbf{46}$$

$$\boldsymbol{MDD} = \mathbf{0.071}$$

Example 3: Near-tetraploid HCT116 cells with 90 chromosomes where 46% of divisions present 1 lagging chromosome, and a resolution rate of 70%.

$$\boldsymbol{MDD} = \left(\frac{(\mathbf{1} \times \mathbf{0.46}) \times (\mathbf{1} - \mathbf{0.7})}{\mathbf{90}}\right) \times \mathbf{46}$$

$$\boldsymbol{MDD} = \mathbf{0.071}$$

See Tables 2 and 3 for more information.

Table A2.2 — CIN rates in human cancers and cancer models

Type	Cancer Status	Sample	Method	Mitotic Phenotype	Observed Frequency	MCD	MDD	Ploidy	Acquisition Method	Ref
Tissue	Cancer	DLBCL	Mitotic Analysis	Lagging + Bridging	31.3	0.0068	0.313	46[a]	Reported	(237)
Cell Line	Cancer	U2OS	Mitotic Analysis	Lagging	32.5	0.00707	0.325	46	Approximate	(286)
Cell Line	Cancer	HeLa	Mitotic Analysis	Lagging	22	0.00268	0.123	82[b]	Approximate	(286)
Cell Line	Cancer	SW-620	Mitotic Analysis	Lagging	22.5	0.00450	0.207	50[b]	Approximate	(286)
Cell Line	Non-cancer	RPE1	Mitotic Analysis	Lagging	2.5	0.00054	0.025	46	Approximate	(286)
Cell Line	Non-cancer	BJ	Mitotic Analysis	Lagging	8	0.00174	0.080	46[b]	Approximate	(286)
Cell Line	Non-cancer	Primary Amniocytes	Mitotic Analysis	Lagging	0	0	0	46	Approximate	(285)
Cell Line	Cancer	DLD1	Mitotic Analysis	Lagging	1	0.0002	0.009	46	Approximate	(285)
Cell Line	Cancer	HCT116	Mitotic Analysis	Lagging + Bridging	23	0.0051	0.235	45[b]	Approximate	(284)
Cell Line	Cancer	HCT116	Mitotic Analysis	Lagging + Bridging	50	0.0056	0.258	90[b]	Approximate	(284)
Cell Line	Cancer	U2OS	Mitotic Analysis	Lagging	-—	0.0100	0.460	46	Reported	(137)
Cell Line	Cancer	CAL51	Mitotic Analysis	Lagging	0.5	0.00011	0.005	44	Approximate	(249)
Cell Line	Non-cancer	RPE1	FISH	—	—	0.00025	0.012	46	Approximate	(122)
Cell Line	Cancer	HCT116	FISH	—	—	0.00025	0.012	45[b]	Approximate	(122)
Cell Line	Cancer	HT29	FISH	—	—	0.0025	0.115	71[b]	Approximate	(122)
Cell Line	Cancer	CACO2	FISH	—	—	0.009	0.414	96[b]	Approximate	(122)
Cell Line	Cancer	MCF-7	FISH	—	—	0.007	0.322	82[b]	Approximate	(122)
Cell Line	Non-cancer	BJ	Mitotic Analysis	Unspecified	5	0.00109	0.050	46[b]	Approximate	(157)
Cell Line	Non-cancer	RPE1	Mitotic Analysis	Unspecified	5	0.00109	0.050	46	Approximate	(157)
Cell Line	Cancer	HCT116	Mitotic Analysis	Lagging	6	0.00133	0.060	45[b]	Approximate	(136)
Cell Line	Cancer	DLD1	Mitotic Analysis	Lagging	2	0.00043	0.020	46[b]	Approximate	(136)
Cell Line	Cancer	HT29	Mitotic Analysis	Lagging	14	0.00197	0.140	71[b]	Approximate	(136)
Cell Line	Cancer	SW-620	Mitotic Analysis	Lagging	12	0.00240	0.120	50[b]	Approximate	(136)

Cell Line	Cancer	MCF-7	Mitotic Analysis	Lagging	17	0.00207	0.095	82[b]	Approximate	(136)
Cell Line	Cancer	HeLa	Mitotic Analysis	Lagging	13	0.00159	0.073	82[b]	Approximate	(136)
Tissue	Cancer	BRCA	Mitotic Analysis	Misaligned + Lagging + Bridging	20	0.0057	0.262	46[a]	Reported	(140)
Organ-oid	Cancer	CRC	Mitotic Analysis	Misaligned + Lagging + Bridging + Multipolar	2 - 50	0.0004 - 0.0068	0.020 - 0.311	45 - 74	Approximate	(138)

Extended from and originally compiled in Lynch et al. eLife. 2022. (***a)*** indicates assumed ploidy value and ***(b)*** indicates ploidy retrieved from ATCC.

Table A2.3 — Mis-segregations per diploid division (MDD)

Mis-segregations per erroneous diploid (tetraploid) division	Penetrance of erroneous divisions (%)						
	0	**10**	**20**	**40**	**60**	**80**	**100**
0 (0)	0	0	0	0	0	0	0
1 (2)	0	0.1	0.2	0.4	0.6	0.8	1
2 (4)	0	0.2	0.4	0.8	1.2	1.6	2
4 (8)	0	0.4	0.8	1.6	2.4	3.2	4
8 (16)	0	0.8	1.6	3.2	4.8	6.4	8
16 (32)	0	1.6	3.2	6.4	9.6	12.8	16

REFERENCES

1. W. T. Kelvin, *Popular Lectures and Addresses: In Three Volumes. Constitution of matter* (MacMillan and Company, 1889).
2. T. Boveri, *Zur frage der entstehung maligner tumoren* (Fischer, 1914).
3. D. Hansemann, Ueber pathologische mitosen. *Archiv für pathologische Anatomie und Physiologie und für klinische Medicin* **123**, 356–370 (1891).
4. D. Hansemann, Ueber asymmetrische Zelltheilung in Epithelkrebsen und deren biologische Bedeutung. *Archiv f. pathol. Anat.* **119**, 299–326 (1890).
5. R. S. Whipple, The History of the Microscope: Compiled from Original Instruments and Documents, up to the Introduction of the Achromatic Microscope (1933).
6. R. Hooke, J. Allestry, J. Martyn, *Micrographia, or, Some physiological descriptions of minute bodies made by magnifying glasses :with observations and inquiries thereupon* (Printed by Jo. Martyn and Ja. Allestry, printers to the Royal Society, 1665).
7. I. M. Davis, “Round, red globules floating in a crystalline fluid” – Antoni van Leeuwenhoek’s observations of red blood cells and hemocytes. *Micron* **157**, 103249 (2022).
8. A. van Leeuwenhoek, Alle de brieven. Deel 4: 1683-1684.

9. R. Brown, XXXV. On the Organs and Mode of Fecundation in Orchideæ and Asclepiadeæ. *Transactions of the Linnean Society of London* **os-16**, 685–738 (1833).

10. H. von Mohl, E. Frisoni, *Über die Verbindung der Pflanzen-Zellen unter einander* (Fues, 1835).

11. R. Remak, Ueber extracellulare Entstehung thierischer Zellen und über Vermehrung derselben durch Theilung. *Archiv für Anatomie, Physiologie und wissenschaftliche Medicin* **1852**, 47–57 (1852).

12. R. Virchow, Cellular-Pathologie. *Archiv f. pathol. Anat.* **8**, 3–39 (1855).

13. F. Redi, *Esperienze intorno alla generazione degl'insetti* (All'insegna della Stella, 1668).

14. C. Darwin, A. Wallace, On the Tendency of Species to form Varieties; and on the Perpetuation of Varieties and Species by Natural Means of Selection. *Journal of the Proceedings of the Linnean Society of London. Zoology* **3**, 45–62 (1858).

15. G. Mendel, Versuche über Plflanzenhybriden. *Verhandlungen des naturforschenden Vereines in Brünn, Bd. IV für das Jahr* **Bd. IV**, 3–47 (1865).

16. R. Dahm, Friedrich Miescher and the discovery of DNA. *Developmental Biology* **278**, 274–288 (2005).

17. O. Hertwig, R. Hertwig, *Experimentelle Untersuchungen über die Bedingungen der Bastardbefruchtung* (G. Fischer, 1885).

18. W. His, F. Miescher. *Die histochemischen und physiologischen Arbeiten von Friedrich Miescher* **1**, 5–32 (1897).

19. J. F. Miescher, *Ueber die chemische Zusammensetzung der Eiterzellen* (1871).

20. J. Arnold, Beobachtungen über Kerntheilungen in den Zellen der Geschwülste. *Archiv für pathologische Anatomie und Physiologie und für klinische Medicin* **78**, 279–301 (1879).

21. W. Flemming, *Zellsubstanz, kern und zelltheilung* (Vogel, 1882).

22. W. Waldeyer, Ueber Karyokinese und ihre Beziehungen zu den Befruchtungsvorgängen. *Archiv f. mikrosk. Anatomie* **32**, 1–122 (1888).

23. H. Zacharias, Key word: Chromosome. *Chromosome Res* **9**, 345–355 (2001).

24. H. Satzinger, Theodor and Marcella Boveri: chromosomes and cytoplasm in heredity and development. *Nat Rev Genet* **9**, 231–238 (2008).

25. O. Hertwig, R. Hertwig, *Uber den Befruchtungs-und Teilungsvorgang des tierischen Eies: unter dem Einflufs äusserer Agentien* (G. Fischer, 1887).

26. T. Boveri, Ein geschlechtlich erzeugter Organismus ohne mütterliche Eigenschaften. Sitz Gesel Morph u Physiol Müchen 5, 73–83 Trans by TH Morgan 1893, as “An organism produced sexually without characteristics of the mother.” *Am Naturalist* **27**, 222–232 (1889).

27. T. Boveri, *Zellen-Studien: Die Befruchtung und Teilung des Eies von Ascaris megalocephala* (G. Fischer, 1888).

28. G. Galeotti, Beitrag zum Studium des Chromatins in den Epithelzellen der Carcinome. *Beitr. Pathol. Anat. Allg. Pathol* **14**, 249–271 (1893).

29. D. Hansemann, *Die mikroscopische Diagnose der bösartigen Geschwülste* (Hirschwald, 1897).

30. P. A. Hardy, H. Zacharias, Reappraisal of the Hansemann–Boveri hypothesis on the origin of tumors. *Cell biology international* **29**, 983–992 (2005).

31. T. Boveri, Ueber mehrpolige Mitosen als Mittel zur Analyse des Zelkerns. *Wurzburg C. Kabitzsch und Verh d Phys Med Ges Zu Wurzburg NF Bd* **35** (1902).

32. C. F. J. E. G. Correns, Mendel's Regel uber das Verhalten der Nachkommenschaft der Rassenbastarde. *Ber. dtsch. botanisch. Ges* **18**, 158–167 (1900).

33. H. M. de Vries, Das Spaltungsgesetz der bastarde. *Ber. dtsch. hot. Ges* **18**, 83–90 (1900).

34. J. Mendel, Verhandlungen des naturforschenden vereines in brünn. *Abhandlungen* **4**, 3–47 (1865).

35. E. Tschermak, *Über künstliche Kreuzung bei Pisum sativum* (E. Tschermak, 1900).

36. T. Boveri, Uber Differenzierung der Zellkerne wahrend der Furchung des Eies von Ascaris megalocephala. *Anat. Anz.* **2**, 688–693 (1887).

37. T. Boveri, *Zellen-Studien: Die Bildung der Richtungskörper bei Ascaris megalocephala und Ascaris lümbricoides* (G. Fischer, 1887).

38. F. Maderspacher, Theodor Boveri and the natural experiment. *Current Biology* **18**, R279–R286 (2008).

39. T. Boveri, *Ergebnisse über die Konstitution der chromatischen Substanz des Zellkerns* (Verlag von Gustav Fischer in Jena, 1904).

40. W. S. Sutton, THE CHROMOSOMES IN HEREDITY. *The Biological Bulletin* **4**, 231–250 (1903).

41. W. S. Sutton, ON THE MORPHOLOGY OF THE CHROMOSO GROUP IN BRACHYSTOLA MAGNA. *The Biological Bulletin* **4**, 24–39 (1902).

42. P. Della Valle, *L'organizzazione della cromatina studiata mediante il numero dei cromosomi: memoria di Paolo Della Valle* (Stabilimento tipografico Francesco Giannini & figli, 1909).

43. A. Volpone, Chromosomenindividualität or Entmischung? The debate between Paolo Della Valle and Edmund B. Wilson. *Hist Philos Life Sci* **36**, 404–414 (2015).

44. M. Boveri, Ueber mitosen bei einseitiger chromosomenbindung. *Jenaische Zeitschrift für Naturwissenschaft* **37**, 401–443 (1903).

45. H. Satzinger, The chromosomal theory of heredity and the problem of gender equality in the work of Theodor and Marcella Boveri in (Berlin, 2005), pp. 101–114.

46. C. B. Bridges, Non-Disjunction as Proof of the Chromosome Theory of Heredity (Concluded). *Genetics* **1**, 107–163 (1916).

47. C. B. Bridges, Direct Proof Through Non-Disjunction That the Sex-Linked Genes of Drosophila Are Borne by the X-Chromosome. *Science* **40**, 107–109 (1914).

48. C. B. Bridges, Non-disjunction of the sex chromosomes of Drosophila. *Journal of Experimental Zoology* **15**, 587–606 (1913).

49. R. R. Gates, Mutation in Oenothera. *The American Naturalist* **45**, 577–606 (1911).

50. R. T. Hance, Variations in the Number of Somatic Chromosomes in OENOTHERA SCINTILLANS De Vries. *Genetics* **3**, 225–275 (1918).

51. C. Ford, Non-disjunction in Oenothera and the genesis of trisomics. *Journal of Genetics* **33**, 275–303 (1936).

52. S. R. Safir, Genetic and Cytological Examination of the Phenomena of Primary Non-Disjunction in DROSOPHILA MELANOGASTER. *Genetics* **5**, 459–487 (1920).

53. R. A. Emerson, Genetical Studies of Variegated Pericarp in Maize. *Genetics* **2**, 1–35 (1917).

54. W. H. Eyster, A Genetic Analysis of Variegation. *Genetics* **9**, 372–404 (1924).

55. H. K. Hayes, Inheritance of a Mosaic Pericarp Pattern Color of Maize. *Genetics* **2**, 261–281 (1917).

56. E. G. Anderson, The Constitution of Primary Exceptions Obtained after X-Ray Treatment of Drosophila. *Genetics* **16**, 386–396 (1931).

57. E. G. Anderson, Studies on a case of high non-disjunction inDrosophila melanogaster. *Z.Ver-erbungslehre* **51**, 397–441 (1929).

58. M. Demerec, J. G. Farrow, Relation between the X-Ray Dosage and the Frequency of Primary Non-Disjunctions of X-Chromosomes in Drosophila virilis1. *Proceedings of the National Academy of Sciences of the United States of America* **16**, 711–714 (1930).

59. J. W. Mavor, Gynandromorphs from X-Rayed Mothers. *The American Naturalist* **58**, 525–529 (1924).

60. J. W. Mavor, The Production of Non-Disjunction by X-rays. *Science* **55**, 295–297 (1922).

61. J. Patterson, X-rays and somatic mutations. *Journal of Heredity* **20**, 261–267 (1929).

62. J. T. Patterson, Proof That the Entire Chromosome Is Not Eliminated in the Production of Somatic Variations by X-Rays in Drosophila. *Genetics* **15**, 141–149 (1930).

63. L. J. Stadler, Genetic Effects of X-Rays in Maize. *Proceedings of the National Academy of Sciences* **14**, 69–75 (1928).

64. G. W. Beadle, Chromosome Aberration and Gene Mutation in Sticky Chromosome Plants of *Zea mays*. *Cytologia* **FujiiJubilaei**, 43–56 (1937).

65. G. W. Beadle, A gene for sticky chromosomes inZea mays. *Z.Ver-erbungslehre* **63**, 195–217 (1933).

66. B. McClintock, A Correlation of Ring-Shaped Chromosomes with Variegation in Zea Mays. *Proceedings of the National Academy of Sciences* **18**, 677–681 (1932).

67. B. McClintock, The Order of the Genes C, Sh and Wx in Zea Mays with Reference to a Cytologically Known Point in the Chromosome. *Proceedings of the National Academy of Sciences* **17**, 485–491 (1931).

68. M. M. Rhoades, A Cytogenetical Study of a Reciprocal Translocation in Zea*. *Proceedings of the National Academy of Sciences* **19**, 1022–1031 (1933).

69. B. McClintock, The Stability of Broken Ends of Chromosomes in Zea Mays. *Genetics* **26**, 234–282 (1941).

70. B. McClintock, The Production of Homozygous Deficient Tissues with Mutant Characteristics by Means of the Aberrant Mitotic Behavior of Ring-Shaped Chromosomes. *Genetics* **23**, 315–376 (1938).

71. B. McClintock, The production of maize plants mosaic for homozygous deficiencies: Simulation of the bm1 phenotype through loss of the Bm1 locus. *Genetics* **22**, 200 (1937).

72. R. J. Ludford, I.—Chemically Induced Derangements of Cell Division*. *Journal of the Royal Microscopical Society* **73**, 1–23 (1953).

73. P. C. Koller, A New Technique for Mitosis in Tumours. *Nature* **149**, 193–193 (1942).

74. P. C. Koller, Abnormal Mitosis in Tumours. *Br J Cancer* **1**, 38–47 (1947).

75. F. Zernike, Das Phasenkontrastverfahren bei der mikroskopischen Beobachtung. *Physik. Zeitschr.* **36**, 848–851 (1935).

76. L. R. Cleveland, The Whole Life Cycle of Chromosomes and Their Coiling Systems. *Transactions of the American Philosophical Society* **39**, 1–97 (1949).

77. A. F. Hughes, M. M. Swann, Anaphase Movements in the Living Cell : A Study With Phase Contrast and Polarized Light on Chick Tissue Cultures. *Journal of Experimental Biology* **25**, 45–72 (1948).

78. S. Inouéa, K. Dan, Birefringenoe of the dividing cell: BIREFRINGENOE OF DIVIDING CELL. *J. Morphol.* **89**, 423–455 (1951).

79. S. Inouéa, Polarization optical studies of the mitotic spindle: I. The demonstration of spindle fibers in living cells. *Chromosoma* **5**, 487–500 (1953).

80. J. F. Enders, General Preface to Studies on the Cultivation of Poliomyelitis Viruses in Tissue Culture. *The Journal of Immunology* **69**, 639–643 (1952).

81. H. Eagle, The specific amino acid requirements of a mammalian cell (strain L) in tissue culture. *Journal of Biological Chemistry* **214**, 839–852 (1955).

82. Go. Gey, Tissue culture studies of the proliferative capacity of cervical carcinoma and normal epithelium. *Cancer research* **12**, 264–265 (1952).

83. T.-C. Hsu, Mammalian chromosomes in vitro: I. The karyotype of man. *Journal of Heredity* **43**, 167–172 (1952).

84. T. C. Hsu, C. M. Pomerat, Mammalian Chromosomes in Vitro: II. A Method for Spreading the Chromosomes of Cells in Tissue Culture. *Journal of Heredity* **44**, 23–30 (1953).

85. T. S. Hauschka, A. Levan, Inverse relationship between chromosome ploidy and host-specificity of sixteen transplantable tumors. *Experimental Cell Research* **4**, 457–467 (1953).

86. I. T. JH, A. Levan, The chromosome number of man. *Hereditas* **42**, 1–6 (1956).

87. The Human Chromosome Study Group, A proposed standard system of nomenclature of human mitotic chromosomes. *Journal of Heredity* **51**, 214–221 (1960).

88. J. D. Watson, F. H. C. Crick, Molecular Structure of Nucleic Acids: A Structure for Deoxyribose Nucleic Acid. *Nature* **171**, 737–738 (1953).

89. A. Levan, J. J. Biesele, ROLE OF CHROMOSOMES IN CANCEROGENESIS, AS STUDIED IN SERIAL TISSUE CULTURE OF MAMMALIAN CELLS. *Ann NY Acad Sci* **71**, 1022–1053 (1958).

90. C. Ford, A SEX-CHROMOSOME ANOMALY IN A CASE OF GONADAL DYSGENESIS (TURNER'S SYNDROME). *The Lancet* **273**, 711–713 (1959).

91. P. A. Jacobs, J. A. Strong, A Case of Human Intersexuality Having a Possible XXY Sex-Determining Mechanism. *Nature* **183**, 302–303 (1959).

92. J. Lejeune, Etude des chromosomes somatiques de neuf enfants mongoliens. *L'Acaddemie des Sciences Paris* **248**, 1713–1727 (1959).

93. P. C. Nowell, A minute chromosome in human chronic granulocytic leukemia. *Science* **132**, 1497 (1960).

94. D. Cox, C. Yuncken, Arthurl. Spriggs, MINUTE CHROMATIN BODIES IN MALIGNANT TUMOURS OF CHILDHOOD. *The Lancet* **286**, 55–58 (1965).

95. J. German, CYTOLOGICAL EVIDENCE FOR CROSSING-OVER IN VITRO IN HUMAN LYMPHOID CELLS. *Science* **144**, 298–301 (1964).

96. T. M. Schroeder, Cytogenetische und cytologische Befunde bei enzymopenischen Panmyelopathien und Pancytopenien. *Hum Genet* **2**, 287–316 (1966).

97. F. Mitelman, The chromosomes of fifty primary Rous rat sarcomas. *Hereditas* **69**, 155–186 (1971).

98. A. I. Spriggs, M. M. Boddington, C. M. Clarke, Chromosomes of Human Cancer Cells. *Br Med J* **2**, 1431–1435 (1962).

99. H. Kato, A. A. Sandberg, Chromosome pulverization in human cells with micronuclei. *Journal of the National Cancer Institute* **40**, 165–179 (1968).

100. I. Cortés-Ciriano, *et al.*, Comprehensive analysis of chromothripsis in 2,658 human cancers using whole-genome sequencing. *Nat Genet* **52**, 331–341 (2020).

101. M. Kneissig, *et al.*, Micronuclei-based model system reveals functional consequences of chromothripsis in human cells. *eLife* **8**, e50292 (2019).

102. P. Ly, *et al.*, Chromosome segregation errors generate a diverse spectrum of simple and complex genomic rearrangements. *Nat Genet* **51**, 705--715 (2019).

103. J. Maciejowski, *et al.*, APOBEC3-dependent kataegis and TREX1-driven chromothripsis during telomere crisis. *Nat Genet* **52**, 884–890 (2020).

104. P. J. Stephens, *et al.*, Massive Genomic Rearrangement Acquired in a Single Catastrophic Event during Cancer Development. *Cell* **144**, 27–40 (2011).

105. C.-Z. Zhang, *et al.*, Chromothripsis from DNA damage in micronuclei. *Nature* **522**, 179–184 (2015).

106. J. Camps, *et al.*, Comprehensive measurement of chromosomal instability in cancer cells: combination of fluorescence in situ hybridization and cytokinesis-block micronucleus assay. *FASEB j.* **19**, 1–19 (2005).

107. M. Seabright, A rapid banding technique for human chromosomes. *The Lancet* **298**, 971–972 (1971).

108. A. Sumner, H. Evans, R. Buckland, New technique for distinguishing between human chromosomes. *Nature New Biology* **232**, 31–32 (1971).

109. J. D. Rowley, A new consistent chromosomal abnormality in chronic myelogenous leukaemia identified by quinacrine fluorescence and Giemsa staining. *Nature* **243**, 290–293 (1973).

110. E. Schröck, *et al.*, Multicolor Spectral Karyotyping of Human Chromosomes. *Science* **273**, 494–497 (1996).

111. M. R. Speicher, S. G. Ballard, D. C. Ward, Karyotyping human chromosomes by combinatorial multi-fluor FISH. *Nat Genet* **12**, 368–375 (1996).

112. A. V. Roschke, *et al.*, Karyotypic Complexity of the NCI-60 Drug-Screening Panel. *Cancer Research* **63**, 8634–8647 (2003).

113. F. Mitelman, H. P. Klinger, *Catalogue of Chromosome Aberrations in Cancer* (Karger Medical and Scientific Publishers, 1983).

114. J. Wang, *et al.*, A cloud-based resource for genome coordinate-based exploration and large-scale analysis of chromosome aberrations and gene fusions in cancer. *Genes, Chromosomes and Cancer* **n/a** (2023).

115. Y. Fan, *et al.*, Frequency of double minute chromosomes and combined cytogenetic abnormalities and their characteristics. *J Appl Genetics* **52**, 53–59 (2011).

116. L. M. Zasadil, E. M. C. Britigan, B. A. Weaver, 2n or not 2n: Aneuploidy, polyploidy and chromosomal instability in primary and tumor cells. *Seminars in Cell & Developmental Biology* **24**, 370–379 (2013).

117. L. A. Ernst, R. K. Gupta, R. B. Mujumdar, A. S. Waggoner, Cyanine dye labeling reagents for sulfhydryl groups. *Cytometry* **10**, 3–10 (1989).

118. J. G. J. Bauman, J. Wiegant, P. Borst, P. van Duijn, A new method for fluorescence microscopical localization of specific DNA sequences by in situ hybridization of fluorochrome-labelled RNA. *Experimental Cell Research* **128**, 485–490 (1980).

119. J. G. Gall, M. L. Pardue, Formation and detection of RNA-DNA hybrid molecules in cytological preparations. *Proceedings of the National Academy of Sciences* **63**, 378–383 (1969).

120. P. R. Langer-Safer, M. Levine, D. C. Ward, Immunological method for mapping genes on Drosophila polytene chromosomes. *Proceedings of the National Academy of Sciences* **79**, 4381–4385 (1982).

121. C. Lengauer, K. W. Kinzler, B. Vogelstein, Genetic instability in colorectal cancers. *Nature* **386**, 623–627 (1997).

122. S. L. Thompson, D. A. Compton, Examining the link between chromosomal instability and aneuploidy in human cells. *J Cell Biology* (2008) https:/doi.org/10.1083/jcb.200712029.

123. D.-S. Yoon, *et al.*, Variable Levels of Chromosomal Instability and Mitotic Spindle Checkpoint Defects in Breast Cancer. *The American Journal of Pathology* **161**, 391–397 (2002).

124. R. G. Gould, The LASER, light amplification by stimulated emission of radiation in (1959), p. 92.

125. D. A. Jackson, R. H. Symons, P. Berg, Biochemical Method for Inserting New Genetic Information into DNA of Simian Virus 40: Circular SV40 DNA Molecules

Containing Lambda Phage Genes and the Galactose Operon of Escherichia coli. *Proceedings of the National Academy of Sciences* **69**, 2904–2909 (1972).

126. T. H. Maiman, Stimulated Optical Radiation in Ruby. *Nature* **187**, 493–494 (1960).

127. O. Shimomura, F. H. Johnson, Y. Saiga, Extraction, Purification and Properties of Aequorin, a Bioluminescent Protein from the Luminous Hydromedusan, Aequorea. *Journal of Cellular and Comparative Physiology* **59**, 223–239 (1962).

128. M. Chalfie, Y. Tu, G. Euskirchen, W. W. Ward, D. C. Prasher, Green Fluorescent Protein as a Marker for Gene Expression. *Science* **263**, 802–805 (1994).

129. D. C. Prasher, V. K. Eckenrode, W. W. Ward, F. G. Prendergast, M. J. Cormier, Primary structure of the Aequorea victoria green-fluorescent protein. *Gene* **111**, 229–233 (1992).

130. W. Deng, X. Shi, R. Tjian, T. Lionnet, R. H. Singer, CASFISH: CRISPR/Cas9-mediated in situ labeling of genomic loci in fixed cells. *Proceedings of the National Academy of Sciences* **112**, 11870–11875 (2015).

131. H. Ma, *et al.*, Multicolor CRISPR labeling of chromosomal loci in human cells. *Proceedings of the National Academy of Sciences* **112**, 3002–3007 (2015).

132. P. Qin, *et al.*, Live cell imaging of low- and non-repetitive chromosome loci using CRISPR-Cas9. *Nat Commun* **8**, 14725 (2017).

133. D. Cimini, *et al.*, Merotelic Kinetochore Orientation Is a Major Mechanism of Aneuploidy in Mitotic Mammalian Tissue Cells. *J Cell Biol* **153**, 517–528 (2001).

134. D. Cimini, D. Fioravanti, E. D. Salmon, F. Degrassi, Merotelic kinetochore orientation versus chromosome mono-orientation in the origin of lagging

chromosomes in human primary cells. *Journal of Cell Science* **115**, 507–515 (2002).

135. D. Cimini, B. Moree, J. C. Canman, E. D. Salmon, Merotelic kinetochore orientation occurs frequently during early mitosis in mammalian tissue cells and error correction is achieved by two different mechanisms. *J Cell Sci* **116**, 4213–4225 (2003).

136. S. F. Bakhoum, *et al.*, The mitotic origin of chromosomal instability. *Curr Biol* **24**, R148–R149 (2014).

137. S. F. Bakhoum, S. L. Thompson, A. L. Manning, D. A. Compton, Genome stability is ensured by temporal control of kinetochore–microtubule dynamics. *Nat Cell Biol* **11**, 27–35 (2009).

138. A. C. F. Bolhaqueiro, *et al.*, Ongoing chromosomal instability and karyotype evolution in human colorectal cancer organoids. *Nat Genet* **51**, 824–834 (2019).

139. L. Nelson, *et al.*, A living biobank of ovarian cancer ex vivo models reveals profound mitotic heterogeneity. *Nat Commun* (2020) https:/doi.org/10.1038/s41467-020-14551-2.

140. J. B. Tucker, *et al.*, Misaligned Chromosomes are a Major Source of Chromosomal Instability in Breast Cancer. *Cancer Research Communications* **3**, 54–65 (2023).

141. D. R. Hoffelder, *et al.*, Resolution of anaphase bridges in cancer cells. *Chromosoma* **112**, 389–397 (2004).

142. S. L. Thompson, D. A. Compton, Chromosome missegregation in human cells arises through specific types of kinetochore–microtubule attachment errors. *Proceedings of the National Academy of Sciences* **108**, 17974–17978 (2011).

143. A. M. Gomes, *et al.*, Micronuclei from misaligned chromosomes that satisfy the spindle assembly checkpoint in cancer cells. *Current Biology* **32**, 4240-4254.e5 (2022).

144. S. A. Godinho, D. Pellman, Causes and consequences of centrosome abnormalities in cancer. *Philosophical Transactions Royal Soc B Biological Sci* **369**, 20130467--20130467 (2014).

145. N. J. Ganem, S. A. Godinho, D. Pellman, A mechanism linking extra centrosomes to chromosomal instability. *Nature* **460**, 278–282 (2009).

146. W. T. Silkworth, I. K. Nardi, L. M. Scholl, D. Cimini, Multipolar Spindle Pole Coalescence Is a Major Source of Kinetochore Mis-Attachment and Chromosome Mis-Segregation in Cancer Cells. *PLOS ONE* **4**, e6564 (2009).

147. A. R. Lynch, N. L. Arp, A. S. Zhou, B. A. Weaver, M. E. Burkard, Quantifying chromosomal instability from intratumoral karyotype diversity using agent-based modeling and Bayesian inference. *eLife* **11**, e69799 (2022).

148. A. S. Zhou, *et al.*, Chromosome missegregation on multipolar spindles is a conserved mechanism of microtubule poisons (in review).

149. Z. Xu, *et al.*, Deep Learning Predicts Chromosomal Instability from Histopathology Images. *Iscience*, 102394 (2021).

150. D. R. Stirling, *et al.*, CellProfiler 4: improvements in speed, utility and usability. *BMC Bioinformatics* **22**, 433 (2021).

151. S. Berg, *et al.*, ilastik: interactive machine learning for (bio)image analysis. *Nat Methods* **16**, 1226–1232 (2019).

152. W. Dittrich, W. Göhde, Notizen: Impulsfluorometrie bei Einzelzellen in Suspensionen. *Zeitschrift für Naturforschung B* **24**, 360–361 (1969).

153. F. Traganos, Z. Darzynkiewicz, T. Sharpless, M. R. Melamed, Nucleic acid content and cell cycle distribution of five human bladder cell lines analysed by flow cytofluorometry. *International Journal of Cancer* **20**, 30–36 (1977).

154. R. Miglierina, M. Le Coniat, R. Berger, A simple diagnostic test for Fanconi anemia by flow cytometry. *Anal Cell Pathol* **3**, 111–118 (1991).

155. H. Hui, *et al.*, Imaging flow cytometry to assess chromosomal abnormalities in chronic lymphocytic leukaemia. *Methods* **134–135**, 32–40 (2018).

156. R. C. Wilkins, M. A. Rodrigues, L. A. Beaton-Green, The Application of Imaging Flow Cytometry to High-Throughput Biodosimetry. *Genome Integr* **8**, 7 (2017).

157. J. T. Worrall, *et al.*, Non-random Mis-segregation of Human Chromosomes. *Cell Reports* **23**, 3366–3380 (2018).

158. L. H. Hartwell, D. Smith, Altered fidelity of mitotic chromosome transmission in cell cycle mutants of S. cerevisiae. *Genetics* **110**, 381–395 (1985).

159. P. Hieter, C. Mann, M. Snyder, R. W. Davis, Mitotic stability of yeast chromosomes: a colony color assay that measures nondisjunction and chromosome loss. *Cell* **40**, 381–392 (1985).

160. M. A. Hoyt, T. Stearns, D. Botstein, Chromosome instability mutants of Saccharomyces cerevisiae that are defective in microtubule-mediated processes. *Mol Cell Biol* **10**, 223–234 (1990).

161. V. W. Mayer, A. Aguilera, High levels of chromosome instability in polyploids of Saccharomyces cerevisiae. *Mutation Research/Fundamental and Molecular Mechanisms of Mutagenesis* **231**, 177–186 (1990).

162. H.-S. Lee, *et al.*, A new assay for measuring chromosome instability (CIN) and identification of drugs that elevate CIN in cancer cells. *BMC Cancer* **13**, 252 (2013).

163. M. Liskovykh, *et al.*, A novel assay to screen siRNA libraries identifies protein kinases required for chromosome transmission. *Genome Res.* **29**, 1719–1732 (2019).

164. S. Markossian, A. Arnaoutov, N. S. Saba, V. Larionov, M. Dasso, Quantitative assessment of chromosome instability induced through chemical disruption of mitotic progression. *Cell Cycle* **15**, 1706–1714 (2016).

165. A. Kallioniemi, *et al.*, Comparative genomic hybridization for molecular cytogenetic analysis of solid tumors. *Science* **258**, 818–821 (1992).

166. S. du Manoir, *et al.*, Detection of complete and partial chromosome gains and losses by comparative genomic in situ hybridization. *Hum Genet* **90**, 590–610 (1993).

167. S. Solinas-Toldo, *et al.*, Matrix-based comparative genomic hybridization: biochips to screen for genomic imbalances. *Genes Chromosomes Cancer* **20**, 399–407 (1997).

168. C. Xie, M. T. Tammi, CNV-seq, a new method to detect copy number variation using high-throughput sequencing. *Bmc Bioinformatics* **10**, 80 (2009).

169. C. A. Klein, *et al.*, Genetic heterogeneity of single disseminated tumour cells in minimal residual cancer. *The Lancet* **360**, 683–689 (2002).

170. C. Le Caignec, *et al.*, Single-cell chromosomal imbalances detection by array CGH. *Nucleic Acids Res* **34**, e68 (2006).

171. M. Kohlruss, *et al.*, A microsatellite based multiplex PCR method for the detection of chromosomal instability in gastric cancer. *Sci Rep* **8**, 12551 (2018).

172. M. Kohlruss, *et al.*, Diverse 'just-right' levels of chromosomal instability and their clinical implications in neoadjuvant treated gastric cancer. *Br J Cancer* **125**, 1621–1631 (2021).

173. P. J. Campbell, *et al.*, Identification of somatically acquired rearrangements in cancer using genome-wide massively parallel paired-end sequencing. *Nat Genet* **40**, 722–729 (2008).

174. D. A. Wheeler, *et al.*, The complete genome of an individual by massively parallel DNA sequencing. *nature* **452**, 872–876 (2008).

175. D. Pinkel, *et al.*, High resolution analysis of DNA copy number variation using comparative genomic hybridization to microarrays. *Nat Genet* **20**, 207–211 (1998).

176. D. Y. Chiang, *et al.*, High-resolution mapping of copy-number alterations with massively parallel sequencing. *Nat Methods* **6**, 99–103 (2009).

177. L. Deleye, *et al.*, Shallow whole genome sequencing is well suited for the detection of chromosomal aberrations in human blastocysts. *Fertil Steril* **104**, 1276-1285.e1 (2015).

178. S.-F. Chin, *et al.*, Shallow whole genome sequencing for robust copy number profiling of formalin-fixed paraffin-embedded breast cancers. *Exp Mol Pathol* **104**, 161–169 (2018).

179. M. Gerlinger, *et al.*, Intratumor heterogeneity and branched evolution revealed by multiregion sequencing. *N Engl J Med* **366**, 883–892 (2012).

180. A. Sottoriva, *et al.*, A Big Bang model of human colorectal tumor growth. *Nat Genet* **47**, 209–216 (2015).

181. L. R. Yates, *et al.*, Subclonal diversification of primary breast cancer revealed by multiregion sequencing. *Nat Med* **21**, 751–759 (2015).

182. M. Jamal-Hanjani, *et al.*, Tracking the Evolution of Non–Small-Cell Lung Cancer. *New Engl J Medicine* **376**, 2109--2121 (2017).

183. Y. A. Jakubek, F. A. San Lucas, P. Scheet, Directional allelic imbalance profiling and visualization from multi-sample data with RECUR. *Bioinformatics* **35**, 2300–2302 (2019).

184. T. B. K. Watkins, *et al.*, Pervasive chromosomal instability and karyotype order in tumour evolution. *Nature*, 1–7 (2020).

185. G. Macintyre, *et al.*, Copy number signatures and mutational processes in ovarian carcinoma. *Nat Genet* **50**, 1262–1270 (2018).

186. R. M. Drews, *et al.*, A pan-cancer compendium of chromosomal instability. *Nature* (2022) https:/doi.org/10.1038/s41586-022-04789-9 (June 16, 2022).

187. S. L. Carter, A. C. Eklund, I. S. Kohane, L. N. Harris, Z. Szallasi, A signature of chromosomal instability inferred from gene expression profiles predicts clinical outcome in multiple human cancers. *Nat Genet* **38**, 1043--1048 (2006).

188. N. J. Birkbak, *et al.*, Paradoxical relationship between chromosomal instability and survival outcome in cancer. *Cancer Res* **71**, 3447–3452 (2011).

189. J. M. Sheltzer, A transcriptional and metabolic signature of primary aneuploidy is present in chromosomally unstable cancer cells and informs clinical prognosis. *Cancer Res* **73**, 6401–6412 (2013).

190. L. N. Redman-Rivera, *et al.*, Acquisition of aneuploidy drives mutant p53-associated gain-of-function phenotypes. *Nat Commun* **12**, 5184 (2021).

191. N. Navin, *et al.*, Tumour evolution inferred by single-cell sequencing. *Nature* **472**, 90--95 (2011).

192. T. Baslan, *et al.*, Genome-wide copy number analysis of single cells. *Nat Protoc* **7**, 1024--1041 (2012).

193. C. Hiley, E. C. de Bruin, N. McGranahan, C. Swanton, Deciphering intratumor heterogeneity and temporal acquisition of driver events to refine precision medicine. *Genome Biology* **15**, 453 (2014).

194. Y. Wang, *et al.*, Clonal evolution in breast cancer revealed by single nucleus genome sequencing. *Nature* **512**, 155--160 (2014).

195. B. Bakker, *et al.*, Single-cell sequencing reveals karyotype heterogeneity in murine and human malignancies. *Genome Biology* **17**, 115 (2016).

196. R. Gao, *et al.*, Punctuated copy number evolution and clonal stasis in triple-negative breast cancer. *Nat Genet* **48**, 1119--1130 (2016).

197. B. E. Stranger, *et al.*, Relative Impact of Nucleotide and Copy Number Variation on Gene Expression Phenotypes. *Science* **315**, 848–853 (2007).

198. E. M. Torres, *et al.*, Effects of aneuploidy on cellular physiology and cell division in haploid yeast. *Science* (2007) https:/doi.org/10.1126/science.1142210.

199. B. R. Williams, *et al.*, Aneuploidy affects proliferation and spontaneous immortalization in mammalian cells. *Science* (2008) https:/doi.org/10.1126/science.1160058.

200. N. Pavelka, *et al.*, Aneuploidy confers quantitative proteome changes and phenotypic variation in budding yeast. *Nature* **468**, 321--325 (2010).

201. S. Stingele, *et al.*, Global analysis of genome, transcriptome and proteome reveals the response to aneuploidy in human cells. *Mol Syst Biol* **8**, 608 (2012).

202. N. Dephoure, *et al.*, Quantitative proteomic analysis reveals posttranslational responses to aneuploidy in yeast. *eLife* **3**, e03023 (2014).

203. Y. Zhao, *et al.*, Single-cell RNA sequencing reveals the impact of chromosomal instability on glioblastoma cancer stem cells. *BMC Medical Genomics* **12**, 79 (2019).

204. J. M. Sheltzer, E. M. Torres, M. J. Dunham, A. Amon, Transcriptional consequences of aneuploidy. *Proceedings of the National Academy of Sciences* **109**, 12644–12649 (2012).

205. M. Dürrbaum, *et al.*, Unique features of the transcriptional response to model aneuploidy in human cells. *Bmc Genomics* **15**, 139 (2014).

206. A. P. Patel, *et al.*, Single-cell RNA-seq highlights intratumoral heterogeneity in primary glioblastoma. *Science* **344**, 1396–1401 (2014).

207. J. Fan, *et al.*, Linking transcriptional and genetic tumor heterogeneity through allele analysis of single-cell RNA-seq data. *Genome Res* **28**, 1217--1227 (2018).

208. A. Serin Harmanci, A. O. Harmanci, X. Zhou, CaSpER identifies and visualizes CNV events by integrative analysis of single-cell or bulk RNA-sequencing data. *Nat Commun* **11**, 89 (2020).

209. R. Gao, *et al.*, Delineating copy number and clonal substructure in human tumors from single-cell transcriptomes. *Nat Biotechnol* **39**, 599–608 (2021).

210. A. De Falco, F. Caruso, X.-D. Su, A. Iavarone, M. Ceccarelli, A variational algorithm to detect the clonal copy number substructure of tumors from scRNA-seq data. *Nat Commun* **14**, 1074 (2023).

211. K. Crasta, *et al.*, DNA breaks and chromosome pulverization from errors in mitosis. *Nature* **482**, 53–58 (2012).

212. M. L. Leibowitz, *et al.*, Chromothripsis as an on-target consequence of CRISPR–Cas9 genome editing. *Nat Genet* **53**, 895–905 (2021).

213. P. C. Nowell, The Clonal Evolution of Tumor Cell Populations. *Science* **194**, 23--28 (1976).

214. S. E. Shackney, *et al.*, Model for the Genetic Evolution of Human Solid Tumors1. *Cancer Research* **49**, 3344–3354 (1989).

215. Y. Gusev, V. Kagansky, W. C. Dooley, Long-Term Dynamics of Chromosomal Instability in Cancer: A Transition Probability Model. *Mathematical and Computer Modelling* **33**, 1253--1273 (2001).

216. Y. Gusev, V. Kagansky, W. C. Dooley, Y. Gussv, Stochastic Model of Chromosome Segregation Errors with Reference to Cancer Cells. *Mathematical and Computer Modelling* **32**, 97--111 (2000).

217. A. V. Roschke, K. Stover, G. Tonon, A. A. Schäffer, I. R. Kirsch, Stable karyotypes in epithelial cancer cell lines despite high rates of ongoing structural and numerical chromosomal instability. *Neoplasia* **4**, 19–31 (2002).

218. M. L. Leung, *et al.*, Single-cell DNA sequencing reveals a late-dissemination model in metastatic colorectal cancer. *Genome Res.* **27**, 1287–1299 (2017).

219. E. H. Lips, *et al.*, Genomic analysis defines clonal relationships of ductal carcinoma in situ and recurrent invasive breast cancer. *Nat Genet* **54**, 850–860 (2022).

220. D. C. Minussi, *et al.*, Breast tumours maintain a reservoir of subclonal diversity during expansion. *Nature*, 1–7 (2021).

221. T. Davoli, *et al.*, Cumulative haploinsufficiency and triplosensitivity drive aneuploidy patterns and shape the cancer genome. *Cell* **155**, 948--962 (2013).

222. I. Ban, L. Tomašić, M. Trakala, I. M. Tolić, N. Pavin, Proliferative advantage of specific aneuploid cells drives evolution of tumor karyotypes. *Biophysical Journal*, S0006349523000334 (2023).

223. S. Elizalde, A. M. Laughney, S. F. Bakhoum, A Markov chain for numerical chromosomal instability in clonally expanding populations. *Plos Comput Biol* **14**, e1006447 (2018).

224. A. M. Laughney, S. Elizalde, G. Genovese, S. F. Bakhoum, Dynamics of Tumor Heterogeneity Derived from Clonal Karyotypic Evolution. *Cell Reports* **12**, 809--820 (2015).

225. D. C. Hintzen, *et al.*, The impact of monosomies, trisomies and segmental aneuploidies on chromosomal stability. *PLoS ONE* **17**, e0268579 (2022).

226. J. M. Sheltzer, A. Amon, The aneuploidy paradox: costs and benefits of an incorrect karyotype. *Trends Genet* **27**, 446--453 (2011).

227. E. M. Torres, B. R. Williams, A. Amon, Aneuploidy: cells losing their balance. *Genetics* **179**, 737--46 (2008).

228. W. Cross, *et al.*, Stabilising selection causes grossly altered but stable karyotypes in metastatic colorectal cancer. *Biorxiv*, 2020.03.26.007138 (2020).

229. A. Mooers, S. B. Heard, Inferring evolutionary process from phylogenetic tree shape. *Q Rev Biology* (1997) https:/doi.org/10.1086/419657.

230. C. Colijn, J. Gardy, Phylogenetic tree shapes resolve disease transmission patterns. *Evol Medicine Public Heal* (2014) https:/doi.org/10.1093/emph/eou018.

231. R. A. Neher, C. A. Russell, B. I. Shraiman, Predicting evolution from the shape of genealogical trees. *Elife* (2014) https:/doi.org/10.7554/elife.03568.

232. J. G. Scott, P. K. Maini, A. R. A. Anderson, A. G. Fletcher, Inferring Tumour Proliferative Organisation from Phylogenetic Tree Measures in a Computational Model. *Systematic Biol* (2019) https:/doi.org/10.1093/sysbio/syz070.

233. B. Bakker, *et al.*, "Predicting CIN rates from single-cell whole genome sequencing data using an *in silico* model" (Cancer Biology, 2023) https:/doi.org/10.1101/2023.02.14.528596 (February 22, 2023).

234. G. J. Kimmel, *et al.*, Intra-tumor heterogeneity, turnover rate and karyotype space shape susceptibility to missegregation-induced extinction. *PLOS Computational Biology* **19**, e1010815 (2023).

235. Y. Hu, *et al.*, Paclitaxel Induces Micronucleation and Activates Pro-Inflammatory cGAS–STING Signaling in Triple-Negative Breast Cancer. *Molecular Cancer Therapeutics* **20**, 2553–2567 (2021).

236. D. Yang, *et al.*, Lineage tracing reveals the phylodynamics, plasticity, and paths of tumor evolution. *Cell* **185**, 1905-1923.e25 (2022).

237. S. F. Bakhoum, O. V. Danilova, P. Kaur, N. B. Levy, D. A. Compton, Chromosomal instability substantiates poor prognosis in patients with diffuse large B-cell lymphoma. *Clin Cancer Res* **17**, 7704--11 (2011).

238. S. F. Bakhoum, *et al.*, Chromosomal instability drives metastasis through a cytosolic DNA response. *Nature* **553**, 467--472 (2018).

239. K. A. Knouse, K. E. Lopez, M. Bachofner, A. Amon, Chromosome Segregation Fidelity in Epithelia Requires Tissue Architecture. *Cell* **175**, 200--211.e13 (2018).

240. A. J. X. Lee, *et al.*, Chromosomal instability confers intrinsic multidrug resistance. *Cancer Res* **71**, 1858--1870 (2011).

241. D. A. Lukow, *et al.*, Chromosomal instability accelerates the evolution of resistance to anti-cancer therapies. *Dev Cell* (2021) https:/doi.org/10.1016/j.devcel.2021.07.009.

242. V. Girish, *et al.*, “Oncogene-like addiction to aneuploidy in human cancers” (Cancer Biology, 2023) https:/doi.org/10.1101/2023.01.09.523344 (January 11, 2023).

243. M. R. Ippolito, *et al.*, Gene copy-number changes and chromosomal instability induced by aneuploidy confer resistance to chemotherapy. *Dev Cell* (2021) https:/doi.org/10.1016/j.devcel.2021.07.006.

244. L. Sansregret, *et al.*, APC/C Dysfunction Limits Excessive Cancer Chromosomal Instability. *Cancer Discov* **7**, 218–233 (2017).

245. A. D. Silk, *et al.*, Chromosome missegregation rate predicts whether aneuploidy will promote or suppress tumors. *Proc National Acad Sci* **110**, E4134--E4141 (2013).

246. W. H. M. Hoevenaar, *et al.*, Degree and site of chromosomal instability define its oncogenic potential. *Nat Commun* **11**, 1501 (2020).

247. B. A. A. Weaver, A. D. Silk, C. Montagna, P. Verdier-Pinard, D. W. Cleveland, Aneuploidy Acts Both Oncogenically and as a Tumor Suppressor. *Cancer Cell* (2007) https:/doi.org/10.1016/j.ccr.2006.12.003.

248. G. J. P. L. Kops, D. R. Foltz, D. W. Cleveland, Lethality to human cancer cells through massive chromosome loss by inhibition of the mitotic checkpoint. *Proceedings of the National Academy of Sciences* **101**, 8699–8704 (2004).

249. L. M. Zasadil, *et al.*, Cytotoxicity of paclitaxel in breast cancer is due to chromosome missegregation on multipolar spindles. *Sci Transl Med* **6**, 229ra43 (2014).

250. J. O'Shaughnessy, W. J. Gradishar, P. Bhar, J. Iglesias, Nab-Paclitaxel for first-line treatment of patients with metastatic breast cancer and poor prognostic factors: A retrospective analysis. *Breast Cancer Res Tr* (2013) https:/doi.org/10.1007/s10549-013-2447-8.

251. C. M. Scribano, *et al.*, Chromosomal instability sensitizes patient breast tumors to multipolar divisions induced by paclitaxel. *Sci Transl Med* **13**, eabd4811 (2021).

252. D. Hanahan, R. A. Weinberg, Hallmarks of Cancer: The Next Generation. *Cell* **144**, 646--674 (2011).

253. J. M. Hancock, M. J. Zvelebil, M. Griffith, O. L. Griffith, "Mitelman Database (Chromosome Aberrations and Gene Fusions in Cancer)" in *Dictionary of Bioinformatics and Computational Biology*, (2004) https:/doi.org/10.1002/9780471650126.dob0996.

254. K. A. Knouse, T. Davoli, S. J. Elledge, A. Amon, Aneuploidy in Cancer: Seq-ing Answers to Old Questions. *Annu Rev Cancer Biology* **1**, 335--354 (2017).

255. B. A. Weaver, D. W. Cleveland, Does aneuploidy cause cancer? *Curr Opin Cell Biol* **18**, 658–667 (2006).

256. F. Foijer, *et al.*, Deletion of the MAD2L1 spindle assembly checkpoint gene is tolerated in mouse models of acute T-cell lymphoma and hepatocellular carcinoma. *Elife* **6**, e20873 (2017).

257. M. S. Levine, *et al.*, Centrosome Amplification Is Sufficient to Promote Spontaneous Tumorigenesis in Mammals. *Dev Cell* **40**, 313--322.e5 (2017).

258. M. R. Ippolito, *et al.*, Aneuploidy-driven genome instability triggers resistance to chemotherapy. *Biorxiv*, 2020.09.25.313924 (2020).

259. D. A. Lukow, *et al.*, Chromosomal instability accelerates the evolution of resistance to anti-cancer therapies. *Biorxiv*, 2020.09.25.314229 (2020).

260. R. A. Denu, *et al.*, Centrosome amplification induces high grade features and is prognostic of worse outcomes in breast cancer. *Bmc Cancer* **16**, 1--13 (2016).

261. J. M. Sheltzer, *et al.*, Single-chromosome Gains Commonly Function as Tumor Suppressors. *Cancer Cell* **31**, 240--255 (2017).

262. A. Vasudevan, *et al.*, Single-Chromosomal Gains Can Function as Metastasis Suppressors and Promoters in Colon Cancer. *Dev Cell* (2020) https:/doi.org/10.1016/j.devcel.2020.01.034.

263. L. C. Funk, *et al.*, p53 Is Not Required for High CIN to Induce Tumor Suppression. *Mol Cancer Res* **19**, 112–123 (2021).

264. B. A. Weaver, D. W. Cleveland, The Aneuploidy Paradox in Cell Growth and Tumorigenesis. *Cancer Cell* **14**, 431–433 (2008).

265. A. Janssen, G. J. P. L. Kops, R. H. Medema, Elevating the frequency of chromosome mis-segregation as a strategy to kill tumor cells. *Proc National Acad Sci* (2009) https:/doi.org/10.1073/pnas.0904343106.

266. C. Swanton, *et al.*, Chromosomal instability determines taxane response. *Proc National Acad Sci* **106**, 8671--8676 (2009).

267. T. Davoli, H. Uno, E. C. Wooten, S. J. Elledge, Tumor aneuploidy correlates with markers of immune evasion and with reduced response to immunotherapy. *Science* **355**, eaaf8399 (2017).

268. S. Santaguida, *et al.*, Chromosome Mis-segregation Generates Cell-Cycle-Arrested Cells with Complex Karyotypes that Are Eliminated by the Immune System. *Dev Cell* (2017) https:/doi.org/10.1016/j.devcel.2017.05.022.

269. N. Jin, *et al.*, Chromosomal instability upregulates interferon in acute myeloid leukemia. *Genes Chromosomes Cancer* **59**, 627–638 (2020).

270. M. Dumont, *et al.*, Human chromosome-specific aneuploidy is influenced by DNA-dependent centromeric features. *Embo J*, e102924 (2019).

271. C. Kim, *et al.*, Chemoresistance Evolution in Triple-Negative Breast Cancer Delineated by Single-Cell Sequencing. *Cell* **173**, 1--15 (2018).

272. M. C. Ravichandran, S. Fink, M. N. Clarke, F. C. Hofer, C. S. Campbell, Genetic interactions between specific chromosome copy number alterations dictate complex aneuploidy patterns. *Gene Dev* **32**, 1485--1498 (2018).

273. J. Zhu, N. Pavelka, W. D. Bradford, G. Rancati, R. Li, Karyotypic Determinants of Chromosome Instability in Aneuploid Budding Yeast. *Plos Genet* **8**, e1002719 (2012).

274. M. Gerstung, *et al.*, The evolutionary history of 2,658 cancers. *Nature* (2020) https:/doi.org/10.1038/s41586-019-1907-7.

275. C. M. Bielski, *et al.*, Genome doubling shapes the evolution and prognosis of advanced cancers. *Nat Genet* **50**, 1189--1195 (2018).

276. S. L. Carter, *et al.*, Absolute quantification of somatic DNA alterations in human cancer. *Nat Biotechnol* **30**, 413–421 (2012).

277. S. Lopez, *et al.*, Interplay between whole-genome doubling and the accumulation of deleterious alterations in cancer evolution. *Nat Genet* (2020) https:/doi.org/10.1038/s41588-020-0584-7.

278. C. Colijn, G. Plazzotta, A Metric on Phylogenetic Tree Shapes. *Systematic Biol* **67**, 113--126 (2018).

279. A. Dayarian, B. I. Shraiman, How to infer relative fitness from a sample of genomic sequences. *Genetics* (2014) https:/doi.org/10.1534/genetics.113.160986.

280. M. Manceau, A. Lambert, H. Morlon, Phylogenies support out-of-equilibrium models of biodiversity. *Ecol Lett* (2015) https:/doi.org/10.1111/ele.12415.

281. K. Csillery, O. Francois, M. G. B. Blum, Abc: An R package for approximate Bayesian computation (ABC). *Methods Ecol Evol* (2012) https:/doi.org/10.1111/j.2041-210x.2011.00179.x.

282. Y. Bollen, *et al.*, Reconstructing single-cell karyotype alterations in colorectal cancer identifies punctuated and gradual diversification patterns. *Nat Genet* **53**, 1187–1195 (2021).

283. G. D. Evrony, A. G. Hinch, C. Luo, Applications of Single-Cell DNA Sequencing. *Annu Rev Genom Hum G* **22**, 1–27 (2021).

284. S. M. Dewhurst, *et al.*, Tolerance of Whole-Genome Doubling Propagates Chromosomal Instability and Accelerates Cancer Genome Evolution. *Cancer Discov* **4**, 175–185 (2014).

285. J. M. Nicholson, *et al.*, Chromosome mis-segregation and cytokinesis failure in trisomic human cells. *eLife* **4**, e05068 (2015).

286. B. Orr, L. Talje, Z. Liu, B. H. Kwok, D. A. Compton, Adaptive Resistance to an Inhibitor of Chromosomal Instability in Human Cancer Cells. *Cell Reports* **17**, 1755--1763 (2016).

287. Y. Gusev, V. Kagansky, W. C. Dooley, A stochastic model of chromosome segregation errors with reference to cancer cells. *Math Comput Model* **32**, 97–111 (2000).

288. M. A. Nowak, *et al.*, The role of chromosomal instability in tumor initiation. *Proc National Acad Sci* **99**, 16226--16231 (2002).

289. B. A. A. Weaver, D. W. Cleveland, The role of aneuploidy in promoting and suppressing tumors. *J Cell Biology* **185**, 935--7 (2009).

290. N. Auslander, *et al.*, Cancer-type specific aneuploidies hard-wire chromosome-wide gene expression patterns of their tissue of origin. *Biorxiv*, 563858 (2019).

291. L. M. Sack, *et al.*, Profound Tissue Specificity in Proliferation Control Underlies Cancer Drivers and Aneuploidy Patterns. *Cell* **173**, 499-514.e23 (2018).

292. M. R. Starostik, O. A. Sosina, R. C. McCoy, Single-cell analysis of human embryos reveals diverse patterns of aneuploidy and mosaicism. *Genome Res* **30**, 814–825 (2020).

293. F. Foijer, *et al.*, Chromosome instability induced by Mps1 and p53 mutation generates aggressive lymphomas exhibiting aneuploidy-induced stress. *Proc National Acad Sci* **111**, 13427--13432 (2014).

294. J. E. Grim, *et al.*, Fbw7 and p53 Cooperatively Suppress Advanced and Chromosomally Unstable Intestinal Cancer. *Mol Cell Biol* **32**, 2160–2167 (2012).

295. C. López-García, *et al.*, BCL9L Dysfunction Impairs Caspase-2 Expression Permitting Aneuploidy Tolerance in Colorectal Cancer. *Cancer Cell* **31**, 79–93 (2017).

296. S. Simoes-Sousa, *et al.*, The p38α Stress Kinase Suppresses Aneuploidy Tolerance by Inhibiting Hif-1α. *Cell Reports* **25**, 749--760.e6 (2018).

297. M. Soto, *et al.*, p53 Prohibits Propagation of Chromosome Segregation Errors that Produce Structural Aneuploidies. *Cell Reports* **19**, 2423–2431 (2017).

298. U. Wilensky, NetLogo. http://ccl.northwestern.edu/netlogo/. *Center for Connected Learning and ComputerBased Modeling Northwestern University Evanston IL* (1999).

299. J. M. Sheltzer, A. Amon, The aneuploidy paradox: costs and benefits of an incorrect karyotype. *Trends in Genetics* **27**, 446–453 (2011).

300. M. Kendall, M. Boyd, C. Colijn, phyloTop: Tools for calculating and viewing topological properties of phylogenetic trees (2018).

301. K. Csillery, M. G. B. Blum, O. E. Gaggiotti, O. Francois, Approximate Bayesian Computation (ABC) in practice. *Trends Ecol Evol* **25**, 410--418 (2010).

302. M. L. Leung, *et al.*, Highly multiplexed targeted DNA sequencing from single nuclei. *Nat Protoc* **11**, 214--235 (2016).

303. T. Garvin, *et al.*, Interactive analysis and assessment of single-cell copy-number variations. *Nat Methods* **12**, 1058--1060 (2015).

304. T. Baslan, *et al.*, Optimizing sparse sequencing of single cells for highly multiplex copy number profiling. *Genome Res* **125**, 714--724 (2015).

305. T. Boveri, *Zur frage der entstehung maligner tumoren* (Fischer, 1914).

306. D. P. von Hansemann, Ueber asymmetrische Zelltheilung in Epithel-krebsen und deren biologische Bedeutung. *Virchow's Archiv fur pathologische Anatomie und Physiologie und fur klinische Medizin*, 299--326 (1890).

307. M. Jamal-Hanjani, *et al.*, Extreme chromosomal instability forecasts improved outcome in ER-negative breast cancer: a prospective validation cohort study from the TACT trial. *Annals of Oncology* **26**, 1340–1346 (2015).

308. R. Roylance, *et al.*, Relationship of Extreme Chromosomal Instability with Long-term Survival in a Retrospective Analysis of Primary Breast Cancer. *Cancer Epidemiology, Biomarkers & Prevention* **20**, 2183–2194 (2011).

309. B. I. Zaki, A. A. Suriawinata, A. R. Eastman, K. M. Garner, S. F. Bakhoum, Chromosomal instability portends superior response of rectal adenocarcinoma to chemoradiation therapy. *Cancer* **120**, 1733–1742 (2014).

310. A. Lashen, *et al.*, The characteristics and clinical significance of atypical mitosis in breast cancer. *Mod Pathol* **35**, 1341–1348 (2022).

311. R. Ohashi, *et al.*, Prognostic utility of atypical mitoses in patients with breast cancer: A comparative study with Ki67 and phosphohistone H3. *Journal of Surgical Oncology* **118**, 557–567 (2018).

312. J. M. Sheltzer, A transcriptional and metabolic signature of primary aneuploidy is present in chromosomally-unstable cancer cells and informs clinical prognosis. **73**, 6401--6412 (2014).

313. K. A. Knouse, J. Wu, C. A. Whittaker, A. Amon, Single cell sequencing reveals low levels of aneuploidy across mammalian tissues. *Proc National Acad Sci* (2014) https:/doi.org/10.1073/pnas.1415287111.

314. M. Brunori, *et al.*, TRF2 inhibition promotes anchorage-independent growth of telomerase-positive human fibroblasts. *Oncogene* **25**, 990–997 (2006).

315. A. Bennett, *et al.*, Cenp-E inhibitor GSK923295: Novel synthetic route and use as a tool to generate aneuploidy. *Oncotarget* **6**, 20921--32 (2015).

316. A. R. Lynch, B. Shermineh, M. E. Burkard, The Reckoning of Chromosomal Instability: past, present, and future. *Under Review*.

317. S. J. Klaasen, *et al.*, Nuclear chromosome locations dictate segregation error frequencies. *Nature* **607**, 604–609 (2022).

318. D. Venet, J. E. Dumont, V. Detours, Most Random Gene Expression Signatures Are Significantly Associated with Breast Cancer Outcome. *PLOS Computational Biology* **7**, e1002240 (2011).

319. A. J. Holland, *et al.*, The autoregulated instability of Polo-like kinase 4 limits centrosome duplication to once per cell cycle. *Gene Dev*, 2684--2689 (2012).

320. A. R. Lynch, M. E. Burkard, CINFER: an interactive, web-based platform for inference of chromosome mis-segregation rates from scDNAseq data. *Under Review*.

321. C. Buccitelli, *et al.*, Pan-cancer analysis distinguishes transcriptional changes of aneuploidy from proliferation. *Genome Res* **27**, 501–511 (2017).

322. E. Laks, *et al.*, Clonal Decomposition and DNA Replication States Defined by Scaled Single-Cell Genome Sequencing. *Cell* **179**, 1207--1221.e22 (2019).

323. Y. Yin, *et al.*, High-Throughput Single-Cell Sequencing with Linear Amplification. *Mol Cell* **76**, 676-690.e10 (2019).

324. N. Donnelly, V. Passerini, M. Durrbaum, S. Stingele, Z. Storchova, HSF 1 deficiency and impaired HSP 90-dependent protein folding are hallmarks of aneuploid human cells. *Embo J* **33**, 2374--2387 (2014).

325. N. K. Chunduri, *et al.*, Systems approaches identify the consequences of monosomy in somatic human cells. *Nat Commun* **12**, 5576 (2021).

326. L. Garribba, *et al.*, Short-term molecular consequences of chromosome mis-segregation for genome stability | Nature Communications. *Nature Communications* **14**, 1353 (2023).

327. K. M. Schukken, J. M. Sheltzer, “Extensive protein dosage compensation in aneuploid human cancers” (Genomics, 2021) https:/doi.org/10.1101/2021.06.18.449005 (December 18, 2021).

328. P. Cheng, *et al.*, Proteogenomic analysis of cancer aneuploidy and normal tissues reveals divergent modes of gene regulation across cellular pathways. *eLife* **11**, e75227 (2022).

329. A. P. Gasch, *et al.*, Further support for aneuploidy tolerance in wild yeast and effects of dosage compensation on gene copy-number evolution. *eLife* **5**, e14409 (2016).

330. E. M. Torres, M. Springer, A. Amon, No current evidence for widespread dosage compensation in S. cerevisiae. *eLife* **5**, e10996 (2016).

331. J. Hose, *et al.*, Dosage compensation can buffer copy-number variation in wild yeast. *eLife* **4**, e05462 (2015).

332. S. A. Godinho, *et al.*, Oncogene-like induction of cellular invasion from centrosome amplification. *Nature* **510**, 167–171 (2014).

333. R. C. Team, R: A language and environment for statistical computing. (2021).

334. I. Scheinin, *et al.*, DNA copy number analysis of fresh and formalin-fixed specimens by shallow whole-genome sequencing with identification and exclusion of problematic regions in the genome assembly. *Genome Res* **24**, 2022–2032 (2014).

335. B. Bushnell, BBMap (2022).

336. T. RStudio, RStudio: Integrated Development for R. (2020).

337. Y. Liao, G. K. Smyth, W. Shi, The R package Rsubread is easier, faster, cheaper and better for alignment and quantification of RNA sequencing reads. *Nucleic Acids Res* (2019) https:/doi.org/10.1093/nar/gkz114.

338. M. D. Robinson, D. J. McCarthy, G. K. Smyth, edgeR: a Bioconductor package for differential expression analysis of digital gene expression data. *Bioinformatics* **26**, 139–140 (2010).

339. M. E. Ritchie, *et al.*, limma powers differential expression analyses for RNA-sequencing and microarray studies. *Nucleic Acids Research* **43**, e47–e47 (2015).

340. C. W. Law, Y. Chen, W. Shi, G. K. Smyth, voom: precision weights unlock linear model analysis tools for RNA-seq read counts. *Genome Biol* **15**, R29 (2014).

341. M. Trakala, *et al.*, Clonal selection of stable aneuploidies in progenitor cells drives high-prevalence tumorigenesis. *Genes Dev.* **35**, 1079–1092 (2021).

342. C. Villarroya-Beltri, *et al.*, Biallelic germline mutations in MAD1L1 induce a syndrome of aneuploidy with high tumor susceptibility. *Science Advances* **8**, eabq5914 (2022).

343. L. M. Zasadil, *et al.*, High rates of chromosome missegregation suppress tumor progression but do not inhibit tumor initiation. *Mol Biol Cell* **27**, 1981–1989 (2016).

344. M. G. B. Blum, O. Francois, On statistical tests of phylogenetic tree imbalance: The Sackin and other indices revisited. *Math Biosci* (2005) https:/doi.org/10.1016/j.mbs.2005.03.003.

345. M. A. Beaumont, Approximate Bayesian Computation. *Annu Rev Stat Appl* **6**, 379–403 (2019).

346. M. A. Beaumont, W. Zhang, D. J. Balding, Approximate Bayesian computation in population genetics. *J Wildl Management* **162**, 2025--2035 (2002).

347. S. Tavare, D. J. Balding, R. C. Griffiths, P. Donnelly, Inferring coalescence times from DNA sequence data. *Genetics* **145**, 505--518 (1997).

348. J. Salecker, M. Sciaini, K. M. Meyer, K. Wiegand, The nlrx r package: A next-generation framework for reproducible NetLogo model analyses. *Methods in Ecololgy and Evolution* **00**, 2041–210X (2019).

349. K. Müller, H. Wickham, D. A. James, S. Falcon, “RSQLite: SQLite interface for R” (2023).

350. W. Chang, *et al.*, “shiny: Web application framework for R” (2022).

351. H. Wickham, *et al.*, Welcome to the tidyverse. *Journal of Open Source Software* **4**, 1686 (2019).

352. J. Melville, “uwot: The uniform manifold approximation and projection (UMAP) method for dimensionality reduction” (2022).

353. A. J. Holland, D. W. Cleveland, Boveri revisited: chromosomal instability, aneuploidy and tumorigenesis. *Nat Rev Mol Cell Bio* **10**, 478--487 (2009).

354. L. Sansregret, B. Vanhaesebroeck, C. Swanton, Determinants and clinical implications of chromosomal instability in cancer. *Nat Rev Clin Oncol* **15**, 139--150 (2018).

355. B. A. Weaver, How Taxol/paclitaxel kills cancer cells. *Mol Biol Cell* **25**, 2677--2681 (2014).

356. G. Fountzilas, *et al.*, A randomized phase III study comparing three anthracycline-free taxane-based regimens, as first line chemotherapy, in metastatic breast cancer. *Breast Cancer Res Treat* **115**, 87–99 (2009).

357. M. Imreh, *et al.*, In vitro culture conditions favoring selection of chromosomal abnormalities in human ES cells. *Journal of cellular biochemistry* **99**, 508–516 (2006).

358. P. Catalina, *et al.*, Human ESCs predisposition to karyotypic instability: Is a matter of culture adaptation or differential vulnerability among hESC lines due to inherent properties? *Molecular Cancer* **7**, 1–9 (2008).

359. N. Gaztelumendi, C. Nogués, Chromosome Instability in mouse Embryonic Stem Cells. *Sci Rep* **4**, 5324 (2014).

360. M. Li, *et al.*, The ATM–p53 pathway suppresses aneuploidy-induced tumorigenesis. *Proceedings of the National Academy of Sciences* **107**, 14188–14193 (2010).

361. S. L. Thompson, D. A. Compton, Proliferation of aneuploid human cells is limited by a p53-dependent mechanism. *Journal of Cell Biology* **188**, 369–381 (2010).

362. J. B. Geigl, A. C. Obenauf, T. Schwarzbraun, M. R. Speicher, Defining 'chromosomal instability.' *Trends in Genetics* **24**, 64–69 (2008).

363. M. Clemente-Ruiz, *et al.*, Gene Dosage Imbalance Contributes to Chromosomal Instability-Induced Tumorigenesis. *Dev Cell* **36**, 290--302 (2016).

364. R. E. A. Gutteridge, M. A. Ndiaye, X. Liu, N. Ahmad, Plk1 Inhibitors in Cancer Therapy: From Laboratory to Clinics. *Molecular Cancer Therapeutics* **15**, 1427–1435 (2016).

365. F. Atrafi, *et al.*, A Phase I Study of an MPS1 Inhibitor (BAY 1217389) in Combination with Paclitaxel Using a Novel Randomized Continual Reassessment Method for Dose Escalation. *Clinical Cancer Research* **27**, 6366–6375 (2021).